



# Fracture by cavitation of model polyurethane elastomers

Antonella Cristiano

## ► To cite this version:

Antonella Cristiano. Fracture by cavitation of model polyurethane elastomers. Chemical Physics [physics.chem-ph]. Université Pierre et Marie Curie - Paris VI, 2009. English. NNT: . pastel-00578499

**HAL Id: pastel-00578499**

**<https://pastel.hal.science/pastel-00578499>**

Submitted on 21 Mar 2011

**HAL** is a multi-disciplinary open access archive for the deposit and dissemination of scientific research documents, whether they are published or not. The documents may come from teaching and research institutions in France or abroad, or from public or private research centers.

L'archive ouverte pluridisciplinaire **HAL**, est destinée au dépôt et à la diffusion de documents scientifiques de niveau recherche, publiés ou non, émanant des établissements d'enseignement et de recherche français ou étrangers, des laboratoires publics ou privés.

**THESE DE DOCTORAT DE  
L'UNIVERSITÉ PIERRE ET MARIE CURIE**

Spécialité

Chimie et Physico-Chimie des Polymères  
(ED 397)

Présentée par

**Mme. Antonella CRISTIANO**

Pour obtenir le grade de

**DOCTEUR de l'UNIVERSITÉ PIERRE ET MARIE CURIE**

Sujet de la thèse :

***FRACTURE BY CAVITATION OF MODEL  
POLYURETHANE ELASTOMERS***

Soutenue le: 08 Juin 2009

Devant le jury composé de :

M. Alain Fradet,	Professeur, Université Pierre et Marie Curie,	Présidente du jury
M. Lucian Laiarinandrasana,	Maître de Recherche, ENSMP,	Rapporteur
M. Laurent Chazeau,	Chargé de Recherche CNRS, INSA de Lyon,	Rapporteur
M. Bruno Fayolle,	Maître de Conférences, Paris, ENSAM,	Examineur
Mme. Alba Marcellan,	Maître de Conférences, UPMC,	Co-directrice de thèse
M. Costantino Creton,	Directeur de Recherche CNRS, ESPCI,	Directeur de thèse



*A mi amado esposo Pablo, Gracias por tu apoyo y tu comprensión*  
*A mis amados Padres, Santina y Antonio, Mi luz e inspiración en este*  
*camino llamado vida*





## Acknowledgments

I am convinced that no thesis project is ever the product of one person's efforts. Now is my turn to express my sincere gratitude to all the people that in different ways contributed to the realization of this Thesis.

First of all, I would like to thank Costantino Creton, my thesis director. Since the very beginning I was sure that working with you was a guarantee of success, and I was right. You gave me the opportunity to come to work in your research group, and it was my pleasure. Your passion to teach and clarity to explain made my way clearer. I want to thank you for the moments of encouragement, for your words telling me go head you can make it!.

The financial support from DSM Research Center in Geelen (The Netherlands). I am particularly grateful to Markus Bulters, Paul Steeman, Bert Kerstra, and Jan Stolk, thank you for all the support and helpful discussions throughout the complete thesis.

I would like to thank to Alba Marcellan, my thesis co-director for the help and support in many different technical aspects.

I would like to thank to: Martine Tessier, for the help with  $^1\text{H}$  NMR,  $^{13}\text{C}$  NMR and Maldi-ToF techniques. Sandrine Mariot for help with DMA experiments. Agnès Pallier for GPC and  $^1\text{H}$  NMR, and Guylaine Ducouret  $^{13}\text{C}$  NMR experiments. Dominique Hourdet for the help with swelling experiments interpretation. Freddy Martin for the technical support and friendship.

A special thank goes to Kay Saalwächter for the kindly help with NMR solid experiments and for further explanations.

I also would like to thank Ludovic Olanier for the design and building of the samples'holder and the different molds. Lucien Laiarinandrasana (ENSMP) for helpful discussions. Fabrice Monti for the programme to calculate volume's change.

Thanks to Professor C.Y. Hui in the department of Theoretical and Applied Mechanics at Cornell University in Ithaca, USA for interesting comments and suggestions, as well as his PhD student L. Rong for the penny-shaped crack FEM simulation.

My special thanks to my friends and colleagues at the lab, who stayed there in different ways supporting me and helping me: Clara Carelli, Harry Retsos, Fanny Deplace (thanks for your help with the cameras and MTS machine), Samy Mzabi (always willing to help), Nick Glassmaker (thanks for the macros in igor), Tetsuo Yamaguchi (for helpful discussions).

To Astrid, Isabelle, Karine, Elise, Leila, Julia, Griffith, Sébastien and Cécile, for the good moments at the lab.

From the personal point of view, I would like to thank my family. Primero quisiera agradecer a mis Padres, Gracias a ustedes hoy estoy aqui culminando una etapa de mi vida a lo largo de la cual ustedes siempre me acompañaron y apoyaron; ustedes han sido el amor y apoyo

incondicional. A mi hermana Vally, quien siempre me ha ayudado y apoyado en todo. A mi hermana Lina y sobrino Claudio por estar allí. A mi familia en Argentina, a quienes tanto quiero. Por supuesto a mi querido Pablo, gracias por estar allí cada día, por tu paciencia, apoyo, ayuda, perseverancia y amor; sin ti no hubiese sido posible llegar a este punto. Gracias a Todos !

L'objectif principal de cette thèse a été de déterminer le rôle joué par l'architecture macromoléculaire du réseau sur les propriétés élastiques non linéaires, la résistance à la rupture et la résistance à la cavitation sous chargement hydrostatique. Nous avons synthétisé, dans des conditions contrôlées, trois réseaux élastomères dits « modèles » de Polyuréthane (PU), à partir d'un triisocyanate et de polyether diols isomoléculaires (PPG). Une caractérisation physico-chimique fine des réactifs et des réseaux a été réalisée en utilisant des techniques telles que : RMN, FTIR et fractions solubles. Les propriétés élastiques non linéaires, viscoélastiques linéaires et la résistance à la rupture en mode I des trois réseaux modèles ont été caractérisées. Les essais de cavitation ont été effectués sur un dispositif expérimental développé pour cette étude, permettant de suivre les mécanismes de formation de cavités, à la résolution optique près, en temps réel. En menant une analyse systématique des conditions de cavitation, en fonction de la vitesse de déformation et de la température, il est apparu que, contrairement au modèle d'instabilité élastique communément utilisé, l'expansion critique de la cavité n'est pas uniquement pilotée par le module élastique; mais dépend fortement de l'énergie de rupture,  $G_C$  et de l'extensibilité limite du réseau.

Par ailleurs, nous avons observé l'apparition de cavités pré-critiques avant la fracture catastrophique ; ce qui met en évidence l'existence de deux critères : l'un, propre au processus de nucléation, principalement piloté par des mécanismes statistiques et activés thermiquement (distribution de défauts, temps, température, etc.) ; et l'autre, lié à la croissance de la cavité en milieu confiné contrôlé par  $G_{IC}$ , et par le comportement aux grandes déformations. Enfin, la présence d'enchevêtrements dans l'architecture du réseau macromoléculaire s'est avérée clairement bénéfique pour stabiliser la croissance de cavités et donc pour renforcer la résistance à la cavitation.

Mots clés : polyuréthane, élastomères, réseaux modèle, fracture, cavitation.

The main objective of this thesis was to establish the role played by the composition and crosslinking structure of an elastomer on its resistance to cavitation under a predominantly hydrostatic pressure. We prepared three polyurethane model networks from triisocyanate and monodisperse polyether diols (PPGs) of various molecular weights, under well controlled conditions and carried out a complete characterization of the reagents and of the networks by using NMR, FTIR, analysis of the solfractions and DMA. We evaluated the nonlinear elastic and linear viscoelastic properties of the three model networks and determined their fracture toughness in mode I with notched samples. We performed cavitation experiments at different strain rates and temperatures on the transparent samples using an original setup developed specifically for the thesis combining a well controlled confining geometry and real-time optical visualization. Failure occurred in two steps: small and stable pre-critical cavities appeared during loading before catastrophic fracture occurred by the rapid growth of a single large cavity at or near the center of the sample. This implied the existence of two separate criteria: one for the nucleation and one for the growth. The critical cavitation stress was found to decrease significantly with decreasing strain rate and increasing temperature in clear disagreement with existing cavitation models by cavity expansion or by fracture. The analysis of the cavitation results strongly suggests a beneficial influence of a high mode I fracture toughness  $G_{IC}$  and of a marked strain hardening of the network on the critical cavitation stress. Moreover, the existence of time dependence of the nucleation rate of the cavities under stress has been pointed out. In terms of materials, we mainly demonstrate that the presence of entanglements toughen the material which stabilizes the crack growth even in confined conditions. We concluded that *the cavitation strength depends not only on the modulus but on the mode I fracture toughness and that the distribution of defects and subcritical crack growth is important for the nucleation rate.*

Keywords: polyurethane, elastomers, model networks, fracture, cavitation.

UPMC Université Paris 06  
Laboratoire PPMD UMR 7615 CNRS  
ESPCI  
10 Rue Vauquelin  
F-75231 Paris Cedex 05



# Table of Contents

GENERAL INTRODUCTION .....	13
CHAPTER 1: Theoretical Concepts.....	17
Introduction .....	19
1.1.- The Networks.....	19
1.1.1.- The Polyurethane (PU) Networks.....	19
1.1.1.1.- Brief History .....	19
1.1.1.2.- Polyurethane components .....	20
1.1.1.2.1.- Polyols.....	20
1.1.1.2.2.- Polyisocyanates.....	20
1.1.1.3.- Polycondensation of isocyanate-polyol to produce Polyurethane .....	21
1.1.1.3.1.- Secondary reactions .....	23
1.1.1.4.- Additives for polyurethanes' preparation .....	24
1.1.2.- Model Networks.....	24
1.1.3.- Bimodal Networks .....	25
1.2.- Self-Assembled Monolayers (SAMs).....	25
1.3.- Rubber elasticity .....	26
1.3.1.- Continuum Mechanics, Small and Large Strain Elasticity .....	27
1.3.2.- Elastic properties at small strains.....	28
1.3.3.- The Strain Energy Function $W$ .....	29
1.3.4.- Strain Invariants.....	30
1.3.5.- The statistical mechanical theory of rubber elasticity.....	31
1.3.5.1.- Statistical theory of rubber elasticity .....	31
1.3.5.1.1.- Affine network model .....	33
1.3.5.1.2.- Phantom network model .....	34
1.3.6.- Thermodynamics of elastomers deformation.....	35
1.3.7.- Deviations from rubber elasticity theory .....	36
1.3.7.1.- Chain entanglements.....	37
1.3.7.2.- Finite extensibility .....	38
1.4.- Compression or Tension under confined conditions .....	40
1.4.1.- Cavitation.....	41
1.4.1.1.- Inflation of a Spherical Shell (Balloon).....	41
1.5.- Viscoelasticity: Effects of Temperature and Frequency.....	42
1.6.- Fracture behaviour .....	44
1.6.1.- The energy balance approach.....	46
1.6.2.- The Threshold Energy: Molecular model.....	48
1.7.- Molecular rate processes with a constant activation energy: relevance for fracture processes.....	49
Bibliography.....	51
CHAPTER 2: Model Networks: Purifications, Synthesis and Characterizations.....	53
Introduction .....	55
2.1.- Materials .....	56
2.2.- Purifications and Characterization.....	56
2.2.1.- Purifications of reagents .....	56
2.2.1.1.- Purification of Poly(propylene) glycols (PPGs): .....	56
2.2.1.2.- Characterization of PPGs.....	57
2.2.1.2.1.- Molecular weight: Nuclear Magnetic Resonance (NMR) .....	57
2.2.1.2.2.- Polydispersity: Gel permeation Chromatography (GPC) .....	61

2.2.1.2.3.- MALDI-ToF .....	61
2.2.1.3.- Purification of DESMODUR RFE to obtain tris(p-isocyanatophenyl) thiophosphate .....	62
2.2.1.4.- Characterization of purified tris(p-isocyanatophenyl) thiophosphate : .....	63
2.3.- Preparation of Model Networks .....	64
2.3.1. Synthesis of PU networks .....	64
2.3.2. Networks molding and curing .....	66
2.4.- Model Networks Characterization .....	68
2.4.1.- Chemical groups identification: ATR-FTIR .....	68
2.4.2.- Density of Polyurethanes networks .....	71
2.4.3.- Sol Fraction and Swelling experiments .....	72
2.4.3.1.- Solfractions .....	72
2.4.3.2.- Swelling experiments .....	72
2.4.4.- Model Networks Homogeneity: Proton Multiple-quantum (MQ) NMR .....	75
2.5.- Small strain behaviour by Dynamical Mechanical Analysis (DMA) .....	78
2.5.1.- DMA results and Thermoelasticity .....	78
2.5.1.1.- Density changes with temperature: Thermal expansion of the networks .....	85
Conclusions .....	88
Acknowledgements .....	89
Appendices A2 .....	90
Appendix A2.1: NMR .....	90
Appendix A2.2: GPC .....	95
Appendix A2.3: MALDI-ToF .....	95
Appendix A2.4: Experimental adjustment of NCO/OH .....	96
Appendix A2.5: Optimization of the time for the curing at 80°C of the polyurethane model networks .....	96
Appendix A2.6: Density calculations .....	97
Appendix A2.7: Solubility parameters .....	97
Appendix A2.8: $D_{res}$ as a function of the swelling percentage in mass .....	97
Appendix A2.9: Thermal expansion .....	98
Bibliography .....	99
CHAPTER 3: Mechanical Properties of the Polyurethane Model Networks .....	101
Introduction .....	103
3.1.-Large strain behaviour: Non-linear elasticity .....	103
3.1.1.- Uniaxial extension: Experimental part and Results .....	105
3.1.2.- Uniaxial Compression: Experimental part and Results .....	109
3.2.- Strain Rate Dependent Properties in the Linear Regime .....	114
3.3.- Fracture Properties .....	119
3.3.1.- Introduction .....	119
3.3.1.1 Estimate of threshold energy for crack growth: $G_0$ .....	121
3.3.2.- Experimental part .....	123
3.3.3.- Fracture Results at standard conditions .....	125
3.3.4.- Fracture Results at different temperatures .....	129
3.3.5.- Fracture Results at different speeds .....	130
Conclusions .....	136
Appendices A3 .....	137
Appendix A3.1: Time-Temperature Superposition for PU4000 .....	137
Appendix A3.2: Time-Temperature Superposition for PU8000 .....	139
Appendix A3.3: Time-Temperature Superposition for PU8000/1000 .....	142

Appendix A3.4: Fracture results .....	145
Bibliography .....	147
CHAPTER 4: Cavitation Phenomena: Experimental Methodology .....	149
Introduction .....	151
4.1.- Literature review: selected geometry .....	151
4.2.- Experimental aspects: Cavitation samples preparation.....	155
4.2.1.- Glass surface modification.....	155
4.2.1.1.- Materials .....	155
4.2.1.2.- Procedure .....	155
4.2.2.- Metallic molds: design and surface modification .....	156
4.2.2.1.-Metallic molds: surface modification .....	157
4.2.2.1.1.- Materials .....	157
4.2.2.1.2.- Procedure .....	157
4.2.3.- Cavitation Samples' preparation – control of the geometry .....	158
4.3.- Design, construction and positioning of samples' holder.....	160
4.4.- Cavitation experiments and data treatment.....	162
4.5.- Analysis of cavitation experiments by FEM Simulation .....	165
4.5.1.- The Geometry and boundary conditions.....	165
4.5.2.- The Material behavior .....	166
4.5.3.- Calculations of the stress distribution (in linear elasticity).....	166
4.5.3.1. Radial evolution of the Hydrostatic stress.....	166
4.5.3.2.- Influence of confinement: the layer thickness .....	168
4.5.1.5.- From the Force to the local hydrostatic stress .....	169
4.6.- Cavitation experiments: FEM Simulation versus experimental results.....	171
Conclusions .....	174
Acknowledgments .....	175
Appendices A4 .....	176
Appendix A4.1: Comparison of 'h' measured by microscopy and directly in the center .....	176
Appendix A.4.2 Samples'holder .....	176
Appendix A4.3: Reproducibility of the curves obtained for cavitation experiments.....	177
Appendix A4.5: Calibration constant calculation .....	178
Appendix A.4.6: Fitting of hyperelastic model with experimental compression and tension data.....	180
Bibliography .....	181
CHAPTER 5: Cavitation Phenomena: Experimental Mechanisms .....	183
Introduction .....	185
5.1.- Experimental cavitation results at standard conditions.....	186
5.1.1. General trends: Shape of the curve and Maximal hydrostatic stress.....	186
5.1.1.1. PU4000 .....	186
5.1.1.2. PU8000.....	189
5.1.1.3-. PU8000/1000 .....	191
5.1.1.4.- Comparative analysis: maximal hydrostatic stresses and critical cavity formation .....	193
5.1.2.- Critical cavity growth - Crack propagation (Region B).....	196
5.1.3.- Morphology of the fracture surfaces.....	197
5.2.- Cavitation results at different temperatures .....	199
5.2.1.- Experimental part and results at different temperatures .....	199



5.2.1.1.- General trends .....	199
5.2.1.2.- Critical cavity size and crack propagation .....	204
5.2.1.3.- Fracture morphology .....	204
5.3.- Cavitation results at different strain rates .....	206
5.3.1.- Experimental part and results at different strain rates .....	206
5.3.1.1.- General trends .....	206
5.2.1.2.- Critical cavity size and crack propagation .....	209
5.2.1.3.- Fracture morphology .....	210
5.4.- Pre-critical cavities analysis .....	211
5.4.1.-Lateral profile: Volume change .....	211
5.4.2.- Conditions of pre-critical cavity formation .....	212
5.4.2.1.- Pre-critical cavities analysis at standard conditions .....	214
5.4.2.2.-Pre-critical analysis at high temperature .....	215
5.4.2.3.-Pre-critical analysis at low strain rate .....	216
Conclusions .....	219
Acknowledgments .....	220
Appendices A5 .....	221
Appendix A5.1: Cavitation results at standard conditions .....	221
Appendix A5.2: Cavitation results at different temperatures .....	223
Appendix A5.3: Cavitation results at different strain rates .....	226
Bibliography .....	227
 CHAPTER 6: Cavitation Models and Analysis .....	229
Introduction .....	231
6.1.- State-of-the-art .....	231
6.1.1.- Prediction of the resistance to cavitation based on the stress field and the elastic instability: Simple Deformation .....	231
6.1.2.- Cavitation resistance prediction considering the surface energy .....	233
6.1.3.- Prediction of the cavitation resistance based on the expansion by fracture .....	235
6.2.- Model-experiment comparisons: Temperature dependence .....	238
6.2.1.- Simple deformation cavitation model .....	238
6.2.2.- Expansion by Fracture: Linear Elastic Fracture Mechanics (LEFM) .....	239
6.2.3.- Non-linear Model: Strain hardening .....	240
6.2.3.1.- Fit of our experimental results with the nonlinear fracture model .....	244
6.3.- Model-experiment comparisons: Speed dependence .....	248
6.3.1.- Fitting of the experimental results at different speeds .....	248
6.4.- Statistics: Number of pre-critical cavities and position distribution .....	250
6.4.1.- Cumulative probability of cavitation .....	250
6.4.2.- Spatial distribution of pre-critical cavities .....	251
Conclusions .....	255
Acknowledgements .....	256
Appendices A6 .....	257
Appendix A6.1: FEM simulation for a penny-shaped crack in an infinite material subjected to internal pressure. ....	257
Appendix A6.2: FEM simulation .....	258
Bibliography .....	260
 GENERAL CONCLUSIONS .....	263
EXTENDED ABSTRACT IN FRENCH .....	269
GENERAL BIBLIOGRAPHY .....	279

## General Introduction

An elastomer is a polymer with the macroscopic property of elasticity at large strains. The molecular structure of elastomers can be imagined as a ‘spaghetti’ and ‘meatball’ structure, with spaghettis being the polymer chains and the meatballs the cross-links. Stress acting on the rubber network will stretch out and orient the chains between the crosslink joints (see Figure 1); this will decrease the entropy of the chains.

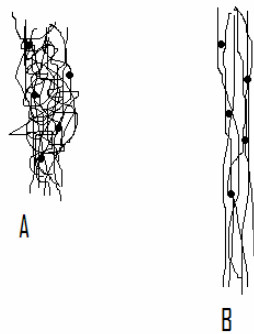


**Figure 1:** *A* is a schematic drawing of an unstressed elastomer. The dots represent cross-links. *B* is the same elastomer under stress. When the stress is removed, it will return to the *A* configuration.

The elasticity is a physical property of a material when it reversibly deforms under stress (e.g. external forces). In an elastomer the covalent cross-linkages ensure that the elastomer will return to its original configuration when the stress is removed. High extensibility and low shear modulus are the most remarkable properties of the elastomers; additionally, they present particular thermoelastic properties due to the entropic origin of the elasticity. The elastomers are used for coatings, seals, adhesives and molded flexible parts, among others.

However crosslinked elastomers are nearly incompressible materials with a low resistance to shear. This makes them prone to failure under tensile hydrostatic stress (see Figure 2).

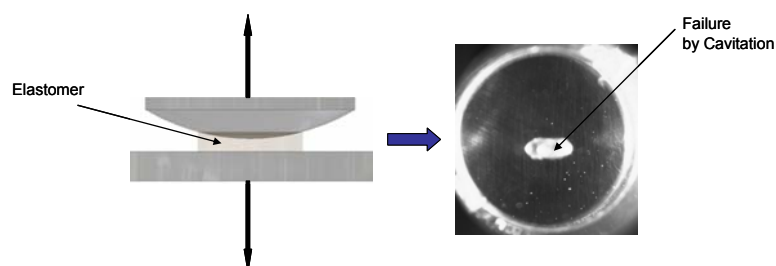


**Figure 2:** Confined elastomer under tensile hydrostatic stress (left) fail by the formation of cavities or cavitation (right)

In such elastomers, the application of a sufficiently large tensile load can cause the appearance of holes that were not previously evident in the material. Upon further loading, these cavities grow in size and may eventually coalesce. When loaded in tension, a critical state is reached when cavities suddenly grow in the body of the rubber, producing a drop in

the extending force. Experimental observations reveal the presence of internal cracks, which can initiate catastrophic failure if the load is increased further. This phenomenon is known as cavitation.

Although the failure by cavitation has been observed experimentally and analyzed decades ago, there have been no systematic investigations since, despite several further theoretical advances. A key aspect which was not investigated experimentally is the role of fracture toughness of the rubber on cavity growth. Initial analyses only focused on deformation and only in 1991, Gent proposed a model for rubber fracture under hydrostatic stress which was subsequently improved by Lin and coworkers in 2005.

The understanding of the resistance to cavitation is very important in applications such as optical fiber coatings where one cavity every kilometer is sufficient to disrupt transmission. It is essential for this application to obtain as high resistance to cavitation as possible while keeping the elastic modulus as low as possible.

The main objective of this thesis was to establish the role played by the composition and crosslinking structure of an elastomer (soft material) on its resistance to cavitation under a predominantly hydrostatic pressure. To accomplish this objective we decided to work with model networks with well defined molecular weight between crosslink points and very few loops, pendant chains and unreacted chains. We prepared polyurethane model networks from triisocyanate and diols (PPGs) of various molecular weights.

The first chapter of this thesis presents a brief selection of some basic concepts of chemistry, physico-chemistry, and mechanics of elastomers. Some well known fundamentals of fracture behaviour of polymers are presented and, the cavitation basics are introduced.

The different experimental procedures used and the results obtained in the Thesis are presented in Chapter 2, 3, 4, 5 and 6.

Chapter 2 focuses on the details of the preparation of the polyurethane model networks. Three different model networks were prepared: two homogeneous networks with two different molecular structures and crosslink densities, and a third bimodal network with the purpose of investigating the effect of adding short chains to long chains on the mechanical properties. The molecular characterization of the reagents and the thermoelastic properties and swelling properties of the networks are presented in order to determine their macromolecular architecture.

Chapter 3 contains the detailed characterization of the mechanical properties of the three networks when they are deformed homogeneously and when they are fractured in a simple mode I geometry. Here are presented the linear viscoelastic properties, the large strain

properties to characterize the effect of entanglements and finite extensibility of the network chains, and the fracture properties at different loading rate and temperatures.

Chapter 4 describes in detail the experimental methodology specifically developed to investigate the failure of the elastomers by cavitation in a reproducible and reliable way. We describe the design of a new original test set-up, the development of a specific methodology for the cavitation sample's preparation, the experimental procedure, the raw experimental results and the data analysis method.

Chapter 5 describes the experimental mechanisms of the observed cavitation phenomena occurring in the three polyurethane model networks under stress. To the best of our knowledge, this thesis reports the first experimental results on cavitation resistance as a function of average strain rate or temperature. Additionally, none of the previous studies have really focused on the early events of cavitation. We designed and performed well controlled cavitation experiments at different strain rates and temperatures and an optical real time visualization of the damage events inside the elastomers during the experiment was designed specifically to capture the early stages of cavity growth.

Chapter 6 discusses how the resistance to cavitation can be predicted from simpler properties such as nonlinear elasticity and fracture resistance in mode I. Results are analyzed in light of the pre-existing theoretical cavitation models and a new picture of the effect of experimental conditions and material properties is constructed.

A final comment to the French speaking reader. This thesis was funded and realized in close collaboration with the DSM Research Center in Geleen (The Netherlands). Specifically we worked with Markus Bulters, Paul Steeman, Bert Kerstra, and Jan Stolk, and we are particularly grateful to them for the continuing support and helpful discussions throughout the thesis. The manuscript has been completely written in English to let them read it. We apologize in advance for the additional effort of having to read in English.



# **Chapter 1**

## **Theoretical Concepts**

Introduction .....	19
1.1.- The Networks.....	19
1.1.1.- The Polyurethane (PU) Networks .....	19
1.1.1.1.- Brief History .....	19
1.1.1.2.- Polyurethane components .....	20
1.1.1.2.1.- Polyols.....	20
1.1.1.2.2.- Polyisocyanates.....	20
1.1.1.3.- Polycondensation of isocyanate-polyol to produce Polyurethane .....	21
1.1.1.3.1.- Secondary reactions .....	23
1.1.1.4.- Additives for polyurethanes' preparation .....	24
1.1.2.- Model Networks.....	24
1.1.3.- Bimodal Networks .....	25
1.2.- Self-Assembled Monolayers (SAMs) .....	25
1.3.- Rubber elasticity .....	26
1.3.1.- Continuum Mechanics, Small and Large Strain Elasticity .....	27
1.3.2.- Elastic properties at small strains.....	28
1.3.3.- The Strain Energy Function W .....	29
1.3.4.- Strain Invariants .....	30
1.3.5.- The statistical mechanical theory of rubber elasticity.....	31
1.3.5.1.- Statistical theory of rubber elasticity .....	31
1.3.5.1.1- Affine network model.....	33
1.3.5.1.2- Phantom network model .....	34
1.3.6.- Thermodynamics of elastomers deformation.....	35
1.3.7.- Deviations from rubber elasticity theory .....	36
1.3.7.1.- Chain entanglements.....	37
1.3.7.2.- Finite extensibility .....	38
1.4.- Compression or Tension under confined conditions .....	40
1.4.1.- Cavitation.....	41
1.4.1.1- Inflation of a Spherical Shell (Balloon) .....	41
1.5.- Viscoelasticity: Effects of Temperature and Frequency .....	42
1.6.- Fracture behaviour .....	44
1.6.1.- The energy balance approach.....	46
1.6.2.- The Threshold Energy: Molecular model .....	48
1.7.- Molecular rate processes with a constant activation energy: relevance for fracture processes.....	49
Bibliography.....	51

## Introduction

This thesis is inherently interdisciplinary combining synthetic chemistry with polymer physics and solid mechanics. In order to follow more easily the aspects of the thesis with which the reader may be less familiar with, we have summarized here the main basic scientific concepts that are used.

We start presenting some chemical reactions and components of Polyurethanes synthesis and the basic chemistry of surface modification by the preparation of Self-Assembled Monolayer (SAM). Then, we present the foundations of rubber elasticity: from its molecular origin to its continuum mechanics description at small (infinitesimal) and most importantly large (finite) strains. This section is then complemented by a brief reminder of the bases of viscoelasticity in polymers such as the time-temperature-superposition, and finally the continuum mechanics description of fracture and some basics of thermally activated processes are described.

### 1.1.- The Networks

#### 1.1.1.- The Polyurethane (PU) Networks

In this thesis we prepared three polyurethane model networks (elastomers) starting from diols and a triisocyanate. In this section we present the general aspects of polyurethane synthesis, including the main and secondary reactions.

##### *1.1.1.1.- Brief History*

In 1849, Würtz was the first using a reaction of a glycol with an isocyanate, but it was Otto Bayer in 1937 who discovered how to transform the product into a useful plastic. The pioneering work on polyurethane polymers was conducted by Otto Bayer and his coworkers at the laboratories of I.G. Farben in Leverkusen, Germany [Farben 1937]. They recognized that using the polyaddition principle to produce polyurethanes from liquid diisocyanates and liquid polyether or polyester diols seemed to point to special opportunities. Their objective was to obtain synthetic fibers and elastomers to substitute natural rubber. The new monomer combination also circumvented existing patents obtained by Wallace Carothers on polyesters. Initially, work focused on the production of fibres and flexible foams. With development constrained by World War II (when PU's were applied on a limited scale as aircraft coating), it was not until 1952 that polyisocyanates became commercially available. Commercial production of flexible polyurethane foam began in 1954, based on toluene diisocyanate (TDI) and polyester polyols. The invention of these foams (initially called imitation swiss cheese by the inventors) was thanks to water accidentally introduced in the reaction mix. These materials were also used to produce rigid foams, gum rubber, and elastomers. The first commercially available polyether polyol, poly(tetramethylene ether) glycol), was introduced by DuPont in 1956 by polymerizing tetrahydrofuran. Between 1965 and 1980 were developed foams based on MDI (diphenylmethane diisocyanate). More recently, building on existing polyurethane spray coating technology and polyetheramine chemistry, extensive



development of two-component polyurea spray elastomers took place in the 1990s. Their fast reactivity and relative insensitivity to moisture make them useful coatings for large surface area projects, such as secondary containment, manhole and tunnel coatings, and tank liners.

### **1.1.1.2.- Polyurethane components**

#### **1.1.1.2.1.- Polyols**

A polyol is a molecule with two or more hydroxyl functional groups  $R'-(OH)_n$ ,  $n \geq 2$ . These hydroxyl functional groups are available for organic reactions. A molecule with two hydroxyl groups is a diol (for linear chains), one with three is a triol (for network chains), one with four is a tetrol (for special foams) and so on. The main use of polymeric polyols is as reactants to make other polymers. They can be reacted with isocyanates to make polyurethanes, and this use consumes most polyether polyols.

In practice, polyols are distinguished from short chain or low-molecular weight glycol chain extenders and crosslinkers such as ethylene glycol (EG), 1,4-butanediol (BDO), diethylene glycol (DEG), glycerine, and trimethylol propane (TMP). Polyols are polymers in their own. They are formed by base-catalyzed addition of propylene oxide (PO), ethylene oxide (EO) onto a hydroxyl or amine containing initiator, or by polyesterification of a di-acid, such as adipic acid, with glycols, such as ethylene glycol or dipropylene glycol (DPG). Polyols extended with PO or EO are polyether polyols (see Figure 1.1). Polyols formed by polyesterification are polyester polyols. The choice of initiator, extender, and molecular weight of the polyol greatly affect its physical state, and the physical properties of the polyurethane polymer. Important characteristics of polyols are their molecular backbone, initiator, molecular weight, percentage of primary hydroxyl groups, functionality, and viscosity.

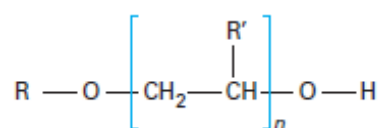


**Figure 1.1:** Polyether Polyol.

#### **1.1.1.2.2.- Polyisocyanates**

A polyisocyanate is a molecule with two or more isocyanate functional groups  $R-(N=C=O)_n$ ,  $n \geq 2$ . The isocyanates are very reactive components characterized by the presence of the group  $-N=C=O$ . The rate of the reaction depends on the family of the isocyanate, the most important parameters being the amount of reactive groups and the functionality. The polyisocyanates are produced by the phosgenation of an amine. Molecules that contain two isocyanate groups are called diisocyanates, and molecules containing three isocyanate groups are called triisocyanates. There exist two main families of aromatic polyisocyanates: TDI

(toluene diisocyanate) and MDI (diphenylmethane diisocyanate) (see Figure 1.2). There exist also aliphatic polyisocyanates, such as hexamethylene diisocyanate (HDI) or isophorone diisocyanate (IPDI).

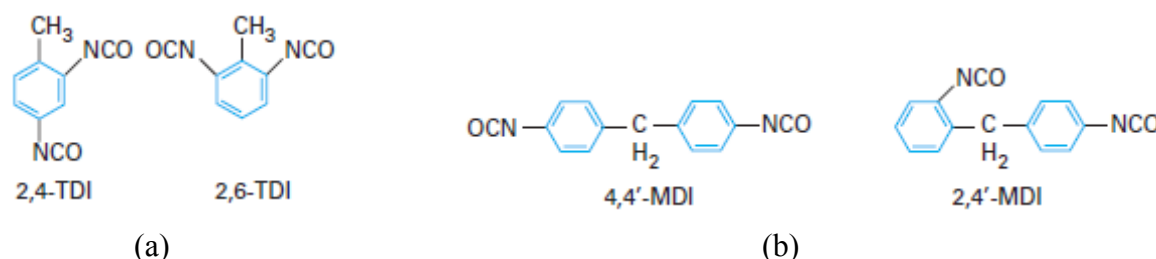


**Figure 1.2:** Isomers of (a) TDI and (b) MDI.

The isocyanates present a double bond  $N=C$  which is quite polar and react with all the components having a mobile hydrogen. Depending on the kind of isocyanate, the charges can be presented in two mesomeric forms [Abder-Rahim 2001] (see Figure 1.3).

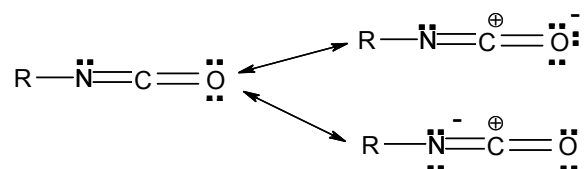


**Figure 1.3:** Mesomeric forms of isocyanate.

#### 1.1.1.3.- Polycondensation of isocyanate-polyol to produce Polyurethane

The polycondensation reaction is exothermic and consists of the chemical reaction of two molecules with different functional groups. For the polyurethane formation (polycondensate) it consists on the reaction of a hydroxyl group ( $-OH$ ), the presence of a free “active” hydrogen and an isocyanate group ( $-NCO$ ) (see Figure 1.4). The base of the chemistry of polyurethanes is the high reactivity of the isocyanates. Since the isocyanate group ( $-NCO$ ) can react with alcohols, amines, carboxylic acids and water (see Figure 1.5), it can form bond of urethane, urea and amides. Reaction of an isocyanate with an alcohol yields a urethane, reaction of an isocyanate with an amine yields a urea, and reaction of an isocyanate with water results in intermediates which decompose to yield carbon dioxide and an amine, which further reacts to again form an urea. The reaction with water is used for the production of foams.

Polyurethanes are in the class of compounds called reaction polymer [Oertel 1985, Ulrich 1996, Woods 1990] and are formed by reacting a monomer containing at least two isocyanate functional groups with another monomer containing at least two alcohol groups, in the presence (or not) of a catalyst. To form a network a reaction either of a triol with a diisocyanate or of a triisocyanate with a diol is needed. The rate of the reaction varies as a function of the kind of alcohol used in the following order: primary alcohol > secondary alcohol > tertiary alcohol > phenol.

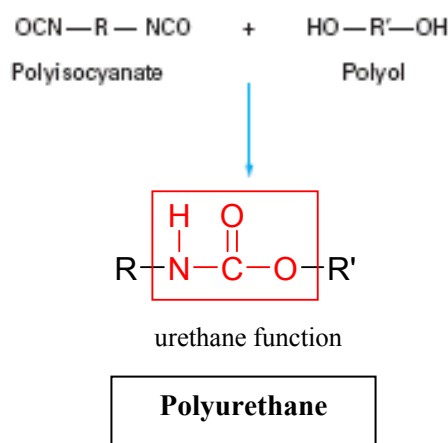


**Figure 1.4:** Polycondensation reaction: Polyurethane formation.

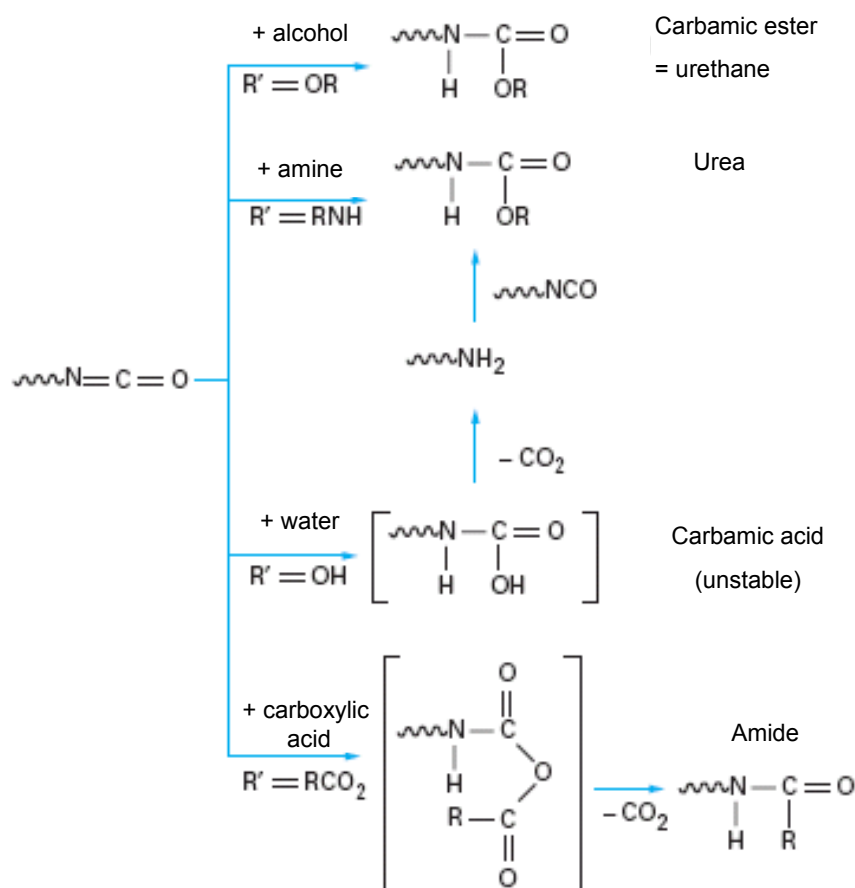


**Figure 1.5:** Principal reactions with a polyisocyanate (taken from “techniques de l’ingenieur”). R’ represents each possible reactive functional group.

Though the properties of the polyurethane are determined mainly by the choice of the polyol, the isocyanate exerts some influence. The cure rate is influenced by the functional group reactivity and the number of functional isocyanate groups per reactive molecule. Polyurethanes are based upon a well-defined stoichiometry. The choice of isocyanate also affects the stability of the polyurethane upon exposure to light. Polyurethanes made with

aromatic isocyanates yellow with exposure to light, then the use of stabilizers may be included in the formulation; whereas those made with aliphatic isocyanates are stable [Randall 2002]. There are several kinds of polyurethanes: cellular, compacts, elastomers, coatings and adhesives. In this thesis we prepared polyurethane elastomers from polyether polyols and a trifunctional isocyanate.

#### 1.1.1.3.1.- Secondary reactions

The urethane and urea groups already formed as presented in Figure 1.6, have other reactive hydrogen atoms that can react with another isocyanate giving as secondary products allophanates and biurets as presented in Figure 1.7.

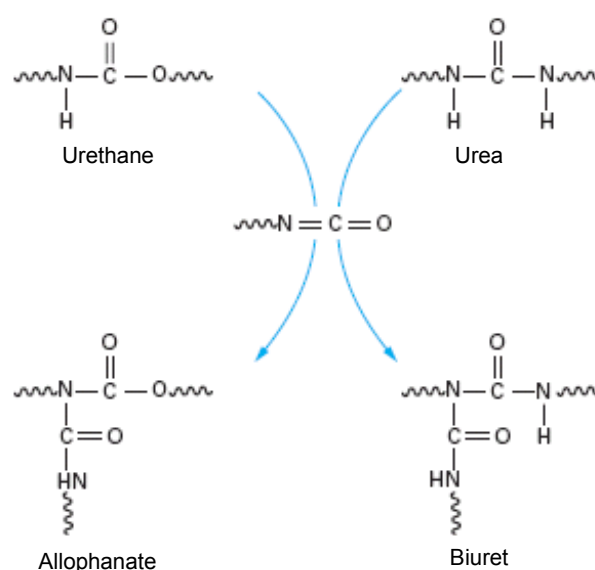


**Figure 1.6:** Secondary reactions of the isocyanate with urethane and urea groups (taken from “techniques de l’ingénieur”).

In the presence of certain “activators”, the isocyanates can react with each other and form by oligomerization, urediones (dimers), isocyanurates (trimers) or carbodiimides, as shown in Figure 1.7.

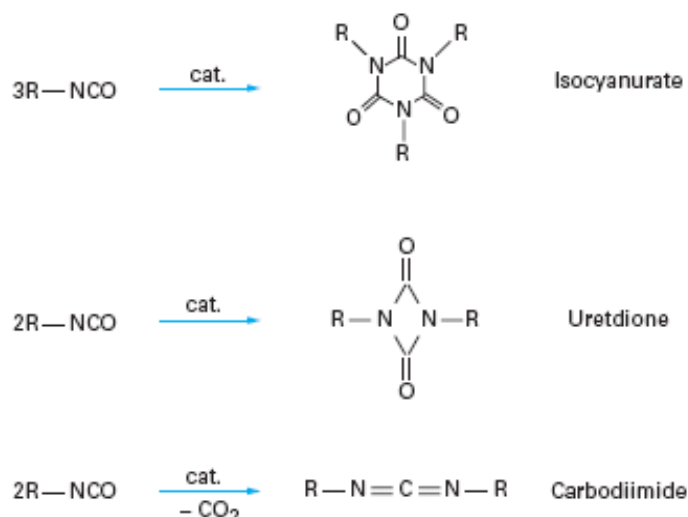


**Figure 1.7:** Secondary reactions of oligomerization of the isocyanates (taken from “techniques de l’ingenieur”).

#### 1.1.1.4.- Additives for polyurethanes’ preparation

The main additives used to produce polyurethanes are catalysts, chains extenders, surfactants, dyes, blowing agents, fillers, etc. The catalysts are accelerators of the reactions and for the polyurethane production they are used to reduce the curing times. There are two main catalysts used, the amines (i.e. Trietilendiamine or TEDA) and metallic salts (i.e. Dibutyldilaurate DBTL). In our case the catalyst was not used due to too fast reactions.

Polyurethanes made with aromatic isocyanates yellow with exposure to light, and the use of stabilizers may be included in the formulation (e.g. Irganox); whereas those made with aliphatic isocyanates are stable [Randall 2002].

#### 1.1.2.- Model Networks

The rubbery networks prepared by random crosslinking of the precursor chains have inhomogeneous structures with a broad length distribution of the network strands; in addition, the characterization of the strand length distribution in elastomers is not possible by current analytical techniques. However end-linking end-reactive precursor chains of known molecular weight using multifunctional crosslinkers afford a tailor-made model network with a well characterized structure. In the case of complete reaction, the molecular mass of the network strands between neighboring crosslinks ( $M_c$ ) is identical to that of the precursor chains, and the junction functionality ( $f_c$ ) is the same as the functionality of the crosslinker. To consider the effect of the incomplete reaction on  $M_c$  and  $f_c$ , the degree of the end-linking reaction ( $p$ ) is estimated from the amount of soluble species extracted after the reaction [Andrady *et al.* 1991, Urayama 2008].

An elastomer model network should have precursors with well known molecular weight and multifunctional crosslinker to be very close of the stoichiometric conditions, controlled lengths

of the network strands, reduced amount of trapped entanglements and inexistent or very few dangling chains [Urayama *et al.* 2009].

### 1.1.3.- Bimodal Networks

Experimentally, a bimodal network combines long- and short-polymer chains, presenting variable crosslinking density. Typically, bimodal networks result from blending difunctional long and short chains and crosslinking them together. They exhibit values of the modulus which increase very substantially at high elongations, thus giving unusually large values of the ultimate strength. This improvement in mechanical properties has been attributed to the limited extensibility of the short chains [Mark 1985, Mark and Erman 1988].

The theoretical analysis of bimodal networks, was first performed by Higgs and Ball [Higgs and Ball 1988]. These networks are composed of two types of chains, conveniently referred to as short and long chains, differing either in their molecular weight or in their chemical structure, thus obeying two distinct probability distribution functions for their end-to-end separations. The original theoretical approach, based on Gaussian phantom network chains for both components, was essentially developed for *random* bimodal networks with a random number of short or long chains connected at a given junction. Later, Kloczkowski *et al.* [Kloczkowski *et al.* 1991] considered the statistical mechanics of *regular* bimodal networks, which, by definition, have a fixed number  $\Phi_S$  and  $\Phi_L$  of short and long chains, respectively, at every junction and hence lend themselves to analytical solutions.

## 1.2.- Self-Assembled Monolayers (SAMs)

During several stages of sample preparation we prepared self-assembled monolayers (SAMs). The main goal of the SAMs preparation was to modify glass surfaces (glass lenses and glass plates) to bond the polyurethane to the glass in a covalent way (as presented in chapter 4). We also modified the surface of metallic molds with SAMs to make an easy release fluoro-terminated coating (also presented in chapter 4).

A self assembled monolayer (SAM) is an organized layer of amphiphilic molecules in which one end of the molecule, the “head group” shows a special affinity for a substrate (glass in our case); SAMs also consist of a tail with a functional group at the terminal end as seen in Figure 1.8 (b) and (c). The SAMs are created by the chemisorption of hydrophilic “head groups” onto a substrate from either the vapor or liquid phase [Schwartz 2001] followed by a slow two-dimensional organization of the “tail groups” (see Figure 1.8(a)) [Wnek and Bowlin 2004]. Initially, adsorbate molecules form either a disordered mass of molecules or form a “lying down phase” [Schwartz 2001], and over a period of hours, begin to form crystalline or semicrystalline structures on the substrate surface [Love *et al.* 2005, Vos *et al.* 2003]. The hydrophilic “head groups” assemble together on the substrate, while the tail groups (that can be hydrophilic or hydrophobic) assemble far from the substrate. Areas of close-packed molecules nucleate and grow until the surface of the substrate is covered in a single monolayer. Adsorbate molecules adsorb readily because they lower the surface energy of the

substrate [Love *et al.* 2005] and are stable due to the strong chemisorption of the “head groups.” These bonds create monolayers that are more stable than the physisorbed bonds of Langmuir-Blodgett films. The monolayer packs tightly due to van der Waals interactions, thereby reducing its own free energy [Love *et al.* 2005, Sullivan 2003, Oclin 2004]. Self-assembled monolayers (SAMs) offer a unique way to confine molecules in two dimensions. Figure 1.1 presents a schematic of self-assembled monolayers structures.

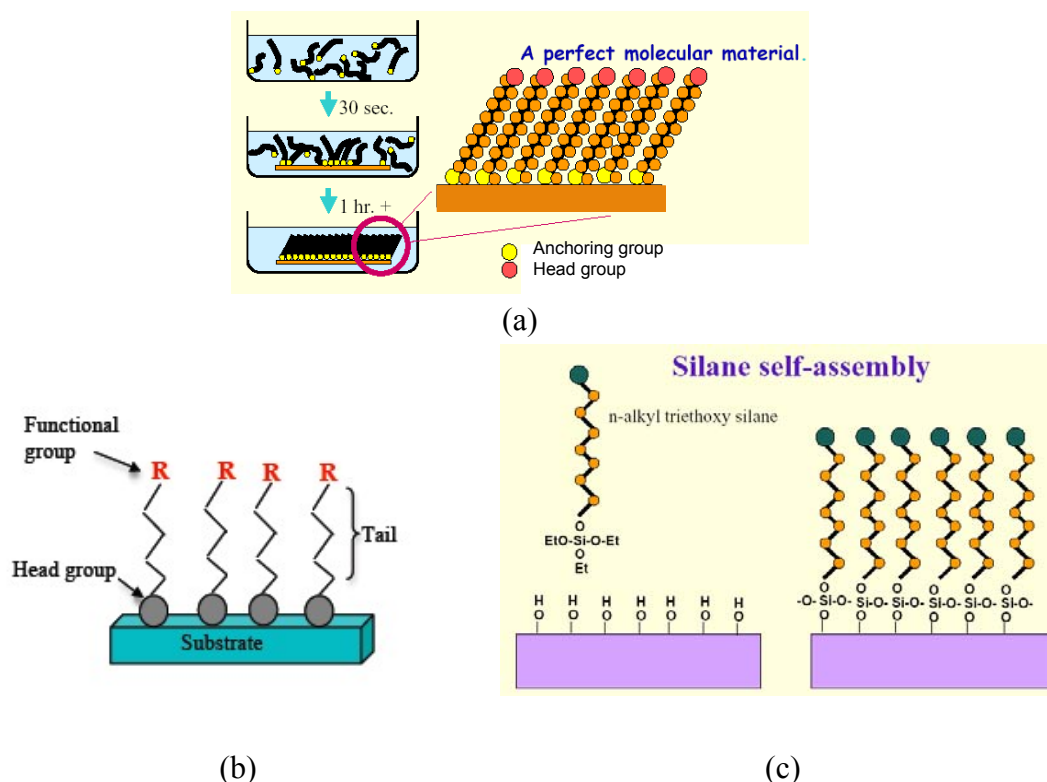


**Figure 1.8:** Schematic of SAM structure: (a) from solution to SAM; (b) schematic of head and functional group on the substrate, and (c) n-alkyl silane on glass.

### 1.3.- Rubber elasticity

In this section we present some fundamental concepts on the elasticity observed in elastomers also called rubber elasticity. These fundamentals are needed to better understand the physical and mechanical characterization of the polyurethane model networks presented in the next chapters.

Historically, the term rubber was used to refer to natural rubber only. The more modern term *elastomer* is sometimes employed in relation to synthetic materials having rubber-like properties, regardless of their chemical composition. The most important physical characteristic of the rubber-like state is a high degree of deformability exhibited under the action of relatively small stresses [Treloar 2005]. High extensibility and low Young’s modulus are the most remarkable properties of the rubber-like material; additionally, elastomers present particular thermal or thermoelastic properties. The thermoelastic effect

dates from Gough [Gough 1805] that made some experimental observations: 1) the elastomer in the stretched state, under a constant load, contracts (reversibly) on heating, and 2) the elastomer gives out heat (reversibly) when stretched. These observations were confirmed fifty years later by Joule [Joule 1859] who worked with perfectly reversible vulcanized rubber. The typical high elasticity of rubber arises from its molecular structure. Because the linear molecules are long and flexible, they take up random configurations under Brownian Thermal motions, like agitated snakes. When they are straightened out by an applied force, and released, they spring back to random shapes as fast as their thermal motion allows. In practice, the molecules are tied together by a few permanent chemical bonds, by a process known as “crosslinking”, to give the material a permanent shape. Thus, after crosslinking, rubber becomes a soft, highly elastic solid. Although rubber has a characteristic ability to undergo large elastic deformations, in practice many rubber springs are subjected only to relatively small strains, rarely exceeding 25% in extension or compression. A good approximation for the corresponding stresses is then given by conventional elastic analysis, assuming simple linear stress-strain relationships, because, like all solids, rubber behaves as a linearly elastic material at small strains. But some features of the behaviour of rubber can be understood only in terms of its response to large deformations. To treat large elastic deformations, we must consider how to characterize the elastic properties of highly extensible, nonlinearly elastic materials when a simple modulus of elasticity is not longer enough.

### 1.3.1.- Continuum Mechanics, Small and Large Strain Elasticity

Simple extension of an incompressible material such as rubber is defined by stretch ratios:  $\lambda_1 = \lambda$ ,  $\lambda_2 = \lambda_3 = 1/\lambda^{1/2}$  (Figure 1.9). This deformation satisfies the incompressibility condition  $\lambda_1 \lambda_2 \lambda_3 = 1$ .

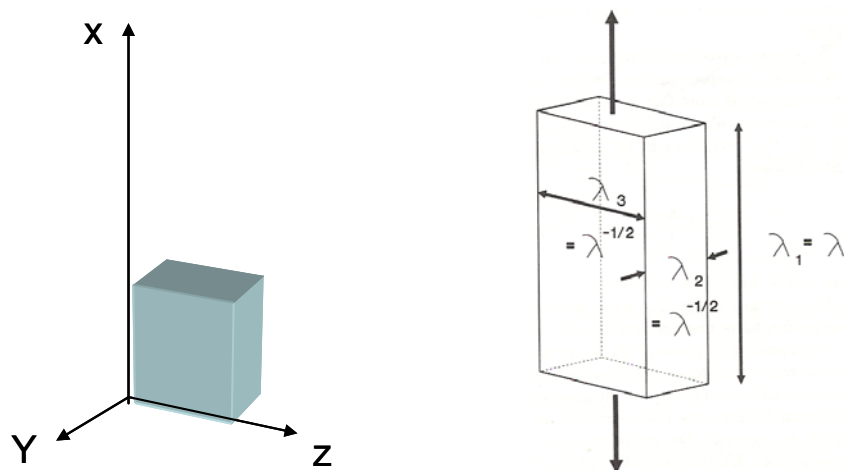


**Figure 1.9:** Principal extension ratios in simple extension.

It is common to measure the stress in terms of the force  $f$  acting on a unit of undeformed cross-sectional area,



$$f = \frac{t}{\lambda} \quad \text{eq. 1.1}$$

This equation is the large-deformation equivalent of a simple result:  $t = \sigma = E\varepsilon$ , applicable at small strains.

### 1.3.2.- Elastic properties at small strains

The elastic materials that are isotropic in their undeformed state can be described by two fundamental elastic constants. The first is related to the resistance to compression in volume under hydrostatic pressure called bulk modulus  $K$ , defined by:

$$P = K \left( \frac{\Delta V}{V_0} \right) \quad \text{eq.1.2}$$

where  $P$  is the applied pressure and  $\Delta V$  is the consequent shrinkage of the original volume  $V_0$ . The second constant describes the resistance to a simple shearing stress  $\tau$ , called shear modulus  $G$ , defined by the relation:

$$G = \frac{\tau}{\gamma} \quad \text{eq. 1.3}$$

where  $\gamma$  is defined as the ratio of the lateral displacement  $d$  to the height  $h$  of the sheared material. The tensile modulus  $E$  (Young's modulus of elasticity), defined by the ratio of a simple tensile stress  $\sigma$  to the corresponding fractional tensile elongation  $\varepsilon$ , is given by:

$$E = \frac{\sigma}{\varepsilon} = \frac{9KG}{3K + G} \quad \text{eq. 1.4}$$

Figure 1.10 shows the schematic of the three main kinds of stress.

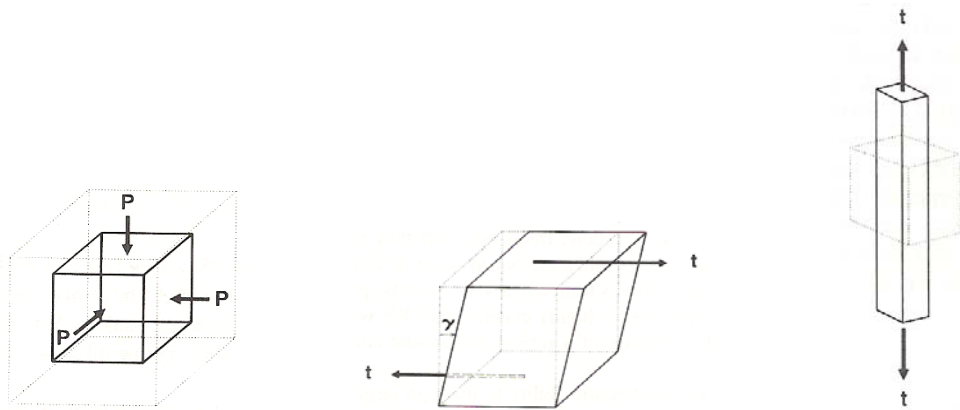


**Figure 1.10:** (a) Bulk compression, (b) Simple shear, (c) Simple tension [Taken from Gent 1992].

The Poisson's ratio  $\nu$ , defined as the ratio of lateral contraction strain  $\epsilon_2$  to longitudinal tension strain  $\epsilon_1$  for a bar subjected to a simple tensile stress, is given by:

$$\nu = \frac{1}{2} \left( \frac{3K - 2\mu}{3K + \mu} \right) \quad \text{eq. 1.5}$$

For rubbers, Poisson's ratio  $\nu$  is close to one-half (typically, 0.4995) and the tensile Young's modulus of elasticity is given almost by  $3\mu$ . If we consider rubber to be completely incompressible in bulk the  $\nu=1/2$  and the elastic behaviour at small strains can be described by a single elastic constant:  $\mu$  [Gent 1992].

### 1.3.3.- The Strain Energy Function W

The finite strain deformation can be described by the deformation of a cube of unit dimensions in the undeformed state to the rectangular parallelepiped (see Figure 1.9), which has edges  $\lambda_1, \lambda_2, \lambda_3$  in the directions x, y, z, respectively. In the deformed state the forces acting on the faces are  $f_1, f_2, f_3$ . The corresponding stress components as defined in the deformed state are  $\sigma_{xx}, \sigma_{yy}, \sigma_{zz}$  where

$$\sigma_{xx} = \frac{f_1}{\lambda_2 \lambda_3} = \lambda_1 f_1 \quad \sigma_{yy} = \frac{f_2}{\lambda_3 \lambda_1} = \lambda_2 f_2 \quad \sigma_{zz} = \frac{f_3}{\lambda_1 \lambda_2} = \lambda_3 f_3 \quad \text{eq. 1.6}$$

and these components of stress are different from those defined for small strain elasticity [Gent 1992]. The work done (per unit of initial undeformed volume) in an infinitesimal displacement from the deformation state where  $\lambda_1, \lambda_2, \lambda_3$  change to  $\lambda_1+d\lambda_1, \lambda_2+d\lambda_2, \lambda_3+d\lambda_3$ , is

$$dW = f_1 d\lambda_1 + f_2 d\lambda_2 + f_3 d\lambda_3 = \frac{\sigma_{xx}}{\lambda_1} d\lambda_1 + \frac{\sigma_{yy}}{\lambda_2} d\lambda_2 + \frac{\sigma_{zz}}{\lambda_3} d\lambda_3 \quad \text{eq. 1.7}$$

For an elastic material the work done can be equated to a change in the stored elastic energy  $U=W$ . In the case of rubbers it is usual to consider a reversible isothermal change of state at constant volume, so that the work done can be equated to the change in the Helmholtz free energy  $A$ , i.e.  $\Delta U=\Delta A$ . Then  $W$  is called the strain energy function because it defines the energy stored as a result of the strain, i.e.

$$W=f(\lambda_1, \lambda_2, \lambda_3) \quad \text{eq. 1.8}$$

Because rubber is an isotropic material the form of this function  $f$  must be independent of the choice of the coordinates axes. For simplicity it should also become zero when denoted

$\lambda_1=\lambda_2=\lambda_3=1$ , i.e. for zero strain. A further requirement is that for small strain, we should obtain Hooke's law for simple tension. An equation which satisfies these requirements is

$$W = C_1(\lambda_1^2 + \lambda_2^2 + \lambda_3^2 - 3) \quad \text{eq. 1.9}$$

where  $C_1$  is half the shear modulus  $\mu$ . To obtain a stress-strain relationship from this equation it is invoked equation 1.10, together with the assumption that rubber is incompressible:  $\lambda_1\lambda_2\lambda_3=1$ , and  $\lambda_1=\lambda$ ,  $\lambda_2=\lambda_3=1/\lambda^{1/2}$ . Then equation 1.9 becomes

$$W = C_1\left(\lambda^2 + \frac{2}{\lambda} - 3\right) \quad \text{eq. 1.10}$$

and from 1.10 we have

$$f = \frac{\partial W}{\partial \lambda} = 2C_1\left(\lambda - \frac{1}{\lambda^2}\right) \quad \text{eq. 1.11}$$

This equation is more usually represented as a consequence of the molecular theories of a rubber network. It follows from purely phenomenological considerations as a simple constitutive equation for the finite deformation of an isotropic, incompressible solid. Materials which obey this relationship are sometimes called neo-Hookean [Ward and Hadley 1998, Gent 1992].

### 1.3.4.- Strain Invariants

A general treatment of the stress-strain relations of rubber-like solids was developed by Rivlin [Rivlin in Eirich 1956], assuming only that the material is isotropic in elastic behaviour in the unstrained state, and incompressible in the bulk. Symmetry considerations suggest that appropriate measures of strain, independent of the choice of the axes, are given by three invariants, defined as:

$$\begin{aligned} I_1 &= \lambda_1^2 + \lambda_2^2 + \lambda_3^2 \\ I_2 &= \lambda_1^2\lambda_2^2 + \lambda_2^2\lambda_3^2 + \lambda_3^2\lambda_1^2 \\ I_3 &= \lambda_1^2\lambda_2^2\lambda_3^2 \end{aligned} \quad \text{eq. 1.12}$$

Moreover, for an incompressible material  $I_3$  is identically unity; hence only two independent measures of strain, namely  $I_1$  and  $I_2$ , remain. It follows that the strain energy density  $W$  (i.e., the amount of energy stored elastically in unit volume of material under the state of strain specified by  $\lambda_1, \lambda_2, \lambda_3$  is a function of  $I_1$  and  $I_2$  only:

$$W = W(I_1 - 3, I_2 - 3) \quad \text{eq. 1.13}$$

(Since  $I_1$  and  $I_2$  take the value 3 when  $\lambda_1 = \lambda_2 = \lambda_3 = 1$ , subtracting this amount gives strain measures that go to zero in the undeformed state). Furthermore, because  $I_1 - 3, I_2 - 3$  are of second order in the strains  $\epsilon_1, \epsilon_2, \epsilon_3$ , the strain energy function at sufficiently small strains must take the form

$$W = C_1(I_1 - 3) + C_2(I_2 - 3) \quad \text{eq. 1.14}$$

where  $C_1$  and  $C_2$  are constants. This particular form of the strain energy function was originally proposed by Mooney [Mooney 1940] and is often called Mooney-Rivlin equation.

### 1.3.5.- The statistical mechanical theory of rubber elasticity

#### 1.3.5.1.- Statistical theory of rubber elasticity

Polymer networks are unique in their ability to reversibly deform several hundreds percent. This deformability arises from the entropic elasticity of the polymer chains. The early molecularly based statistical mechanical theory was developed by Wall [Wall 1942] and Flory and Rehner [Flory and Rehner 1943], with the simple assumption that chain segments of the network deform independently and on a microscopic scale in the same way as the whole sample (affine deformation). The simplest model that captures this idea is the *affine network* model originally proposed by Kuhn (see Figure 1.11). The main assumptions of the affine model are the following [Gedde 1999]: 1) the chain segments between crosslinking points can be represented by Gaussian chains; 2) the networks consist of  $N$ -chains per unit volume. The entropy of the system is the sum of the entropies of the individual chains; 3) the relative deformation of each network strand is the same as that on a macroscopic level i.e. the relative deformation imposed on the whole network is affine; then the crosslinks are assumed to be fixed in space at positions exactly defined by the specimen deformation ratio; 4) the unstressed network is isotropic; and 5) the volume remains constant during the deformation.

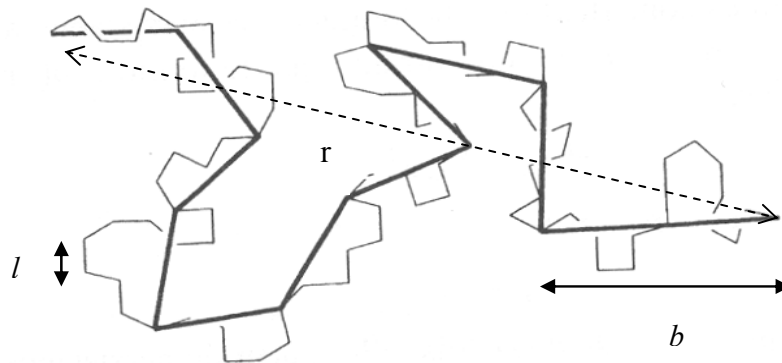


**Figure 1.11:** Schematic representation of the equivalent chain of Kuhn. Assembly of ' $n$ ' rigid rods with a fixed length ' $l$ '.

James and Guth [James and Guth 1943] avoiding the assumptions made in the *affine model*, treated a *phantom network* consisting of Gaussian chains having no material properties. In the *phantom model*, the ends of the network strands are joined at crosslinking functions that can fluctuate (are not fixed in the space as in the affine model). These two theories are in a sense ‘limiting cases’ with the affine network model giving an upper bound modulus and the phantom network model theory the lower bound. Figure 1.12 shows schematically the differences between the *affine and phantom network model*.

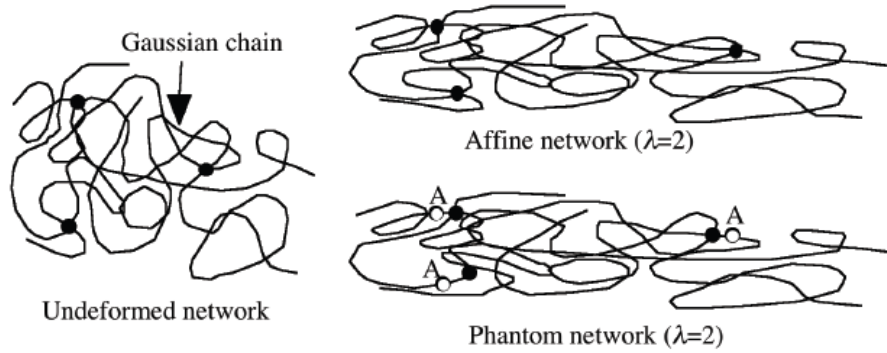


**Figure 1.12:** Schematic representation of the deformation of a network according to the affine network model and the phantom network model. The unfilled circles indicate the position of the crosslinks assuming affine deformation (phantom network) [Taken from Gedde 1999].

The simplest way to describe a polymer chain is with the freely jointed chain model which assumes a polymer chain as a random walk and neglects interactions between monomers (see Figure 1.11). Because a long, flexible molecule can be represented to good approximation by a randomly arranged chain of ‘n’ freely joint links, each of length ‘l’, the distribution of the end-to-end lengths ‘r’ obeys a Gaussian probability function, at least for small end-to-end distances:

$$P(r) = C \exp(-\beta^2 r^2) \quad \text{eq. 1.15}$$

where the parameter  $\beta^2$  is given by  $3/2nl^2$ . The mean square distance between the ends for free chain (phantom chains) averaged over all configurations is denoted by  $\langle r^2 \rangle_0$  and is given by  $nl^2$  or  $3/2\beta^2$ . Then the distribution of end-to-end lengths ‘r’ is well represented by [Flory 1985, Gedde 1999]:

$$P(r) = \left( \frac{3}{2\pi \langle r^2 \rangle_0} \right)^{3/2} \exp \left[ - \left( \frac{3}{2 \langle r^2 \rangle_0} \right) r^2 \right] \quad \text{eq. 1.16}$$

Boltzmann’s entropy relationship ( $S = k \ln P$ ) is useful here:

$$S = k \ln(P(r)) = k \left( \frac{3}{2} \ln \left( \frac{3}{2\pi \langle r^2 \rangle_0} \right) - \left( \frac{3r^2}{2\langle r^2 \rangle_0} \right) \right) \quad \text{eq. 1.17}$$

which after simplification becomes

$$S = C - k \left( \frac{3r^2}{2\langle r^2 \rangle_0} \right) \quad \text{eq. 1.18}$$

where C is a constant.

#### 1.3.5.1.1- Affine network model

Figure 1.13 presents the sketch of a molecular strand in a network in the undeformed state (end-to-end vector  $\mathbf{r}_0 = (x_0, y_0, z_0)$ ) and in the deformed state (end-to-end vector  $\mathbf{r} = (x, y, z)$ ). The deformed and undeformed configurations are related through the stretch  $(\lambda_1, \lambda_2, \lambda_3)$  by:

$$x = \lambda_1 x_0 \quad y = \lambda_2 y_0 \quad z = \lambda_3 z_0$$

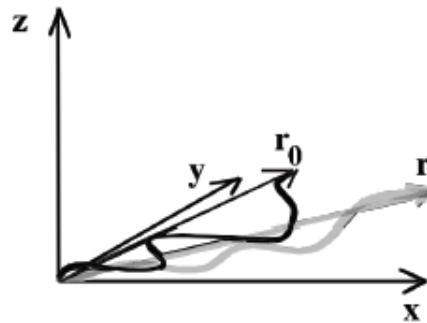


**Figure 1.13:** Affine deformation of a single chain from the unstretched state  $\mathbf{r}_0 = (x_0, y_0, z_0)$  to the stretched state  $\mathbf{r} = (x_0 \lambda_1, y_0 \lambda_2, z_0 \lambda_3)$ .

Recalling the assumptions and definitions made above it is possible to compute the difference in entropy  $\Delta S$  between  $n$  chains in the stretched and unstretched state. Each chain being composed of ' $N$ ' Kuhn monomers of length ' $l$ ' with end-to-end vector ' $\mathbf{r}$ ', we have:

$$\Delta S = -\frac{1}{2} nk (\lambda_1^2 + \lambda_2^2 + \lambda_3^2 - 3) \quad \text{eq. 1.19}$$

where  $k$  is the Boltzmann constant. Assuming that the main contribution to the free energy of the network comes from the changes in entropy the free energy required to deform a network is given by:

$$\Delta F_{network} = -T\Delta S_{network} = \frac{nkT}{2}(\lambda_1^2 + \lambda_2^2 + \lambda_3^2 - 3) \quad \text{eq.1.20}$$

If the number of chains  $n$  is now expressed per unit volume, the prefactor in equation 1.20 has the meaning of a shear modulus  $\mu$ :

$$\mu = \frac{nkT}{V} = \nu k T = \frac{\rho RT}{M_s} \quad \text{eq. 1.21}$$

where,  $\nu$  ( $=n/V=\rho N_{av}/M_s$ ) is the number of network strands per unit volume,  $\rho$  is the density,  $M_s$  is the number-average molar mass of network strand, and  $R$  is the gas constant. The network modulus increases linearly with the temperature because its origin is entropic, analogous to the pressure of an ideal gas. The modulus also increases linearly with the number density of network strands. The equation 1.24 states that the modulus of any network polymer is  $kT$  per strand. The affine predictions for the engineering stress in uniaxial deformation at constant network volume can be rewritten using the shear modulus [Rubinstein and Colby 2003]:

$$\sigma_{nominal} = \mu \left( \lambda - \frac{1}{\lambda^2} \right) \quad \text{eq. 1.22}$$

These classical stress-stretch equations are quite general, and the physics behind such classical models is the entropic elasticity of polymer chains.

#### 1.3.5.1.2- Phantom network model

In this model, the ends of network strands are attached to other strands at crosslinks, which can fluctuate around their average position. These fluctuations lead to a net lowering of the free energy of the system by reducing the cumulative stretching of the network strands. The principal parameter of the phantom network is the functionality ' $f$ ' given by the number of segments between crosslinking points, which adds a corrective term to the shear modulus [Rubinstein and Colby 2003]:

$$\mu = \nu k T \frac{f-2}{f} = \frac{\rho RT}{M_s} \left( 1 - \frac{2}{f} \right) \quad \text{eq.1.23}$$

For any functionality  $f$ , the phantom network modulus is lower than the affine network modulus because allowing the crosslinks to fluctuate in space makes the network softer. The typical functionality of a network is 3 or 4. For  $f=3$ , the phantom prediction is one third of the affine network modulus. In the limit of high functionality  $f$ , the crosslinks in the phantom network do not fluctuate and are almost fixed in space as in the affine network model.

### 1.3.6.- Thermodynamics of elastomers deformation

To better understand the physics of the rubber elasticity it is important to separate the elastic force into entropic and energetic contributions. Stress acting on the rubber network will stretch out and orient the chains between the crosslink joints. This will decrease the entropy of the chains and hence give rise to an entropic force. The change in chain conformation is expected to change the *intramolecular* internal energy. The packing of the chains may also change affecting the *intermolecular*-related internal energy. Both the *intra*- and *intermolecular* potentials contribute to the force. The following thermodynamic treatments yield expressions differentiating between the entropic and energetic contributions to the elastic force.

According to the first and second laws of thermodynamics, the internal energy change ( $dU$ ) in a uniaxially stressed system exchanging heat ( $dQ$ ) and deformation and pressure volume work ( $dW$ ) reversibly is given by:

$$dQ = TdS \quad \text{eq. 1.24}$$

$$dW = -pdV + fdL \quad \text{eq. 1.25}$$

then,

$$dU = TdS - pdV + fdL \quad \text{eq. 1.26}$$

where  $dS$  is the differential change in entropy,  $p dV$  is the pressure volume work and  $f dL$  is the work done by deformation. The force is a vector (denoted  $\mathbf{f}$ ) but in this treatment is treated as a scalar (denoted  $f$ ; being the absolute value of the vector). Because of the very small compressibility of elastomers  $P dV$  is much smaller than  $f dL$  under most circumstances, and we can approximate the work as  $f dL$ . The Helmholtz free energy  $F$  is defined as internal energy minus the product of the temperature and entropy:

$$F = U - TS \quad \text{eq. 1.27}$$

The change in the Helmholtz free energy is a thermodynamics state function of variables  $T$ ,  $V$ , and  $L$ :

$$\begin{aligned} dF &= dU - d(TS) = dU - TdS - SdT \\ &= -SdT - pdV + fdL \end{aligned} \quad \text{eq. 1.28}$$

The change in Helmholtz free energy can be written as a complete differential:



$$dF = \left( \frac{\partial F}{\partial T} \right)_{V,L} dT + \left( \frac{\partial F}{\partial V} \right)_{T,L} dV + \left( \frac{\partial F}{\partial L} \right)_{T,V} dL \quad \text{eq. 1.29}$$

Combining equation 1.29 with 1.30, we identify the partial derivatives of the Helmholtz free energy:

$$\left( \frac{\partial F}{\partial T} \right)_{V,L} = -S \quad \text{eq. 1.30}$$

$$\left( \frac{\partial F}{\partial V} \right)_{T,L} = -p \quad \text{eq. 1.31}$$

$$\left( \frac{\partial F}{\partial L} \right)_{T,V} = f \quad \text{eq. 1.32}$$

The force applied to deform a network consists then of two contributions:

$$\left( \frac{\partial F}{\partial L} \right)_{T,V} = f = \left( \frac{\partial U}{\partial L} \right)_{T,V} + T \left( \frac{\partial f}{\partial T} \right)_{V,L} = f_E + f_S \quad \text{eq. 1.33}$$

where  $f_E$  is the energetic contribution to the force, related to the change in internal energy with sample length, and  $f_S$  is the entropic term, product of the temperature and the change in entropy with sample length. In ‘ideal networks’ there is no energetic contribution to the elasticity, so  $f_E = 0$  [Treloar 2005, Gedde 1999, Rubinstein and Colby 2003].

### 1.3.7.- Deviations from rubber elasticity theory

Both affine and phantom network models predict the same dependence of stress on deformation. However, a comparison of the classical forms with experiments indicates two major disagreements (see Figure 1.14). Experiments demonstrate softening at intermediate deformations and hardening at higher deformations. In unfilled rubbers the softening indicates the presence of entanglements in addition to crosslinks, while in filled rubbers it is typically due to the breakup of interactions between fillers. The strain hardening at high deformations can be explained by the non-Gaussian statistic of strongly deformed chains. The finite extensibility is the major reason for strain hardening at high elongations.

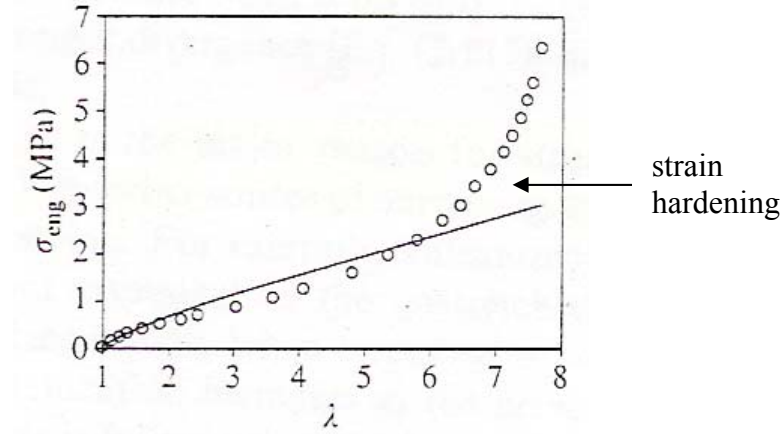


**Figure 1.14:** Engineering stress in tension for a crosslinked rubber. The solid line the classical nominal stress fit to small strain data [taken from Treloar 2005].

### 1.3.7.1.- Chain entanglements

In the affine network model strands are fixed in space, and in the phantom network model strands are allowed to fluctuate around some fixed position in space. In both models, chains are only aware that they are strands of a network because their ends are constrained by crosslinks. In real networks, the chains impose topological constraints on each other because they can not cross, and these topological constraints are called entanglements. The surrounding chains on a given strand is represented in the Edwards tube model by a quadratic constraining potential acting on every monomer of each network strand; in this model fluctuations driven by the thermal energy  $kT$  are allowed. The tube diameter  $a$  can be interpreted as the end-to-end distance of an entanglement strand of  $N_e$  monomers ( $a = bN_e^{1/2}$ ) where  $b$  is the Kuhn segment length. The strand between entanglement has an average molar mass  $M_e = N_e M_0$ . For a purely entangled system,  $M_e$  substitutes the average molecular weight between network strands in the determination of the modulus [Rubinstein and Colby 2003]:

$$\mu_e = \frac{\rho RT}{M_e} \quad \text{eq. 1.34}$$

The small strain modulus of an entangled and crosslinked polymer network can be approximated by:

$$\mu \cong \mu_x + \mu_e \approx \rho RT \left( \frac{1}{M_x} + \frac{1}{M_e} \right) \quad \text{eq. 1.35}$$

Then, the modulus is controlled by crosslinks for low molar mass strands between crosslinks ( $\mu \sim \mu_x$  for  $M_x < M_e$ ) and by entanglements for high molar mass ( $\mu \sim \mu_e$  for  $M_x > M_e$ ).

As the material is being stretched the entanglements (unlike the fixed chemical crosslinks) can slip and effectively reorient strands in the tensile direction resulting in a reduction of the

apparent modulus and hence a softening observed relatively to an unentangled network with an identical small strain modulus. Several molecularly based models have been proposed to account for the presence of entanglements in the network and a good review can be found in [Rubinstein and Panyukov 2002].

A detailed comparison between models and experimental data would go beyond the purpose of this thesis. Rubinstein and Panyukov proposed however a particularly simple expression for the engineering stress as a function of  $\lambda$  based on a so-called slip-link model which introduces a confining potential around the chains. Their prediction for uniaxial deformation is given by:

$$f^*(\lambda^{-1}) = \frac{\sigma}{\left(\lambda - \frac{1}{\lambda^2}\right)} \quad \text{eq. 1.36}$$

where  $f^*(\lambda^{-1})$  is the prediction of the Mooney ratio on the nonaffine tube model.

Figure 1.15 shows a comparison of cross-linked PDMS with the Mooney-Rivlin expression, nonaffine tube model, and the sliptube model.

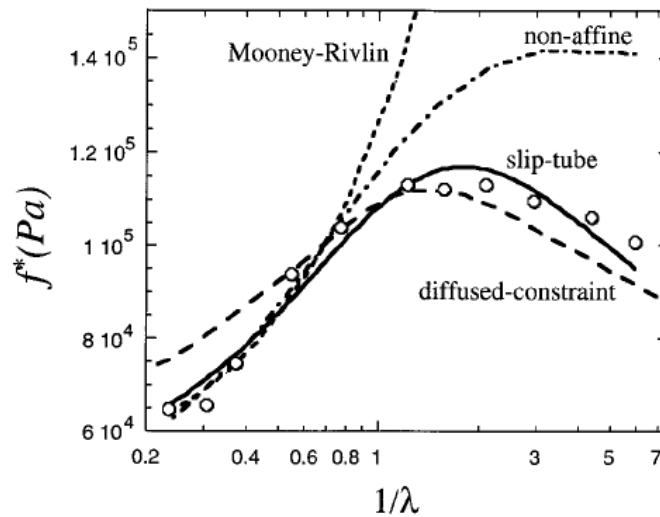


**Figure 1.15:** Comparison of cross-linked PDMS (open circles) with the Mooney-Rivlin expression (dotted line), nonaffine tube model (dash-dotted line), and the sliptube model (solid line) (taken from Rubinstein and Panyukov 2002).

### 1.3.7.2.- Finite extensibility

The assumption of Gaussian chain statistics does not predict any finite extensibility of polymer chains. At high strains, polymer chains are not organized as random coils and orient

themselves along the direction of the elongation. The Gaussian assumption is not valid at large strains when the chains approach their limiting stretched states. It is valid only for end-to-end distance much inferior to the maximal end-to-end distance  $r_{\max}$  (i.e.  $\langle r_0^2 \rangle \ll r_{\max} = nl$ ). Several molecular models have been proposed to account for the finite extensibility of the polymer chains. The best known one is the Langevin model for the extension of a single chain [ref Treloar]. It is unfortunately difficult to implement in a three dimensional case. A commonly used molecularly based 3-D model including finite extensibility is the Vilgis-Edwards models [Edwards and Vilgis 1986]. This model contains the notion of entanglements (described slightly differently from the Rubinstein-Panyukov model) and of finite extensibility leading to strain hardening. The four independent parameters are however difficult to match directly with a molecular structure.

A relatively simple phenomenological model accounting for limiting chain extensibility is the Gent model [Gent 1996]. At small and moderate deformations:

$$W = \frac{E}{6} J_1 \quad \text{eq. 1.37}$$

where  $W$  is the neo-Hookean strain energy function defined earlier,  $E$  is the Young's modulus,  $J_1 = I_1 - 3 = \lambda_1^2 + \lambda_2^2 + \lambda_3^2 - 3$ . Gent postulated that the finite extensibility of the network chains would result in a limiting value  $J_m$  of the variable  $J_1$ .

The phenomenological equation proposed by Gent becomes then:

$$W = -\frac{E}{6} J_m \ln \left( 1 - \frac{J_1 - 3}{J_m} \right) \quad \text{eq. 1.38}$$

that diverges for  $J_1 \rightarrow J_m$ , becoming the neo-Hookean equation at small strains ( $J_1 \rightarrow 0$ ). From this expression, the engineering stress-strain relation in uniaxial deformation is given by:

$$\sigma_{Engt} = G \frac{\lambda - \lambda^{-2}}{\left( 1 - \frac{J_1}{J_m} \right)} \quad \text{eq. 1.39}$$

This empirical equation can be used to fit uniaxial experimental data and the determined parameters  $E$  and  $J_m$  can then be used to simulate the behaviour of the material in an arbitrary geometry.

## 1.4.- Compression or Tension under confined conditions

In this section we presented some general considerations applying when the material is confined between two rigid plates. These considerations are useful to understand the cavitation phenomenon presented on chapters 4 and 5.

When a thin rubber block bonded on both faces is compressed (or extended) the deformation can be decomposed in two parts: a pure homogeneous compression or extension of amount  $\epsilon$ , requiring a uniform compressive or tensile stress  $\sigma_1 = 3G^*\epsilon$ , and a shear deformation restoring points in the planes of the bonded surfaces to their original positions in these planes [Gent and Lindley 1959, Gent and Meinecke 1970].

The stress distribution of the compressed bonded block is shown schematically in Figure 1.16. Although it is incorrect at the edges of the block because the assumption of a simple shear deformation cannot be valid at this singular line, experiments show that it provides satisfactory approximations over the major part of the bonded surfaces [Gent *et al.* 1974].

The effect of constraints at the bonded surfaces has been to increase the effective compression modulus from  $E (=3G)$  by a factor of  $(1 + a^2/2h^2)$  (where ‘a’ and ‘h’ are the radius and thickness of the cylindrical block, respectively). For thin blocks of large radius the effective value of Young’s modulus  $E$  is much larger than the real value. Indeed for values of the ratio  $a/h$  greater than about 10, a significant contribution to the observed displacement comes from volume compression or dilation because  $E$  is now so large that it becomes comparable to the modulus  $K$  of bulk compression.

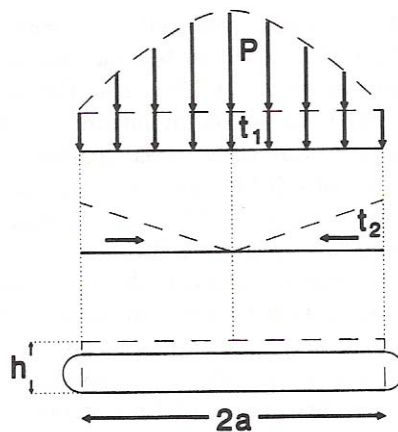


**Figure 1.16:** Stress distribution for a bonded block in compression (taken from Gent 1992).

When a thin bonded block is subjected to tensile loading, a state of approximately equal triaxial tension ( $-P$ ) is set up in the central region. Under an outwardly directed tension, any small cavity that might exist in the central region of the block will expand uniformly in size. Failure is governed by a “critical strain energy release rate”, not by a simple maximum strain criterion, so that a rather detailed calculation is necessary to find out what mean compressive

(or tensile) stress can be tolerated. As a first approximation it is assumed that a bonded block can support a strain energy density in critical regions of the same magnitude that could be imposed many times on a homogeneously deformed specimen in simple tension [Gent 1992].

#### 1.4.1.- Cavitation

On polymers, the application of sufficiently large tensile load can cause the appearance of holes that were not previously evident in the material. Upon further loading, these cavities grow in size and eventually coalesce. When loaded in tension, a critical state is reached when cavities suddenly grow in the body of the rubber, producing a drop in the extending force. Subsequent analysis of the samples reveals the presence of internal cracks, which can initiate catastrophic failure if the load is increased further. This phenomenon is known as cavitation. [Gent 1992]. The state of the art and the theoretical models pertaining to the description of cavitation in the bulk of a rubber will be presented in the relevant chapters 5 and 6.

##### 1.4.1.1- Inflation of a Spherical Shell (Balloon)

To understand the type of unstable deformation occurring when a cavity expands in the rubber it is however useful to consider the inflation of a thin membrane such as that of a rubber balloon. The pressure  $P_1$  required to inflate a spherical shell of initial radius  $r_0$  and thickness  $t_0$  to an inflated radius  $\lambda r_0$  and thickness  $d_0/\lambda^2$  can be obtained from equation 1.40, using Laplace's relation between the stresses  $t$  in the plane of the shell and inflating pressure (Figure 1.17):

$$P_1 = \frac{2td_0}{\lambda^3 r_0} \quad \text{eq. 1.40}$$

The inflating pressure  $P_1$  generates a tension stress  $t$  in the curved shell (Figure 1.25). On substituting for  $\sigma$  in equation 1.40, the relation between inflation pressure  $P_1$  and inflation ratio  $\lambda$  is obtained as follow:

$$P_1 = 4 \left( \frac{d_0}{r_0} \right) \left( W_1 + \lambda^2 W_2 \right) (\lambda^{-1} - \lambda^{-7}) \quad \text{eq. 1.41}$$

where  $W_1$  and  $W_2$  are the derivatives of the strain energy function under different types of strain. This is highly nonlinear and a plot of the predicted behaviour (assuming  $W_2=0$ ) is presented in Figure 1.17. The inflation pressure is seen to pass through a sharp maximum at an expansion ratio of 38% and then decrease upon further inflation. This is a well-known feature of balloons: after a relatively small inflation it is much easier to continue inflating them. This instability is at the origin of the instability observed in the bulk of the rubber when cavities appear.

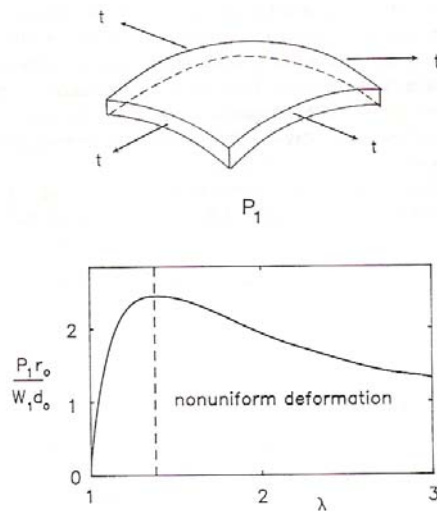


**Figure 1.17:** Inflation of a spherical shell (balloon).

## 1.5.- Viscoelasticity: Effects of Temperature and Frequency

In this section, we focus our attention to the time-temperature superposition principle, which we use in chapter 2 to characterize the viscoelastic behaviour of the polyurethane model networks.

The main cause of delayed elastic response in rubbers is the internal viscosity between molecular chains. This property is strongly affected by the temperature. It depends on the rate at which small segments of a molecule move to new positions as a result of Brownian motions. A typical feature of the mechanical behavior of polymers is the way in which their mechanical response to an applied stress or strain depends upon the rate or time period of loading [Young and Lovell 1991, Ward 1983]. For example, if a polymer is subjected to a constant load, the deformation or strain (compliance) exhibited by the material will increase over a period of time. This occurs because the material under a load undergoes molecular rearrangement in an attempt to minimize localized stresses [Young and Lovell 1991, Alkonis 1972].

The mechanical behavior of polymers depends upon the testing rate as well as the temperature and it is found that there is a general equivalence between time or frequency of observation and temperature. The mechanical response can be represented in a procedure known as time-temperature superposition (TTS). In a series of mechanical measurements made over a range of temperatures at different testing frequencies, the data can be put onto a simple 'master curve' by shifting the data measured at one temperature along the frequency axis by a factor which is a function only of the test temperature, as represented in Figure 1.18. This is a very general property of many polymers and is due to the fact that the spectrum of relaxation times of a polymer has typically the same temperature dependence. Using a «master curve" the material property of interest at a specific temperature can be predicted over a broad time scale. The bases for time-temperature superposition are: 1) that the processes involved in molecular relaxation or rearrangements in viscoelastic materials occur at accelerated rates at

higher temperatures and 2) that there is a direct equivalency between time (the frequency of measurement) and temperature [Alkonis *et al.* 1972, Hiemenz and Timothy 2007, Young and Lovell 1991, Halary and Lauprêtre 2006].

If a reference temperature  $T_s$  is taken to fix one curve then if  $f_s$  (where  $\omega_s = 2\pi f$ ) is the frequency of a point on the curve at  $T_s$  with a particular modulus and  $f$  is the frequency of a point with the same modulus on a curve at different temperature then the amount of shift required to superpose the two curves is a displacement of  $(\log f_s - \log f)$  along the log frequency axis and the “shift factor”  $a_T$  is defined by

$$\text{Log } a_T = \log f_s - \log f = \log (f_s/f) \quad \text{eq. 1.42}$$

And this parameter is a function only of temperature. Here,  $f$  is the time that is required to give a specified response at a certain temperature, and  $f_s$  is the time required to give an identical response at the reference temperature. The essential requirement for a substance to be rubbery is that it consists of long flexible chainlike molecules. The molecules themselves must therefore have a “backbone” of many non-colinear single valence bonds, about which rapid rotation is possible as a result of thermal agitation. Thousands of the molecular sub-units of rubbery polymers linked together into a chain constitute a typical molecule of the elastomers. They take up random conformations in a stress-free state but assume somewhat oriented conformations if tensile forces are applied at their ends. One of the first questions to consider, then, is the relationship between the applied tension  $f$  and the mean chain end separation  $r$ , averaged over time or over a large number of chains at one instant in time. Moderately elevated temperatures may cause the exchange of crosslinks and formation of additional crosslinks, leading to some hardening of the rubber [Gent 1992].

In a range of temperatures between  $T_g$  and  $T_g + 100^\circ\text{C}$ , the relationship between the test temperature and this factor  $a_T$  is often given by an equation of the form

$$\log a_T = \frac{-C_1 (T - T_{ref})}{C_2 + (T - T_{ref})} \quad \text{eq. 1.43}$$

where  $C_1$  and  $C_2$  are constants and  $T_{ref}$  is a reference temperature. This equation is normally termed the WLF (Williams-Landel-Ferry) equation and is based on the notion that molecular mobility depends on the available free volume which vanishes for a finite temperature  $T_\infty$ .



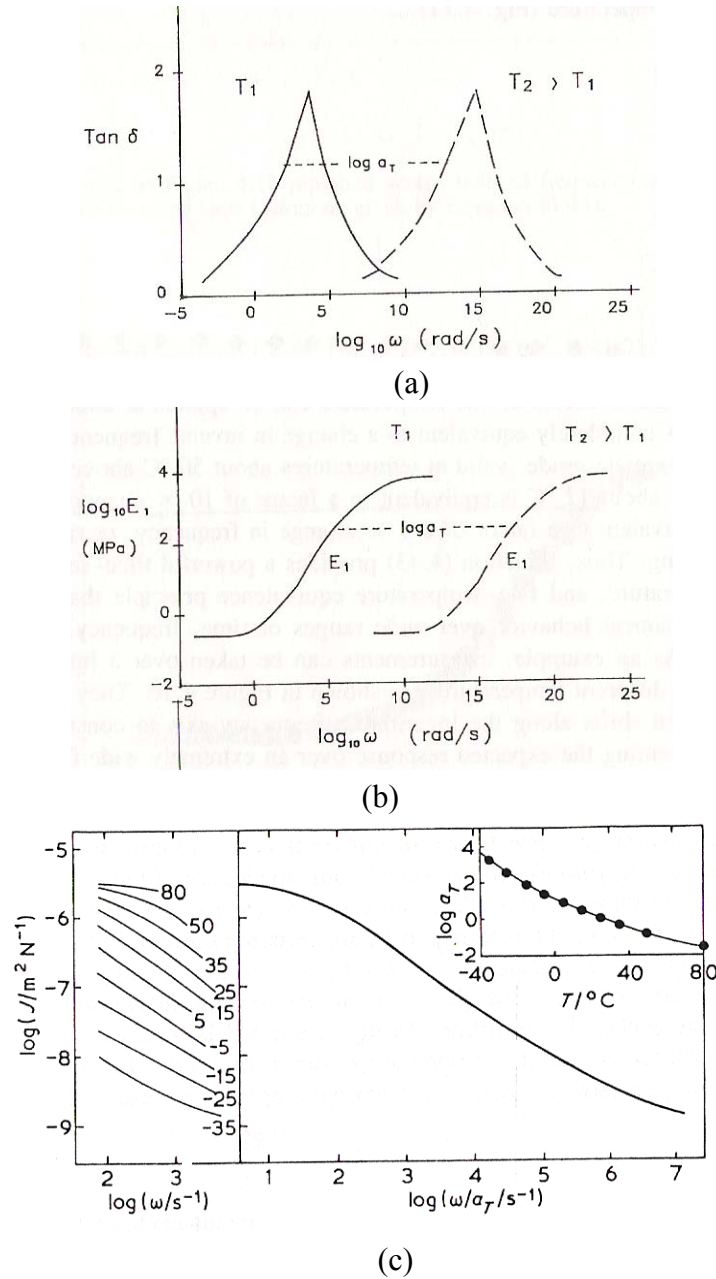


**Figure 1.18:** Building a master-curve with the time-temperature superposition: a) Dynamic  $\tan \delta$ , and b) Dynamic modulus, versus the frequency and two temperatures  $T_2 > T_1$ ; and c) example of time-temperature superposition principle using shear compliance,  $J$  [Gent 1992, Young and Lovell 1991].

## 1.6.- Fracture behaviour

In this section, the general fracture behaviour of polymers is briefly summarized in order to build up the theoretical background needed to study the fracture of the three polyurethane model networks, which is directly related to the cavitation phenomenon.

Fracture mechanics, which leads to the concept of fracture toughness, has been largely based on the work of A. A. Griffith [Griffith 1920] who, amongst other things, studied the

behaviour of cracks in brittle materials. He recognized that the macroscopic potential energy of the system consisting of the internal stored elastic energy and the external potential energy of the applied loads, varied with the size of the crack. Therefore fracture is associated with the consumption of energy. Once a crack is propagated throughout a material, the extension of the crack resulted in the creation of new crack surface. New free surfaces are created at the faces of a crack, which increases the *surface energy* of the system. One such model used to demonstrate the propagation of a crack in a brittle material is called the *elastic strain energy model*.

At the beginning, Griffith considered that the fracture was related to the creation of new surface energy and postulated that the energy necessary to create new surface was balanced with the decreasing of the stored elastic energy. Later, to explain the large differences between theoretical and experimental results, he proposed that the stored elastic energy was not uniformly distributed in all the material, but concentrated at the crack tip. Then the fracture would occur by propagation of pre-existing cracks in the material.

### **Griffith - Orowan - Irwin Failure Criteria**

The process of fracture consists of crack initiation and crack propagation. If there was a perfectly elastic body with a slit already present. For the slit to propagate thereby increasing its surface, it needs a certain amount of energy. This energy is called the energy of fracture. With the formation of a new surface the strain in the corresponding area will be reduced which results in the release of corresponding elastic energy from the body.

$$\delta\tau = G * \delta \quad \text{eq. 1.44}$$

where  $\delta\tau$  is the energy of fracture necessary for the formation of a new fracture surface area.  $G$  is the energy released into the crack tip per unit area of the crack (rate of elastic strain energy release), and  $\delta$  is the crack growth increment.

The strain energy release rate is higher for higher loads and larger cracks. If the strain energy so released exceeds a critical value  $G_c$ , then the crack will grow spontaneously. For brittle materials,  $G_c$  can be equated to the surface energy of the (two) new crack surfaces; in other words, in brittle materials, a crack will grow spontaneously if the strain energy released is equal to or greater than the energy required to grow the crack surface(s). The stability condition can be written as

$$\text{elastic energy released} = \text{surface energy created}$$

If the elastic energy released is less than the critical value, then the crack will not grow; equality signifies neutral stability and if the strain energy release rate exceeds the critical value, the crack will start growing in an unstable manner. For ductile materials, energy associated with plastic deformation has to be taken into account. When there is plastic

deformation at the crack tip, the energy to propagate the crack may increase by several orders of magnitude as the work related to plastic deformation may be much larger than the surface energy. In such cases, the stability criterion has to restated as

$$\text{elastic energy released} = \text{surface energy} + \text{plastic deformation energy}$$

Practically, this means a higher value for the critical value  $G_c$ . From the definition of  $G$ , we can deduce that it has dimensions of work (or energy)/area or force/length [Anderson 1995, Lawn 1993, Knott 1973]. The Stress Intensity Factor,  $K$ , is used in fracture mechanics to more accurately predict the stress state ("stress intensity") near the tip of a crack caused by a remote load or residual stresses.

### 1.6.1.- The energy balance approach

The basis of the fracture mechanics approach is the use of the strain energy release rate as a means of characterizing crack growth behaviour. If a specimen of material under stress is considered, the specimen will contain a certain amount of strain energy,  $U$  say. In the presence of a crack,  $U$  will be altered by an amount that depends on the crack length; if the specimen is considered at constant deformation, so that the external forces do no work, the stored energy will be decreased and the strain energy release rate can be defined as [Rivlin and Thomas 1953, Thomas 1994]

$$G = -\partial U / \partial A \quad \text{eq. 1.45}$$

where  $A$  is the area of one fracture surface of the crack and the partial derivative refers to constant deformation. (The latter condition is imposed merely for convenience of definition. In some calculations, it is more straightforward to allow movement of the external forces and then to take into account the work done, in calculating  $G$ ).

The development of the fracture mechanics approach for elastomers was greatly facilitated by the realization that  $G$  could be determined for certain specimen geometries without the need to solve the complex stress distribution around the crack tip. This has allowed the validity of the approach to be investigated experimentally [Rivlin and Thomas 1953, Thomas 1994, Thomas 1960, Lake, *et al.* 1969].

If  $dW$  is the amount of work (due to external force) necessary to propagate a crack, and  $dU$  is the variation of the elastic energy  $U$  during the propagation, then the difference between these two quantities  $dW - dU$  is the available energy to create new surface. For a crack of  $dl$  width, we can write the condition for crack propagation:

$$\frac{dW}{dl} - \frac{dU}{dl} \geq \gamma_s \frac{dA}{dl} \quad \text{eq. 1.46}$$

where  $\gamma_s$  is the surface energy. If the global deformation of the system is zero when the crack propagates, we have  $dW = 0$  and equation 1.46 becomes:

$$-\frac{dU}{dl} \geq \gamma_s \frac{dA}{dl} \quad \text{eq. 1.47}$$

We also define the energy release rate  $G$

$$G = \frac{dW}{dA} - \frac{dU}{dA} = e_0 \left[ \frac{dW}{dc} - \frac{dU}{dc} \right] \quad \text{eq. 1.48}$$

where  $e_0$  is the sample thickness. Then the fracture occurs when  $G$  reach a critical value  $G_c$ .

In order for the approach to be useful, it is necessary that the rate of growth be uniquely defined by  $G$  (at least to within the rather large variability that is commonly observed for fracture measurements). Under many circumstances, but not all, this has been found to be the case for elastomers. The results all fall essentially on the same relationship which thus constitutes a characteristic, geometry-independent property of the material [Thomas 1960, Lake, *et al.* 1969]. A crack in a solid may be loaded in three different modes presented in Figure 1.19.

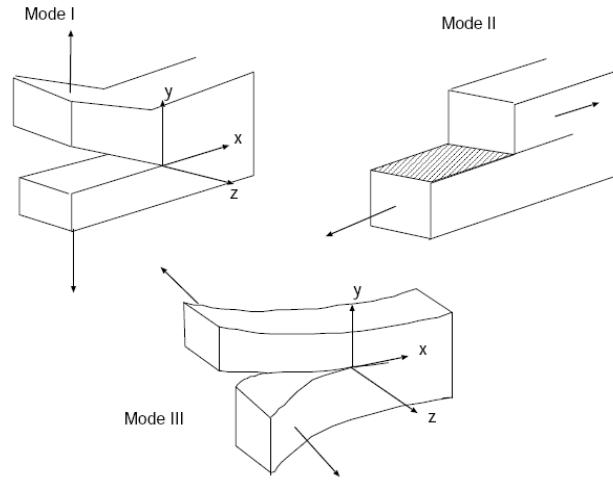


**Figure 1.19:** Three modes for loading a crack: Mode I, in tension, opening mode; Mode II, in-plane shear, sliding mode; mode III, out-of-plane shear, tearing mode.

At first sight, it is perhaps surprising that an approach, in which the parameter used to characterize fracture is derived from considerations remote from the crack tip, should prove helpful in describing fracture phenomena. However, the energy release rate is in fact closely related to the strain energy density in the material at the tip (where fracture occurs), this relationship being of the form [Thomas 1955]

$$G = U_t d \quad \text{eq. 1.49}$$

where  $U_t$  is a suitably averaged value of the strain energy density at the tip and  $d$  is the effective tip diameter.

Thus  $G$  is, in fact, closely related to the stress concentration at the crack tip via the local strain energy density. It may be noted that the tip diameter,  $d$ , is also important and must be substantially unaffected by test piece geometry if the approach is to work [Lake 2003].

### 1.6.2.- The Threshold Energy: Molecular model

According to Lake and Thomas [Lake and Thomas 1967] the effect of crosslinking is twofold. The shorter the molecular length between points of crosslinking, the fewer the number of bonds which must be stressed in order to break a molecular chain. On the other hand, when the chains are short there will be a greater number of them crossing a randomly chosen fracture plane. These two factors do not cancel out; their net effect is a predicted dependence of the fracture energy  $G_0$  upon the average molecular weight  $M_c$  of chains between points of crosslinking. The plane of crack propagation ahead of a crack tip will be crossed by a number of molecular chains, like illustrated in Figure 1.20, whose end points (crosslinks) lie on opposite sides of the plane.

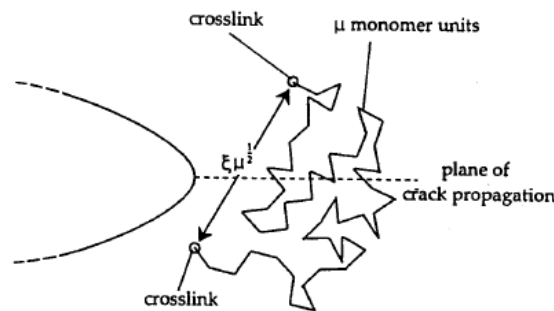


**Figure 1.20:** Schematic diagram showing a molecular chain crossing the fracture plane ahead of the crack tip in the unstrained state. The chain is supposed to contain  $\mu$  freely jointed segments each of length  $\xi$ .

Recalling equation 1.49

$$G = U_t d$$

this gives  $d \cong \xi \mu^{1/2}$ ,  $\xi$  is the length of a monomer unit and ' $\mu$ ' is the number of units between crosslinks. The maximum possible energy density will be of the order of  $bJ$ , where  $b$  is the number of single bonds per unit volume and  $J$  is the energy stored by each single bond at its rupture point [Lake 2003, Gent 1992]. Substituting in equation 1.49 yields,

$$G_0 = bJ\xi\mu^{1/2} \quad \text{eq. 1.50}$$

The equation 1.50 predicts the threshold energy for crack growth:  $G_0$  proposed by Lake and Thomas [Lake and Thomas 1967]. The important result here is that  $G_0$  is predicted to scale with  $M_c^{1/2}$ , i.e. the more crosslinked the elastomer and the lower its threshold fracture energy.

### 1.7.- Molecular rate processes with a constant activation energy: relevance for fracture processes.

In this last section, we present some basics of the Arrhenius type equations that can govern physicochemical processes. The bases of all these approaches are the Brownian motion of the molecules due to thermal fluctuations. All molecules in liquids can move around their mean positions. As a result interatomic distances are not fixed but vary and there is a finite non zero probability to go over the activation barrier and break a bond. Elastomers behave like liquids at the molecular scale and therefore bond breakage under stress will be a probabilistic event.

The Arrhenius equation is a simple, but remarkably accurate, formula for the temperature dependence of the rate constant. The diffusion coefficient for example  $D$ , is written as:

$$D = D_0 \exp\left(\frac{-E_d}{RT}\right) \quad \text{eq. 1.51}$$

where  $D_0$  is a frequency factor correlating with the initial concentration dependence of  $D$ ,  $T$  is temperature,  $R$  the gas constant, and  $E_d$  is the activation energy for diffusion. In addition, an Arrhenius equation applies to the kinetics of chemical reactions:

$$k = A \exp\left(\frac{-E_a}{RT}\right) \quad \text{eq. 1.52}$$

Where  $k$  is the rate of the chemical reaction, the frequency factor  $A$  is concerned with molecular collisions, and the activation energy  $E_a$  is the critical energy needed for reaction to occur. Common sense and chemical intuition suggest that the higher the temperature, the faster a given chemical reaction will proceed. Quantitatively this relationship between the rate a reaction proceeds and its temperature is determined by the Arrhenius Equation. At higher temperatures, the probability that two molecules will collide is higher. This higher collision rate results in a higher kinetic energy, which has an effect on the activation energy of the reaction. The activation energy is the amount of energy required to ensure that a reaction happens.

The Eyring equation also known as Eyring–Polanyi equation in chemical kinetics relates the reaction rate to temperature. It was developed almost simultaneously in 1935 by Eyring, and Evans and Polanyi [Evans and Polanyi 1935, Eyring 1935]. This equation follows from

the transition state theory (*aka*, activated-complex theory) and contrary to the empirical Arrhenius equation this model is theoretical and based on statistical thermodynamics. The general form of the Eyring–Polanyi equation somewhat resembles the Arrhenius equation:

$$k = \frac{k_B T}{h} e^{-\frac{\Delta G}{RT}} \quad \text{eq.1.53}$$

where  $\Delta G$  is the Gibbs energy of activation,  $k_B$  is Boltzmann's constant, and  $h$  is Planck's constant. It can be rewritten as:

$$k = \left( \frac{k_B T}{h} \right) \exp\left(\frac{\Delta S}{R}\right) \exp\left(-\frac{\Delta H}{RT}\right) \quad \text{eq. 1.54}$$

To find the linear form of the Eyring-Polanyi equation:

$$\ln \frac{k}{T} = \frac{-\Delta H}{R} * \frac{1}{T} + \ln \frac{k_B}{h} + \frac{\Delta S}{R} \quad \text{eq.1.55}$$

where:  $k$  = reaction rate constant,  $T$  = absolute temperature,  $\Delta H$  = enthalpy of activation,  $R$  = gas constant,  $k_B$  = Boltzmann constant,  $h$  = Planck's constant,  $\Delta S$  = entropy of activation. A certain chemical reaction is performed at different temperatures and the reaction rate is determined. The plot of  $\ln(k/T)$  versus  $1/T$  gives a straight line with slope  $-\Delta H/R$  from which the enthalpy of activation can be derived and with intercept  $\ln(k_B/h) + \Delta S/R$  from which the entropy of activation is derived [Evans and Polanyi 1935, Eyring 1935, Polanyi 1987].

The general Eyring model includes terms that have stress and temperature dependences (in other words, the effect of changing temperature varies, depending on the levels of other stresses). Most models in actual use do not include any interaction terms, so that the relative change in acceleration factors when only one factor changes does not depend on the level of the other factors. Henry Eyring's contributions to chemical reaction rate theory have led to a very general and powerful model for acceleration known as the Eyring Model.

$$\frac{dr}{dt} = r_0 \exp\left(-\frac{\Delta H}{RT}\right) \sinh\left(\frac{\sigma V a}{RT}\right) \quad \text{eq. 1.56}$$

These Eyring equations are commonly used to explain temperature activated processes such as fluid viscosity, plasticity and yield stress and also molecular fracture. In the late part of the manuscript we will explore briefly how this probabilistic analysis can apply to the process of nucleation of cavities.

## Bibliography

- Abder-Rahim, D. « Synthèse in situ de microparticules polyuréthane par addition interfaciale dans un monomère epoxide ». Chapter II. PhD Thesis INSA de Lyon, (2001).
- Alkonis, J.J. , Maxknight, W.J. and Shen, M., Introduction to polymer viscoelasticity, Wiley–Interscience/Wiley, New York (1972).
- Anderson T.L., Fracture Mechanics: Fundamentals and Applications, CRC Press, Boston (1995).
- Andrews, E. H., Proc. Phys. Soc. 77, 483 (1961).
- Baker, J.W., Holdsworth, J.B, Journal of Chemical Society, 713–726, (1947).
- Edwards, S. F. and Vilgis, T., Polymer, 27, 483-492 (1986).
- Evans, M.G. and Polanyi M., Trans. Faraday Society, 31, 875 (1935).
- Eyring, H., Journal of Chemistry Physics, 3, 107 (1935).
- Farben, I.G., German Patent 728.981, (1937)
- Flory, P.J. and Rehner, J., Journal of Chemistry Physics, 11, 512 (1943).
- Flory, P.J., Polymer Journal, 17, 1, 1-12 (1985).
- Gedde, ULF. W., Polymer Physics, Kluwer Academic Publishers (1999).
- Gent, A. N. Engineering with Rubber, Hanser Publishers, USA (1992).
- Gent, A. N. Rubber Chemistry and Technology, 69, 59-61 (1996).
- Gent, A.N. and Lindley, P.B., Proc. Royal Society London, Ser. A, 249, 195 (1959)
- Gent, A.N. and Meinecke, E.A., Polymer Engineering Science, 10, 48 (1970).
- Gent, A.N. and Thomas, A.G., Journal of Polymer Science, 28, 265 (1958).
- Gent, A.N. and Wang, C., Journal of Materials Science, 26, 3392 (1991).
- Gent, A.N. and Tompkins, D.A., Journal of Applied Physics, 40, 2520 (1969).
- Gent, A.N., Henry, R.L. and Roxbury, M.L., Journal of Applied Mechanics, 41, 855 (1974).
- Gough, J., Mem. lit. Philosophical Society Manchester, 1, 288 (1805).
- Griffith, A.A., Phil. Trans. Royal Society, A221, 163-198 (1920).
- Halary, J.L. and Lauprête, F., De la macromolécule au matériau polymère, editions Belin (2006).
- Halary, J.L., Lauprête, F. and Monnerie, L., Mécanique des matériaux polymères, editions Belin (2008).
- Hiemenz, P. C., and Timothy P. L., Polymer Chemistry. 2nd ed. Florida: Taylor & Francis Group, 486-491 (2007).
- James, H. M. and Guth, E., Journal of Polymer Science, 4, 153-182 (1943).
- Joule, J.P., Phil. Trans. Royal Society, 149, 91 (1859).
- Knott, J.F., Fundamentals of Fracture Mechanics (1973).
- Lake G.J. and Thomas A.G., Proc. R. Soc. London, Ser. A, 300, 108 (1967).
- Lake, G. J., Lindley, P. B. and Thomas, A. G., Proc. Int. Conf Fract., 2nd, Brighton, Chapman and Hall, London, p. 493 (1969).
- Lake, G.J., Rubber Chemistry and Technology, 76, 567-591 (2003).
- Lawn B., Fracture of Brittle Solids, Cambridge University Press, 2nd edition (1993).



- Love, J.C., Estroff, L.A., Kriebel, J.K., Nuzzo, R.G. and Whitesides, G.M., *Chemical Review*, 105, 1103-1169 (2005).
- Mooney, M., *Journal of Applied Physics*, 11, 582 (1940).
- Oclin, S. "A Molecular Printboard on Glass", PhD thesis, University of Twente, The Netherlands, (2004).
- Odian, G., *Principles of polymerization*, Wiley, New York, 1981.
- Oertel, G., *Polyurethane Handbook*. New York: Macmillen Publishing Co., Inc (1985).
- Polanyi, J.C., *Science*, 236 (4802), 680–690 (1987).
- Randall, D.; Lee, Steve, *The Polyurethanes Book*. New York: Wiley. (2002).
- Rivlin, R. S. and Thomas, A.G., *Journal of Polymer Science*, 10, 291 (1953).
- Rivlin, R.S. in Eirich, F.R., Ed., *Rheology, Theory and Applications*, Vol. 1, Academic Press, New York, Chapter 10, (1956).
- Rubinstein M. and Colby R.H., *Polymer Physics*, University Press, Oxford (2003).
- Rubinstein, M. and Panyukov, S. *Macromolecules* 35, 6670-6886 (2002).
- Schwartz, D.K., *Annu. Review of Physical Chemistry*. 52, 107 (2001).
- Sullivan, T. P. and Huck, W. T. S., *Eur. Journal of Organic Chemistry*, 17-29, (2003).
- Techniques de l'ingenieur: Berthier, J. C., *Polyurethane PUR*, AM 3 425 v2.
- Thomas, A. G. "The Development of Fracture Mechanics for Elastomers," Goodyear Medal paper presented to the American Chemical Society Rubber Division Meeting, Chicago, April 1994; *RUBBER CHEM. TECHNOL.* 67, G50 (1994).
- Thomas, A. G., *Journal of Applied Polymer Science*, 3, 168 (1960).
- Thomas, A. G., *Journal of Polymer Science*, 18, 177 (1955).
- Treloar, L.R.G., *The Physics of Rubber Elasticity*, 3<sup>rd</sup> ed., Clarendon Press, Oxford, (2005).
- Ulrich, H., *Chemistry and Technology of Isocyanates*. New York: John Wiley & Sons, Inc (1996).
- Vos, J., G., Forster, R. J., Keyes, T. E., *Interfacial Supramolecular Assemblies*. Wiley, John & Sons, Incorporated, 88-94 (2003).
- Wall, F.T., *Journal of Chemistry Physics*, 10, 132 (1942).
- Ward, I.M. and Hadley, D.W., *An Introduction to the Mechanical Properties of Solid Polymers*, John Wiley and Sons, England (1998).
- Williams, M.L. and Schapery, R.A, *Int. Journal of Fracture Mechanics*, 1, 64 (1965).
- Wnek, G. and Bowlin, G. L., *Encyclopedia of Biomaterials and Biomedical Engineering*. Informa Healthcare, 1331-1333 (2004).
- Woods, G., *The ICI Polyurethanes Book*. New York: John Wiley & Sons, Inc. (1990).
- Young, R.J. and Lovell, P.A., *Introduction to Polymers*, Chapman & Hall, (2nd Edition), London (1991).

# **CHAPTER 2**

## **Model Networks: Purifications, Synthesis and Characterizations**

Introduction .....	55
2.1.- Materials .....	56
2.2.- Purifications and Characterization .....	56
2.2.1.- Purifications of reagents .....	56
2.2.1.1.- Purification of Poly(propylene) glycols (PPGs): .....	56
2.2.1.2.- Characterization of PPGs .....	57
2.2.1.2.1.- Molecular weight: Nuclear Magnetic Resonance (NMR) .....	57
2.2.1.2.2.- Polydispersity: Gel permeation Chromatography (GPC) .....	61
2.2.1.2.3.- MALDI-ToF .....	61
2.2.1.3.- Purification of DESMODUR RFE to obtain tris(p-isocyanatophenyl) thiophosphate .....	62
2.2.1.4.- Characterization of purified tris(p-isocyanatophenyl) thiophosphate : .....	63
2.3.- Preparation of Model Networks .....	64
2.3.1. Synthesis of PU networks .....	64
2.3.2. Networks molding and curing .....	66
2.4.- Model Networks Characterization .....	68
2.4.1.- Chemical groups identification: ATR-FTIR .....	68
2.4.2.- Density of Polyurethanes networks .....	71
2.4.3.- Sol Fraction and Swelling experiments .....	72
2.4.3.1.- Solfractions .....	72
2.4.3.2.- Swelling experiments .....	72
2.4.4.- Model Networks Homogeneity: Proton Multiple-quantum (MQ) NMR .....	75
2.5.- Small strain behaviour by Dynamical Mechanical Analysis (DMA) .....	78
2.5.1.- DMA results and Thermoelasticity .....	78
2.5.1.1.- Density changes with temperature: Thermal expansion of the networks .....	85
Conclusions .....	88
Acknowledgements .....	89
Appendices A2 .....	90
Appendix A2.1: NMR .....	90
Appendix A2.2: GPC .....	95
Appendix A2.3: MALDI-ToF .....	95
Appendix A2.4: Experimental adjustment of NCO/OH .....	96
Appendix A2.5: Optimization of the time for the curing at 80°C of the polyurethane model networks .....	96
Appendix A2.6: Density calculations .....	97
Appendix A2.7: Solubility parameters .....	97
Appendix A2.8: $D_{res}$ as a function of the swelling percentage in mass .....	97
Appendix A2.9: Thermal expansion .....	98
Bibliography .....	99

## Introduction

The main objective of this thesis is to establish the role played by the composition and crosslinking structure of a rubber (soft material) on its resistance to cavitation under a predominantly hydrostatic pressure. To accomplish this objective we decided to work with model networks. An elastomeric model network is typically made by endlinking precursors with known molecular weights and functionality to a multi-functional cross-linker in well controlled stoichiometric conditions very close to the theoretical ones. This should give a very homogeneous network with a well defined molecular weight between crosslink points and very few loops, pendant chains and unreacted chains..

Most of the work reported in the literature about elastomer model networks [Beshah *et al.* 1986, Garrido *et al.* 1988, Andrady *et al.* 1992, Takeuchi and Cohen (1999), Yoo and Cohen (2006), Urayama *et al.* 2009, among others] has been done on polydimethylsiloxane (PDMS), which gives very elastic and transparent samples; however, monodisperse precursors are not commercially available in large quantity and typical stoichiometries used tend to be far from ideal because of side reactions. This has motivated us to use for our purpose a different model network system than PDMS.

Another kind of elastomer model network already developed and available in the literature was the one prepared by Bos and Nusselder in 1994 [Bos and Nusselder 1994]. They prepared polyurethane model networks from triisocyanate and diols (PPGs) of various molecular weights. The use of commercially available poly (propylene) glycols (PPGs) very monodisperse, with relatively low molecular weights let them obtain very well defined molecular structures and very elastic materials. The use of unfilled materials also meant that the samples were transparent, an essential quality to follow optically and in real time the phenomena of cavitation (position, shape and number of cavities) during the tensile experiments in confined conditions (Chapters 4 and 5).

Based on that model system, we however had to design a different protocol of purification for the reagents, and used different PPGs molecular weights. Three different model networks were prepared: the first one based on a PPG with molecular weight of 4000g/mol and triisocyanate (PU4000); a second one based on a PPG with molecular weight of 8000g/mol and triisocyanate (PU8000). These two networks were made with the purpose of having two different molecular structures with two different crosslink densities, close to and above the average molecular weight between entanglements ( $M_e \sim 3000$ g/mol [Florez *et al.* 2006]). A third network, a bimodal network, was prepared based on PPG8000g/mol and PPG1000g/mol and triisocyanate (PU8000/1000); this network was made with the purpose of investigating the effect of adding short chains (PPG1000) to long chains (PPG8000) on the mechanical properties, which based on recent publications, can have an important effect on mechanical properties [i.e. Youn Kim *et al.* 1986].

This Chapter describes the synthesis conditions: purification and characterization of the reagents (PPGs and DESMODUR RFE), procedure to prepare the three polyurethane model

networks and the characterization of the linear viscoelastic, local dynamics and swelling properties of the networks in order to determine their macromolecular architecture.

## **2.1.- Materials**

The following chemicals were used without further purification: dry toluene (Aldrich); IRGANOX<sup>®</sup> 1035: sulphur containing primary (phenolic) antioxidant and heat stabilizer (kindly supplied by CIBA<sup>®</sup>). All solvents (acetone, cyclohexane, toluene, dichloromethane, and ethanol) were purchased from either Aldrich or Sigma.

The following materials were purified before being used: ACCLAIM<sup>®</sup> 4200, Polyether Polyol with nominal molecular weight 4000 g/mol; and ACCLAIM<sup>®</sup> 8200, Polyether Polyol, with nominal molecular weight 8000g/mol (kindly supplied by Bayer). POLY-G<sup>®</sup> 20-112 Urethane grade, Polyether diol, with nominal molecular weight 1000g/mol (kindly supplied by Arch Chemicals, Inc.); DESMODUR<sup>®</sup> RFE, solution of tris(p-isocyanatophenyl) thiophosphate in 27% of ethyl acetate (purchased from Bayer).

## **2.2.- Purifications and Characterization**

### **2.2.1.- Purifications of reagents**

In order to avoid the presence of additives, solvents, water and other impurities, the reagents necessary for the preparation of the polyurethane model networks were purified. This purification was made to have better control on the stoichiometry of the reaction. All glassware used to perform purifications and synthesis was every time cleaned, rinsed with acetone and dried @ 120°C. The synthesis was carried out under nitrogen atmosphere (inside the gloves box, H<sub>2</sub>O < 0.5 ppm).

#### **2.2.1.1.- Purification of Poly(propylene) glycols (PPGs):**

The three PPGs that were used belong to the chemical family of polyether polyol, and are diols. Since the PPG is hygroscopic, an azeotropic distillation had to be carried out; this kind of distillation is used whenever further separation by conventional distillation is no longer possible. The azeotropic distillation consists of the separation of a liquid mixture containing azeotropes, at which the composition, temperature, and pressure of the liquid phase become equal to those of the vapor phase. By adding a selected entrainer to the mixture (in this case cyclohexane), it is often possible to “break” the azeotrope and thereby to achieve the desired separation [Seader 2005].

To do the azeotropic distillations, the PPG was poured into a balloon with cyclohexane and brought to the rotavap. At ~80°C, under vacuum (~2mbar) the cyclohexane and water are distilled. This procedure was repeated for every PPG used. The purified product was then

poured into a clean and dry bottle and stored inside the gloves box. Figure 2.1 shows the scheme of this purification procedure.

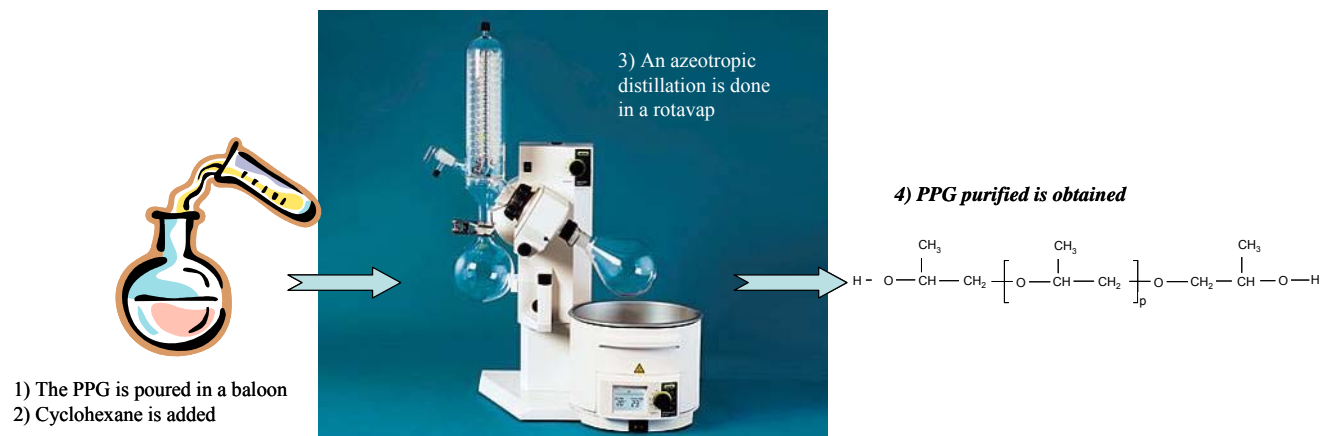


**Figure 2.1:** Scheme of purification of Poly (propylene) glycol (PPGs)

#### 2.2.1.2.- Characterization of PPGs

Based on the technical data sheets of Bayer [Bayer data sheets], the ACCLAIM series (PPG diols) are the products with lowest percentage of monol (i.e. only one hydroxyl functional group per chain) content in the market: PPG 4200 has 2% of monol, and PPG 8200 has 4% of monol content. Additionally, the ACCLAIM series is said to have a very narrow molecular weight distribution:  $I_p \sim 1.05$ -1.15. These two characteristics were the main reasons to choose the series ACCLAIM for our samples' preparation.

Once the PPGs were purified, a characterization was done to obtain a reliable molecular weight value (to be used in the stoichiometric calculations), the molecular weight distribution and the concentration of the hydroxyl numbers of each PPG.

We used three techniques. The " $M_n$ " (used to calculate the stoichiometry of the reaction and the functionality), and " $n$ " values were obtained by NMR and Maldi-TOF and the  $I_p$  values (polydispersity or molecular weight distribution) were obtained by GPC. The PPG functionality was assumed to be two (diol).

##### 2.2.1.2.1.- Molecular weight: Nuclear Magnetic Resonance (NMR)

In its simplest form NMR allows identification of individual atoms in a pure molecule. NMR is based in quantum mechanical properties of nuclei, and as such it is very reliable, predictable and reproducible. When a sample is placed in a magnetic field, NMR active nuclei (like  $^1\text{H}$  or  $^{13}\text{C}$ ) resonate at a specific frequency, dependent on strength of the magnetic field [Pavia and Lampman, 2000].

The structures of the three PPGs were investigated using  $^1\text{H}$  and  $^{13}\text{C}$  NMR spectroscopy. Because the PPGs are hygroscopic we used both techniques (proton and carbon) to verify that the molecular weight obtained by  $^1\text{H}$  NMR was correct.

The three PPGs were analysed before and after purification. The conditions used to perform the experiments were the following:  $^1\text{H}$  NMR spectra were recorded in TFA/ $\text{CDCl}_3$  (1/4 v/v) on a Bruker 400 MHz spectrometer @  $\sim 25^\circ\text{C}$ .  $^{13}\text{C}$  NMR spectra were recorded in  $\text{CDCl}_3$  + Crom(acac) $_2$  on a « Avance 300 » with a sonde BBO 10 mm; and the program for analysis was Xwinnmr. The  $^1\text{H}$  and  $^{13}\text{C}$  chemical shifts were referenced to residual  $\text{CHCl}_3$  at 7.26 ppm and to  $\text{CDCl}_3$  at 76.9 ppm, respectively. The  $^1\text{H}$  NMR spectra were recorded after the hydroxyl end groups were reacted with trifluoroacetic anhydride (TFA).

The proton and carbon numbering used for NMR analysis is described as follows:

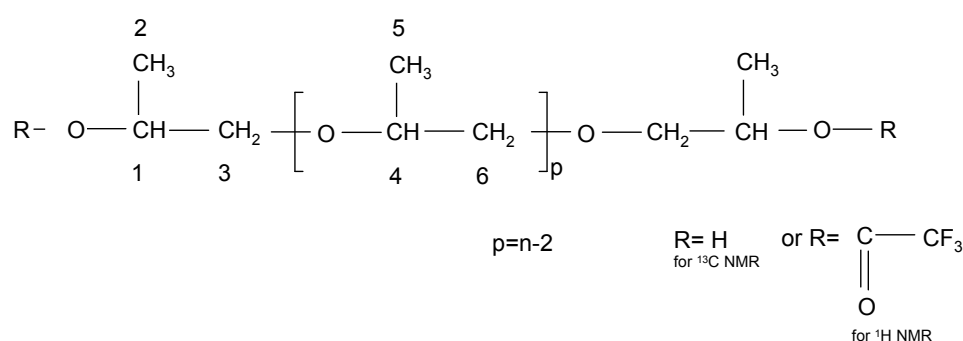


**Table 2.1:** Assignment of  $^1\text{H}$  NMR chemical shifts of PPG when  $\text{R} = \text{COCF}_3$

<b>n° H</b>	<b>1</b>	<b>4</b>	<b>3</b>	<b>6</b>	<b>2</b>	<b>5</b>
<b>δ(ppm)</b>	5.22	3.85-3.67	3.67	3.70-3.42	1.32	1.15

The software Xwinnmr allowed the analysis of the each peak to understand how many protons give rise to the peak. This integration of the area under each peak gives a relative value that is assigned to the chemical shifts (protons n°1, 2, 3, etc.). In appendix A2.1, an example of calculation is presented for the PPG 4000 purified. The resulting values calculated for each PPG by this methodology are reported in Table 2.2. The value “n”, which is the

number of times that the monomer repeats in the polymer, was calculated experimentally to obtain  $M_n$  for each PPG and these values are also reported in Table 2.2.

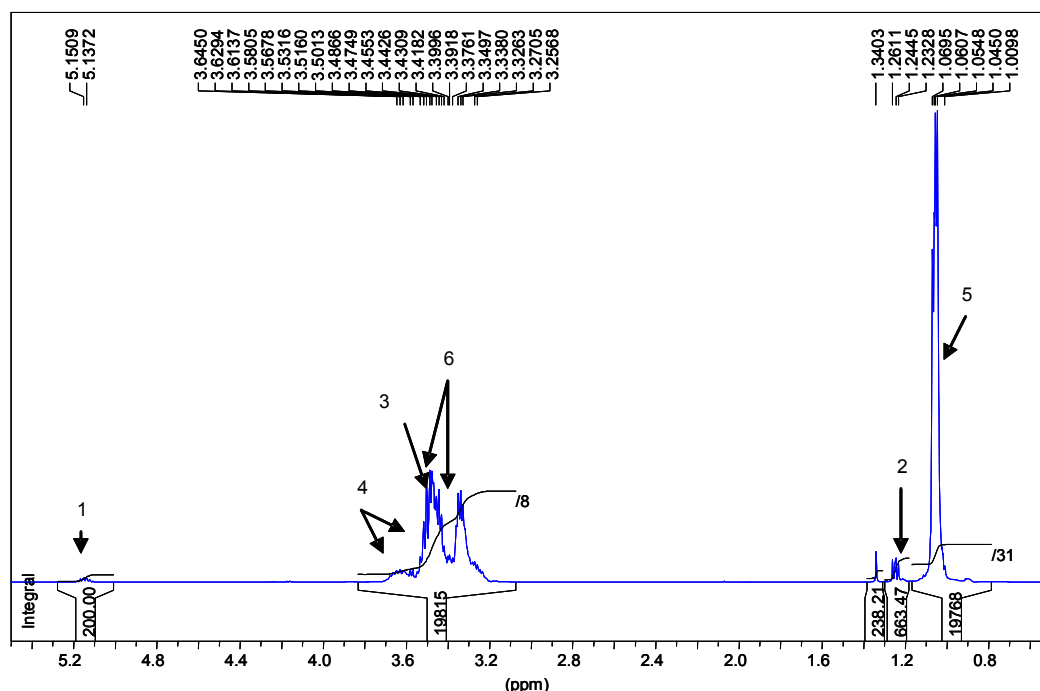


**Figure 2.2:**  $^1\text{H}$  NMR spectrum of PPG 4000 purified

The three PPGs studied have all secondary hydroxyl end groups as the doublet at  $\sim 4.42$  ppm relative to methylene protons in  $\alpha$  position of trifluoroacetylated hydroxyl end group (i.e.  $\text{CF}_3\text{-CO-O-CH}_2\text{-CH}(\text{CH}_3)\text{-}$ ) is not observed.

Two values were also calculated for the PPGs to know the concentration of hydroxyl functions (OH) are the  $\text{C(OH)}$  [mmol/gr] and the hydroxyl number [mg KOH/g]. Using values of  $M_n$  obtained by  $^1\text{H}$  NMR, the  $\text{C(OH)}$  [mmol/g] can be calculated assuming that the functionality given by the supplier is correct (2 OH per PPG molecule). An example of this calculation is also given in Appendix A2.1 for PPG4000. The resulting values are reported in Table 2.2. The measured hydroxyl numbers correspond quite well to the values reported by the suppliers for these three PPGs [Bayer data sheet].

**Table 2.2:** Molecular weight  $M_n$ , value of the repetitive unit “n”, and calculated  $\text{C(OH)}$  mmol/g and hydroxyl number I (OH) of the three PPGs, obtained by  $^1\text{H}$  NMR.

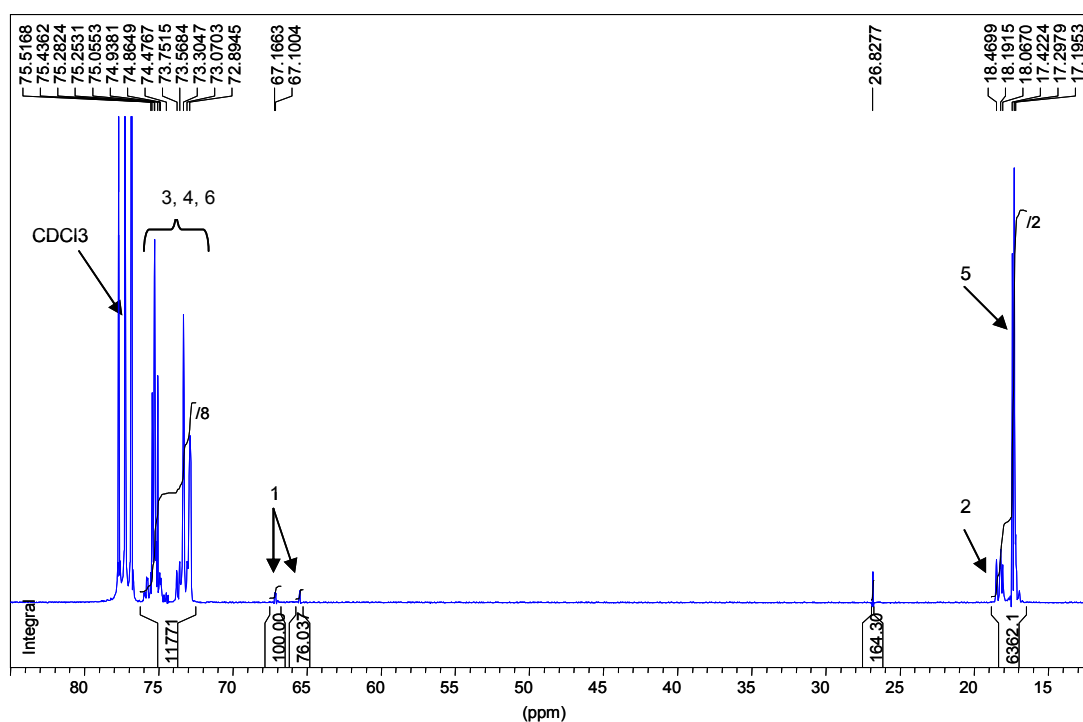
Nominal $M_n$ PPG [g/mol]	$^1\text{H}$ NMR $M_n$ [g/mol]	$^1\text{H}$ NMR “n”	$\text{C(OH)}$ mmol/g [N° mmol OH/g PPG]	Hydroxyl Number I(OH) [mg KOH/ g]
1000	990	16.7	2.02	113.3
4000	3887	66.7	0.51	28.6
8000	7987	137.4	0.25	14.0



Figure 2.3 shows a spectrum (for PPG4000, purified) as an example of the kind of resulting spectra we obtained by  $^{13}\text{C}$  NMR. The peak assignment is reported in Table 2.3. An example of how  $M_n$  can be calculated by using  $^{13}\text{C}$  NMR spectra, integration peaks (for PPG4000 purified) as well as the spectra of  $^{13}\text{C}$  NMR for PPG8000 and PPG1000 are presented in appendix A2.1.

**Table 2.3:** Assignment of  $^{13}\text{C}$  NMR chemical shifts of PPG when R = H

n° H	1	4	3	6	2	5
$\delta(\text{ppm})$	66-67	74-75	74	73-75	18-19	17



**Figure 2.3:**  $^{13}\text{C}$  NMR spectrum of PPG 4000 purified

The number average molecular weights  $M_n$  and the degree of polymerization “n” obtained for the three PPGs by  $^1\text{H}$  NMR and  $^{13}\text{C}$  NMR are summarized in Table 2.4. The values obtained by the two techniques are close, and we used for further calculations the values obtained by  $^1\text{H}$  NMR.

**Table 2.4** Values of molecular weights  $M_n$  and “n” for PPGs obtained by  $^1\text{H}$  NMR and  $^{13}\text{C}$  NMR

Material	$^1\text{H}$ NMR		$^{13}\text{C}$ NMR	
	$M_n[\text{g/mol}]$	$n$	$M_n[\text{g/mol}]$	$n$
PPG 1000	990	16.7	946	16
PPG 4000	3887	66.7	3960	68
PPG 8000	7987	137.4	7960	137

#### 2.2.1.2.2.- Polydispersity: Gel permeation Chromatography (GPC)

Size exclusion chromatography (SEC) also called gel permeation chromatography (GPC) allows the separation of polymer molecules based on their hydrodynamic radius. For our experiments THF was used as solvent and the three PPGs were studied. The set up we used had three detectors: (1) Refractometer; (2) Viscometer; (3) Light scattering.

For PPG 1000 (purified and not purified) there was not enough signal in the light scattering detector, so a universal  $\log [\eta] M_n$  in function of the elution volume calibration curve was used as reference.

The GPC technique presents some limitations regarding the accuracy of the  $M_n$  value obtained. Then, since we had the NMR results, the  $M_n$  obtained by GPC was used only for comparison. However, this technique is quite good to obtain the molecular weight distribution or polydispersity ( $I_p$ ) of the polymers.

In Table 2.5 are reported the  $I_p$  values obtained by GPC for each PPG. It can be observed that the three PPGs are very monodisperse, as reported by the supplier. An example of the monodispersity of the samples is shown in Appendix A2.2.

**Table 2.5:** Reported values of  $I_p$  obtained by GPC for PPG 1000, PPG 4000 and PPG 8000

Material	$I_p$
PPG 1000	1.08
PPG 4000	1.08
PPG 8000	1.10

#### 2.2.1.2.3.- MALDI-ToF

MALDI-ToF was used as the third technique to characterize the PPGs because in principle this technique is one of the most accurate to determine  $M_n$ . However as we will see in the results, when the molecular weight is higher ( $\geq$ PPG 4000) the technique is not that precise anymore.

The principle is that ions are generated by a Matrix-Assisted Laser Desorption/Ionisation (MALDI), accelerated by a high electric potential, and separated by the time taken to reach a detector (*Time-of-Flight (ToF)*). The time-of-flight is directly proportional to the mass-to-charge ratio of an ion, and hence a mass spectrum is obtained [Pasch and Schrepp 2003].

The three PPGs were studied (before and after purification) by MALDI-ToF. The samples were prepared in MeOH + DHB (70% can, 0.1% TFA) and NaCl (high molecular weight species). The same molecular weight was measured for non-purified and purified PPGs, as expected. An example of the spectra obtained by MALDI-ToF is presented in A2.3.

The  $M_n$  obtained by MALDI-ToF for PPG 4000 and PPG8000 are presented in Table 2.6 in comparison with the  $M_n$  obtained by  $^1\text{H}$  NMR. The measured values were systematically lower than the ones obtained by the other techniques.

**Table 2.6:** Values of the molecular weight  $M_n$  obtained by Maldi-ToF and  $^1\text{H}$  NMR, for the three PPGs.

Material	MALDI-ToF $M_n[\text{g/mol}]$	$^1\text{H}$ NMR $M_n[\text{g/mol}]$
PPG 1000	941	990
PPG 4000	3306	3887
PPG 8000	6875	7987

Then, based on these results, and considering the limitation of each technique, the values of  $M_n$  and “n” obtained by  $^1\text{H}$  NMR, and the  $I_p$  obtained by GPC were considered the most reliable.

#### 2.2.1.3.- Purification of DESMODUR RFE to obtain tris(p-isocyanatophenyl) thiophosphate

The DESMODUR RFE, because of its high reactivity, is sold commercially by Bayer and consists of a solution of tris(p-isocyanatophenyl) thiophosphate in 27% of ethyl acetate and an oily solution with additives. For the purification, this solution was poured into a balloon and brought to the rotavap; using a temperature up to  $\sim 80^\circ\text{C}$  and vacuum ( $\sim 2\text{mbar}$ ) the ethyl acetate was distilled. The remaining oily solution (additives + tris(p-isocyanatophenyl) thiophosphate) was poured into a flask, and after cooling down ( $\sim 40^\circ\text{C}$ ), some milliliters of cyclohexane were added. The flask was then heated up to  $\leq 80^\circ\text{C}$ . This heated solution was left to cool down; during the cooling, a phase separation took place between the “oily solution”(additives) and the “whitish solution” containing crystallized (tris(p-isocyanatophenyl) thiophosphate + cyclohexane). The “whitish solution” was left to cool down completely until room temperature and the crystallized solid was vacuum filtrated until obtaining a fine white powder that was put on a cresol and taken to a desiccator for a final drying step under vacuum during  $\sim 2.5$  h. In Figure 2.4, shows schematically the procedure of purification of the DESMODUR RFE to obtain tris(p-isocyanatophenyl) thiophosphate.

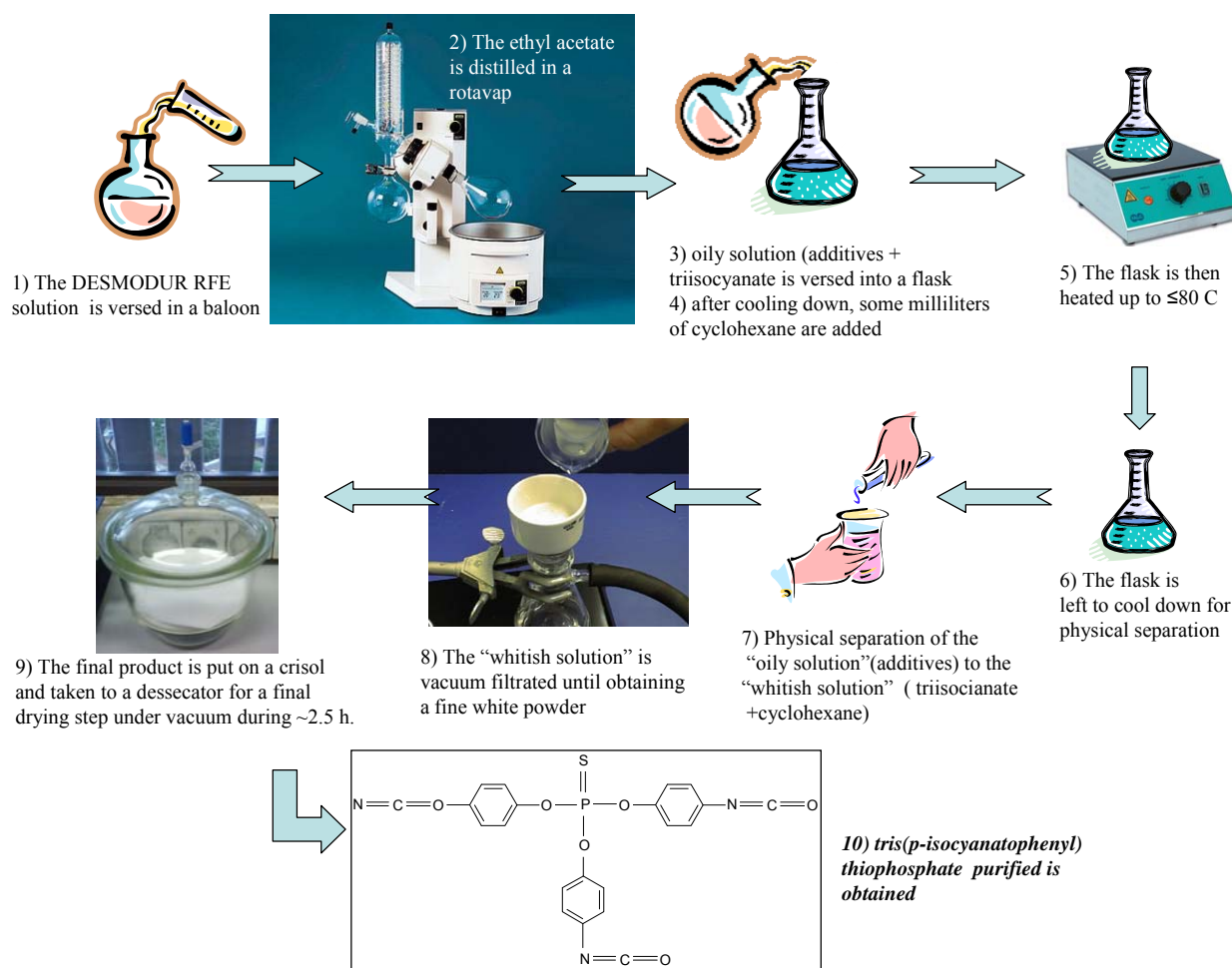


**Figure 2.4:** Schematic of the purification of the tris(p-isocyanatophenyl) thiophosphate.

#### 2.2.1.4.- Characterization of purified tris(p-isocyanatophenyl) thiophosphate :

Once the tris(p-isocyanatophenyl) thiophosphate was purified from DESMODUR RFE, a characterization was done by  $^1\text{H}$  NMR to evaluate how pure was the resultant product. The NCO groups in the tris(p-isocyanatophenyl) thiophosphate are quite reactive, they can react with themselves, with humidity, etc. then, special care has to be taken. The characterization as well as the synthesis using this product had to be done immediately after purification to avoid the loss of the available NCO groups.

To do the characterization by NMR, a few milligrams of the purified product were put inside an NMR tube together with chloroform, and this samples' preparation was done inside the gloves box. Figure 2.5 shows a typical spectrum. The quantitative analysis of the spectrum showed that the final product was  $>96\%$  of tris(p-isocyanatophenyl) thiophosphate; the remaining percentage corresponding to impurities and cyclohexane. This result was taken into account when making the calculations of the stoichiometry for the preparation of the model networks.

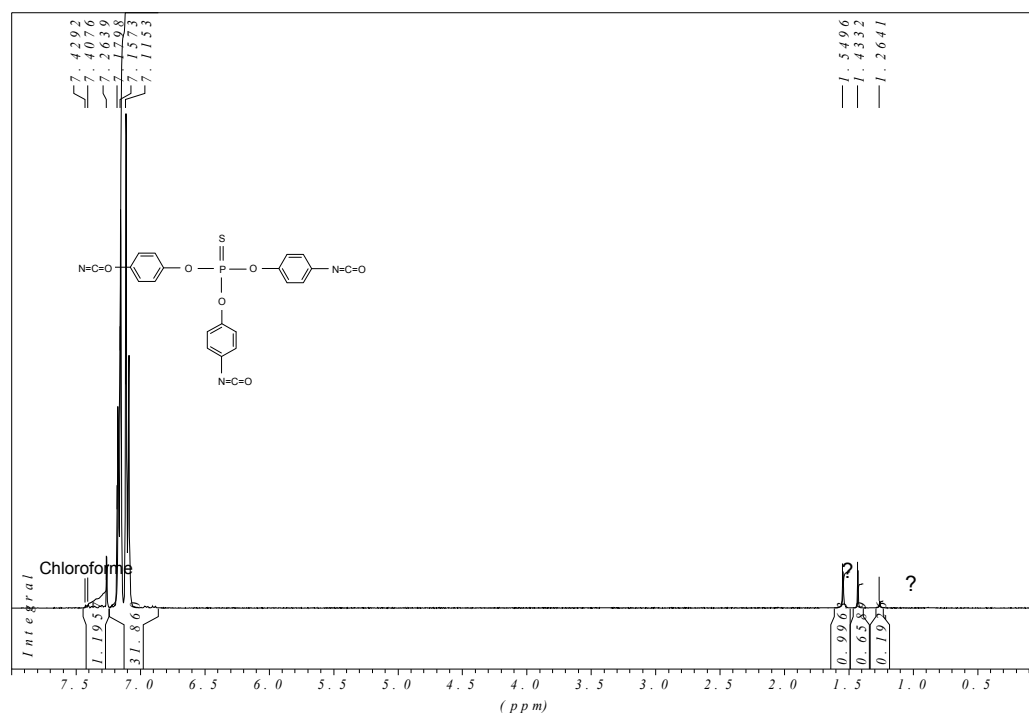


**Figure 2.5:**  $^1\text{H}$  NMR Spectrum of purified DESMODUR RFE.

## 2.3.- Preparation of Model Networks

### 2.3.1. Synthesis of PU networks

Due to the reactivity of the reagents, once purified, the synthesis of the networks had to immediately follow the purifications steps. On the basis of a blend of diol with triisocyanate, the stoichiometry for full conversion to obtain the polyurethanes was calculated by:

$$M_c^{\text{theor}} = M_{\text{PPG}} + 2/3 M_{\text{DESMODUR}}$$

where, for  $M_{\text{PPG}}$ , we used the  $M_n$  obtained by  $^1\text{H}$  NMR and for  $M_{\text{DESMODUR}}$  we used the nominal value 465.18 g/mol. The general chemical reaction of the poly diol with the triisocyanate is shown in Figure 2.6.

To determine the extent of conversion of these reagents into polyurethane, the solfractions, i.e. the amount of extractable material, was measured, using dichloromethane at room temperature. This technique was used to fine tune the stoichiometry by choosing the stoichiometry giving the lowest solfraction. There might be several reasons justifying the necessity of this final adjustment: the high reactivity of the NCO groups with impurities which depends on the experimental conditions but also the remaining solvents after purification of the DESMODUR RFE. Appendix A2.4 shows an example of the curve we used to obtain the lowest solfraction and the corresponding NCO/OH ratio.

After these adjustments, three polyurethane model networks were prepared following the formulations reported in Table 2.7.

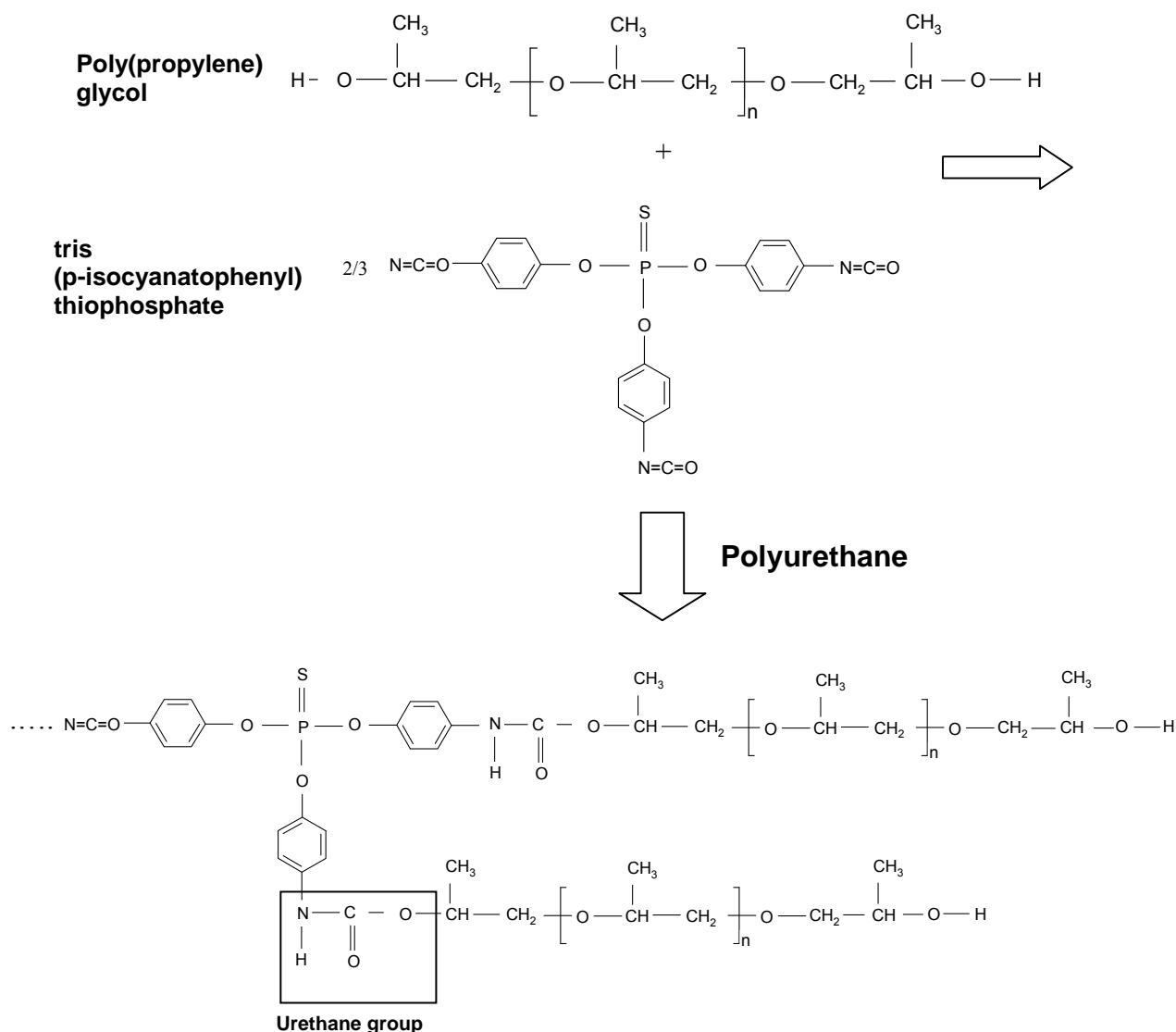


**Figure 2.6:** Chemical reaction of Poly (propylene) glycol and tris(p-isocyanatophenyl) thiophosphate: Polyurethane formation.

**Table 2.7:** Formulation of the three polyurethane model networks

Materials	Chain extender	Crosslinker	Antioxidant	Experimental NCO/OH
<b>PU 4000</b>	PPG 4000	tris(p-isocyanatophenyl) thiophosphate	0.1%wt. Irganox 1035	1.05
<b>PU 8000</b>	PPG 8000			1.10
<b>PU 8000/1000</b>	34% molar PPG 8000 66% molar PPG 1000			1.10 1.0

The synthesis of these three polyurethane model networks was carried out inside the gloves box to guarantee anhydrous conditions. The reagents were weighed on a scale (Summit

230g/0.1mg) in a beaker, and using the proportions of the formulations reported in Table 2.7 were mixed in a beaker, heated up to ~80°C and agitated using a magnetic stirrer, until the fluid solution became transparent. This procedure was repeated for every polyurethane prepared. After heating and stirring, the solutions were degassed during ½ hour.

### **2.3.2. Networks molding and curing**

The reagents were poured into the molds which were either:

- 1) a Petri dish to prepare films
- 2) the mold for cavitation samples (see chapter 5 for cavitation samples' preparation); and
- 3) the Teflon mold to prepare compression samples.

Then, a new degassing of another ½ hour was done.

The internal surface of the Petri dishes had to be previously modified chemically with SAMs of dichlorodimethylsilane, for later demolding.

The amount of material (volume) was calculated to obtain films of ~1mm-thick. All the films obtained were transparent and quite homogeneous. It is worthwhile to note that the presence of the antioxidant prevented yellowing.

All the molds with the isocyanates and polyols (still viscous liquids), were taken out of the gloves box and placed in a vacuum oven where cycles of vacuum and nitrogen were done, and finally the samples were left with nitrogen flow in the oven. The curing program in the oven was heating up @35°C during 48h (to increase viscosity in a controlled way) followed by 80°C during 80h for the complete crosslinking. Figure 2.7, shows a schematic of the synthesis of the polyurethane model networks.

The optimization of the timing and temperatures selected for the complete cure of the networks was done based on the results of the sol fraction which were carried out for several curing times and temperatures in the oven (for an example of timing see Appendix A2.5). The main requirement for curing was to obtain fully cured networks and cavitation samples without bubbles. To achieve the second requirement a first curing step of 35°C during 48h was necessary to increase the viscosity before going to higher temperatures (80°C).

To shorten the curing time, several tests were done using catalysts in the first part of the thesis. For this, the curing procedure was changed by using, during the mixture preparation, DBTDL (dibutyltin dilaurate) and also tin (II) 2-ethylhexanoate as catalysts, at different percentages of content (0.001, 0.01 and 0.1%). The results were fast curing reactions without enough time to do the degassing, and it was a problem mainly for the cavitation's samples. In view of these difficulties, the "long" uncatalyzed curing inside the oven, was used.

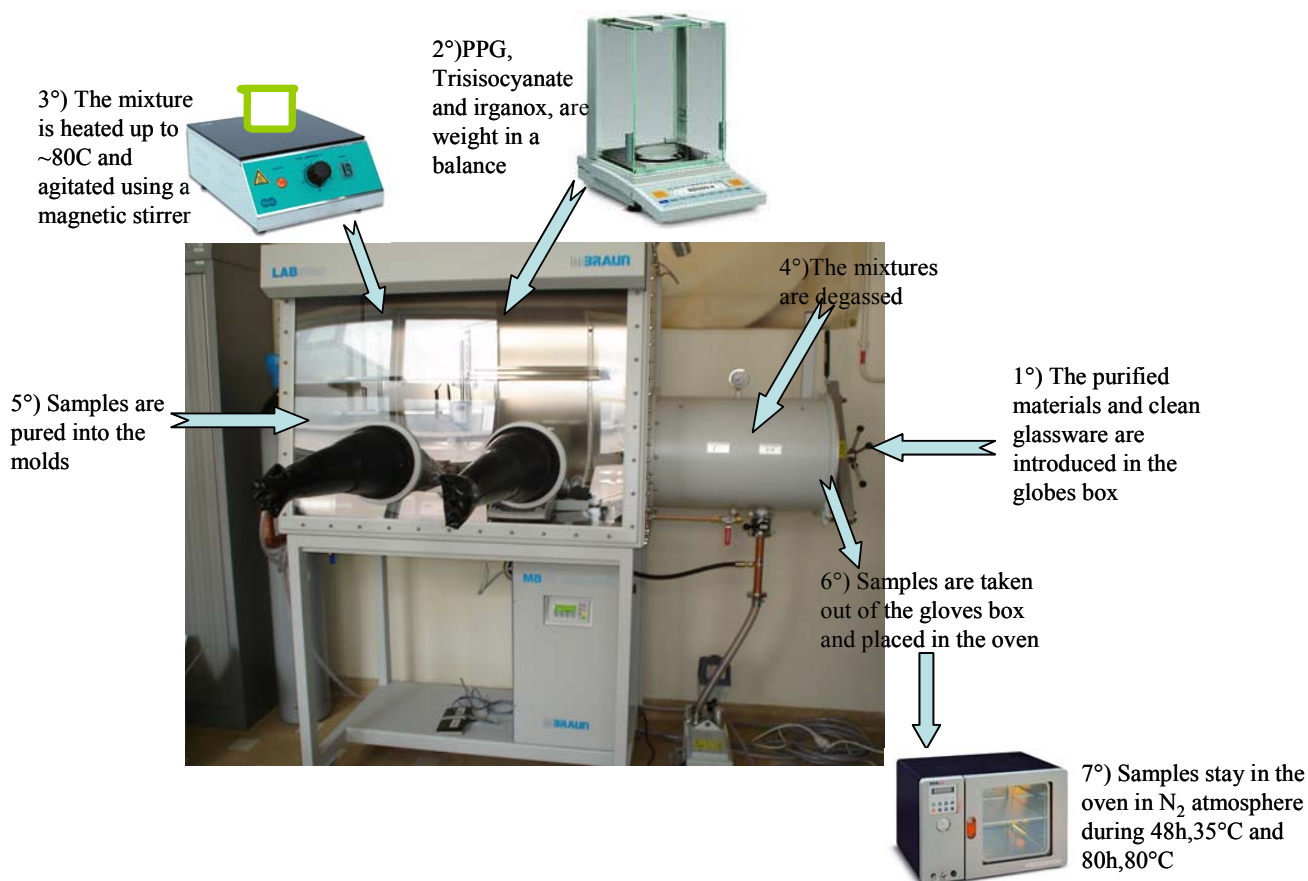


**Figure 2.7:** Schematic of the Synthesis of Polyurethane model networks

We prepared three kinds of polyurethane model networks, the first one based on a PPG with molecular weight of 4000g/mol and triisocyanate (called from now on PU 4000); a second one based on a PPG with molecular weight of 8000g/mol and triisocyanate (called from now on PU 8000). These two networks were made with the purpose of having two monomodal polyurethane networks with different crosslinking densities. The third network, an expected bimodal network, based on 34% mol/mol of PPG 8000g/mol and 66% mol/mol of PPG1000g/mol and triisocyanate (called from now on PU 8000/1000); this last network was made with the purpose of studying the effect on the mechanical properties of adding short chains (PPG 1000) to long chains (PPG 8000). In Figure 2.8 are summarized the three polyurethane model networks that were prepared (and characterized) to be used for all the mechanical study in the next Chapters.



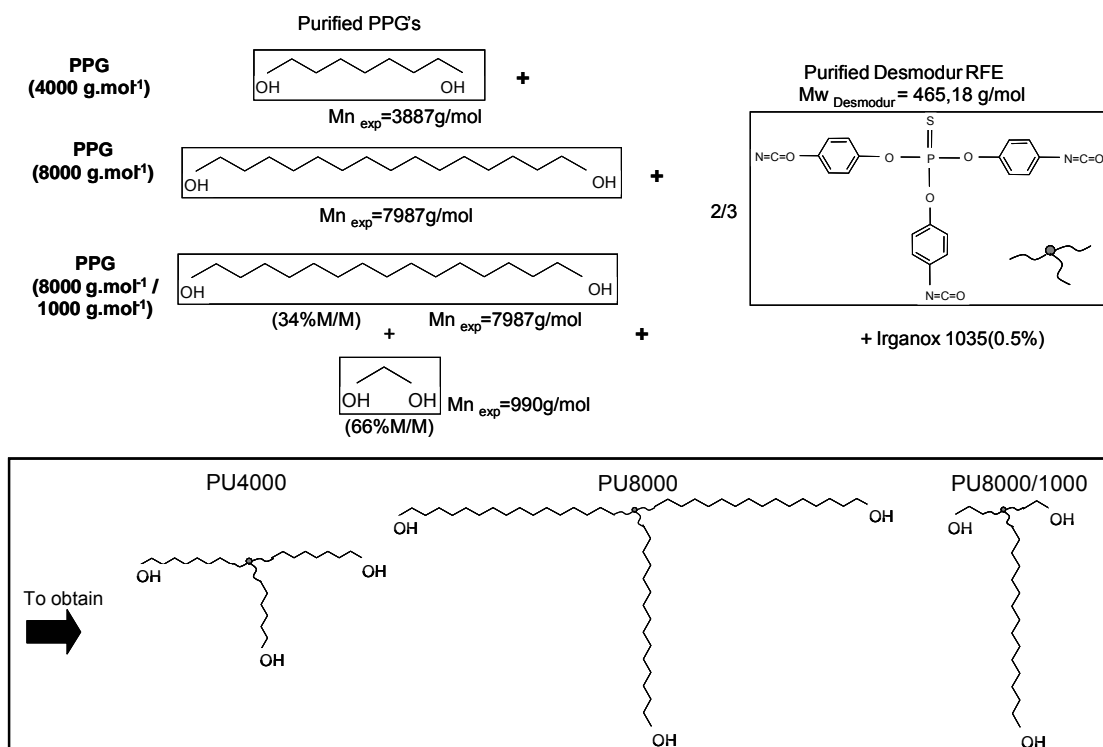


**Figure 2.8:** Scheme of the polyurethane model networks prepared for the mechanical testing

## 2.4.- Model Networks Characterization

### 2.4.1.- Chemical groups identification: ATR-FTIR

Internal reflection spectrometry or attenuated total reflectance infrared (ATR/IR) spectrometry was used to analyze our polyurethane networks. It is considered one simple, direct and sensitive in situ infrared technique. ATR-FTIR spectroscopy was used to identify the main functional groups present in the synthesized polyurethanes.

Mid-infrared spectra are obtained by pressing small pieces of sample against an internal reflection element (IRE), e.g., zinc selenide (ZnSe). IR radiation is focused onto the end of the IRE. Light enters the IRE and reflects down the length of the crystal. At each internal reflection, the IR radiation actually penetrates a short distance ( $\sim 1 \mu\text{m}$ ) from the surface of the IRE into the sample (Figure 2.9).

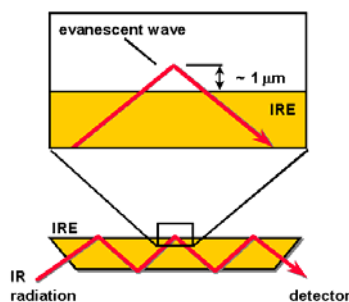
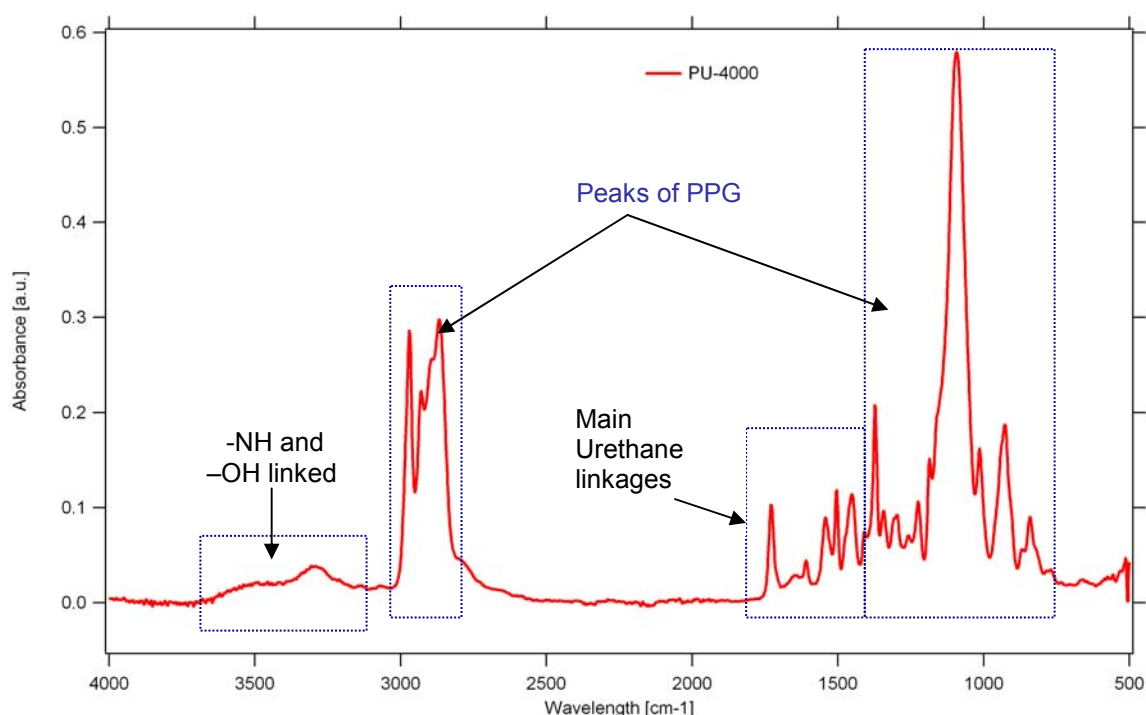


**Figure 2.9:** Total internal reflection at the interface of an internal reflection element. Depth of penetration of the evanescent wave is approximately  $1 \mu\text{m}$ .

The mid-infrared, absorption of radiation is related to fundamental vibrations of the chemical bonds. Internal reflection spectrometry provides information related to the presence or absence of specific functional groups, as well as the chemical structure of polymer membranes. Absorption bands are assigned to functional groups (e.g., C=O stretch and C-H bend). Shifts in the frequency of absorption bands and changes in relative band intensities indicate changes in the chemical structure or changes in the environment around the polymer [Marek 1996, Smith 1995].

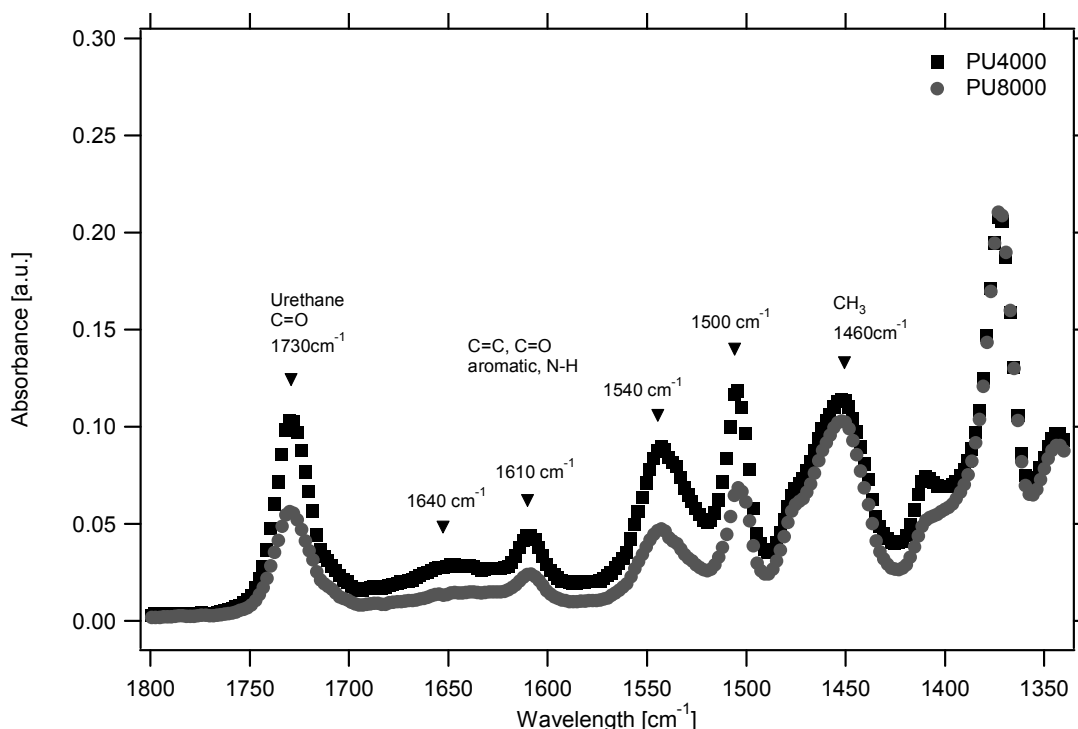
To perform the experiments, every sample was placed on the horizontal face of the internal reflectance crystal where total internal reflection occurs along the crystal-sample interface. Spectra were acquired on a Spectrometer Bucker, Tensor 37, with a spectral scan of 4000-400  $\text{cm}^{-1}$ , 31 scans. A first scan was done to obtain the reference (that includes humidity, etc.), and this reference was subtracted from the samples' spectrum.

Figure 2.10 shows the spectrum of PU4000, pointing out the main peaks corresponding to the PPG, and the peaks related to the urethane bond. The same kind of spectra was obtained for the three PU networks, meaning that in the three cases the same kind of reactions occurred for the formation of the polyurethane. It can be seen that there are no peaks in the region 2276-2240  $\text{cm}^{-1}$ , which means that all the NCO reacted, which was anyway expected in view of the high reactivity of the NCO group.



**Figure 2.10:** ATR-FTIR spectra of Polyurethane PU 4000.

Figure 2.11 shows a zoom of the region between 1800-1350  $\text{cm}^{-1}$ , where the main urethane linkages are present for PU 4000 and PU 8000. The peak C=O (band at 1730 $\text{cm}^{-1}$ ) corresponding to urethane carbonyl group is clearly observed.



**Figure 2.11:** ATR-FTIR spectra of Polyurethane PU 4000 and PU 8000. Zoom of the urethane links

The only differences that were observed among the spectra of the three polyurethane networks is the height of some peaks, which is expected, since the mole fraction of urethane changes for each sample (e.g. PPG 4000 to PPG 8000); however, the height of the peaks was not normalized. In Table 2.8, are reported the FTIR bands assignments for the associated peaks in the polyurethanes.

It is important to note that in the regions  $1400\text{--}1750\text{ cm}^{-1}$  and  $3600\text{--}3000\text{ cm}^{-1}$  appear only the peaks related to the urethane formed. There are no peaks related to urea for any of the samples at  $1680\text{--}1715\text{ cm}^{-1}$ ; however, in the region  $3320\text{--}3420\text{ cm}^{-1}$  the urea and the  $\text{--NH}$  urethane group related could be overlapped. A peak  $\text{--NH}$  ( $3300\text{ cm}^{-1}$ ) related to urethane group (and possible urea group) appear in all samples and it increases when the amount of isocyanates present in the reaction increases. We found no evidence of the presence of allophanates in the samples, which could appear for an excess of isocyanates, but this peak could be overlapped in the region of  $1409\text{ cm}^{-1}$ .

This FTIR study was not meant to be exhaustive, but we could identify the main groups present in our polyurethanes and show that side reactions are not detectable and should be negligible.

**Table 2.8:** FTIR band assignments for polyurethane [Smith 1995, O’Sickey 2002, Griffiths De Haseth 2007]

Wave number [cm <sup>-1</sup> ]	Assignment	Assignment to PU
2980	~(CH <sub>3</sub> ) v asym	PPG
2860	~(CH <sub>2</sub> ) v sym	PPG
3500	(NH) linked	Urethane
3000	OH linked	Urethane (or urea)
2270	(N=C=O)	Isocyanate, not present
<b>1730</b>	<b>C=O urethane carbonyl</b>	<b>Urethane</b>
1600-1515	C=C aromatic	Aromatic part of isocyanate
1100-1000	C=O stretching	PPG
924-820	C-H, C-C	PPG
1460	~(CH <sub>3</sub> ) v asym	PPG
1380-1370	~(CH <sub>3</sub> ) v sym, CH	PPG
1550-1500	C=C	Urethane
1452	CH <sub>3</sub> bend	PPG
1180-1160	C=O stretch aliphatic alcohols	PPG

#### 2.4.2.- Density of Polyurethanes networks

The density of the model networks was measured in the simplest way. Cylinders and rectangles were prepared to have two kinds of geometries for each polyurethane network, all the dimensions were measured as accurately as possible and these measurements were done at room temperature. Every cylinder and rectangle was weighed. The volumes were obtained by using the area and the thickness of the samples (see Appendix A2.6). The density was calculated by dividing the Mass/Volume=Density. Table 2.9 reports the density values obtained for each polyurethane at room temperature (25°C).

**Table 2.9:** Calculated density values for the three model networks at room temperature.

Material	Density $\rho^{25^\circ\text{C}}$ [Kg/m <sup>3</sup> ]
<b>PU 4000</b>	1036 ± 8
<b>PU 8000</b>	965 ± 9
<b>PU 8000/1000</b>	1079 ± 6

The density value obtained by this methodology is very close to the density obtained by Bos and Nusselder [Bos 1994] for PU 4000, which was  $\rho=1034 \text{ Kg/m}^3$ .

### 2.4.3.- Sol Fraction and Swelling experiments

#### 2.4.3.1.- Solfractions

The experimental conversion can be calculated by FTIR in situ, rheology and/or sol fractions. However while the first two techniques are very good for the initial stages of the reaction, the last one is by far the most sensitive for a nearly completely crosslinked network. As mentioned earlier, the sol fractions were used to optimize the stoichiometry of the reactions to prepare the polyurethanes networks, and the swelling was used to optimize the curing time.

Systematically, for every batch of polyurethane networks, the sol fractions were determined in dichloromethane after a period of one week, at room temperature, and the amount of extractable material was measured. This technique was used together with DMA to check the reproducibility of each batch.

The average sol fractions ( $w_s$ ) for the films and the cavitation samples, are listed in Table 2.10 as a function of the PU;  $w_s$  ranges from ~2-3% for all the samples. These results show that only a small amount of non reacted material is left in the PUs. Due to the very long curing procedure and the high sensibility of the reagents to react with humidity before being completely cured, we investigated with this method the possible effect of curing in a completely confined environment (cavitation sample, see chapter 4 for cavitation samples' preparation) relative to an "open" environment (films). In Table 2.10, we can see that for the cavitation samples the solfractions are lower than for the films, which is expected given the difference in curing; however we do not expect this difference to have an important impact on the mechanical properties.

**Table 2.10:** Minimum sol Fractions ( $w_s$ ) obtained for the polyurethane networks in dichloromethane

Material	Sol fractions ( $w_s$ ) [%]
PU4000 film	$2.7 \pm 0.1$
PU4000 cavitation sample	$2.3 \pm 0.2$
PU8000 film	$3.1 \pm 0.3$
PU8000 cavitation sample	$2.7 \pm 0.1$
PU8000/1000 film	$2.9 \pm 0.2$
PU8000/1000 cavitation sample	$2.5 \pm 0.2$

#### 2.4.3.2.- Swelling experiments

Additionally to the solfractions which indicate the level of unreacted material, swelling experiments were performed for the three polyurethanes, mainly as a way to characterize and compare the network structure of the cavitation samples and the films and to estimate possible differences between them. The swelling experiments may be more sensitive than the solfractions.

The theories of rubber elasticity have been developed in parallel with the theory of swelling proposed originally by Flory and Rehner [Flory and Rehner 1943] (correlated to the affine model). The principle is simple: As the rubber swells with liquid, the polymer chains stretch and the equilibrium value is dictated by the equilibrium in the chemical potential of the solvent molecules inside and outside of the network.

The swelling experiments were carried out in dichloromethane which has a solubility parameter ( $\delta$ ) close to that of the PPG (see Appendix A2.7). The experiments were done at room temperature ( $\sim 25^\circ\text{C}$ ) during one week until equilibrium was reached.

The mass of each sample ( $m_d$  = mass dry samples) was obtained before swelling experiments; and after one week, the mass loss was obtained by weighing the samples every minute during 15 minutes. Using this data were made graphs of mass versus time and the mass at  $t=0\text{s}$  ( $m_s$ ) was extrapolated. This value of mass represents the equilibrium mass in the swollen state ( $m_s$ ). From  $m_d$  and  $m_s$  can be obtained the swelling in mass ( $Q_p$ ) using equation 2.1

$$Q_p = \frac{\text{mass}_{\text{swollen}}}{\text{mass}_{\text{dry}}} = \frac{m_s}{m_d} = \text{Swelling ratio in mass} \quad \text{eq. 2.1}$$

And, the swelling ratio in volume ( $Q_v$ ) can be obtained by equation 2.2:

$$Q_v = 1 + [(Q_p - 1) * \rho_2 / \rho_1] \quad \text{eq. 2.2}$$

where  $\rho_1$  is the density of the solvent and  $\rho_2$  is the density of the polymer (reported in Table 2.9). In Table 2.11, are reported the  $Q_v$  values obtained for the three PUs.

**Table 2.11:** Swelling ratio in volume ( $Q_v$ ) for films and cavitation samples

Material	$Q_v$
<b>PU4000 film</b>	$5.4 \pm 0.02$
<b>PU4000 cavitation sample</b>	$5.3 \pm 0.01$
<b>PU8000 film</b>	$6.6 \pm 0.03$
<b>PU8000 cavitation sample</b>	$6.9 \pm 0.03$
<b>PU8000/1000 film</b>	$5.8 \pm 0.02$
<b>PU8000/1000 cavitation sample</b>	$5.9 \pm 0.01$

Based on the solfractions and swelling ratios reported in Table 2.11, there are no significant differences in structure between cavitation samples and films. Comparing the 3 materials, the degree of swelling goes as: PU 8000 > PU 8000/1000 > PU 4000.

We can now try to estimate an average value of the molecular weight between crosslinks from the swelling theory of Flory and Rehner [Flory 1943] which gives at equilibrium:

$$[\ln (1-(\phi_2) + (\phi_2 + \chi_{12}*\phi_2^2))] = V_1 n [(\phi_2/2)- \phi_2^{1/3}] \quad \text{eq. 2.3}$$

with  $\phi_2$  the volume fraction of polymer in the swollen mass,  $V_1$  the molar volume of the solvent,  $v$  is the number density of network chain segments bound on both ends by crosslinks, and  $\chi_{12}$  is the Flory solvent-polymer interaction term (If  $\chi_{12} < 0.5$  the solvent is considered a good solvent). For  $\phi_2$  small, this equation is often simplified to explicitly calculate the number of crosslinks per unit volume  $v$  (mole/cm<sup>3</sup>), from which the average molecular weight between crosslinks  $M_c$  can be directly obtained:

$$M_c = \frac{V_1 \rho_2 ((\phi_2/2) - \phi_2^{1/3})}{\ln(1 - \phi_2) + \phi_2 + \chi_{12} \phi_2^2} \quad \text{eq. 2.4}$$

where  $\rho_2$  is the density of the dry polymer. The main difficulty of using equation 2.3 or 2.4 is the accuracy of  $\chi_{12}$  for a given system. It has been shown [Petrovic 1987] that the  $\chi$  parameter of a copolymer network depends on the interactions between the solvent and the individual components of the networks and between these components themselves. In the polymer Handbook [Polymer Handbook], when non-polar solvents are used, the value of  $\chi_{12}$  can be calculated by using the equation (2.5).

$$\chi_{12} = [(\delta_1 - \delta_2)^2 V_1 / RT] + 0.34 \quad \text{eq. 2.5}$$

Using equation 2.5, we obtained a  $\chi_{12} \sim 0.34$  for the three polyurethanes in dichloromethane. This result suggests that the equation 3.3 is probably not the right one to be used for our systems given the complexity of the interactions. However it is interesting to see from Table 2.12 that the predicted  $M_c$  values obtained with equation 2.4 and  $\chi_{12} \sim 0.34$  are reasonably close to the values expected from the molecular weights of the PPG used to make the networks. Furthermore the differences observed in swelling ratios between the films and cavitation samples are only very small in terms of  $M_c$  values.

**Table 2.12:**  $M_c$  values calculated by using Flory-Rehner equation 2.4.

Polymer and Solvent	Mc [g/mol]
	Flory-Rehner
<b>PU 4000 cavitation sample</b>	3870
<b>PU 4000 film</b>	3995
<b>PU 8000cavitation sample</b>	5987
<b>PU 8000 film</b>	6301
<b>PU 8000/1000 cavitation sample</b>	4920
<b>PU 8000/1000 film</b>	5090

#### 2.4.4.- Model Networks Homogeneity: Proton Multiple-quantum (MQ) NMR

Although average properties can be readily obtained from macroscopic experiments, the dispersion of chain length in the network can only be probed with a more molecular technique such as NMR. Solid-state NMR has proved to be a very powerful tool to study polymer chain dynamics and some very sophisticated pulse sequences and analyses methodologies have been developed specifically to address the question of local relaxation times.

The homogeneity of our three polyurethane model networks was studied by solid-state NMR by Prof. Kay Saalwächter at Martin-Luther-Universität in Halle-Wittenberg, Germany.

##### General introduction to the technique

The NMR technique offers the advantage that a local chain order parameter  $S_b$  can be quantified by this technique in the undeformed state; this quantity is directly proportional to macroscopic measures of the cross-link density such as the elastic modulus or the equilibrium degree of swelling [Saalwächter and Sommer 2007]. A detailed explanation of this technique is beyond the scope of the thesis and the reader is referred to the literature [Saalwächter and Sommer 2007, Saalwächter 2007, Saalwächter *et al.* 2003]. We just note that the actual important NMR observable is a “residual dipolar coupling”,  $D_{\text{res}}$ , which is directly proportional to  $S_b$  and thus to the cross-link density.

Experimental results about the distribution of relaxation times in bimodal model networks have been published by Saalwächter [Saalwächter and Sommer 2007, Saalwächter 2007, Saalwächter *et al.* 2003] and are shown in Figure 2.12 as an example. The fitting of these curves Figure 2.12(a) can be performed by using specific distribution models such as Gaussian or gamma distribution. The corresponding distribution curves of the order parameter in Figure 2.12 (b) demonstrate the two components nature of these distributions for bimodal networks. The local (dynamic) segmental order parameter  $S_b$  of the polymer backbone reflects the conformational space that is set by the presence of the cross-links or topological constraints.  $S_b$  directly depends on  $N^{-1}$ , the inverse number of segments in a network chain, and is thus proportional to crosslink density.

Figure 2.12 (a) shows that shorter chains appear at lower excitation time than longer chains. In Figure 2.12 (b) the peak indicates a specific component with defined average crosslink density (which roughly scales with  $1/M_c$ ), and the area is proportional to its fraction if the peak is wide, there is an additional intrinsic heterogeneity. Apart from the so-determined heterogeneities in the local crosslink density, other defect structures such as loops, dangling ends, extractable free chains and/or all the defects which do not contribute to the elasticity of the network, can also be detected by the technique.



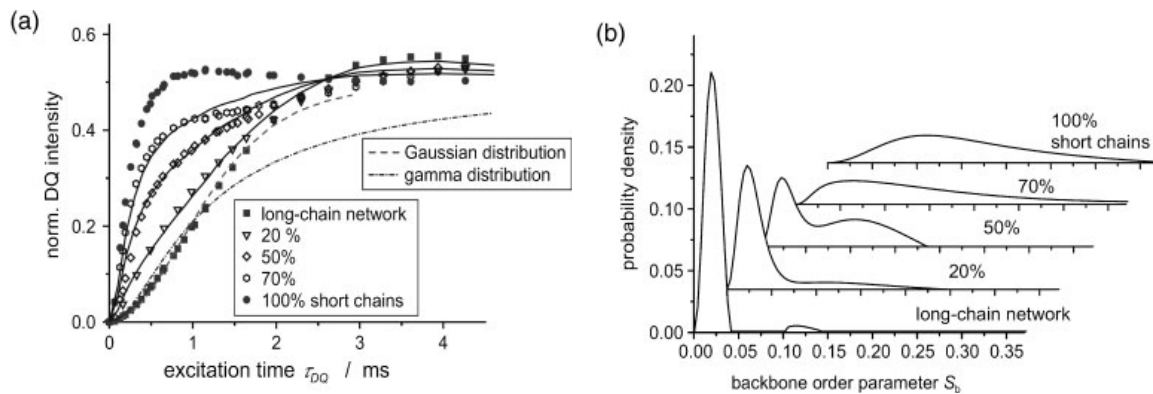


**Figure 2.12:** (a) Normalized DQ (nDQ) build-up curves of bimodal end-linked PDMS networks. Long and short chains have  $M_n=47$  and  $0.8$  kg/mol, respectively. The solid lines are weighted superpositions of the experimental pure-component curves, and the dashed and dash-dotted lines are fits using different distribution models. (b) Order parameter distributions for the same networks, obtained by numerical regularization analysis of the build-up curves in (a). Taken from [Saalwächter and Sommer 2007, Saalwächter 2007].

### Analysis of our model networks: Results

Solid-state NMR experiments were performed on the three networks using low-field instrumentation, to study the homogeneity of the networks, and in the following we report results in terms of “ $D_{res}$ ”, being proportional to  $S_b$  [Saalwächter and Sommer 2007]. The experiments were performed at high temperature ( $70^\circ\text{C}$ ) to follow fast motions of the chains (at  $T > T_g$ ), to see the coupling; however, the results are temperature-independent after normalization if the temperature is high enough.

In Figure 2.13 the results for the three networks are presented. The “sum” curves (open symbols) were needed for normalization purposes, they do not carry information on the crosslink density, but from these curves, slowly relaxing defect components can be identified which correspond to the non-crosslinked chains.

“x%y” means that there are x% of a component with a long relaxation time of “y” milliseconds. The “nDQ” build-up curves contain the info on crosslink density. In general, the steeper the initial raise, the higher the crosslink density. The order of increasingly quick rise does correspond to the samples ordered by their modulus, which from higher to lower the modulus are PU4000>PU8000/1000>PU8000 (as will be shown in the next section).

Quantitatively, the “residual dipolar coupling” in Hz is proportional to crosslink density. This is the number in brackets given besides the fit curve (distribM2 fit). The first values are the average residual coupling (which scales with the modulus, thus  $1/M_c$ ), and the second is the width of the distribution (standard deviation, also in Hz). For the fitting of these three polyurethanes only one Gaussian was sufficient, meaning that no phase separation could be observed, even for the bimodal network. The ratio of standard deviation/average (std dev./average=111/261; 72/204 and 108/254) was similar for the three networks, about 35 to 43%, which indicates a moderate distribution width (networks with much microscopic

disorder have standard deviations that are just as large as the averages), such that these networks can be considered to be relatively homogenous. Importantly, the two types of chains in the “bimodal” network (PU8000/1000) must be considered to be intimately mixed.

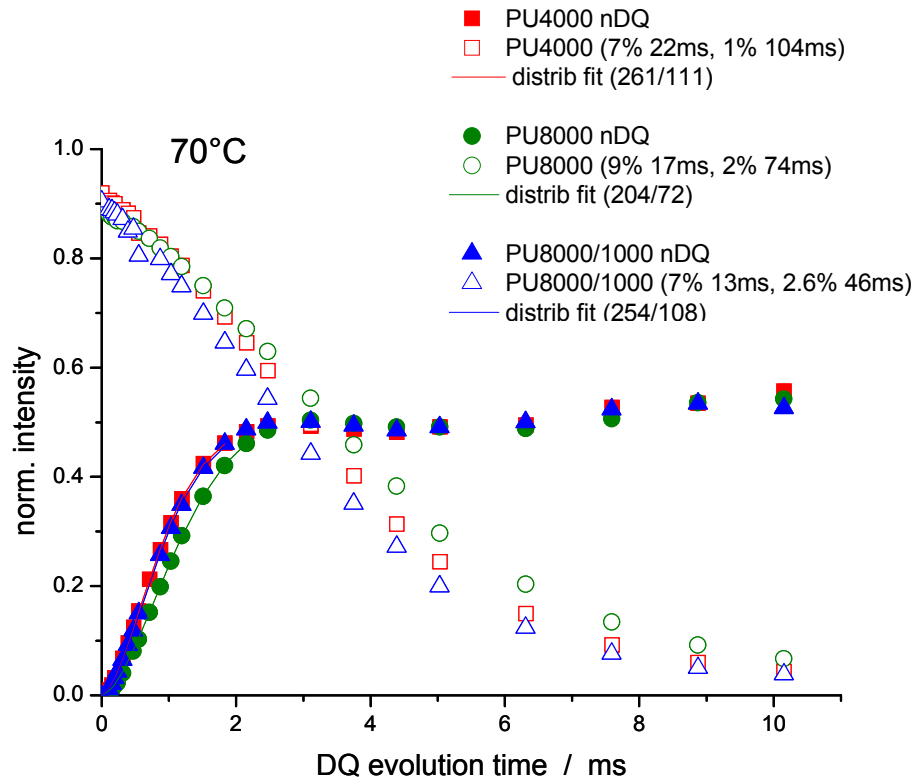


**Figure 2.13:** Normalized DQ build-up curves of PU4000, PU8000 and PU8000/1000 (“bimodal”).

These experiments show that PU4000 and PU8000/1000 have ~7% of defects and PU8000 ~9% of defects. Considering that about 2-3 % of these defects are extractable free chains (as reported in Table 2.10) the remaining amount of heterogeneities might be loops and dangling ends.

Now, if  $D_{\text{res}}$  is proportional to  $1/M_c + 1/M_e$  (where  $M_e$  is the average molecular weight between entanglements), then the graph in Figure 2.14 is considered to show the proportion of entanglements. The fitting of this curve gives  $y_0=106$  Hz which is considered to be the relative contribution of entanglements for this set of materials. Therefore on a relative scale, there is a higher entanglements contribution to  $M_c$  for  $\text{PU8000} > \text{PU8000/1000} \cong \text{PU4000}$ . However, since the fitting was done only with three materials, the result remains qualitative. In Appendix A2.8 a plot of  $D_{\text{res}}$  is presented as a function of swelling ratio.

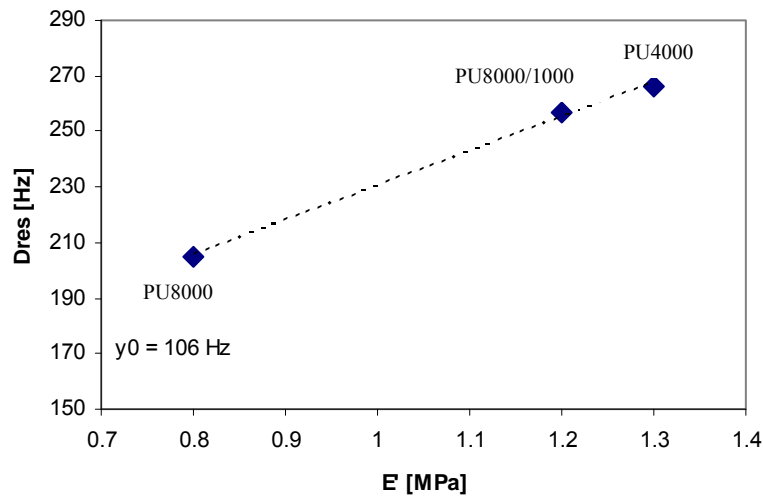


**Figure 2.14:** Fitting of  $D_{res}$  [Hz] as a function of the Modulus of the polyurethane model networks.

## 2.5.- Small strain behaviour by Dynamical Mechanical Analysis (DMA)

Dynamical mechanical analysis (DMA) is a technique which measures the modulus (stiffness) and the energy dissipation of materials in the linear viscoelastic regime (at small strain). When an oscillating stress, or load, is applied to a material it responds by deforming sinusoidally. This deformation, or strain, depends on how much viscous and elastic behaviour the material possesses. Two independent parameters are typically extracted from a DMA test: the stiffness of the material and the phase lag, i.e. the ratio between the viscous and elastic component [Sepe 1998]. Because these parameters are related to the molecular structure and architecture of the network, the DMA is sometimes called mechanical spectroscopy.

In DMA, the modulus is measured as a function of time, temperature and frequency. By scanning the temperature at a fixed frequency, during a DMA experiment, the glass transition  $T_g$  or alpha relaxation  $T_\alpha$ , can be observed. DMA can also be used to investigate the frequency (and therefore time) dependent nature of the transition at a fixed temperature. [Menard 1997].

In our case we can extract several informations about our model networks. First of all the direct knowledge of the elastic modulus as a function of temperature and frequency will be necessary to interpret the fracture and cavitation tests, then the  $E'(f, T)$  and  $E''(f, T)$  values can be used to extract information about the structure of the network using a rubber elasticity model.

### 2.5.1.- DMA results and Thermoelasticity

The thermoelasticity is the increase of the force with temperature for strained elastomeric systems due to a restoring force of entropic origin. This is the opposite behaviour of most solids, especially metals, and has long been recognized as a fundamental characteristic of

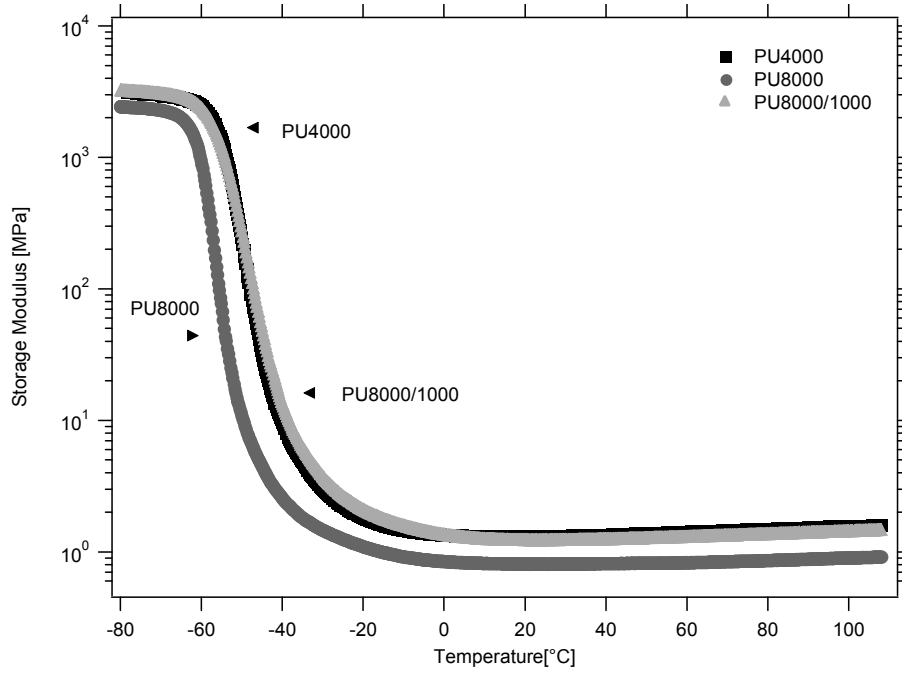
elastomers [Treloar 2005, Marchessault *et al.* 1985]. The extent of the thermal contraction of elastomers under tension is directly related to their molecular structure, chain configurations, and morphology [Treloar 2005, Flory 1953].

The elastic modulus as a function of temperature and the  $T_\alpha$  transition temperature was studied by DMA for each polyurethane network. A DMA model Q800 of TA instruments was used in tension mode. The frequency was set at 1Hz and the amplitude at 14 $\mu$ m, a temperature ramp of 2°C/min was applied in a range of temperatures from -80°C to 110°C. Samples bars with dimensions of 4x30x1 mm<sup>3</sup> (Lo~15mm) were used.

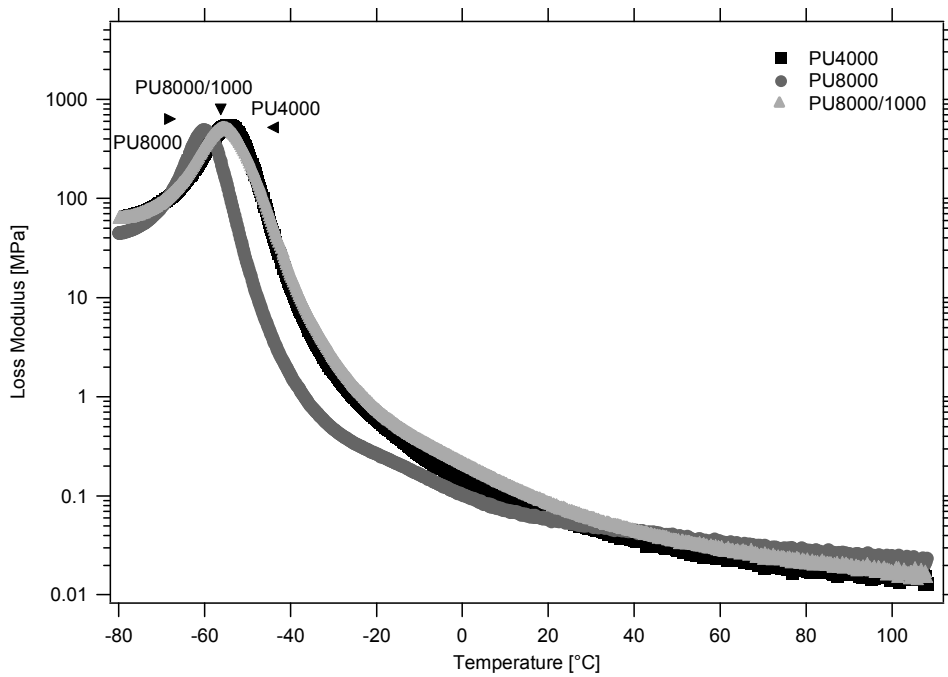
DMA experiments (together with solfractions) were done for every batch prepared, as a way to verify the modulus of the networks and the reproducibility of the batches. The results showed that we were able to have reproducible polyurethane model networks (with reproducible properties) from one batch to another.

Figure 2.15 shows a graph of the storage modulus of PU4000, PU8000 and PU8000/1000 as a function of temperature for the complete temperature range. The storage modulus  $E'$ , is a measurement of the energy stored during deformation and is related to the elastic portion of the elastomer. Since  $G'$  is typically used for deformations in shear and  $E'$  is used for deformations in traction, in our experiments we used  $E'$ . For nearly incompressible materials the two parameters are simply related by the expression:  $E = 3 G$  which is valid of course for both storage and viscous component.

The glass transition temperature  $T_\alpha$  was obtained from the maximum peak of the loss modulus  $E''$  [Steeman and Nusselder 1995]. The loss modulus  $E''$  is the measurement of the energy lost (usually lost as heat) during the deformation and related to monomer friction in the elastomer. Figure 2.16 shows the complete graph of  $E''$  as a function of  $T$  and it can be observed that if the three polyurethanes are compared, the  $T_\alpha$  are very close. However, interestingly at temperatures over 20°C, the curves cross over and the loss modulus  $E''$  is higher for PU8000, which becomes more dissipative.



**Figure 2.15:** Storage Modulus of PU4000, PU8000 and PU8000/1000 as a function of temperature.



**Figure 2.16:** Loss Modulus of PU4000, PU8000 and PU8000/1000 in function of temperature.

At room temperature and above, the three materials are very elastic as shown on Figure 2.17 showing the graph of  $\tan \delta = \frac{E''}{E'} = \frac{G''}{G'}$  as a function of T. Values of  $\tan \delta$  vary between 0.01 and 0.07 over the experimentally relevant range for our fracture and cavitation experiments. Again it is important to note that at room temperature and above the PU8000 is more dissipative than the PU8000/1000 and that the PU4000.

Table 2.13 summarizes the transition temperature  $T_{\alpha}$ , storage modulus  $E'$  @ 25°C, and  $\tan\delta$  @ 25°C for the three polyurethane networks.

**Table 2.13:** Values of  $E'$ ,  $T_{\alpha}$  and  $\tan\delta$ , for the three polyurethane networks

Material	$T_{\alpha}$ (°C)	$E'$ [MPa] @25°C	$\tan \delta$ @25°C
PU4000	$-54.1 \pm 0.5$	$1.3 \pm 0.08$	$0.041 \pm 0.005$
PU8000	$-59.8 \pm 0.5$	$0.8 \pm 0.06$	$0.067 \pm 0.006$
PU8000/1000	$-56.4 \pm 0.4$	$1.2 \pm 0.07$	$0.057 \pm 0.004$

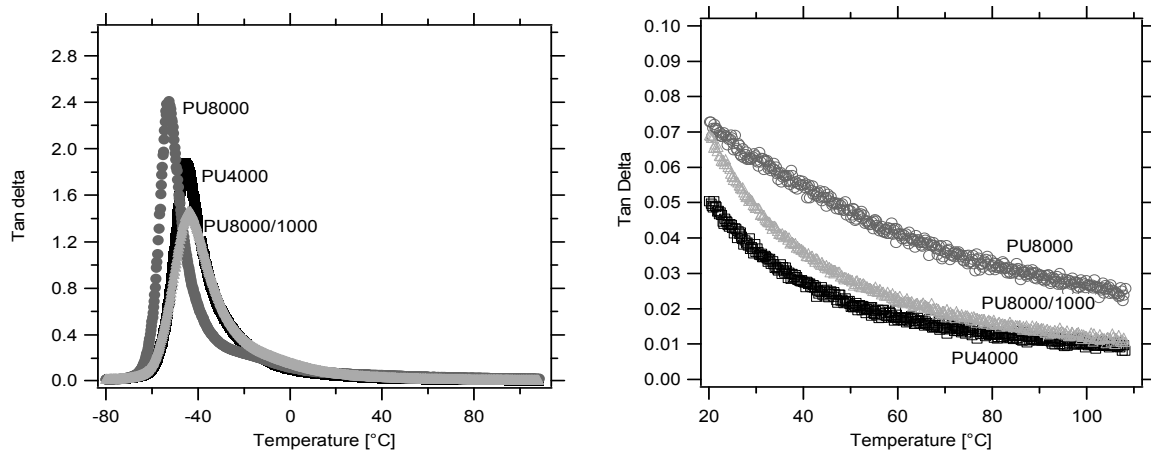


**Figure 2.17:**  $\tan \delta$  of PU4000, PU8000 and PU8000/1000 as a function of temperature.

For our fracture and cavitation experiments we chose four temperatures,  $T=25^{\circ}\text{C}$  which will be also referred to as standard conditions, and three higher temperatures,  $T=50^{\circ}\text{C}$ ,  $T=70^{\circ}\text{C}$  and  $T=100^{\circ}\text{C}$ . Figure 2.18 shows the storage modulus as a function of these four temperatures, for the three polyurethane networks.

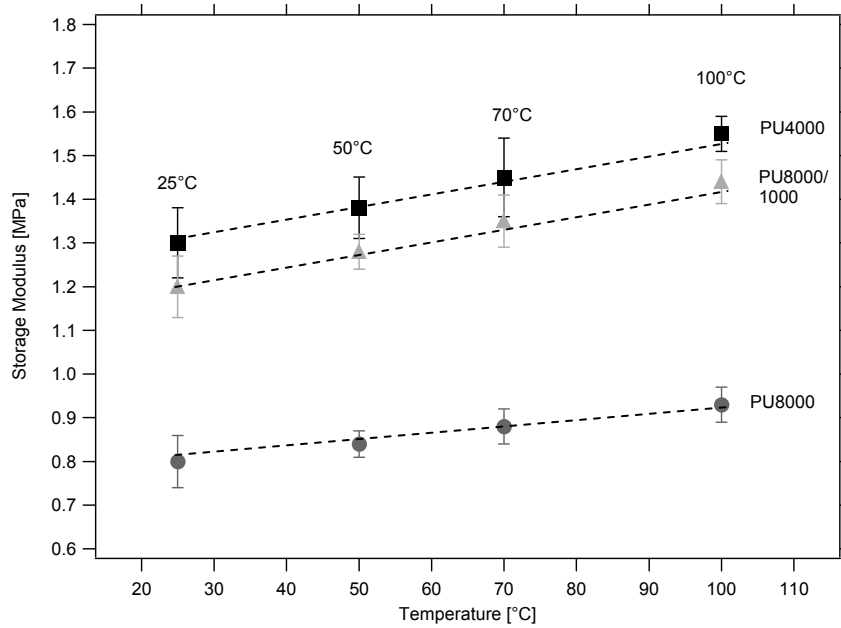


**Figure 2.18:** Storage modulus as a function of temperature, for four selected temperatures.

Table 2.14, summarizes the storage modulus  $E'$  at these four temperatures. It is clear that the modulus increases when temperature increases, for the three polyurethanes. This increase of  $E'$  with temperature suggests that the thermoelastic behaviour dominates the response of the material. It is a telling sign of the very homogeneous and defect free character of the network, since any significant chain relaxation would have led to a modulus staying constant or even decreasing with temperature. This is particularly true at such low strains (below 0.1%) where entropic elasticity is not expected to dominate as much.

**Table 2.14:** Storage Modulus  $E'$  of PU4000, PU8000 and PU8000/1000 as a function of temperature.

Material	$E'$ [MPa] @25°C	$E'$ [MPa] @50°C	$E'$ [MPa] @70°C	$E'$ [MPa] @100°C
PU4000	$1.3 \pm 0.08$	$1.38 \pm 0.07$	$1.45 \pm 0.09$	$1.55 \pm 0.04$
PU8000	$0.8 \pm 0.06$	$0.84 \pm 0.03$	$0.88 \pm 0.04$	$0.93 \pm 0.04$
PU8000/1000	$1.2 \pm 0.07$	$1.28 \pm 0.04$	$1.35 \pm 0.06$	$1.44 \pm 0.05$

Since all three networks present a very clear thermoelastic behaviour, it is interesting to extract molecular structure parameters from the modulus. According to the kinetic rubber elasticity theory (affine or phantom network), The tensile storage modulus of the networks in the rubbery region ( $E_r$  [MPa]) should be proportional to the absolute temperature [Treloar 2005, Gedde 1999]:

$$E_{affine} = \frac{3\rho RT}{Mc} \quad \text{eq. 2.6}$$

$$E_{phantom} = \frac{\rho RT}{M_c} \quad \text{eq. 2.7}$$

where  $\rho$  [Kg/m<sup>3</sup>] is the density of the elastomer,  $R$  the gas constant,  $T$ [K] the absolute temperature and the  $M_c$  is the number average molar mass between the cross-links.

The theoretical  $M_c$  of the three polyurethane networks can be calculated from the knowledge of the chemistry:  $M_c^{theor} = Mn_{PPG} + \frac{2}{3}M_{Desmodur}$  [g/mol] [Bos and Nussleder 1994, Steeman and Nusselder 1995]. For the calculation of the  $M_c^{theor}$ , it is assumed that full conversion is reached, and that no physical crosslinks are present. The  $M_c$  theoretical values are calculated using  $M_{Desmodur}=465.18\text{g/mol}$  and  $M_n$  of PPGs obtained by <sup>1</sup>H NMR, and the  $M_c$  experimental values are calculated by rubber elasticity (eq. 2.6 and eq. 2.7) using  $T=298\text{K}$ ,  $R=8,314\text{ J/mol}\cdot\text{K}$ . The results are summarized in Table 2.15.

**Table 2.15:** <sup>1</sup>H-NMR Molecular weight  $M_n$  of the PPGs, density at 25°C, experimental storage modulus ( $E'$ ), theoretical and experimental molecular weight between crosslinking points  $M_c$ , for the three polyurethane networks.

Material	Density [Kg/m <sup>3</sup> ] @ 25°C	$M_n$ of PPG [g/mol]	$M_c^{theor}$ [g/mol]	$E_r^{exp}$ [MPa] @25°C	$M_c^{exp}$ Affine Model [g/mol]	$M_c^{exp}$ Phantom model [g/mol]
<b>PU4000</b>	1036 ± 8	3887	4197	1.3 ± 0.08	5920	1975
<b>PU8000</b>	965 ± 9	7987	8297	0.8 ± 0.06	8965	2990
<b>PU8000/1000</b>	1079 ± 6	7987/990	3679	1.2 ± 0.07	6680	2230

The main assumption of the affine network is that the crosslink junctions are fixed in space and are displaced affinely with the whole network. In the phantom model the ends of the network strands are joined at crosslink functions that can fluctuate. These fluctuations lead to a reduction of the cumulative stretching of the network [Rubinstein and Colby 2003].

Table 2.14 and Figure 2.19 show that the  $M_c^{theor}$  has values in between the  $M_c^{exp}$  affine model and the  $M_c^{exp}$  phantom model. The affine model gives higher predicted values than  $M_c^{theor}$ . This model assumes that the network is “perfect” (which means no entanglements and no dangling ends); however, based on the characterization we did, 2-3% of free chains, and an additional 4-6% of heterogeneities (NMR proton) coming from loops and dangling ends are present. These small percentages of ‘imperfectness’ can modify the experimentally measured modulus and hence affect the predictions for  $M_c$ . From the possible networks defects, the defect called “loose ends” was treated quantitatively by Flory [Flory 1944] who showed that if there are defects it could lead to errors in the prediction of  $M_c$  [Treloar 2005, Flory 1944].

Additionally, the triisocyanate may undergo side reactions during the different steps before obtaining the final cured network, effectively reducing its functionality, which would give a resultant network with longer  $M_c^{exp}$  than expected.



The molecular weight between crosslink points ( $M_c$ ) and crosslink density are critical parameters in the network synthesis, affecting mechanical properties such as modulus, strength, and toughness as well as swelling. Attention should be paid to the effect of the presence of entanglements molecular weight on the measured molecular weight between crosslink points ( $M_e$ ) [Mark 2003, Andradý and Sefcik 1983, Zhuang *et al.* 1999, Erman and Mark 1997]. Based on the literature [Florez *et al.* 2006], the entanglements molecular weight of PPG is  $M_e \sim 3000 \text{ g/mol}$ . It is generally accepted that both crosslink points and entanglements, which are trapped during curing, contribute to the elastic modulus of the networks [Termonia 1992]. The contribution to the elastic modulus from entanglements increases as crosslink density decreases and the molecular weight between crosslink points increases. Then we may have more entanglements for PU8000 than for the other two networks, but a complementary study about the effect of the entanglements on the molecular structure may be done and will be presented in Chapter 3.

Since the size of our crosslinker (roughly  $\sim 3.6 \text{ nm}$ ) is considered to be relatively large and immobile when compared to the PPG chains it would be expected to have all  $M_c^{\text{exp}}$  closer to the affine model than to the phantom model and this is the case for PU8000. In Figure 2.19, a summarizing graph of  $M_c^{\text{theor}}$  as a function of  $M_c^{\text{exp}}$  for the different models is analysed. In this graph, the swelling obtained by Flory-Rehner (also affine model) seems to be closest to the  $M_c^{\text{theor}}$ , however, since the  $\chi_{12}$  parameter was not obtained accurately, the results remain only qualitative.

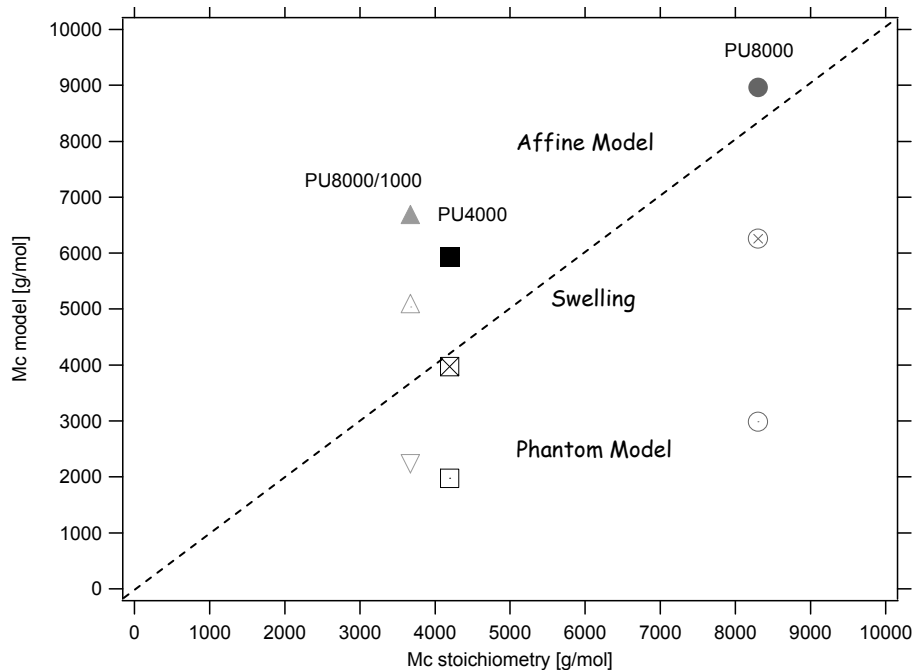


**Figure 2.19:**  $M_c^{\text{theor}}$  in function of  $M_c^{\text{exp}}$  for the different models analysed.

The rubber elasticity assumes that the contribution of an increasing temperature on the modulus is merely entropic. In the thermodynamic treatment of thermoelasticity, the tensile force required to maintain a constant extension is presented as the sum of the internal energy

and entropy [Treloar 2005, Mark 1976]. The slope of the curves in Figure 2.16 is proportional to  $3\rho R/Mc$  for the affine model and to  $\rho R/Mc$  for the phantom model. Due to thermal expansion, the density changes with the temperature (which is related to the internal energy of the system), then the thermal expansion coefficient was evaluated for the three polyurethane networks were.

#### ***2.5.1.1.- Density changes with temperature: Thermal expansion of the networks***

Thermal expansion means that as the "thermal" energy (and temperature) of a material increases, so does the vibration of its atoms/molecules; and this increased vibration results in what can be considered a stretching of the molecular bonds - which causes the material to expand. Of course, if the thermal energy (and temperature) of a material decreases, the material will shrink or contract [Mark 1976]. This is a volume effect acting on the density and does not cause any deformation of the material per se, simply a change in average distance between molecules.

For a long sample the main thermal expansion occurs along the length of the sample and is related to a change in temperature ( $T_f - T_o$ ), the final temperature minus the initial temperature. If the change in temperature is positive we have thermal expansion, and if negative, thermal contraction. The linear coefficient of expansion is given by  $\alpha$  (alpha) and is the fractional change in length per degree change in temperature.

The expansion coefficient for the three polyurethane model network was measured by DMA. A constant force of 0.1N and an increasing temperature of 1°C/min were used and the length change for each sample was measured. The graph of the change of strain as a function of temperature is given in Appendix A2.9. Using the experimental values, the linear thermal expansion is calculated by:

$$\frac{\Delta L}{L_o} = \alpha * \Delta T \Rightarrow \alpha = \frac{\Delta L}{L_o * \Delta T} \quad \text{eq. 2.8}$$

In Table 2.16, are presented the expansion coefficient values, for the three networks. The thermal expansion coefficient published [Polymer Handbook 1975] for natural rubber is  $2-2.5 \cdot 10^{-4} \text{K}^{-1}$ , but for the three polyurethane model networks were obtained lower coefficient values.

**Table 2.16:** Thermal expansion coefficient for the three polyurethane model networks, obtained by DMA

Material	$\alpha$ [K <sup>-1</sup> ] Temperature range 20-100°C
<b>PU4000</b>	$2.43 \cdot 10^{-4}$
<b>PU8000</b>	$2.34 \cdot 10^{-4}$
<b>PU8000/1000</b>	$2.22 \cdot 10^{-4}$

Using the value obtained for the expansion coefficient for each polyurethane, the density can be calculated as a function of temperature. If it is assumed that the change in length due to expansion is the same in the three directions, then:  $\frac{\Delta V}{V_0} = 3\alpha\Delta T$  and:

$$\rho = \rho_0(1 - 3\alpha\Delta T) \quad \text{eq. 2.9}$$

Table 2.17, shows the predicted values of densities for each material at different temperatures.

**Table 2.17:** Densities corrected at four chosen different temperatures from the thermal expansion coefficient

Material	$\rho_0$ [Kg/m <sup>3</sup> ] at T= 298K	$\rho_1$ [Kg/m <sup>3</sup> ] at T=323K	$\rho_2$ [Kg/m <sup>3</sup> ] at T=343K	$\rho_3$ [Kg/m <sup>3</sup> ] T=373K
<b>PU4000</b>	$1036 \pm 8$	1018	1002	980
<b>PU8000</b>	$965 \pm 9$	948	934	914
<b>PU8000/1000</b>	$1079 \pm 6$	1061	1046	1025

These calculated densities can now be used to represent the storage modulus as a function of  $\rho T$  as shown in Figure 2.20 graph of storage modulus in function of the temperatures multiply by the density, and now the slope is due only to entropic contributions and the intercept  $y_0$  should be the enthalpic contribution. The slope of the curves in Figure 2.20 is proportional to  $3R/Mc$  for the affine model and to  $R/Mc$  for the phantom model. By doing a fitting of the curves, the intercept (which is proportional to the enthalpic contribution) at  $y_0$  gives negligible values for the three polyurethanes. The slope gives  $4.42 \cdot 10^{-6}$ ,  $3.97 \cdot 10^{-6}$  and  $2.46 \cdot 10^{-6}$ , for PU4000, PU8000/1000 and PU8000, respectively.

This result shows that in our polyurethane model networks the increment of the modulus with the increment of temperature is due merely to entropic contributions.

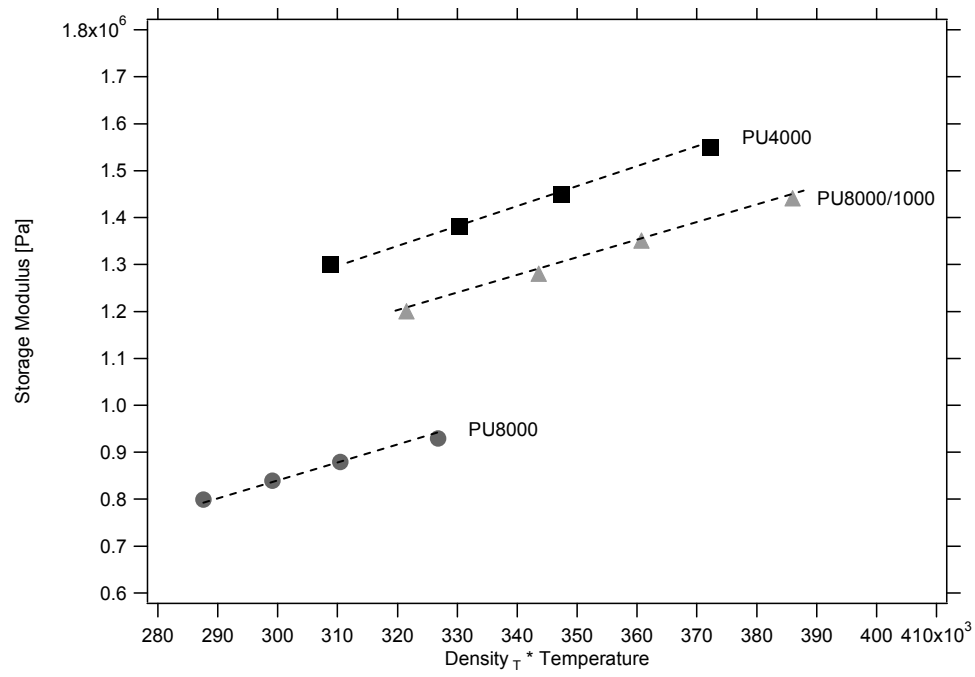


**Figure 2.20:** Storage modulus versus the Temperature multiplied by the Density, for the four chosen temperatures.

## Conclusions

The objective of this chapter was to present the synthesis method and molecular characterization of the PU model networks that will be the focus of the rest of the thesis. One of the goals of this work was the careful design of very simple networks with a very well-defined network architecture and this was the reason to use polyurethane chemistry. We can draw from our results a series of conclusions:

### On the synthesis:

- Despite the difficulty in obtaining purified products and the reactivity of the isocyanate, we have developed a protocol of purification of the reagents to have control on the stoichiometry of the reactions. A systemic and in-depth characterization of the reagents showed that the precursor chains are monodisperse, and the molecular weights are very close to the values given by the manufacturers.
- Using a fully uncatalyzed two-stage curing procedure, we have been able to synthesize reproducible polyurethane model networks with well defined molecular structures and to prepare these networks in different types of molds without any problems of bubbles, macroscopic heterogeneities or degradations due to oxidation. Three different kinds of polyurethanes model networks were prepared with the idea of establishing comparisons among them regarding the molecular structure and the mechanical properties (studied in the next chapters).

### On the structure of the networks:

- The networks obtained have very low sol fractions (below 3%), and a *very elastic behavior above room temperature* implying a very high degree of perfection. The stoichiometric ratio used to obtain the networks was very close to the theoretical one.
- The *low level of defects* of the networks is confirmed by
  - The clear thermoelastic behavior dominated mainly by entropic elasticity
  - The multiple quantum NMR result showing very homogeneous and defect-free network architecture for the three networks.
- Based on the DMA results and on the rubber elasticity theory, all three polyurethane model networks show a deformation behavior between the affine and phantom models.
- The results obtained by extraction of the solfractions and swelling experiments for the three polyurethanes, show that the films cured in ‘open’ configuration and the cavitation samples ‘close’ environments do not have significantly different structures.

### On the differences between the three networks

- The storage modulus of the networks increases from PU8000 < PU8000/1000 < PU4000. On the other hand the PU8000 is *more dissipative* than the other two materials above 20°C but has a lower  $T_g$  and a lower density.
- The comparison between the value of  $M_c$  obtained from the chemistry and that obtained from the elastic modulus suggests that the PU8000 contains both *entanglements and crosslinks*. This is not the case at all for the PU4000 and may be partially true for the PU8000/1000.
- The preparation of a true phase-separated bimodal network PU8000/1000 did not really reach its objective since the material remains very homogeneous (no clustering from solid-state NMR data).

This concludes this chapter on the molecular structure. It is now necessary to characterize the mechanical properties of the materials at large strains and their fracture properties, which is the objective of Chapter 4 and will be essential to interpret the cavitation experiments.

### **Acknowledgements**

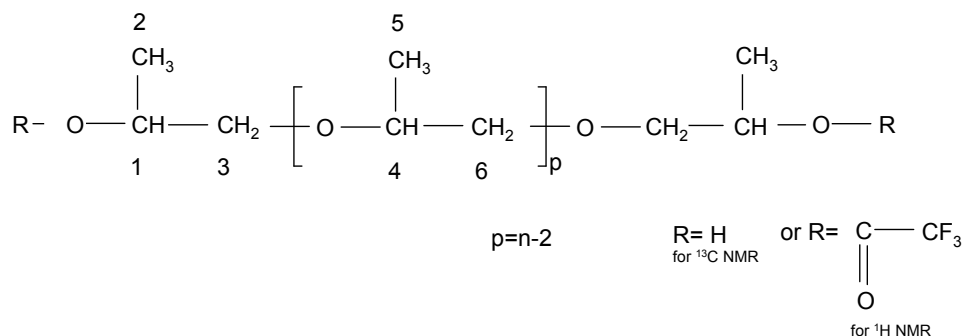
In this Chapter we would like to thank to: Martine Tessier, for the help with  $^1\text{H}$  NMR,  $^{13}\text{C}$  NMR and Maldi-ToF techniques. Sandrine Mariot for help with DMA experiments. Agnès Pallier for GPC and  $^1\text{H}$  NMR, and Guylaine Ducouret  $^{13}\text{C}$  NMR experiments. Kay Saalwächter for NMR solid experiments and for further explanations. Dominique Hourdet for the help with swelling experiments interpretation. Freddy Martin for the technical support.

## Appendices A2

### Appendix A2.1: NMR

Analysis software (Xwinnmr) allows analysis of the size of peaks to understand how many protons give rise to the peak. The peak was integrated; the integrated area is proportional to the number of protons, or any other observed nucleus, in the very simplest one-dimensional NMR experiments.

The proton and carbon numbering used for NMR analysis is described as follows:



And, the chemical shifts and assignments of  $^1\text{H}$  NMR signals are reported in Table A2.1.

**Table A2.1:** Assignment of  $^1\text{H}$  NMR chemical shifts of PPG when  $\text{R} = \text{COCF}_3$

$n^\circ \text{H}$	1	4	3	6	2	5
$\delta(\text{ppm})$	5.22	3.85-3.67	3.67	3.70-3.42	1.32	1.15

#### A2.1.1: $^1\text{H}$ NMR spectrum of PPG 4000 purified

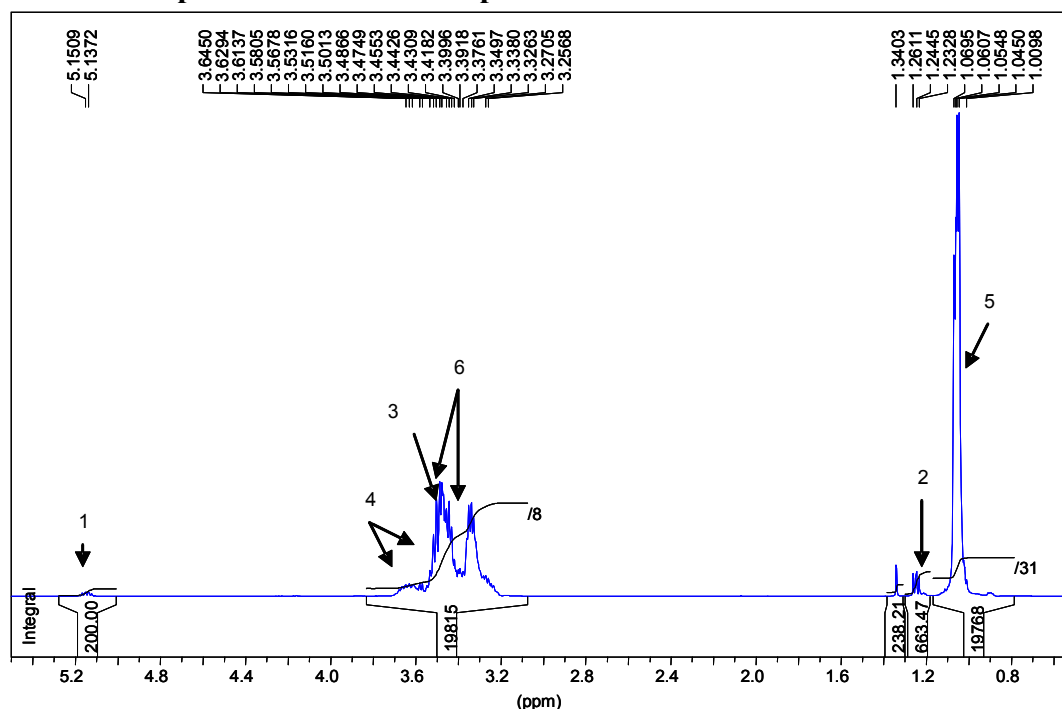


**Figure A2.1:**  $^1\text{H}$  NMR spectrum of PPG 4000 purified

Example of calculation of Mn for PU4000.

2 protons n°1 (OH terminal group), corresponds to 5.15 ppm, Integration = 200 = A

6 protons n°2 (OH terminal group), corresponds to 1.26 ppm, Integration = 663 = C

Then, the massive ~3.5ppm =  $\left. \begin{array}{l} 4 \text{ protons } n^{\circ}3 \\ 1p \text{ proton } n^{\circ}4 \\ 2p \text{ proton } n^{\circ}6 \end{array} \right\}$  here, Integration = 19815 = B = 4 + 3p

$$B/A = 19815/200 = 4+3p / 2 = 2 + 3/2p \rightarrow p=64.7$$

$$n = p+2 = 66.7$$

$$Mn = n \times 58 + 18 = 66.7 \times 58 + 18 = 3887 \text{ g/mol}$$

An example of the calculations done to obtain the concentration of hydroxyl functions (OH) are presented here, using values of Mn obtained by <sup>1</sup>H NMR.

C(OH) mmol/g == N° de mmol OH/g PPG :

$$\frac{2OH}{3887 \text{ g/molPPG}} \times 1 \text{ molPPG} = 0.00051 \text{ molOH} / \text{g} = 0.51 \text{ mmol} / \text{gPPG}$$

Hydroxyl number I(OH) [mg KOH/g]:

$$3887 \text{ g/mol} \Rightarrow 0.51 \text{ mmol OH /g PPG}$$

$$= (0.51 \text{ mmol OH/1g PPG}) \times 56.09 \text{ g KOH/mol KOH}$$

$$= 28.6 \text{ mg KOH / g PPG}$$



### A2.1.2: $^1\text{H}$ NMR spectrum of PPG 8000 purified

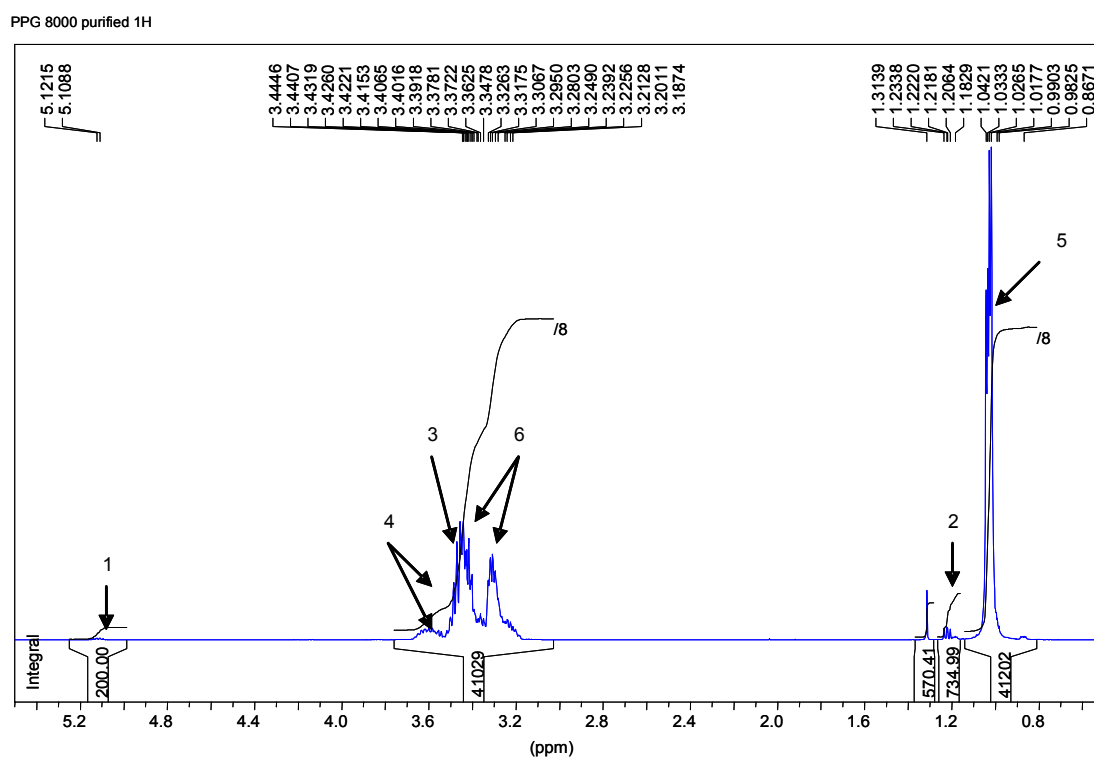


Figure A2.2:  $^1\text{H}$  NMR spectrum of PPG 8000 purified

### A2.1.3: $^1\text{H}$ NMR spectrum of PPG 1000 purified

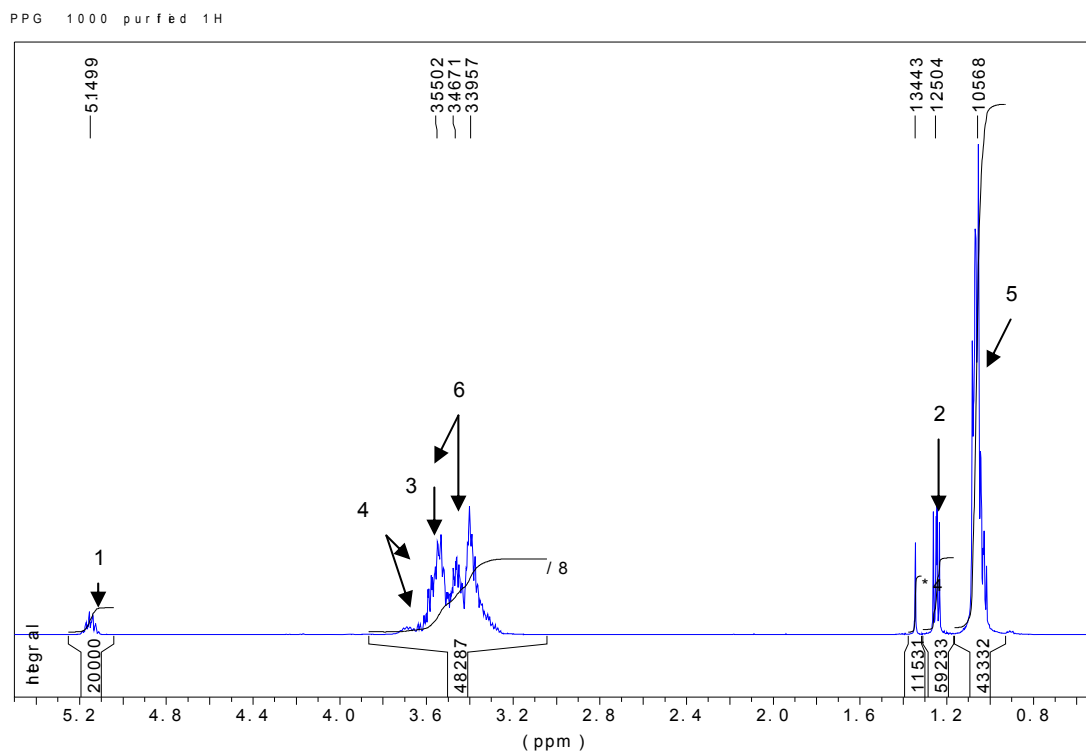


Figure A2.3:  $^1\text{H}$  NMR spectrum of PPG 1000 purified

### A2.1.4: $^{13}\text{C}$ NMR spectrum of PPG 4000 purified

Here it is presented an example of how can be calculated Mn by using  $^{13}\text{C}$  NMR spectra, integration peaks. The example is given for PPG 4000 purified.

2 carbon n°1 (CH terminal group), corresponds to 66.0 and 67.0 ppm,  $I = 100 + 76.03 = B$

Then, the massive ~75ppm =  $\left. \begin{array}{l} 2 \text{ carbon n}^\circ 3 \\ 1 \text{p carbon n}^\circ 4 \\ 1 \text{p carbon n}^\circ 6 \end{array} \right\} \quad I = 11771 = A = 2p + 2$

$A/B = 11771/176 = (2p + 2)/2 \rightarrow p = 66$

$n = p + 2 = 68$

$M_n = n \times 58 + 18 = 68 \times 58 + 18 = 3962 \text{ g/mol}$

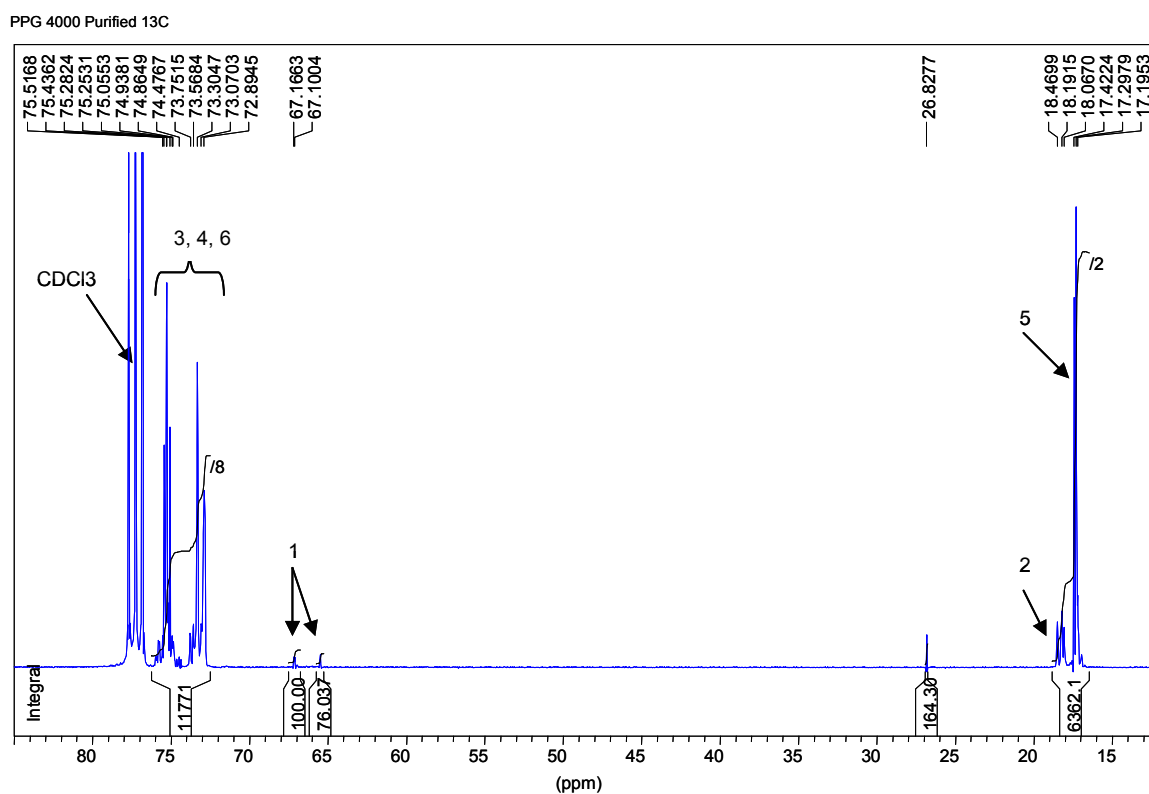


**Figure A2.4:**  $^{13}\text{C}$  NMR spectra of PPG 4000 purified

### A2.1.5: $^{13}\text{C}$ NMR spectrum of PPG 8000 purified

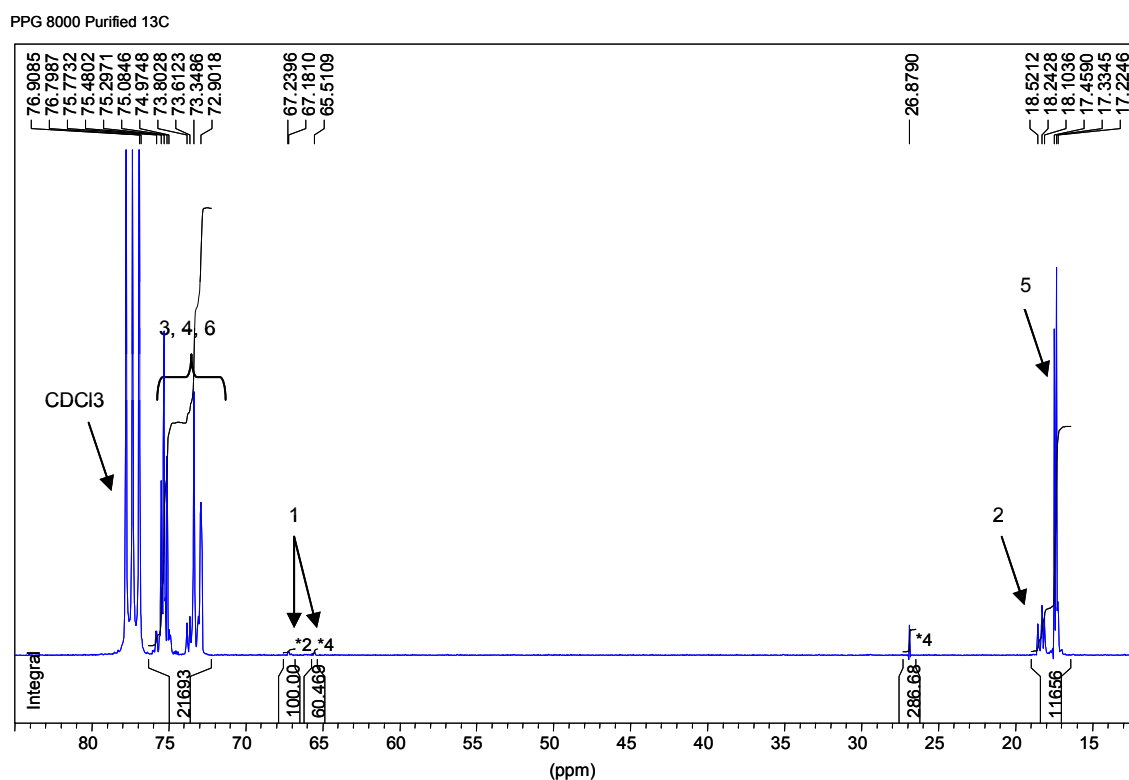


Figure A2.5:  $^{13}\text{C}$  NMR spectra of PPG 8000 purified

### A2.1.6: $^{13}\text{C}$ NMR spectrum of PPG 1000 purified

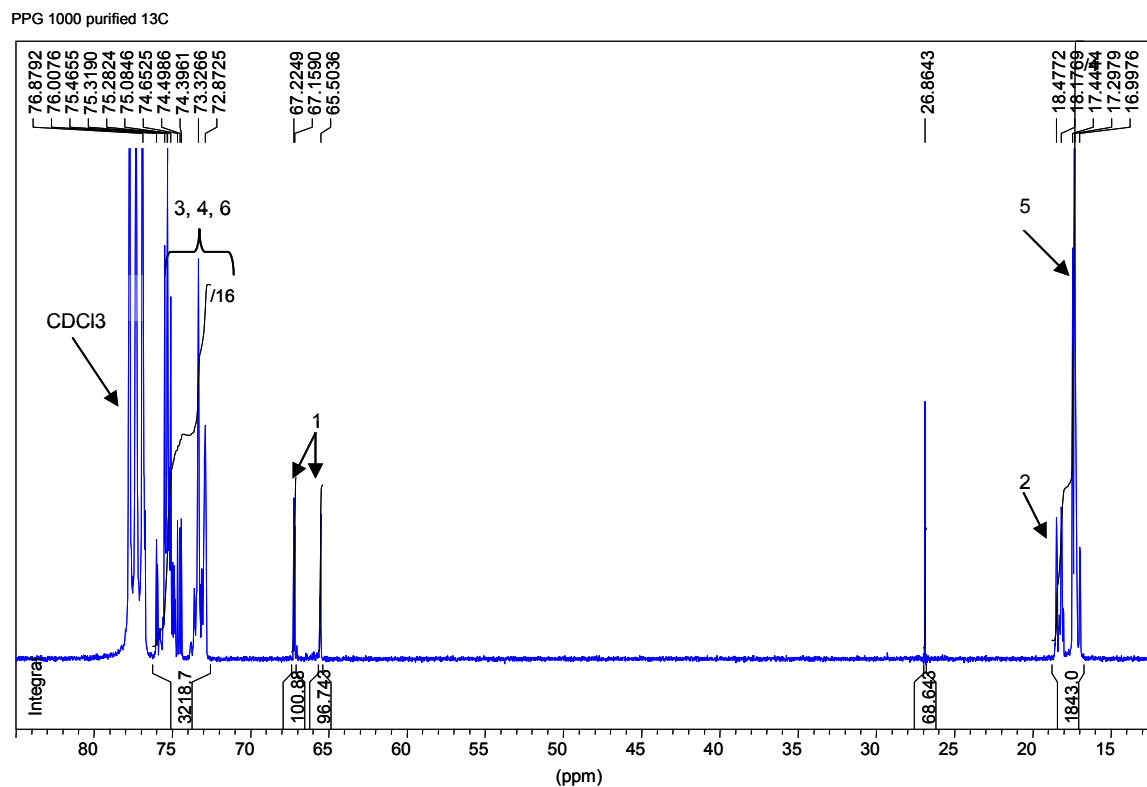
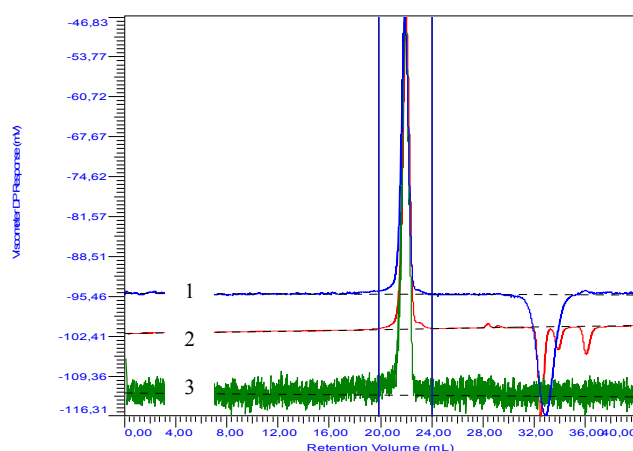


Figure A2.6:  $^{13}\text{C}$  NMR spectra of PPG 1000 purified

## Appendix A2.2: GPC

Example of polydispersity obtained by GPC for PPG8000.



**Figure A2.7:** GPC of PPG 8000g/mol : (1) Viscometer; (2) Refractometer; (3) Light scattering.

## Appendix A2.3: MALDI-ToF

In Figure A2.8 a comparison between PPG 4000 purified and non-purified is presented.

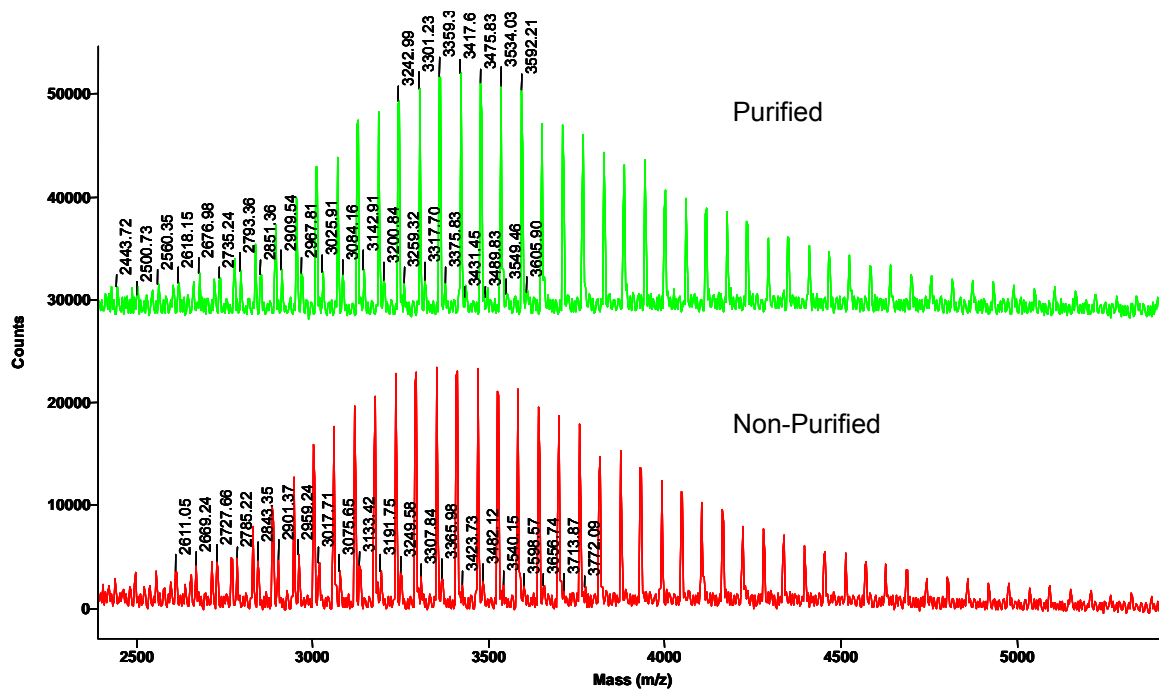


**Figure A2.8:** Comparison PPG 4200 purified and non-purified ( $\text{Na}^+$  distributions). High molecular weight species.

## Appendix A2.4: Experimental adjustment of NCO/OH

Example of experimental adjustment of the ratio NCO/OH. The same procedure was applied for the other two materials.

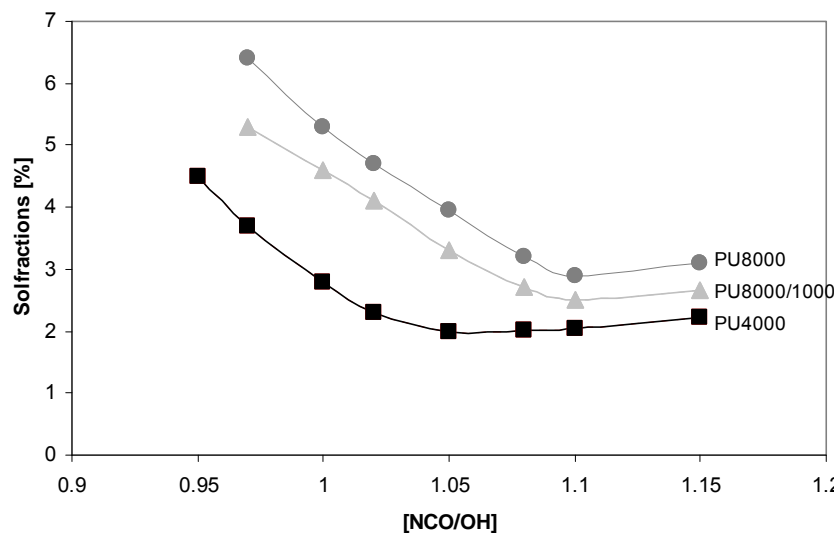


**Figure A2.9:** Stoichiometry adjusted by solfractions. For PU4000, PU8000, and PU8000/1000.

## Appendix A2.5: Optimization of the time for the curing at 80°C of the polyurethane model networks

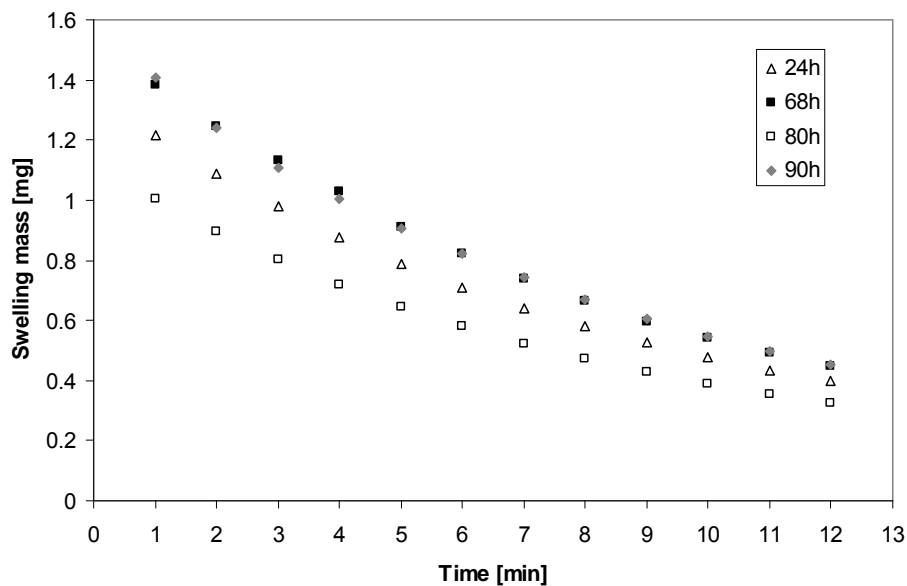


**Figure A2.10:** Curing time adjusted by swelling. Example for PU4000.

## Appendix A2.6: Density calculations

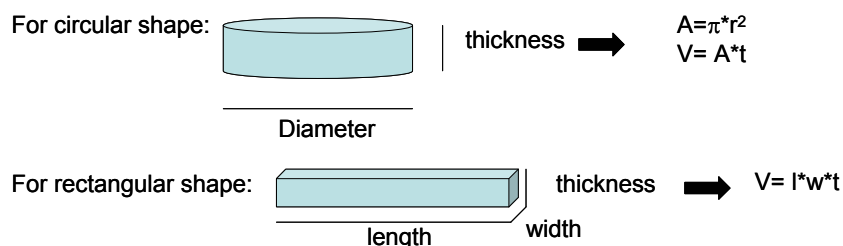


**Figure A2.11:** Scheme of cylinders and rectangles of model networks measured. Typical values of the parameters are: diameter  $\sim 5$ mm; length  $\sim 6$ mm, width  $\sim 5$ mm; thickness  $\sim 1$ mm.

## Appendix A2.7: Solubility parameters

The solubility parameters can be calculated from cohesive energy densities,  $E_{\text{coh}}$ , and the volume contribution of the atomic groups by using equation [Polymer Handbook, Petrovic 1987]:

$$\delta^2 = (\Sigma E_{\text{coh}}) / (\Sigma V_m)$$

**Table A2.7:** Solubility parameters [Polymer Handbook, Petrovic 1987, Petrovic 1989]

<i>Polymer</i>	Solubility parameter ( $\text{J/cm}^3$ ) <sup>1/2</sup>
<b>PPG 1000</b>	17.65
<b>PPG 4000</b>	17.21
<b>PPG 8000</b>	17.10
<b>DESMODUR RFE (polyurethane form)</b>	31.9
<i>Solvent</i>	
<b>Dichloromethane</b>	18.4
<i>Polyurethane</i>	
<b>PU4000</b>	18.34
<b>PU8000</b>	17.70
<b>PU8000/1000</b>	17.91

## Appendix A2.8: $D_{\text{res}}$ as a function of the swelling percentage in mass

Both  $D_{\text{res}}$  and  $1/Q_p$  are proportional to  $1/M_c$ , and the fitting of the graph shows the entanglement contributions.

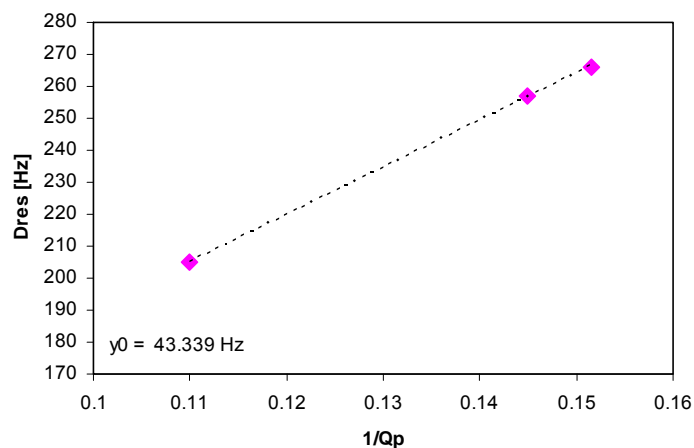


**Figure A2.12:** Fitting of  $D_{\text{res}}$  [Hz] in function of the swelling percentage in mass of the polyurethane model networks.

Note: According to Flory-Rehner theory, the modulus (and also the NMR observable) is proportional to  $1/Q^{(5/3)}$ . This is only valid for high  $Q$ , but since  $Q=7-8$  is probably OK for this approximation.

#### Appendix A2.9: Thermal expansion

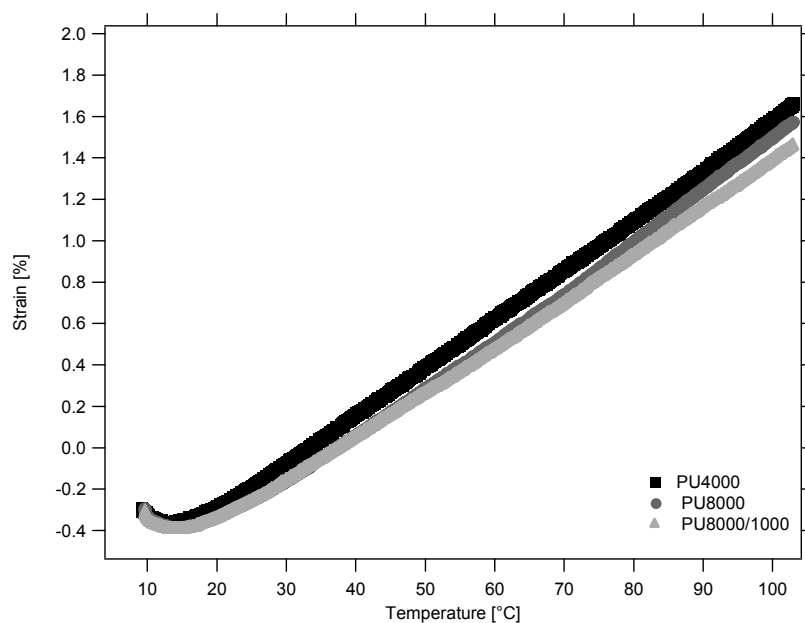


**Figure A2.13:** Change in strain for PU4000, PU8000 and PU8000/1000 in function of temperature.

## Bibliography

- Andrady, A.L., Llorente, M. A. and Mark, J. E., Polymer Bulletin, 28, 103-108 (1992).
- Andrady, A.L. and Sefcik, M.D., Journal of Polymer Science: Polymer Physics Ed., 21, 2453 (1983)
- Bayer data sheets ACCLAIM series (4000 and 8000g/mol), and Arch Chemical data sheets (1000g/mol)
- Beshah, K., Mark, J.E., Ackerman, J.L., Himstedt, A., Journal of polymer science. Polymer physics edition, 24, n°6, 1207-1225 (1986).
- Bos, H. L. and Nusselder J. J. H., Polymer, 35, 13: 2793-2799 (1994).
- Boulares A., Tessier M. and Marechal E., Journal of Macromolecular Science-Pure Appl. Chem., A35 (6): 933-953 (1998)
- Erman, B. and Mark, J.E., Oxford University Press, New York (1997)
- Florez, S., Muñoz, M.E. and Santamaría, A., Macromolecules Materials Engineering, 291, 1194-1200 (2006).
- Flory, P. J., Principles of polymer chemistry. Cornell University Press, Ithaca, NY. 1953.
- Flory, P.J., Chem.Rev, 35, 51 (1944)
- Flory, P.J. and Rehner, J. J., Chem. Physics, 11, 521 (1943).
- Garrido, L., Mark, J.E., Ackerman, J.L., Kinsey, R.A., . ; KINSEY R. A., Journal of polymer science. Part B. Polymer physics, 26, n°11, 2367-2377 (1988).
- Geede ULF. W., Polymer Physics, Kluwer Academic Publishers, 3<sup>rd</sup> edition (1999).
- Goldwasser, J.M. and Adolph, H.G., Polymer Engineering Science, 26, 1510 (1986)
- Griffiths, P. R. and De Haseth, J. A., Fourier Transform Infrared Spectrometry (Chemical Analysis: A Series of Monographs on Analytical Chemistry and Its Applications), Wiley-Interscience, 2 edition (2007)
- Pasch, H. and Schrepp, W., MALDI-TOF Mass Spectrometry of Synthetic Polymers, Springer; 1 edition (2003)
- [http://scholar.lib.vt.edu/theses/available/etd-04122002-012440/unrestricted/chapter\\_4.pdf](http://scholar.lib.vt.edu/theses/available/etd-04122002-012440/unrestricted/chapter_4.pdf)
- [http://scholar.lib.vt.edu/theses/available/etd-04122002-012440/unrestricted/chapter\\_2.pdf](http://scholar.lib.vt.edu/theses/available/etd-04122002-012440/unrestricted/chapter_2.pdf)
- Marchessaultt, R., Bluhm, E. Rirem Gharapetianan, H., Pudupadr, D., Sundarakaj, I., Can J. Chem. 63. (1985)
- Marek W. Urban, Attenuated Total Reflectance Spectroscopy of Polymers: Theory and Practice, Oxford University Press (1996).
- Mark, J. E. Macromolecules Rev. 11, 135 (1976).
- Mark, J.E., Macromolecules Sym., 77, 201 (2003)
- Menard, K.P., Dynamic Mechanical Analysis: A Practical Introduction, CRC-Press; 1 edition (1997)
- O'Sickey, M. J. PhD thesis, 2002. University Library Virginia Tech, Chapter 2 and 4
- Pavia, D. L. and Lampman, G. M., Introduction to Spectroscopy, Brooks Cole; 3 edition (2000).
- Petrovic, Z. S. and MacKnight, W. J., Bull.Slovenian Chem.Soc., 36(4), 405-422 (1989).



- Petrovic, Z. S., MacKnight, W. J., Koningsveld, R. and Dusek, K., *Macromolecules* 20, 1088 (1987).
- Polymer Handbook, Brandrup, J. and Immergut, E.A. ; Wiley-Interscience : New York, p IV (1975).
- Rubinstein, M. and Colby, R.H., *Polymer Physics*, Oxford University Press, USA (2003)
- Saalwächter K., *Progr. NMR Spectrosc.*, 57, 1–35 (2007).
- Saalwächter K., Sommer, J-U., *Macromolecular Rapid Communications*, 28, 1455-1465 (2007).
- Saalwächter K., Ziegler, P., Spyckerelle, O., Haidar, B., Vidal, A., Sommer, J.-U., *J. Chem. Phys.*, 119, 3468 (2003).
- Seader, J. D. and Henley E. J., *Separation Process Principles*, Wiley; 2 edition ( 2005)
- Sepe, M., *Dynamical Mechanical Analysis for plastics engineering*, Dickten & Masch Manufacturing, Wisconsin, USA (1998).
- Smith, B. C., *Fundamentals of Fourier Transform Infrared Spectroscopy*, CRC, 1 edition (1995).
- Steeman, P.A.M. & Nusselder, J.J.H., *Polymer Gels and Networks*, 3: 159-177 (1995).
- Takeuchi, H, and Cohen, C., *Macromolecules*, 32, 6792. (1999).
- Termonia, Y., in: S.M. Aharoni, Eds., *Plenum Press*, New York, p.201 (1992)
- Treloar, L.R.G., *The Physics of Rubber elasticity*, Oxford Classic Texts, third edition (2005).
- Urayama, K., Kawamura, T., Kohjiya, S., *Polymer* 50, 347-356 (2009)
- Yong, Z. and Wu, M., *Gaofenzi Xuebao*, 6, 401 (1988)
- Yoo, S. Y., Cohen, C and Hui, C.-H., *Polymer*, 47, 6226 (2006).
- Youn Kim.C.S, Ahmad, J., Bottaro, J. and Farzan, M., *Journal of applied polymer science*, 32, 1, 3027-3038 (1986).
- Zhuang, H., Sankarapandian, M.S., Ji, Q. and McGrath, J.E., *Journal of Adhesion*, 71, 231 (1999)

# **Chapter 3**

## **Mechanical Properties of the Polyurethane Model Networks**

Introduction .....	103
3.1.-Large strain behaviour: Non-linear elasticity .....	103
3.1.1.- Uniaxial extension: Experimental part and Results .....	105
3.1.2.- Uniaxial Compression: Experimental part and Results .....	109
3.2.- Strain Rate Dependent Properties in the Linear Regime .....	114
3.3.- Fracture Properties .....	119
3.3.1.- Introduction.....	119
3.3.1.1 Estimate of threshold energy for crack growth: $G_0$ .....	121
3.3.2.- Experimental part.....	123
3.3.3.- Fracture Results at standard conditions .....	125
3.3.4.- Fracture Results at different temperatures .....	129
3.3.5.- Fracture Results at different speeds .....	130
Conclusions .....	136
Appendices A3 .....	137
Appendix A3.1: Time-Temperature Superposition for PU4000 .....	137
Appendix A3.2: Time-Temperature Superposition for PU8000 .....	139
Appendix A3.3: Time-Temperature Superposition for PU8000/1000 .....	142
Appendix A3.4: Fracture results .....	145
Bibliography.....	147

## Introduction

In order to properly interpret the results of the cavitation experiments, it is essential to characterize in detail the mechanical properties of the elastomers when they are deformed homogeneously and when they are fractured in a simple geometry.

The mechanical properties of main interest for our study (in addition to DMA results presented in Chapter 2) are the linear viscoelastic properties, the large strain properties to characterize the effect of entanglements and finite extensibility of the network chains, and the fracture properties.

The viscoelastic dissipation of the three polyurethane networks was obtained from DMA multifrequency experiments, and time-temperature superposition master curves were constructed. Then, these results were correlated to the fracture results. Tensile tests were carried out and analyzed to extract the relative contribution of entanglements and crosslinks to the modulus and uniaxial compression experiments were carried out to characterize the finite extensibility of the chains and the strain hardening.

Finally the fracture properties were studied at different temperatures and rates with the purpose of knowing the critical energy release rate  $G_{IC}$ , which is a material parameter, of the three polyurethane model networks. By decreasing strain rate and increasing temperature, the experimental threshold energy  $G_0$ , to initiate mechanical crack, may be obtained. The fracture energies and mechanical properties obtained in this Chapter will then be used to interpret the cavitation results (shown in Chapters 4 and 5) in light of existing models.

### 3.1.-Large strain behaviour: Non-linear elasticity

Although at small strains rubbers display linear elasticity, this ceases to be true at larger strains and although they remain mostly elastic, the dependence between stress and strain becomes non-linear. This is called non-linear elasticity or hyperelasticity. The nonlinear elastic behaviour needs to be characterized if any modelling needs to be done at large strains with realistic material parameters. Furthermore the nonlinear elastic behaviour is very sensitive to the network architecture and the existence of entanglements and the finite extensibility of the chains between crosslinks can be extracted from the analysis of the large strain behaviour. Different types of simple experiments can typically be done to characterize the homogeneous large strain behaviour: (1) simple extension (tensile), (2) uniaxial compression or equi-biaxial extension, and (3) shear. Although any of these geometries could be in principle used to characterize the material, experimental considerations dictated the use of uniaxial extension and compression in this Thesis.

The uniaxial compression creates a state of strain equivalent to the one obtained in equi-biaxial extension but with the addition of a compressive hydrostatic component to the stress. In uniaxial compression it is typically possible to achieve higher values of extension than in uniaxial extension before macroscopic fracture occurs. Figure 3.1 shows an example of the complete uniaxial extension and compressive curves [Treloar 2005].

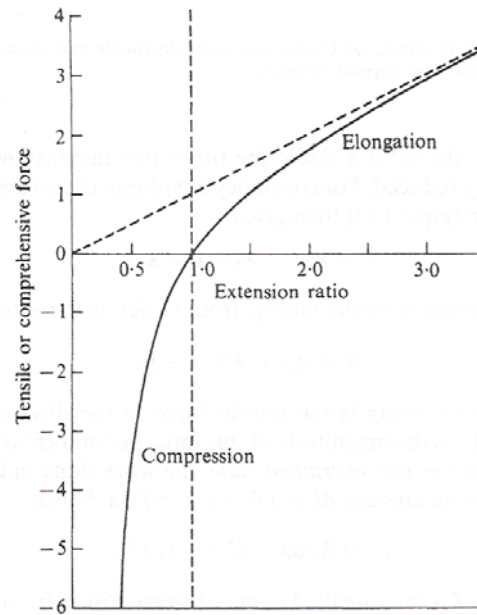


**Figure 3.1:** Complete extension and compression curves. Compression data from equivalent two-dimensional extension [Taken from Treloar 2005].

For elastomer model networks, rupture criteria based on the strains, stresses or energy, were developed by several authors using experimental data determined from simple and biaxial tension tests on unfilled and carbon black filled elastomers. Smith [Smith 1958, 1960], Bueche [Bueche 1962], Bueche and Halpin [Bueche and Halpin 1964], studied the fracture properties of unfilled elastomers (e.g. unfilled SBR), considering the visco-hyperelastic behaviour of these materials. They also introduced the concept of ‘failure envelope’ for elastomers, which is a unique curve for all strain rates and test temperatures. For their criteria they used the principle of time-temperature superposition, which gives the possibility of determining for a given material the limiting properties of strain rate and temperature in relation to a reference temperature by using William, Landel and Ferry (WLF) equation [Ward and Hadley 1998, Hamdi, A. 2006].

Dickie and Smith [Dickie and Smith 1969], studied the ultimate properties of an unfilled styrene-butadiene rubber vulcanizate in equal biaxial tension by inflating a circular membrane into a bubble. They used several extension rates and temperatures and evaluated from the pressure the stress in the vicinity of the pole when rupture occurred, as well as the radius of curvature, and the extension ratio  $\lambda$ . They obtained that values of the ultimate properties in truly equal biaxial tension were somewhat greater than those obtained from uniaxial extension. They concluded that no simple failure criterion was applicable for interrelating data obtained under the several states of combined stress. Kawabata [Kawabata 1973], studied experimentally the mechanical properties of vulcanized unfilled natural rubber and SBR under finite deformation using the biaxial stress relaxation method. The first technique he used was the stretching of thin films in two perpendicular directions, and the second technique was the inflation of a thin membrane into a bubble. He obtained that the maximal

elongation did not depend on the nature of the loading, and that the maximal stresses were higher under biaxial extension than on uniaxial extension.

Several authors have considered that the rupture of elastomers can initiate from intrinsic pre-existing defects. These defects may be microfractures that grow under loading. Based on this hypothesis Mars and Fatemi [Mars and Fatemi 2001, 2002] have used filled elastomers of natural rubber and SBR under cycling loading and defined a criterion of crack initiation in fatigue based on the ‘cracking strain energy density’ ( $W_c$ ).

### 3.1.1.- Uniaxial extension: Experimental part and Results

Tensile tests were performed on a standard tensile Instron machine (model 5565) equipped with a video extensometer, which allows an accurate measurement of the strain. The machine used a 10N load cell with a resolution of 16mN. The films of the three polyurethane model networks, prepared as mentioned in Chapter 2, were used to prepare the sample; the films were cut by using a metallic punching system with a dog-bone shape (see Figure 3.2). The experiments were performed at an initial strain rate of  $\sim 0.7\%/s$  ( $0.007\text{ s}^{-1}$ ) and at room temperature ( $\sim 25^\circ\text{C}$ ).

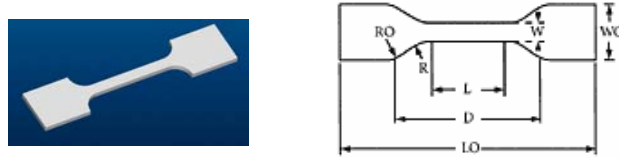


**Figure 3.2:** Geometry of the samples used for the tensile tests. The dimensions were  $L=25\text{mm}$ ;  $D=40\text{mm}$ ;  $W=4\text{mm}$ ,  $W_0=12.5\text{mm}$ ,  $R_0=12.5\text{mm}$  and  $R=8\text{mm}$  (Iso 4661-1 Standard).

To perform the tensile experiments, an initial gauge length was put on the sample with a special marker, inside the region of the central  $L=25\text{mm}$ , for the recognition of the sample by the video extensometer. In Figure 3.3, there is an example of the experiment and how is the field of view of the video extensometer at the beginning and close to the end of the experiment.

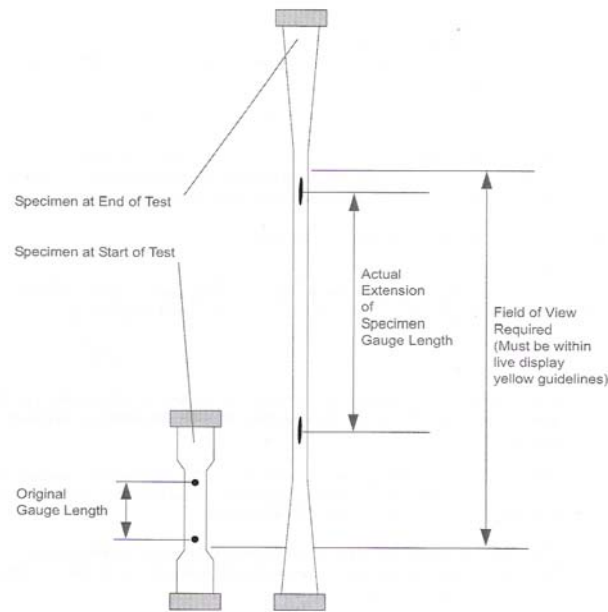


**Figure 3.3:** Scheme of the tensile test at the beginning and close to the end (before breaking). Video extensometer following the marks.

Figure 3.4 shows the results obtained for the tensile experiments for the three polyurethane networks. All three curves are markedly non-linear and softening and no obvious evidence of strain hardening (i.e. a stiffer behaviour than a neo-Hookean rubber with an equivalent initial modulus) is visible. All three materials break at moderate extension values and the maximal extension values scale inversely with the initial modulus as is typically observed for simple elastic networks. Fracture is brittle with a non-controlled crack propagation in all cases.

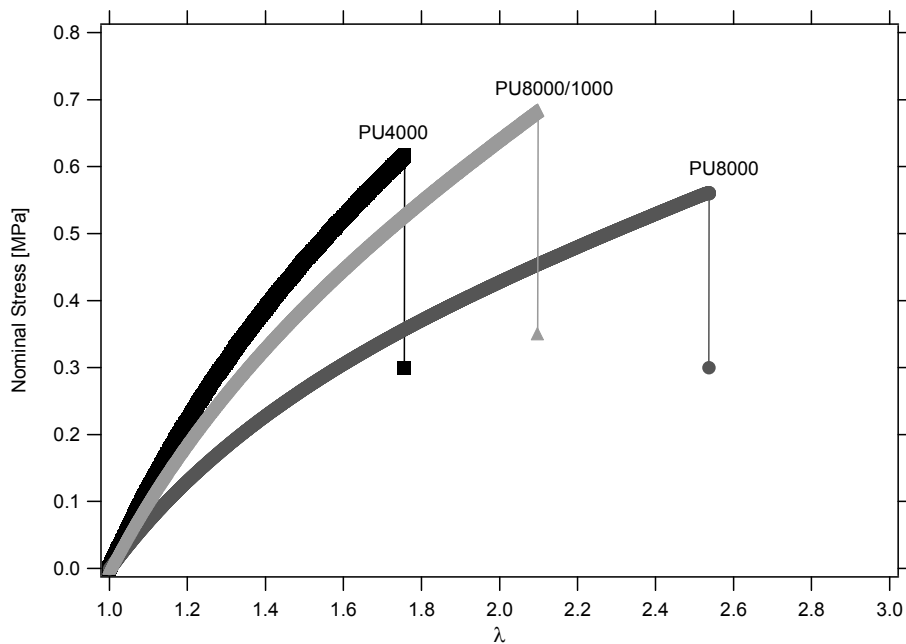


**Figure 3.4:** Uniaxial extension. Nominal stress versus  $\lambda$ , for the three polyurethane model networks.

The intrinsic nonlinear behaviour appears more clearly using the Mooney stress  $\sigma_R$  defined as:

$$\sigma_R = \frac{\sigma_N}{\left(\lambda - \frac{1}{\lambda^2}\right)} \quad \text{eq. 3.1}$$

where  $\sigma_R$  is the reduced stress,  $\sigma_N$  is the nominal stress and  $\lambda$  is the strain ratio. This representation normalizes the measured stress by the predicted behaviour of a neo-Hookean rubber in uniaxial extension and is usually plotted as a function of  $1/\lambda$  (known as Mooney plot). In Figure 3.5, is presented an example of a Mooney plot, where can be seen the softening and the hardening of the network.

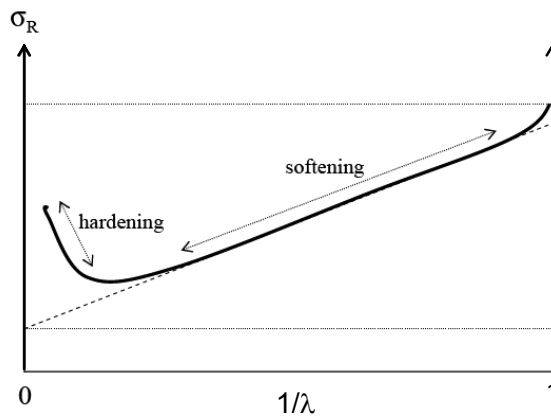


**Figure 3.5:** Example of a Mooney plot.

Plotting our tensile results as Mooney plot (see Figure 3.6), we observe that the three networks have some small degree of softening. In general, the softening is related to the presence of entanglements in the molecular structure, which contribute to the elastic modulus of the networks. As was mentioned in Chapter 2, the average molecular weight between entanglements of a PPG-based polyurethane is  $M_e \sim 3000 \text{ g/mol}$  [Florez *et al.* 2006]. Our results showing that the network PU8000 softens more than the others, suggest that the most entanglements are present in the PU8000. Interestingly the bimodal network does not show much softening implying that the presence of low molecular weight component in the network prevents any relaxation of the entanglements which are effectively trapped.

Rubinstein and Panyukov developed a molecular model for entangled and crosslinked networks, that separates the respective contributions to the shear elastic modulus  $G$  of crosslink points and from entanglements [Rubinstein and Panyukov 2002]. In this model the topological constraints imposed by the neighbouring network chains on a given network are represented by the confining potential that changes upon network deformation. This topological potential restricts fluctuations of the network chain to the nonaffinely deformed confining tube. Network chains are allowed to fluctuate and redistribute their length along the contour of their confining tubes. In this model, the stress  $\sigma$  and  $\lambda$  are usually represented in



the form of the reduced stress  $\sigma_R$  (Mooney stress). Then, the prediction of the model for the stress is given by:

$$\sigma_R = G_c + \frac{G_e}{0.74\lambda + 0.61\lambda^{-1/2} - 0.35} \quad \text{eq. 3.2}$$

where  $G_c$  and  $G_e$  are the respective contribution of the crosslinks and entanglements to the small strain modulus. This model has two advantages over the more widely used Mooney-Rivlin model [Mooney 1940, Rivlin 1948]: the fitting parameters are directly related to the network architecture, and the model fits the softening equally well in tension and compression. Table 3.1 shows the values of  $G_c$  and  $G_e$  obtained from fitting the data with equation 3.2. The contribution of the entangled network modulus is almost negligible for the PU4000, while it is slightly higher for the PU8000/1000 and becomes of the order of 20% for the PU8000.

**Table 3.1:** Values obtained for the tensile experiments,  $G_c$ ,  $G_e$  and  $E$ , by using Rubinstein and Panyukov fitting.

Material	$G_c$ [MPa]	$G_e$ [MPa]	$G$ [MPa]	$E$ [MPa]	$E'$ [MPa] @25°C, DMA
<b>PU4000</b>	0.44	0.001	0.441	1.32	$1.3 \pm 0.08$
<b>PU8000</b>	0.20	0.05	0.250	0.75	$0.8 \pm 0.06$
<b>PU8000/1000</b>	0.37	0.01	0.380	1.14	$1.2 \pm 0.07$

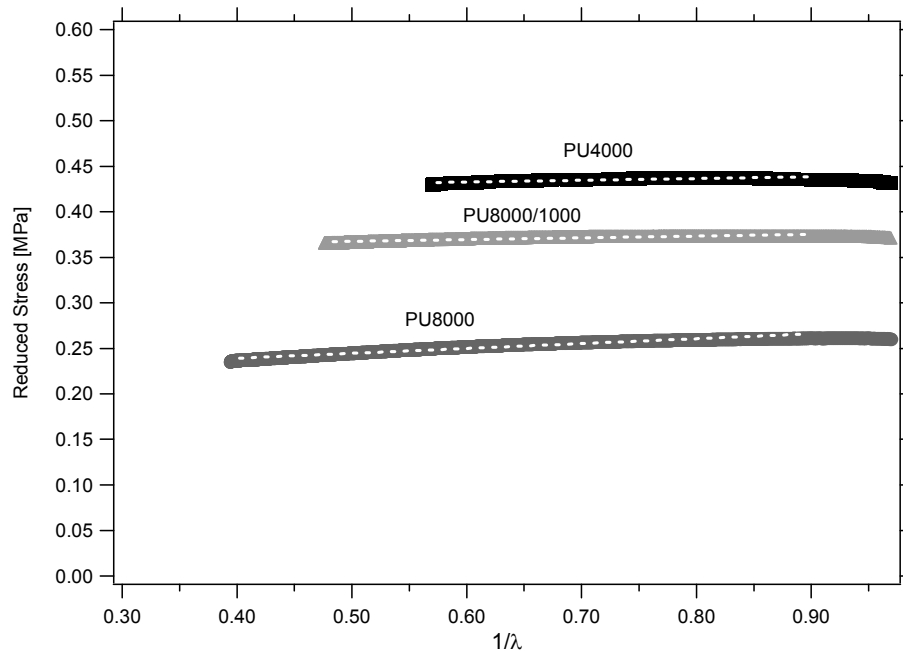


**Figure 3.6:** Mooney plot and Rubinstein and Panyukov fitting (dots line in white) of tensile results for the three polyurethane model networks.

It is worthwhile to note that the moduli reported in Table 3.1, obtained by the Rubinstein-Panyukov fit, are very close to the moduli obtained by DMA, reported in Chapter 2, and this together with the relatively low contribution of the entangled network modulus for the PU4000, PU8000/1000 and still for PU8000, show that the three materials are model networks at small and large strain.

### 3.1.2.- Uniaxial Compression: Experimental part and Results

Given the brittleness of the three polyurethane networks in uniaxial tension preventing any characterization of the strain hardening at very large strains, we first considered doing experiments of bubble inflation which submits films to equi-biaxial extension in its center. To perform these experiments of equi-biaxial extension, thin films of the three networks were prepared; however, problems such as low viscosity, surface tension and difficulties in demolding made very difficult to obtain the required samples.

Since for incompressible or nearly incompressible materials, equal biaxial extension of a specimen creates a state of strain equivalent to uniaxial compression, the only difference being the nature of the applied stress, we performed uniaxial compression experiments for the three networks.

The state of strain known as uniaxial compression is obtained by the application of inwardly directed forces to a pair of opposite surfaces of a cylinder, in a direction parallel to the axis, while the lateral surfaces are free of stress. This type of stress is formally identical to simple extension, but in this case  $\lambda$  (the compression ratio) is less than 1 [Treloar 2005, Gent 1994]. The actual displacement during compression is very small and great care must be taken to measure only the specimen compliance and not the stiffness of the instrument itself or friction. The experiments were performed in a hydraulic MTS 810 machine with a load cell with a maximum capacity of 2.5 kN and a resolution of  $\pm 0.5$  N. The samples were cylinders ( $d_0=5\text{mm}$  in diameter and  $h_0\sim 5\text{mm}$  in height). These cylinders were obtained by using a Teflon mold machined with holes with the exact diameter and height, and the support of the mold was a glass plate (chemically modified for demolding). All the experiments were performed at room temperature ( $\sim 25^\circ\text{C}$ ). An example of the compression experiment is presented in Figure 3.7.

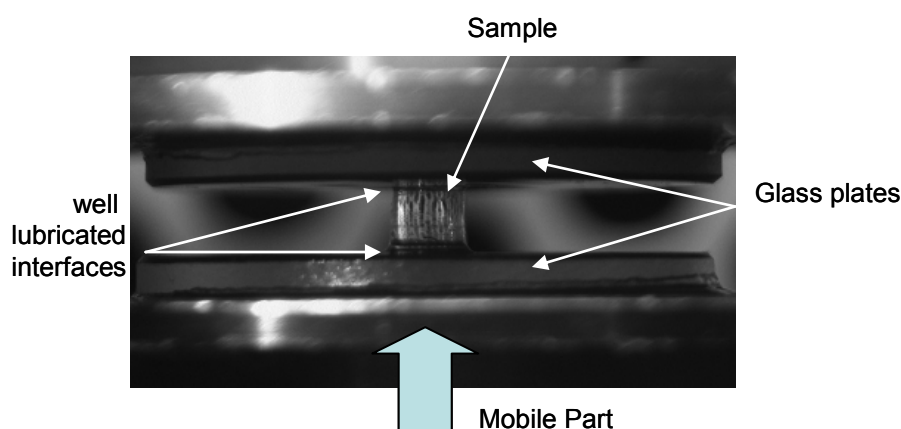


**Figure 3.7:** Example of the compression experiment

The compression test consisted of an initial compressive contact to -1 N to ensure a starting point of complete contact between the sample and glass surfaces. The interfaces between the sample and the glass plates were lubricated with a silicone oil to avoid friction and to obtain an homogeneous strain field. The tests were performed at constant crosshead rate and at an initial compressive strain rate of 0.6%/s ( $0.006 \text{ s}^{-1}$ ). The stretch is defined as  $\lambda = h/h_0$ , where  $h_0$  is the undeformed height of the sample and  $h$  is the deformed height. The samples in undeformed and deformed geometry are schematically shown in Figure 3.8.

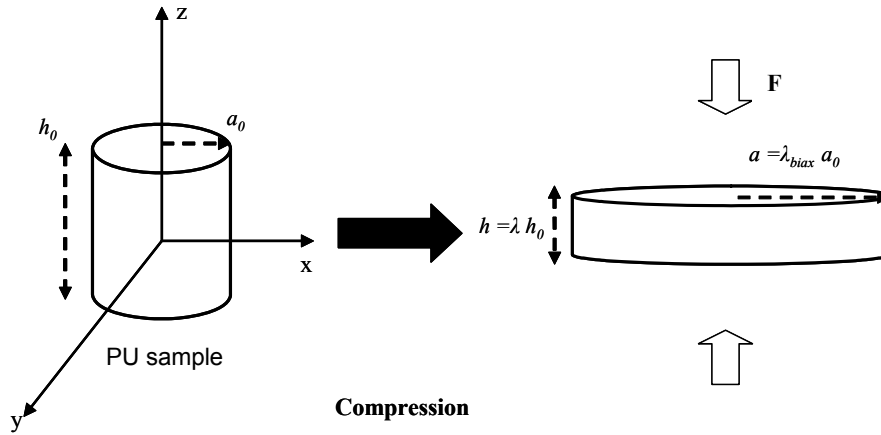


**Figure 3.8:** Schematic representation of a compression test [taken from Miquelard-Garnier 2007].

Figure 3.9 shows the results of the compressive nominal stress versus lambda  $\lambda$  for the three networks while Figure 3.10 shows the Mooney stress. The clear upswing in reduced stress at low values of  $\lambda$  can be observed for the three materials. However, since the moduli are different for all materials a more precise fit of the data has to be carried out.

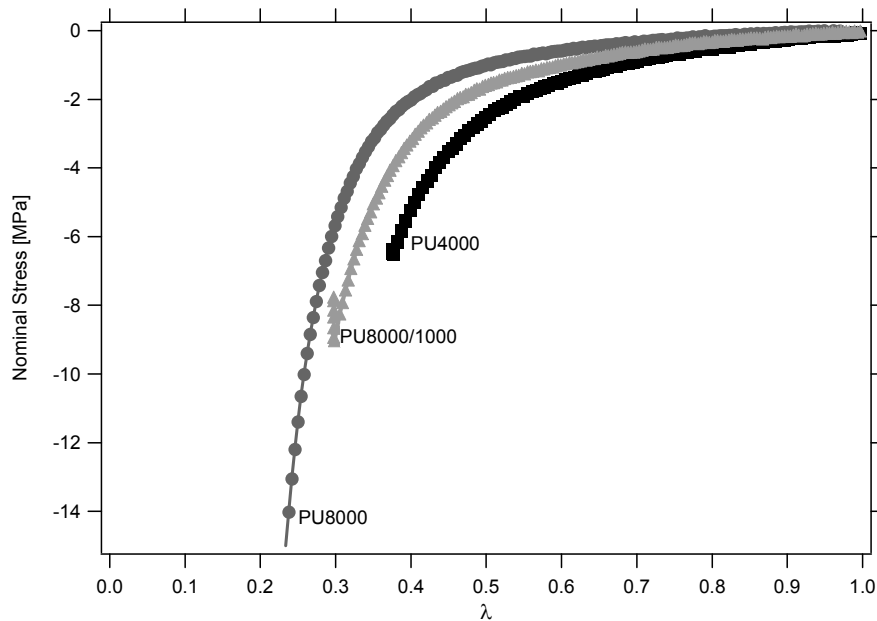


**Figure 3.9:** Compression results for the three polyurethane model networks (at room temperature).

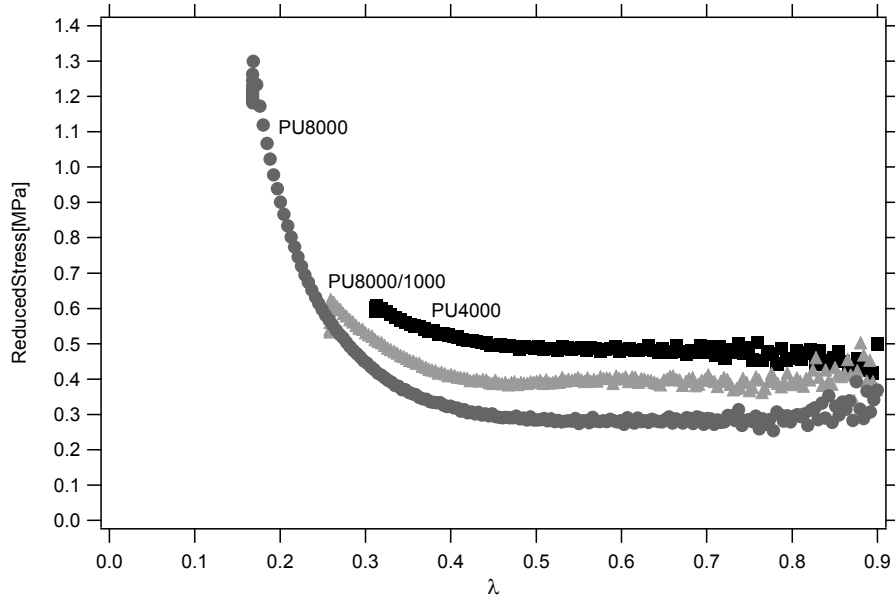


**Figure 3.10:** Mooney plot of compression results for the three polyurethane model networks.

The Mooney-Rivlin model predicts softening in tension and hardening in compression which is not very physical, while the Rubinstein and Panyukov model does not have any hardening built in. However the literature is full of mechanical models including hardening parameters [e.g. Gent 1996, Arruda and Boyce 1993]. Most of these models are simply designed to fit the data as closely as possible to the expense of the physical interpretation of the parameters. To our knowledge the only physically based molecular model including strain hardening is the Edwards-Vilgis model [Edwards and Vilgis 1988] using 4 parameters. However, the use of 4 parameters does make the fitting more ambiguous given the limited range of our experimental data. A simpler fitting model was developed by Seitz *et al.* [Seitz *et al.* 2008] and consists of an exponential fitting. This model has two parameters, one free parameter  $J_m$ , and one fixed parameter  $E'$  since the value of the Young's modulus is known from the network's small strain behaviour. Then at small strain this model is equivalent to the Neo-Hookean model. At large strains the finite extensibility of the chains is taken into account by  $J_m$ , similarly to the Gent's model [Gent 1996]. To characterize our tensile and compression data we used the strain energy function,  $U$  ( $=W$ , see equation 3.3) developed by Seitz *et al.* [Seitz *et al.* 2008] for large strain behaviour:

$$U = \frac{E}{6} J_m \left( \exp \left( \frac{J_1}{J_m} \right) - 1 \right) \quad \text{and} \quad J_1 = \lambda_x^2 + \lambda_y^2 + \lambda_z^2 - 3 \quad \text{eq. 3.3}$$

where  $E$  is the small strain Young's modulus and  $\lambda_x$ ,  $\lambda_y$  and  $\lambda_z$  are the principal extension ratios. Since our materials are incompressible  $\lambda_x^2 \lambda_y^2 \lambda_z^2 = 1$ . The  $x$  and  $y$  directions are equivalents  $\lambda_x = \lambda_y = \lambda_z^{-1/2}$  in the compression experiments, then the nominal stress ( $\sigma_N$ ) is given by:

$$\sigma_N = \frac{E}{3} \left( \lambda_y - \frac{1}{\lambda_y^2} \right) \exp \left( \frac{J_1}{J_m} \right) \quad \text{and} \quad J_1 = \lambda_y^2 + \frac{2}{\lambda_y} - 3 \quad \text{eq. 3.4}$$

The equation 3.4 was then used to fit the compression and tensile data. Seitz *et al.* found that equation 3.3 provides a better description of the data than in Gent's model and avoids divergent energies at finite strains which can be problematic when using FEM. Figure 3.11, presents the complete tensile and compression experimental curves for the three polyurethane networks and the fitting, we observe that the initial modulus fits well for both experiments implying that our lubricated compression experiments have been carried out properly.

Table 3.2 shows the results of the fitting for the tensile and compression data. By using this model, the fitting values for the extension are over predicted; the values of Young's Modulus are lower than the ones obtained by DMA. This may be expected since this model does not take into account the contribution of the entanglements to the modulus but only the strain hardening. In fact, in extension the model predicts better the behaviour of PU4000 than the other two materials.

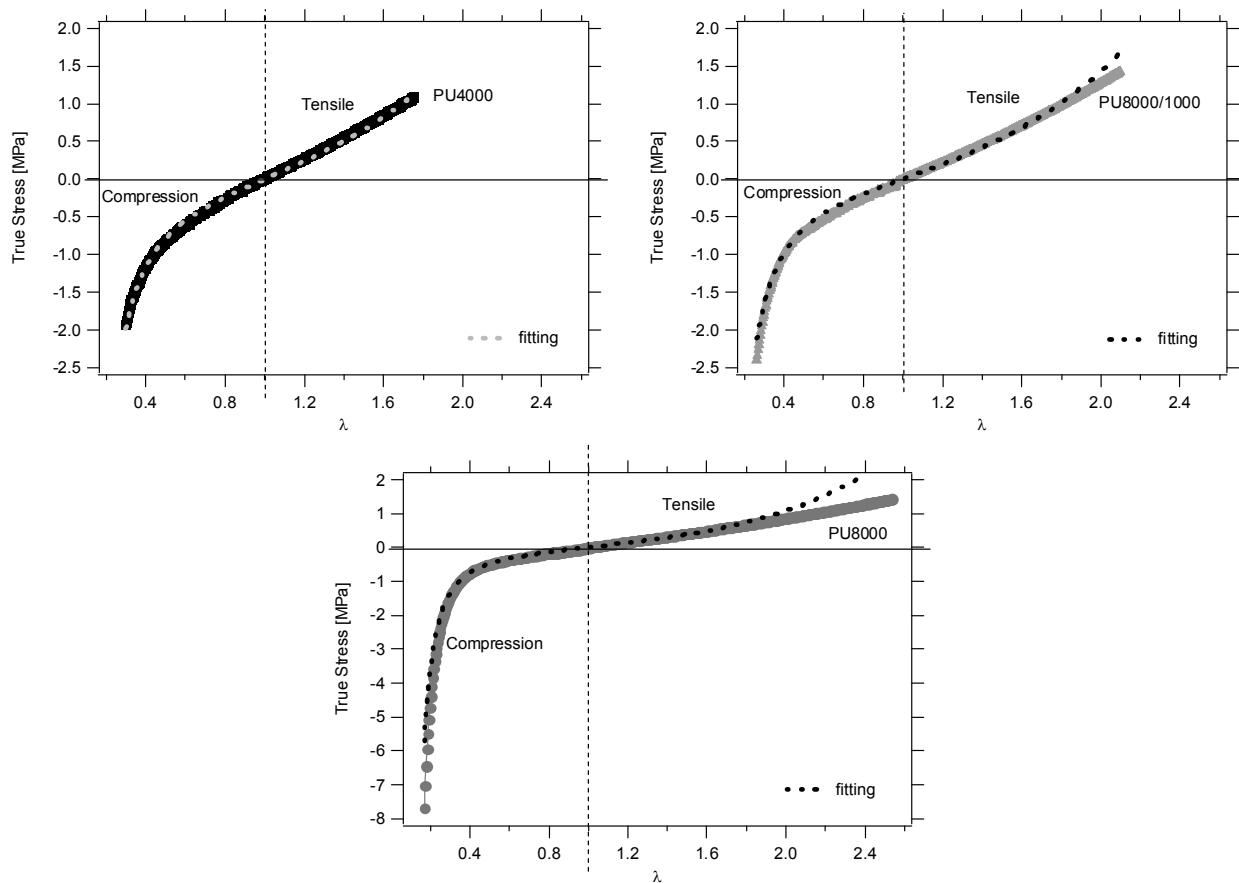


**Figure 3.11:** Fitting of the complete tensile and compression curves for the three polyurethane model networks.

**Table 3.2:** Fitting of tensile and compression data by using the exponential model

<b>Material</b>	<b>Young's Modulus (fitting tensile data) <math>E'</math> [MPa]</b>	<b>Maximal extensibility (fitting compression data) <math>J_m</math></b>
<b>PU4000</b>	$1.17 \pm 0.01$	$9.26 \pm 0.70$
<b>PU8000</b>	$0.69 \pm 0.02$	$5.62 \pm 0.36$
<b>PU8000/1000</b>	$0.98 \pm 0.02$	$7.37 \pm 0.34$

Regarding the fitting for the compression data we observe that it is very good for the three materials (see Figure 3.11). However, when the strain hardening parameter  $J_m$  is compared for the three materials, there is a surprising result, since theoretically for materials with longer chains (PU8000) a higher value of the strain hardening parameter would be expected than for materials with shorter chains (PU4000). Yet Table 3.2 shows that the obtained order is inverted. This result may be due to microfracture events occurring during the compression before complete fracture for the two more fragile materials (PU4000 and PU8000/1000). To prove the existence of these ‘microfractures’ loading/unloading cycles were carried out on the three materials and the results are presented in Figure 3.12. We can see that when the materials are loaded in a second cycle they show fracture before completing the second load (Figure 3.12(a) and (b)), while PU8000 (Figure 3.12(c)) resisted the complete second load/unload. Hence the value of strain hardening for PU8000 will be mainly used in Chapter 6 for the cavitation prediction model, and the strain hardening of PU4000 and PU8000/1000 will be used for comparison.

Since the compression data is representative of the biaxial extension which is equivalent to the inflation of a cavity, the exponential model is considered a good approximation to predict the strain hardening.

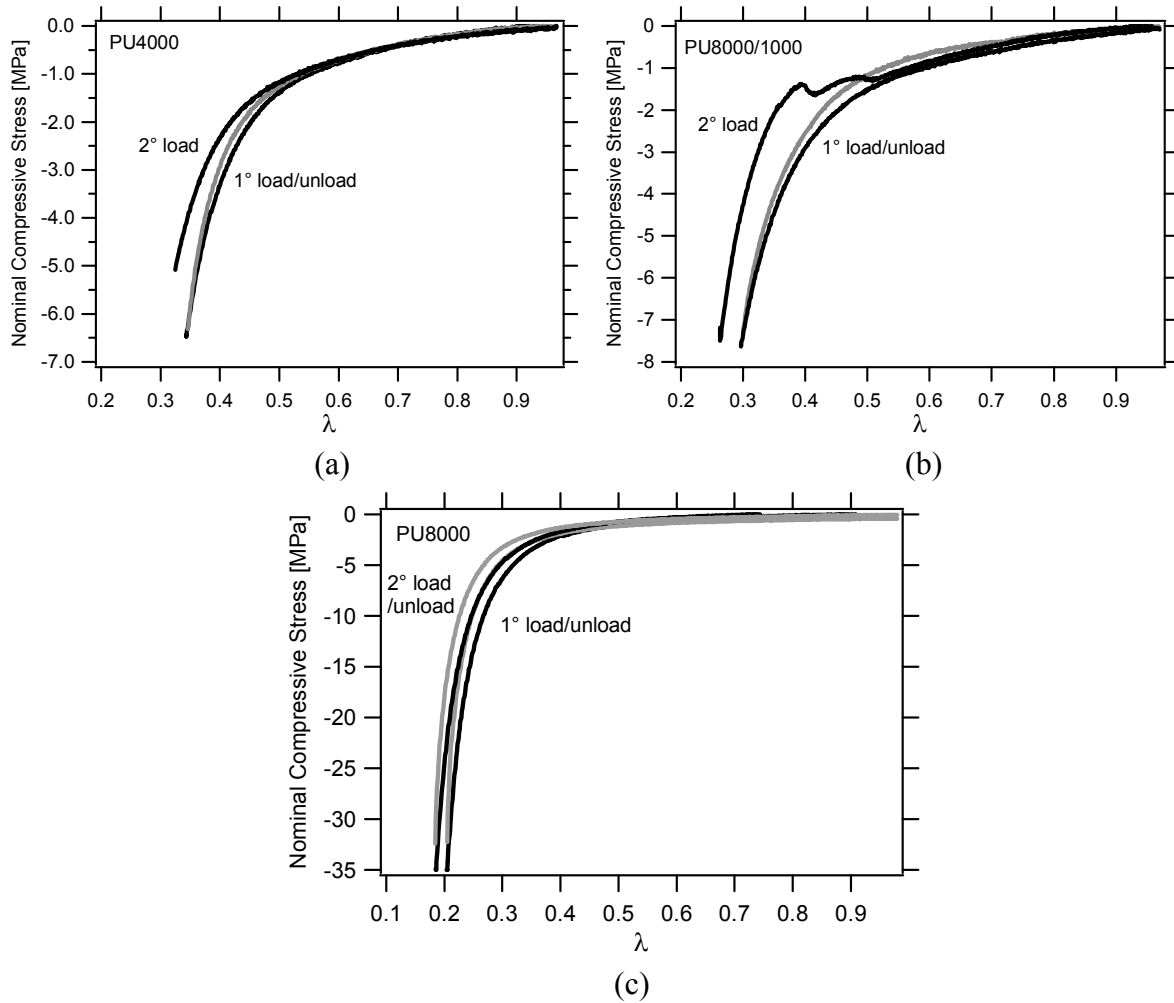


**Figure 3.12:** Nominal compressive stress versus the compression ratio for the three polyurethane model networks for two loading/unloading cycles.

### 3.2.- Strain Rate Dependent Properties in the Linear Regime

Although our elastomer networks have been designed to be as elastic as possible and show a clear thermoelastic behaviour (see chapter 2), some degree of viscoelasticity is always present. The DMA experiments presented in chapter 2 explored the temperature dependence of the viscoelastic behaviour but to characterize the variety of strain rates occurring during fracture and also during cavitation it is important to have the response of the material as a function of strain rate. This can be easily done in the linear regime by performing dynamical mechanical characterizations at different temperatures and strain rates and use the time-temperature superposition principle to build master curves.

Dynamical mechanical experiments were performed on sample bars with dimensions of  $5 \times 30 \times 1 \text{ mm}^3$  ( $L_0 \sim 15 \text{ mm}$ ) at five frequencies: 0.1, 0.5, 1, 5, 10 Hz, every  $2^\circ\text{C}/\text{min}$  in a range of temperatures between  $-80$  and  $+100^\circ\text{C}$ . The reference temperature was chosen as  $T_s = 25^\circ\text{C}$ , which is the temperature of the experiments performed at standard conditions.

For the  $E'$  and  $E''$  moduli in the rubbery state, there should be a slight vertical shift due to the thermal expansion. Two main corrections should be taken into account on theoretical grounds:

dividing the modulus by the temperature corrects for the changes in modulus due to the inherent dependence of the modulus in temperature while division by the density corrects for the changing number of chains per unit volume with temperature variation [Alkonis *et al.* 1972]. In practice the horizontal shifts can be defined with the  $\tan \delta$  (independent of these corrections) and vertical shifts are optimized empirically while checking that the values remain compatible with the theoretically predicted values close to 1.

The complete viscoelastic response of any polymer under any experimental conditions can then be obtained from the knowledge of any of two of the following three functions: the master curve at any temperature, the modulus-temperature curve at any time and the shift factors relative to some reference temperature.

Figure 3.13 (a) and 3.13 (b), shows the master curve of  $\tan \delta$  and  $E'$  as a function of the logarithm of the frequency ( $f = \omega/2\pi$ ) for PU4000 at a reference temperature  $T_s = 25^\circ\text{C}$ .

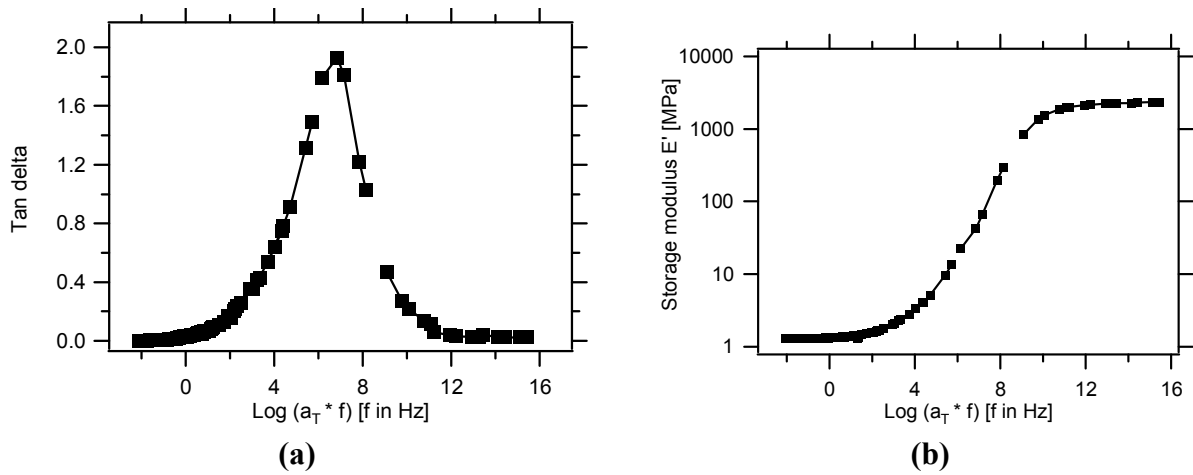


**Figure 3.13:** Master curves for PU4000 at  $T = 25^\circ\text{C}$ : (a)  $\text{Tan delta}$  as a function of frequency, and (b)  $\text{Storage modulus } E'$  as a function of the frequency.

Figure 3.14, shows the graph of  $\text{Log } a_T$  in function of the inverse of the temperature. The physical meaning of  $a_T$  is that of an acceleration (when  $a_T$  is below zero) or deceleration factor relative to the reference temperature. This means that to achieve a certain molecular arrangements at higher temperatures than  $T_s$ , the corresponding time will be much lower (much faster process) than the time to achieve the same molecular arrangement at a lower temperature.  $\text{Log } a_T$  is traditionally plotted as a function of  $1/T$  to be easily comparable to theoretical predictions.



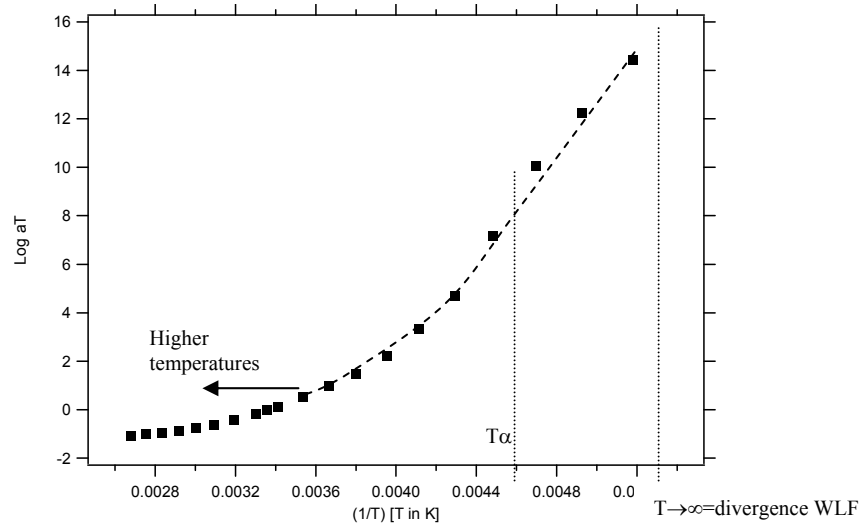


**Figure 3.14:** Log  $a_T$  versus the inverse of the temperature ( $1/T$ ), at temperatures between -80 and +100°C, for PU4000.

William, Landel and Ferry (WLF), based on free volume considerations, proposed that  $a_T$  in the vicinity of the glass transition should only depend on the difference between the absolute temperature and a fixed temperature called  $T_\infty = T_s - C_2$ , where the relaxation time is infinitely long [Halary *et al.* 2008]. Then the functional dependence of  $a_T$  would be given by an equation of the form

$$\text{Log} a_T = \frac{-C_1(T - T_s)}{C_2 + (T - T_s)} \quad \text{eq. 3.5}$$

where  $C_1$  and  $C_2$  are constants that depend on the polymer and the reference temperature, and  $T_s$  is the reference temperature [Alkonis *et al.* 1972, Young and Lovell 1991, Halary and Lauprêtre 2006]. This functional form is only valid at temperatures around and above  $T_g$  (DSC), typically in a range of 50°C to about 100°C above.

The shift factor  $a_T$  can be used to predict the behavior of the material as a function of time. The extrapolation needs to be performed over an extended temperature range. To perform a linear fit, the WLF equation can be re-written as:

$$\text{Log} a_T = \frac{-C_1(T - T_s)}{C_2 + (T - T_s)} \Rightarrow \frac{(T_s - T)}{\text{Log} a_T} = \frac{C_2}{C_1} + \frac{1}{C_1}(T - T_s) \quad \text{eq. 3.6}$$

The linear fitting of the data gives the constants  $C_1$  and  $C_2$ . For PU4000,  $C_1 = 2.97$  and  $C_2 = 108.17^\circ\text{C}$  at a reference temperature of 25°C. The values of  $C_1$  and  $C_2$  at 25°C are reported in Table 3.3 and the details of the fits are in Appendix 3.1. Because the fracture and cavitation experiments have been also performed at 50°C, 70°C and 100°C, the respective shift factors for these temperatures relative to standard conditions are reported in Table 3.4.

**Table 3.3:** WLF constants values  $C_1$  and  $C_2$  for the three polyurethane model networks, at  $T_s=25^\circ\text{C}$ .

Material	$C_1$	$C_2 [^\circ\text{C}]$
<b>PU4000</b>	2.97	108.17
<b>PU8000</b>	2.34	105.80
<b>PU8000/1000</b>	3.53	109.54

Figure 3.15 and 3.16 shows  $\tan \delta$  and  $E'$  as a function of the logarithm of the frequency for PU8000 and PU8000/1000 respectively at  $T_s=25^\circ\text{C}$ . Details of the shift factors determination are in appendix 3.2 and 3.3. For all three materials the peak in dissipation occurs in the MHz range at room temperature, and at even higher frequencies for higher temperatures.

**Table 3.4:** Shift factors for the three polyurethane model networks at  $25^\circ\text{C}$ ,  $50^\circ\text{C}$ ,  $70^\circ\text{C}$  and  $100^\circ\text{C}$ .

Material	Temperature $[^\circ\text{C}]$	Log $a_T$	$a_T$
<b>PU4000</b>	25	0	1
	50	-0.62	0.24
	70	-0.87	0.13
	100	-1.09	0.081
<b>PU8000</b>	25	0	1
	50	-0.47	0.34
	70	-0.68	0.21
	100	-0.92	0.12
<b>PU8000/1000</b>	25	0	1
	50	-0.69	0.28
	70	-0.98	0.11
	100	-1.31	0.05

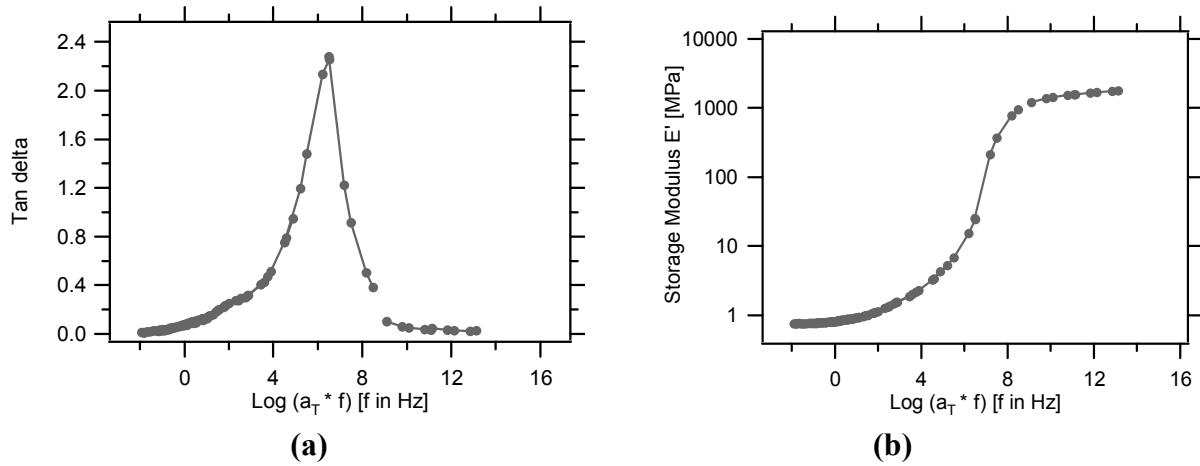


**Figure 3.15:** Master curves for PU8000 at  $T = 25^\circ\text{C}$ : (a) Tan delta as a function of the frequency, and (b) Storage modulus  $E'$  as a function of frequency.

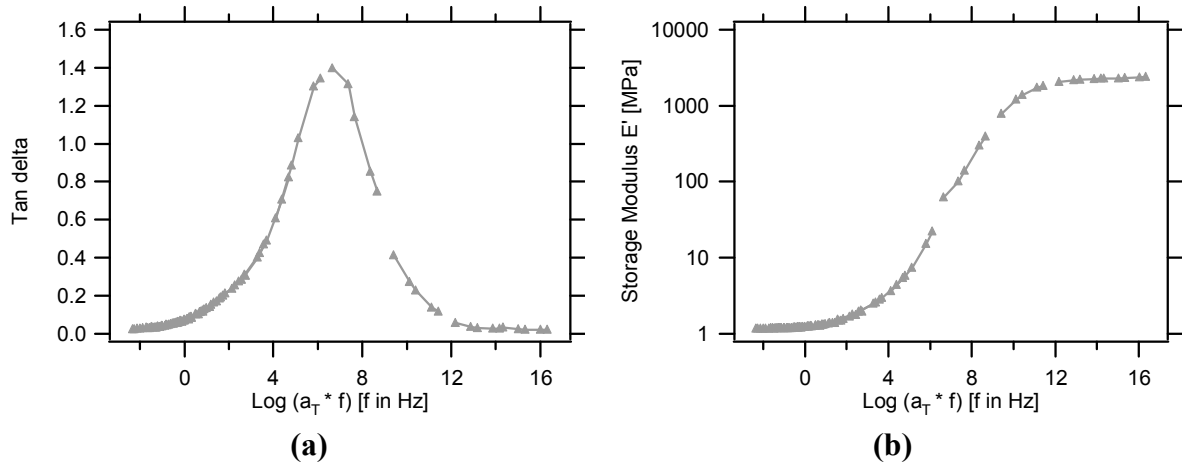


**Figure 3.16:** Master curves for PU8000/1000 at  $T = 25^\circ\text{C}$ : (a) Tan delta as a function of the frequency, and (b) Storage modulus  $E'$  as a function of frequency.

Because the three networks are rather similar in their general behaviour, it is useful to plot the same data in the relevant range of strain rates for the fracture and cavitation experiments which will be ideally between  $10^{-3}$  and 100 Hz.

Figure 3.17 (a) and (b) shows the master curves of tan delta and  $E'$ , respectively, for the three polyurethane model networks, between  $10^{-3}$  and 100 Hz at room temperature, which is the region of interest. At  $25^\circ\text{C}$  the dissipation starts to increase  $\sim 0.5$  %/s for the three networks, and it is observed that at higher frequencies PU8000 and PU8000/1000 becomes significantly more dissipative than PU4000. Figure 3.17 (b) also shows that at higher frequencies and lower temperatures the storage modulus increases.

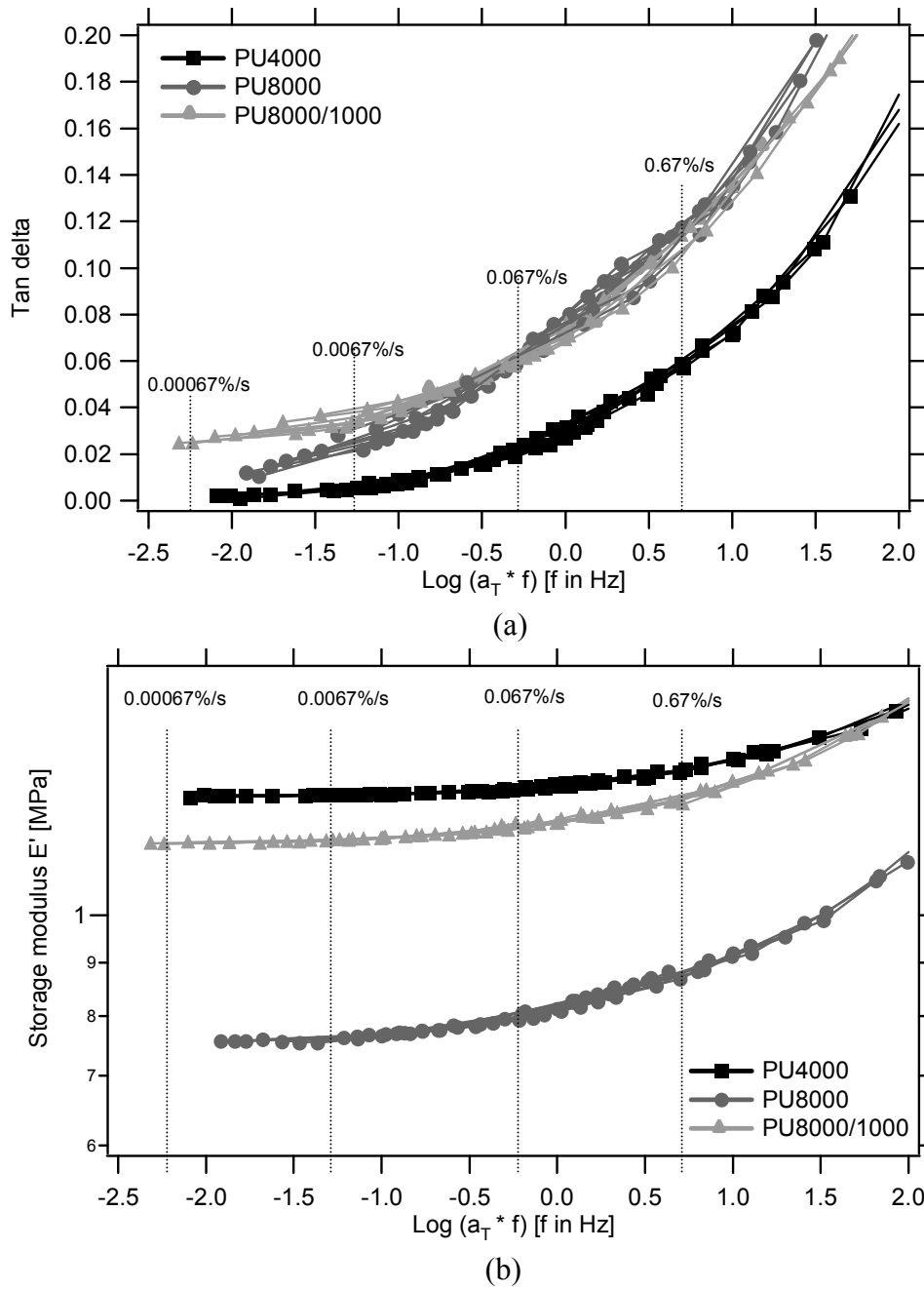


**Figure 3.17:** Master curves of (a) tan delta and (b) storage modulus  $E'$ , for the three polyurethane model networks at 25°C. Note that vertical shifting has been used to adjust for thermoelasticity effects.

### 3.3.- Fracture Properties

#### 3.3.1.- Introduction

The fracture behaviour of brittle materials was first studied by Griffith [Griffith 1920]. The Griffith's theory of fracture is the earliest statement of linear elastic fracture mechanics (LEFM) and is an energetic approach, where the fracture energy 'G' is calculated. Although it was initially conceived to describe the propagation of a crack in a perfectly elastic material at

small elastic strains (linear elastic), subsequent work has shown that it can be applied to other situations including localized plastic deformation at the crack tip [Ward and Hadley 1998]. Later was introduced the concept of ‘tearing energy’ ‘T’ which is a characteristic of the material, and equivalent to G, but for elastomers showing non-linear elasticity [Rivlin and Thomas 1953, Greensmith 1955, 1956, 1960, 1963 and 1964, Greensmith and Thomas 1955, Thomas 1955]. They proposed different geometries of specimens to calculate ‘T’ by using simple empirical relationships, and where the total energy is independent of the shape of the test piece and the manner in which the deformed forces are applied. Rice [Rice 1968] introduced a parameter called J-Integral, equivalent to G, which can be used in non-linear elasticity. All ‘G’, ‘T’ and ‘J’, allow the determination of the critical energy needed to propagate a pre-existing crack.

In fracture, when a crack grows, irreversible processes occur in the vicinity of the moving tip, leading to energy losses that must be made up from the available elastic energy [Griffith 1920, Gent 1992]. In the case of fracture of rubbers more specifically, the magnitude of these losses is determined by the properties of the rubber, the strain field at the crack tip region, and the growth rate of the crack. These losses can be large even for rubbers for which the bulk losses are negligible, such as model networks. Thus the energy necessary to propagate a crack at a particular rate is likely to be a characteristic of the rubber itself, even though it greatly exceeds the thermodynamics surface free energy, and may therefore be independent of the overall shape of the test piece [Gent 1992].

In principle the ideal crack should be very sharp but in reality the crack that is obtained for elastomers is not sharp but rather blunted, as shown in the sketch below (Figure 3.18).

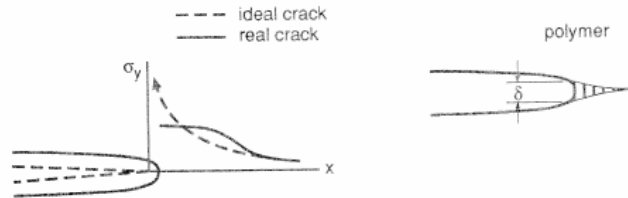


**Figure 3.18:** Sketch of crack opening in elastomers.

This kind of crack opening is also linked to the fact that the elastomers generally show non-linear elastic behaviour, in particular at the crack tip. As presented in section 3.1, this is the case for the three polyurethane model networks and in particular the PU8000. The use of Linear Elastic Fracture Mechanics (LEFM) as an approximation for the fracture experiments becomes then questionable. We used a more global approach developed specifically for fracture of rubbers [Gent 1992, Rivlin and Thomas 1953, Greensmith and Thomas 1955, Greensmith 1963], which uses the stored-energy density (the area under the stress-strain curve in a fracture experiment) as the main parameter. When a small cut is made in one edge of a test piece stretched in simple extension the change in stored elastic energy in the test piece is given by [Rivlin and Thomas 1953]:

$$W_i - W = K(\lambda)c^2hU \quad \text{eq. 3.7}$$

where  $W_i$  and  $W$  are the total stored energies before and after the cut is made,  $c$  and  $h$  are, the length of the cut and the thickness of the test piece, respectively, measured in the undeformed state,  $U$  is the stored-energy density to the extension ratio  $\lambda$  in the simple extension ratio and  $K(\lambda)$  is a numerical factor that varies with  $\lambda$ . Equation 3.7 assumes that: 1) the grip separation 'l' is kept constant, 2) 'c' is large compared with the radius of curvature of the tip of the cut, 3) 'c' is small compared with the width of the test piece, and 4) the cut is sufficiently far from the grips to affect only the central region of the simple extension.

Equation 3.7 is equivalent, in terms of strain energy, to the expression for the stress concentration produced by the cut or tear. Differentiating equation 3.7 with respect to 'c', with a constant 'l', gives the energy release rate. The value of  $K(\lambda)$  can be determined by performing experiments with different cut lengths [Rivlin and Thomas 1953, Greensmith 1963]. For a tensile strip with an edge crack,  $G$  is given by [Gent 1992]:

$$G = 2 * K * U * c \quad \text{eq. 3.8}$$

where  $G$  is the fracture energy, and  $K(\lambda)$  is a slowly varying function of the strain given approximately by

$$K = \frac{3}{\sqrt{\lambda}} \quad \text{eq. 3.9}$$

This dependence of  $K$  on extension appears to be directly associated with the lateral contraction of the test piece (and crack) in simple extension (which also goes as  $1/\sqrt{\lambda}$ ). Equations 3.8 and 3.9 were used in the experimental part to determine the energy release rate  $G$  and hence the fracture toughness  $G_c$  at the onset of crack propagation.

### ***3.3.1.1 Estimate of threshold energy for crack growth: $G_0$***

Rivlin and Thomas [Rivlin and Thomas 1953] found that two characteristic tearing energies could be defined, one for very low rates of tearing ( $37 \text{ J/m}^2$ ) and one for catastrophic growth ( $13 \times 10^4 \text{ J/m}^2$ ) and that both quantities were independent of the shape of the test piece. Later [Greensmith and Thomas 1955, Mullins 1959] reported values of tear energy ranging from about  $10^2$  to about  $10^5 \text{ J/m}^2$  determined from normal tearing experiments, and which depend upon the rate of tearing, test temperature, and elastomer composition. A threshold value for the fracture energy of elastomers was first pointed out by Lake and Lindley from studies of fatigue crack growth on noncrystallizing SBR [Lake and Lindley 1964, Lake and Lindley 1965]. They found by extrapolation that a minimum amount of mechanical energy, about  $50 \text{ J/m}^2$  of surface, was required for a crack to propagate, this value being much smaller than the values reported for normal tearing. Mueller and Knauss [Mueller and Knauss 1971] succeeded in measuring low tearing energies, independent of rate and temperature, by

employing low rates of tear, high temperatures, and a urethane elastomer composition swollen in toluene; under these near-equilibrium conditions they obtained a lower limit of about 40 J/m<sup>2</sup> for tear energy of their elastomer, in good agreement with Lake and Lindley's extrapolated value. Moreover, from a simple molecular model of the fracture process in elastomers, Lake and Thomas [Lake and Thomas 1967] calculated the theoretical threshold fracture energy for hydrocarbon elastomers, and obtained a value of about 20 J/m<sup>2</sup>. A detailed comparison between theory and experiments using two hydrocarbon elastomers differing in structural regularity was made by Ahagon and Gent [Ahagon and Gent 1975]; they observed threshold values ranging from 40 to 80 J/m<sup>2</sup>, at extremely low rates of tearing, at high temperatures, and in the swollen state. They found these values to be independent of the temperature and rate of tearing, and also on the degree of swelling and the nature of the swelling liquid.

The similarity of  $G_0$  values for different elastomers suggest that it may be governed by the primary strength of the carbon-carbon bonds.  $G_0$  is the minimum fracture energy required to start breaking bonds. An estimate of  $G_0$  can be made using equation 3.10 if it is assumed that the tip diameter has its smallest possible value, which for an elastomer is of the order of the distance between crosslinks in the unstrained state.

$$G = U_t d \quad \text{eq. 3.10}$$

where  $U_t$  is the strain energy density at the tip and 'd' is the diameter of the semicircular tip. This gives  $d \approx \xi \mu^{1/2}$ , where  $\xi$  is the length of a monomer unit and ' $\mu$ ' is the number of units between crosslinks. Assuming forces to be transmitted primarily via the crosslinks, the energy stored by the carbon-carbon bonds will be small at the breaking force of the single bonds; also, if the chains are substantially straight at rupture, the force on each bond will be essentially the same [Lake 2003, Gent 1992]. Then the maximum possible energy density will be of the order of  $bJ$ , where  $b$  is the number of single bonds per unit volume and  $J$  is the energy stored by each single bond at its rupture point. Substituting in equation 3.10 yields,

$$G_0 = bJ\xi\mu^{1/2} \quad \text{eq. 3.11}$$

Equation 3.11 [Lake and Thomas 1967], predicts for the three polyurethanes model networks  $G_0 = 11.76 \text{ J/m}^2$ , for PU4000,  $G_0 = 17.53 \text{ J/m}^2$  for PU8000 and  $G_0 = 12.54 \text{ J/m}^2$  for PU8000/1000 (as reported in Table 3.5). As predicted by Lake and Thomas the values decrease somewhat with increasing crosslinking density.

**Table 3.5:** Predicted values by Lake and Thomas for the three polyurethane model networks

Materials	$G_0$ [J/m <sup>2</sup> ]
PU4000	11.8
PU8000	17.5
PU8000/1000	12.5

### 3.3.2.- Experimental part

As mentioned in Chapter 1, a crack can propagate in a material in several modes. Our DEN test aimed at fracturing the sample in pure mode I (see Figure 3.19) out of simplicity.

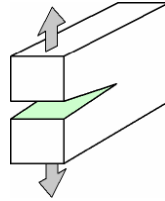
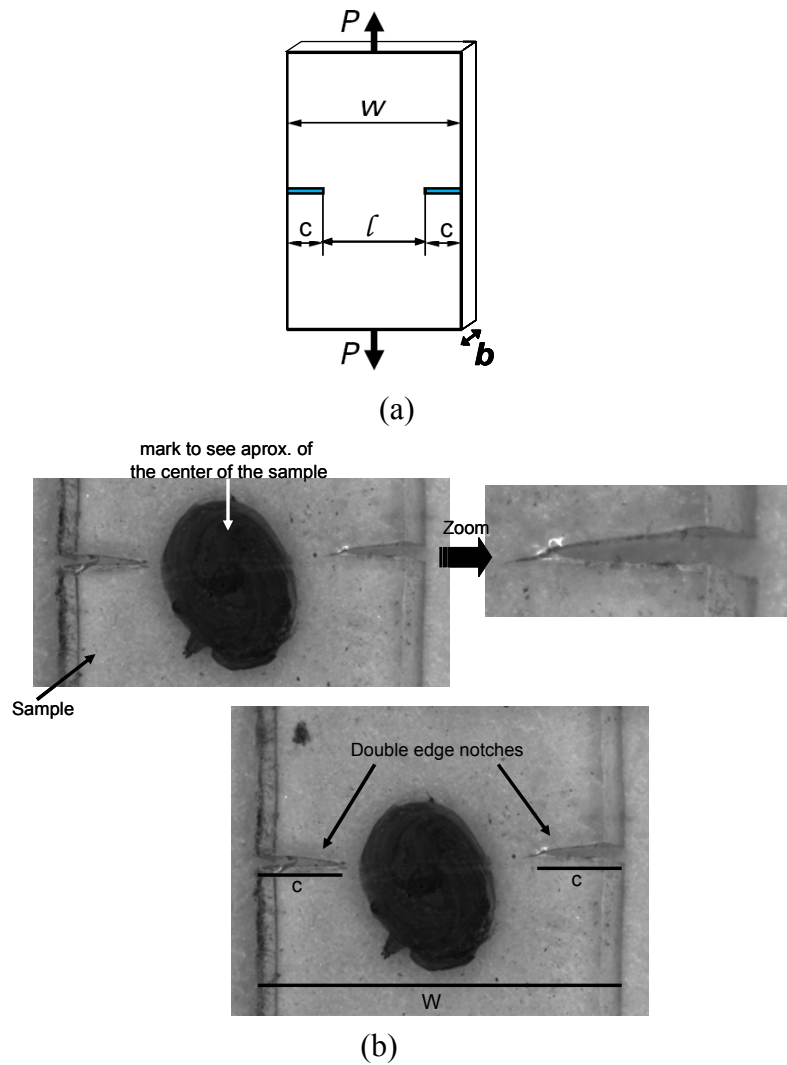


**Figure 3.19:** Mode I for crack propagation.

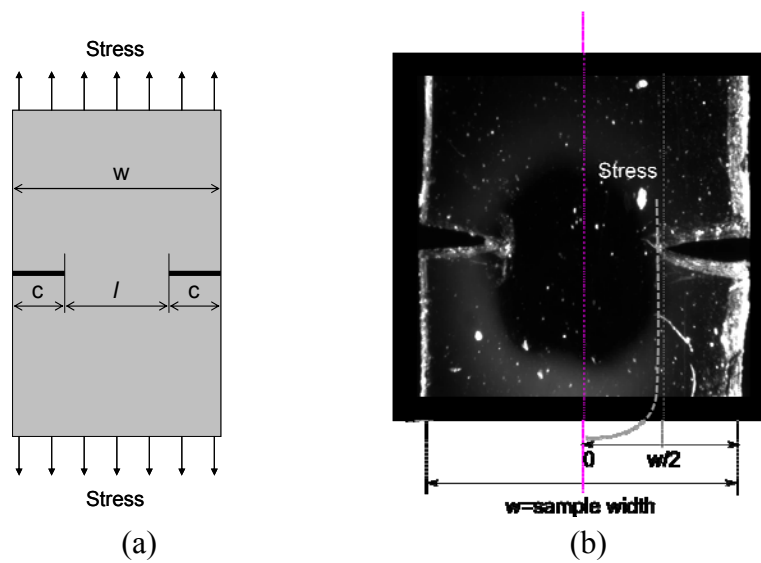
A double edge notch (DENT) geometry was used for the fracture experiments, as shown in Figure 3.20(a) while Figure 3.20 (b) shows the picture of a real sample with the double notch. This geometry was used because it was easy to obtain the samples from the molded PU sheets. The fracture experiments were performed in a DMA, model Q800 of TA instruments, in tension mode. The fracture toughness of the three polyurethane networks was first measured under standard conditions, which were defined as:  $T = 25^\circ\text{C}$  and initial strain rate of  $0.67\%/s$ , and then at different temperatures and strain rates. All fracture experiments were carried out with samples bars with dimensions of  $4 \times 30 \times 1 \text{ mm}^3$  ( $L_0 \sim 15\text{mm}$ ). For each sample  $c \leq 1 \text{ mm}$  long notch was made on each side by using a razor blade.

Figure 3.21 (a) shows the stress distribution in the far field when double edge notch (DEN) geometry is used. Figure 3.21 (b) shows the locally stress distribution close to the crack tip; it is observed that the higher stress is presented at the crack tip and the stress decreases to the center of the sample



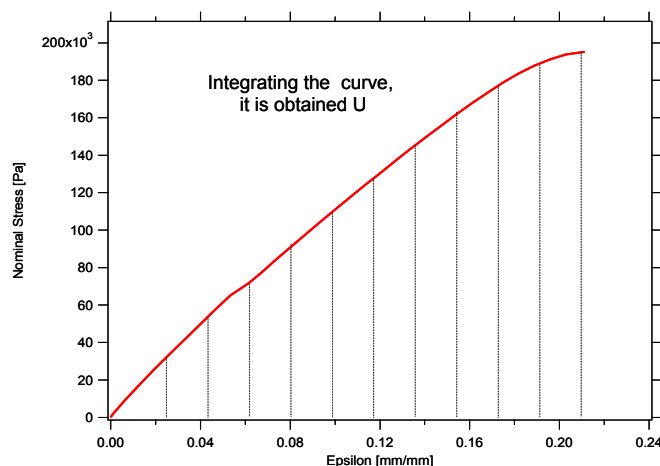


**Figure 3.20:** (a) Schematic DENT geometry; (b) Real sample showing the double edge notch.



**Figure 3.21:** Stress distribution (a) far away from the notch and (b) close to the notch.

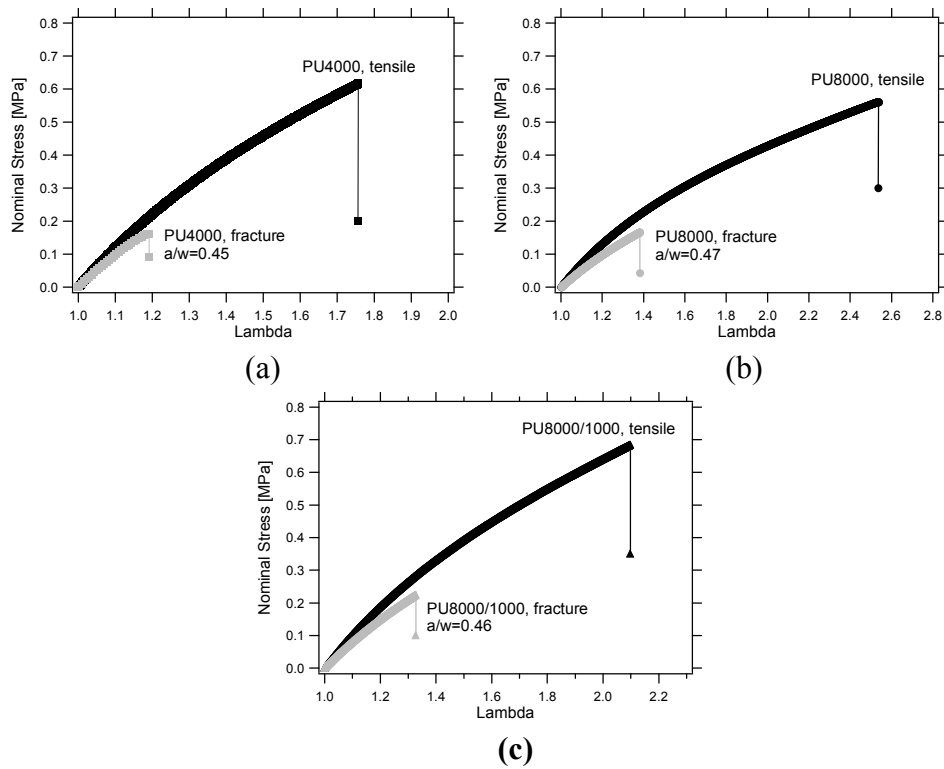
Figure 3.22 shows an example of a typical curve obtained in these fracture experiments. The integral of the curve of the nominal stress (in Pa) versus epsilon (mm/mm) gives the elastic energy density  $U$ , and the maximal value of this integral  $U_{\max}$  is used to calculate  $G_{IC}$ , using equations 3.8 and 3.9.



**Figure 3.22:** Example of a typical fracture result. After integration of this curve,  $U_{\max}$  is used to calculate  $G_{IC}$ .

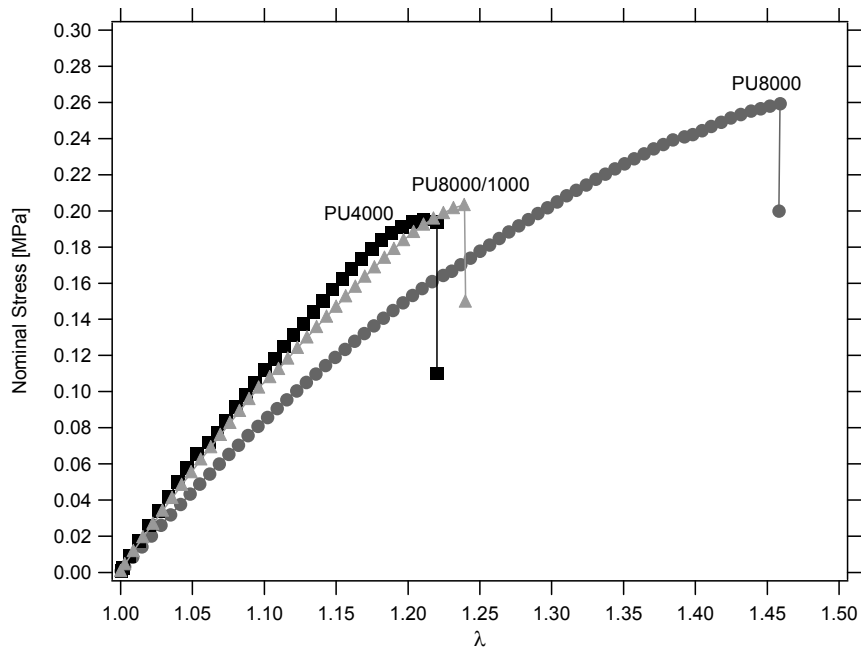
### 3.3.3.- Fracture Results at standard conditions

Figure 3.23 (a), (b) and (c), shows tensile results on unnotched samples and fracture results on notched samples for the three polyurethane model networks. The difference in the area under the curve, is related to the stored elastic energy of the material, and is given by a difference of the size of the notch.



**Figure 3.23:** Tensile results and fracture experiments at standard conditions  $T = 25^\circ\text{C}$  and  $\dot{\epsilon} = 0.67\%/s$  for (a) PU4000, (b) PU8000 and (c) PU8000/1000.

Figure 3.24 shows a comparison of the fracture results for the three networks. The difference in toughness between the PU8000 and the two other networks is apparent.



**Figure 3.24:** Fracture experiments at standard conditions,  $T = 25^\circ\text{C}$  and  $V = 0.67\%/s$ , for the three polyurethane networks (PU4000  $a/w = 0.43$ , PU8000  $a/w = 0.32$ , PU8000/1000  $a/w = 0.41$ ).

The average values of the fracture toughness  $G_{IC}$  obtained over three measurements are given in Table 3.6 for the three polyurethane networks. It is clear from the data that the fracture toughness at 25°C is much larger than the predicted threshold value. This is not unusual for elastomers but indicates that a significant amount of dissipation must take place at the crack tip for all three materials at least at 25°C. One of the reasons of this large dissipated energy lies in the strain rate.

**Table 3.6:** Fracture toughness  $G_{IC}$  obtained for the three polyurethane model networks, at standard conditions, 25°C and  $\dot{\epsilon}=0.67\%/s$ .

Materials	$G_{IC}[\text{J/m}^2]$ @25°C	$G_0 [\text{J/m}^2]$ (threshold)
<b>PU4000</b>	$136 \pm 5$	11.8
<b>PU8000</b>	$252 \pm 4$	17.5
<b>PU8000/1000</b>	$145 \pm 5$	12.5

Fowlkess [Fowlkess 1974] studied the fracture toughness of rigid polyurethane foam ( $d=87.82\text{Kg/m}^3$ ) using specimens with single-edge-notch (SENT), double-edge-notch (DENT) and centred-notch in tension; he used LEFM to calculate  $G_{IC}$ , since the polyurethane rigid foam is considered a brittle material. He obtained similar values of critical fracture toughness for all the geometries  $G_{IC}= 192.94 \pm 10\% \text{ J/m}^2$ . He compared these result with other dense cast plastics such as polyester cast and polystyrene cast, which had the same order of magnitude. Our results (as reported in Table 3.6) are comparable with the fracture toughness obtained by Fowlkess, indicating that the three polyurethane model networks are rather brittle and have relatively low  $G_{IC}$  considering that the tear energy for typical commercial filled elastomers under ‘standard conditions’ range from about  $10^2$  to about  $10^5 \text{ J/m}^2$  [Greensmith and Thomas 1955, Mullins 1959]. These values are however rather typical for unfilled and noncrystallizing rubbers.

### **Estimate of the strain rate at the crack tip**

Most of the experiments were done in the DMA (in a closed environment), and the crack propagation process was not directly observed. Some experiments were however carried out in a standard tensile Instron machine (model 5565) using a load cell of 10N with resolution of 16mN. This procedure allowed us also to film the fracture and to obtain an estimate of the crack velocity. Figure 3.25 shows an example of the sequence of images during fracture.

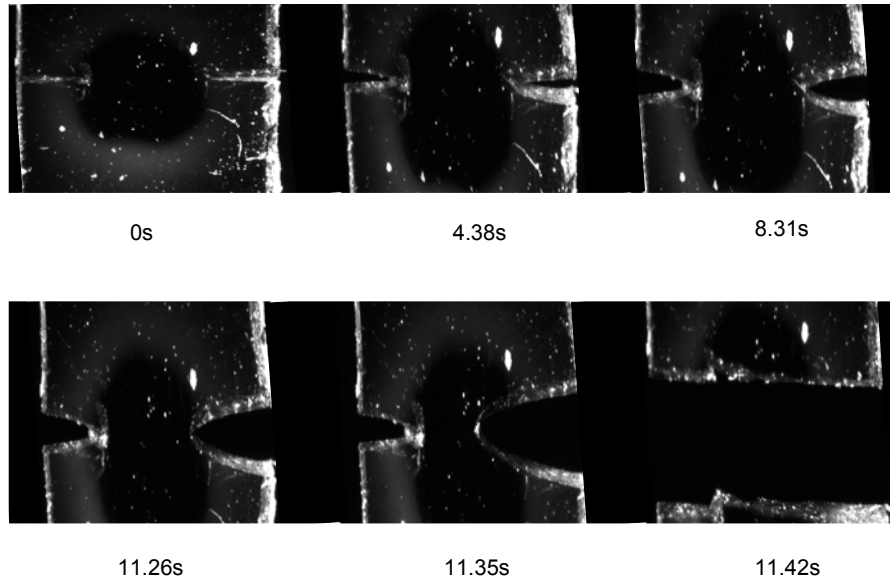


**Figure 3.25:** Sequence of images in a video during a fracture experiment for PU8000/1000. Applied strain rate 0.006%/s-Estimated local strain rate at the crack tip  $\sim 6\%/s$ .

It is interesting to estimate the actual strain rate that the material sees at the crack tip to relate the fracture results with the viscoelastic properties in the linear regime. Very close to the notch there is a stress concentration which of course decreases toward the center of the sample. A measurement of the strain field ahead of the crack tip for a similar elastomer [Mzabi, unpublished work] showed that the approximate size of the zone where the stress concentration is significant was around  $100\ \mu\text{m}$  and the maximum strain directly ahead of the crack tip was of the order of 10 times the average nominal strain. From the videos of the crack propagation, an average crack velocity could be measured and from the size and shape of the highly strained zone we could estimate the local strain rate ahead of the crack tip.

For PU8000/1000 deformed at an initial average strain rate of 0.006%/s, the local strain rate near the crack tip was estimated at  $\sim 6\%/s$ , and similar values would be expected for the other two networks. As was experimentally shown in section 3.2 (see Figure 3.17), a higher strain rate means more dissipation due to viscoelastic processes.

The crack propagation in rubber-like materials has been described and modelled by de Gennes [de Gennes 1988] and discussed by Gent [Gent 1996]. Although de Gennes' model based on scaling arguments was not easily comparable with experimental data, he argued clearly that the resistance to crack propagation was mostly due to rate dependent viscoelastic dissipative mechanisms at the crack tip and set the foundation of a methodology to calculate these viscoelastic losses. Persson *et al.* [Persson *et al.* 2005] proposed a more quantitative model to calculate the crack propagation energy (per unit area)  $G$  from the linear viscoelastic properties of the rubber and argued, contrary to Gent, that the observed results could be explained without considering nonlinear deformations very close to the crack tip.

In an effort to establish a lower bound on the fracture energy ( $G_0$ ), one is then led to investigate the fracture process at temperatures well above the glass transition temperature

and at crack velocities approaching zero. Experimentally this can be difficult; the question is whether the true limit below which propagation is impossible has been reached. The maximum test temperature is limited by the possibility of thermal degradation of the material [Mueller and Knauss 1971]. Within the frame of these limitations it may be possible however to observe experimentally the lower bound of fracture energy. For us finding the threshold energy ( $G_0$ ) was also important to use it as an input parameter for the cavitation model presented in Chapter 6.

### 3.3.4.- Fracture Results at different temperatures

The fracture toughness of the three networks was also measured at 50°C, 70°C and 100°C. Figure 3.26 shows typical curves (in this case for PU4000) of fracture experiments carried out at different temperatures. In all cases the fracture was uncontrolled and brittle but the values of the fracture stress (and strain) sharply decrease with increasing temperature, while the modulus (the slope of the curves) increases with temperature due to thermoelasticity. This behaviour was observed for all three materials and the curves for PU8000 and PU8000/1000 are presented in Appendix A3.4.

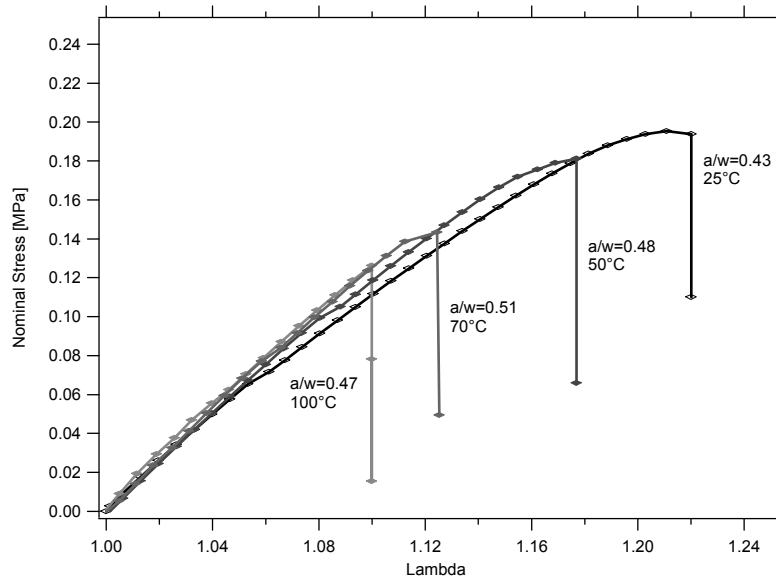


**Figure 3.26:** Fracture experiments at different temperatures. Example given for PU4000.

Table 3.7 shows the fracture toughness  $G_{IC}$  of each material at different temperatures as obtained from the peak stress and calculated from equation 3.8 and 3.9. These results are presented graphically in Figure 3.27 and clearly show that for higher temperature the fracture toughness decreases significantly suggesting that the viscoelastic dissipation processes at the crack tip decrease. Interestingly even at 100°C, there is no evidence of a plateau and it is not clear that a threshold value has been reached. Unfortunately time constraints prevented us from carrying out more experiments at higher temperatures and we will have to assume that the 100°C values are close to the  $G_0$  threshold values.

**Table 3.7:** Values of fracture toughness  $G_{IC}$  obtained for the three polyurethane model networks at different temperatures

Materials	Temperature[°C]	$G_{IC}[J/m^2]$
<b>PU4000</b>	25	$136 \pm 5$
	50	$104 \pm 4$
	70	$60 \pm 4$
	100	$41 \pm 4$
<b>PU8000</b>	25	$252 \pm 4$
	50	$140 \pm 6$
	70	$106 \pm 7$
	100	$66 \pm 3$
<b>PU8000/1000</b>	25	$145 \pm 5$
	50	$94 \pm 5$
	70	$58 \pm 6$
	100	$39 \pm 2$

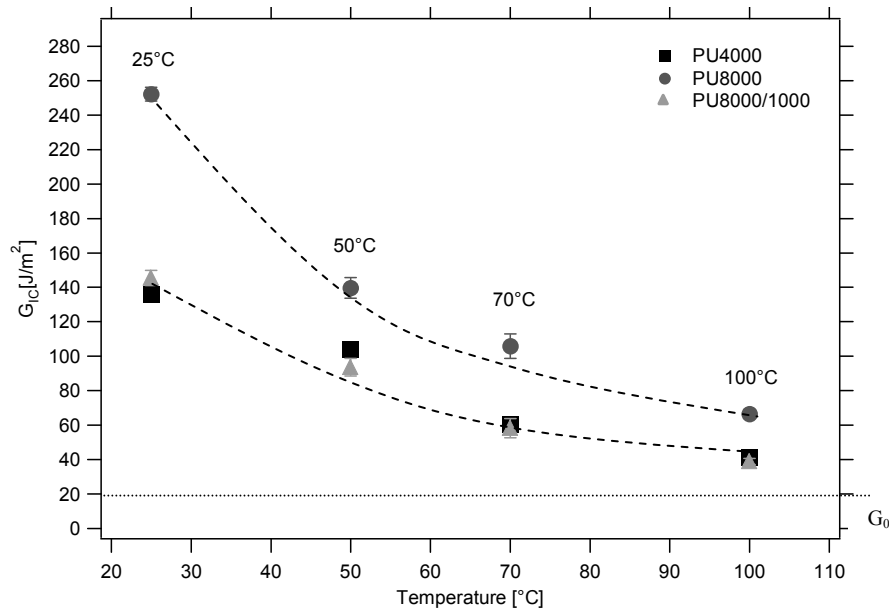


**Figure 3.27:** Fracture energy  $G_{IC}$  as a function of temperature for PU4000, PU8000 and PU8000/1000.

### 3.3.5.- Fracture Results at different speeds

In 1953 Rivlin and Thomas [Rivlin and Thomas 1953] established an energy criterion for fracture of nonlinear elastic rubbers with the same form as the fracture criterion for linear elastic materials derived by Griffith [Griffith 1920] on the basis of the energy conservation. Later it was shown by Greensmith and Thomas [Greensmith and Thomas 1955] that, if this

criterion is extended to propagating cracks, the fracture energy becomes a monotonically increasing function of the rate of propagation. Since the energy dissipation caused by the viscoelasticity of the material is included in the fracture energy, the question that arises is how much of the rate dependence of the fracture energy is solely attributed to viscous energy dissipation around the crack tip and how much is rate sensitivity of the bulk material, if any [Mueller and Knauss 1971].

The fracture toughness was measured for the three networks at different average initial strain rates (the crosshead velocity was kept at a constant value), which were: 0.067%/s, 0.0067%/s and 0.00067%/s, at 25°C. Figure 3.28 shows a typical curve (PU4000) of fracture experiments carried out at different strain rates. Similar trends are observed for the other two materials and results are presented in Appendix A3.4. It is clear that the fracture toughness of the network depends strongly on the applied strain rate suggesting the existence of crack tip dissipation mechanisms at high strain rates.

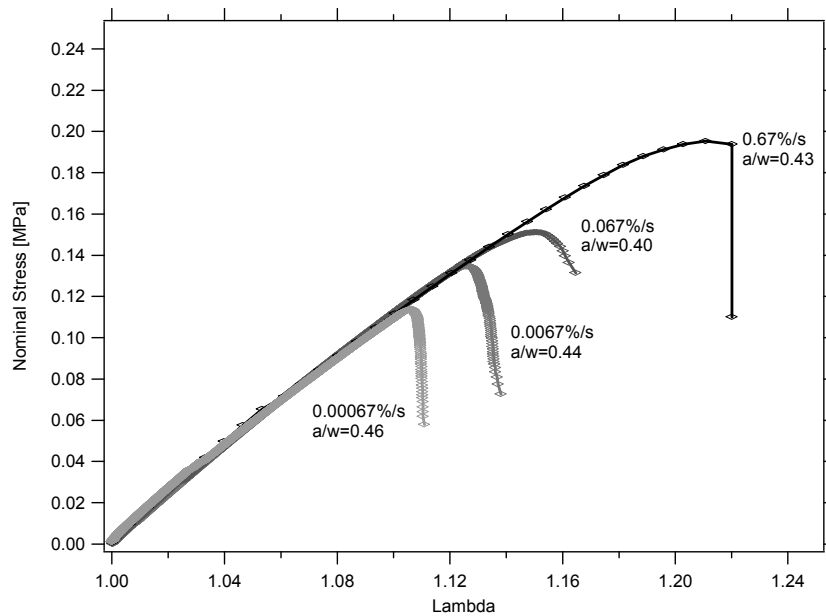


**Figure 3.28:** Fracture experiments at different strain rates for PU4000.

Table 3.8, shows the value of  $G_{IC}$  calculated from the peak stress by using equations 3.8 and 3.9 and the same results are presented graphically on Figure 3.29. They show that for lower strain rates the fracture toughness decreases significantly.

This rate effect is large and strongly suggests that significant rate dependent dissipative mechanisms exist at the crack tip, deserving further analysis. The comparison of the temperature and rate effects qualitatively suggest the existence of a time temperature equivalence observed by others. A simple way to check such an equivalence is to use the shift factors determined in linear viscoelasticity to shift the results obtained at different temperatures along the frequency scale. This has been done in Figure 3.30 and the results demonstrate conclusively that for all three materials, while linear viscoelastic shift factor goes qualitatively in the right direction, it does not lead to master curves. We can deduce from this



that the temperature dependence of the relaxation mechanisms active at the crack tip is much more complex than a simple Arrhenius or WLF dependence and may depend on strain level. Since we do not have a series of experiments at different strain rates and temperatures it is impossible to go further at this stage.

**Table 3.8:** Values of fracture energy  $G_{IC}$  obtained for PU4000, PU8000 and PU8000/1000 at different strain rates

Materials	Strain rate[%/s]	$G_{IC}$ [J/m <sup>2</sup> ]
<b>PU4000</b>	0.67	$136 \pm 5$
	0.067	$89 \pm 4$
	0.0067	$51 \pm 4$
	0.00067	$43 \pm 1$
<b>PU8000</b>	0.67	$252 \pm 4$
	0.067	$117 \pm 4$
	0.0067	$76 \pm 1$
	0.00067	$53 \pm 1$
<b>PU8000/1000</b>	0.67	$145 \pm 5$
	0.067	$90 \pm 1$
	0.0067	$56 \pm 1$
	0.00067	$38 \pm 2$

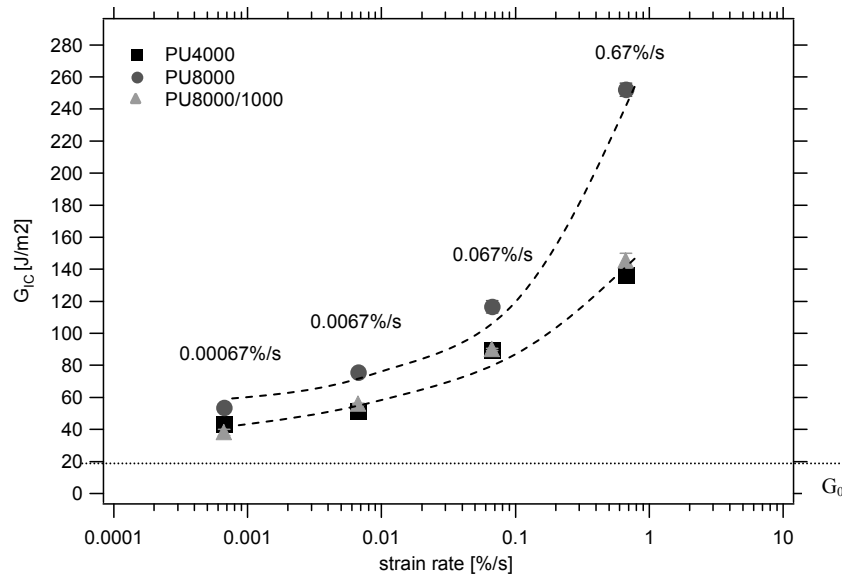


**Figure 3.29:** Fracture energy  $G_{IC}$  as a function of the strain rate for PU4000, PU8000 and PU8000/1000.

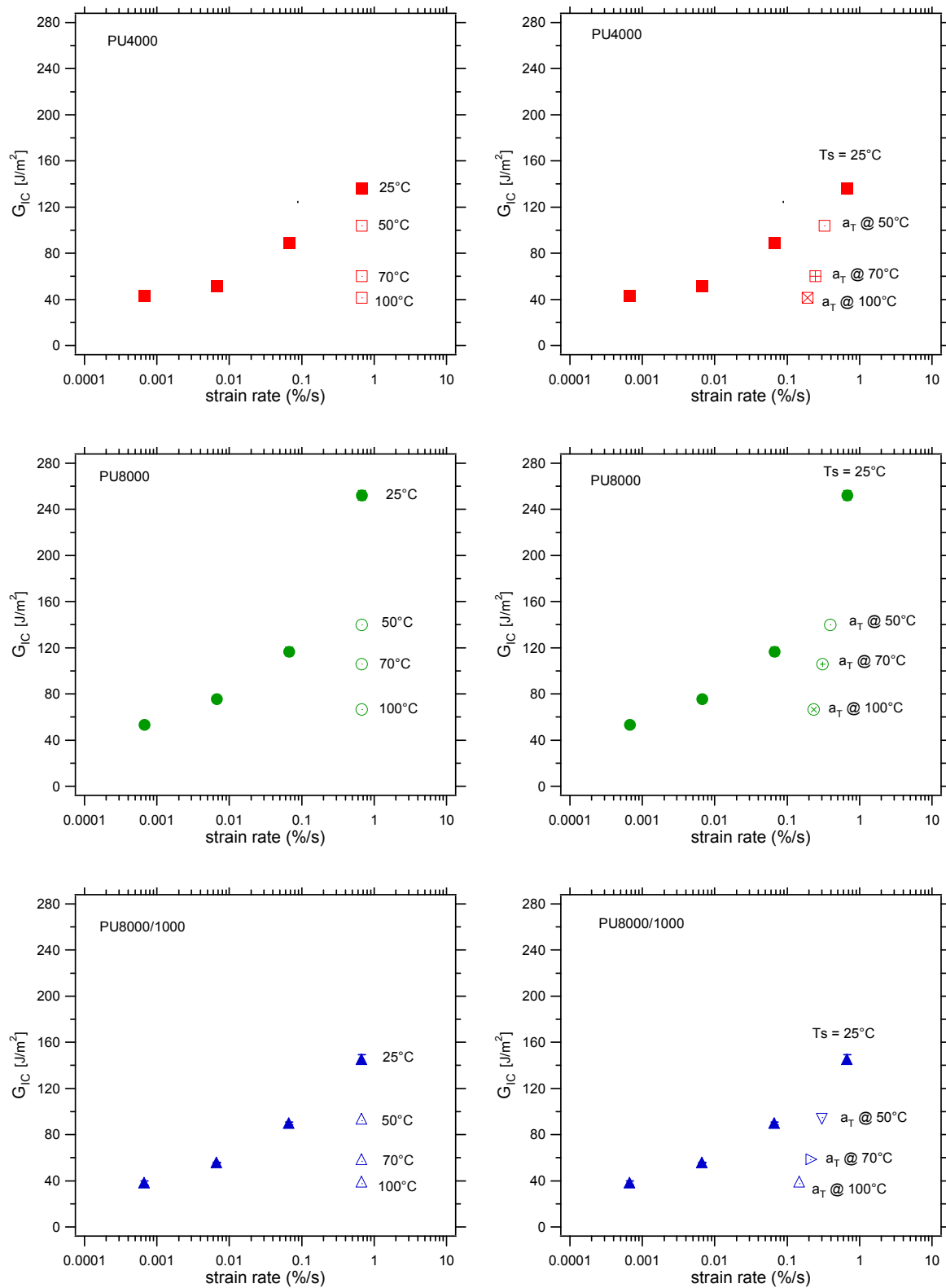


**Figure 3.30:** Summary of fracture experiments. Right captions (open symbols) show temperature results shifted by the experimental values of  $a_T$  obtained in section 3.2.

The predicted threshold  $G_0$  values from the Lake-Thomas theory for the three polyurethane networks (see Table 3.5) are much lower than the lowest values measured experimentally for

$G_{IC}$  at 100°C and at 0.00067%/s. Then, either the values obtained are not yet the threshold values of the materials, or the prediction is underestimating the actual values because it does not take into account the entanglements and other possible complex properties of these particular materials (such as hydrogen bondings).

Indeed for most elastomers, including these polyurethanes networks, the minimal value of tear strength than can be measured is much greater than a theoretical value of  $G_0$ . The discrepancy may be due to the nonlinear viscoelastic behaviour (e.g. entanglements) of the material at the crack tip.

As was mentioned before, the threshold fracture energies measured experimentally by Ahagon and Gent [Ahagon and Gent 1975] for polybutadiene elastomers, at very low rates and high temperatures range from 40 to 80 J/m<sup>2</sup>, and these values are in good agreement with our experimental results at high temperature and at low speed (see Tables 3.7 and 3.8). Also the results of Mueller and Knauss [Mueller and Knauss 1971] for polyurethane elastomers, and Lake and Lindley [Lake and Lindley 1965] for a variety of elastomers from fatigue crack studies, are in good agreement with our range of results. As was mentioned before we will have to assume that either the 100°C or the 0.00067%/s values are close to the  $G_0$  threshold values.

Alternative expressions that we did not use in this Thesis were reported by Mazich *et al.* [Mazich *et al.* 1991]. He presented the threshold fracture energy for several lightly cross-linked PDMS networks, and proposed two alternative expressions for  $G_0$  based on the role of trapped entanglements on the fracture mechanism.

To summarize our results in a single graph, Figure 3.31 shows the critical fracture energy at different temperatures and different strain rates as a function of the elastic modulus  $E'$ , for the three polyurethane model networks. We can observe that there is no obvious correlation between toughness and modulus, which is hardly surprising but will be interesting to compare to the cavitation resistance data where the conventional wisdom predicts a resistance to cavitation scaling with the elastic modulus.

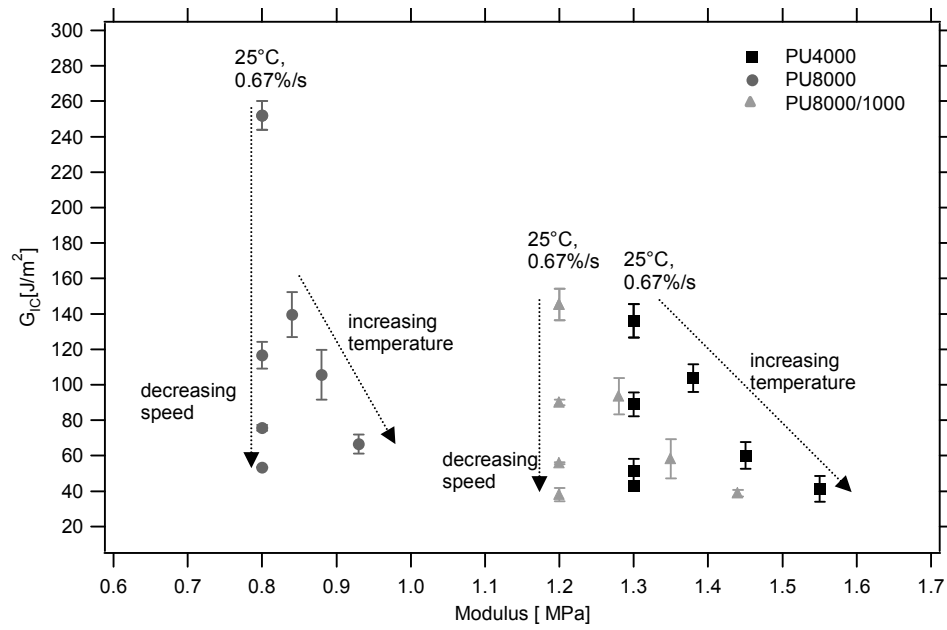


**Figure 3.31:** Fracture energy for different temperatures and different speeds as a function of the modulus for the three polyurethane model networks.

## Conclusions

The mechanical properties of the three model networks were investigated in detail in this chapter. Several conclusions can be drawn from these results:

### On the tensile properties and the effect of entanglements

- The tensile tests showed that the three model networks are brittle rubbers, as expected for very elastic materials. The Mooney plot revealed low (PU8000/1000) or no (PU4000) level of softening, except for the PU8000 where a fit to the Rubinstein-Panyukov model implied ~20% of contribution of entanglements to the modulus.

### On the finite extensibility

- Compression experiments showed that the three model networks strain harden. By using an 'exponential' model (two parameters) the fitting of the tensile and compression data was possible, implying that our lubricated compression experiments were carried out properly. This model predicted quite well the compression data and since the last is representative of the biaxial extension which is equivalent to the inflation of a cavity, the exponential model is considered a good approximation to predict the strain hardening.

### On the Fracture properties

- The fracture energies  $G_{Ic}$  decrease significantly with increasing temperature and decreasing strain rate. These results were not expected for such elastic materials, implying that significant viscoelastic dissipation is active at the crack tip. The PU8000 was tougher than the two other networks at all temperatures, qualitatively consistent with the higher level of viscoelastic dissipation at high strain rate observed for PU8000 and PU8000/1000 than for PU4000.
- The lowest values of  $G_c$  measured (at high temperature or at very low strain rate) were probably close to threshold values and hence representative of the fracture of the network strands without much contribution of viscoelasticity.

## Appendices A3

### Appendix A3.1: Time-Temperature Superposition for PU4000

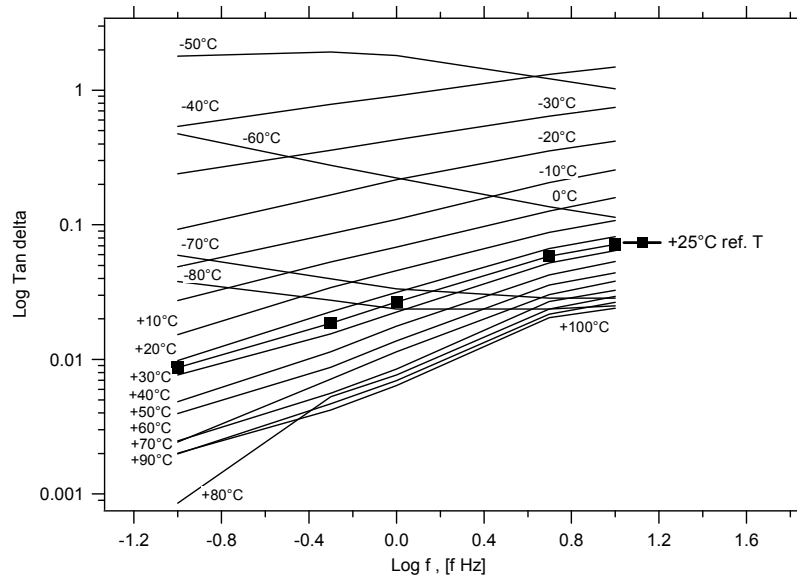


**Figure A3.1:** Variation of  $\tan \delta$  in function of the frequency for a range of temperatures between -80 to +100 °C, for PU4000.

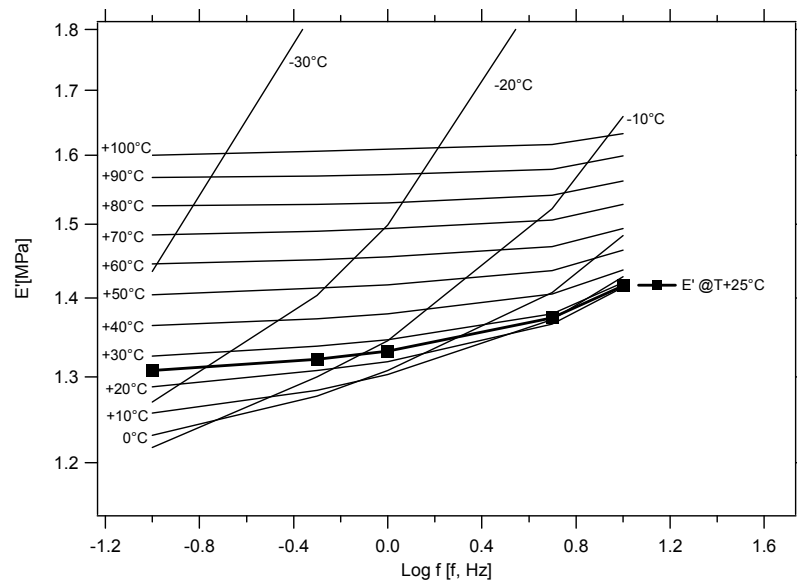


**Figure A3.2:** Variation of storage modulus in function of the frequency for PU4000. It is shown only the range between -30°C to +100°C.

Graphically, it was obtained an offset in x axis and this was used to build up the master curve of  $\tan \delta$  (where only horizontal shift is made) and this shift is reported in Table A3.1. To build up the master curve of the storage modulus a vertical shift was made and it is reported also in Table A3.1 as  $\nu_T$ .

**Table A3.1:** Values of  $\text{Log } a_T$ ,  $a_T$  and  $v_T$ , for each temperature, for PU4000.

Temperature [°C]	Log $a_T$	$a_T$	$v_T$
-80	14.43	$26.91 \cdot 10^{13}$	-756.49
-70	12.23	$16.98 \cdot 10^{11}$	-737.58
-60	10.08	$12.02 \cdot 10^9$	-272.29
-50	7.15	$14.12 \cdot 10^6$	12.368
-40	4.71	$51.28 \cdot 10^3$	0.3567
-30	3.33	$21.37 \cdot 10^2$	0.2756
-20	2.23	169.82	0.1715
-10	1.49	30.90	0.1388
0	1.03	10.71	0.1058
+10	0.49	3.09	0.0578
+20	0.12	1.32	0.0221
+25	0	1	0
+30	-0.18	0.66	-0.0208
+40	-0.43	0.37	-0.0609
+50	-0.62	0.24	-0.1025
+60	-0.77	0.17	-0.1427
+70	-0.87	0.13	-0.1829
+80	-0.95	0.11	-0.2218
+90	-1.01	0.098	-0.2621
+100	-1.09	0.081	-0.3009

In Figure A3.3, is presented the results as  $y=(T_s-T)/\text{Log } a_T$  versus  $x=T-T_s$ .

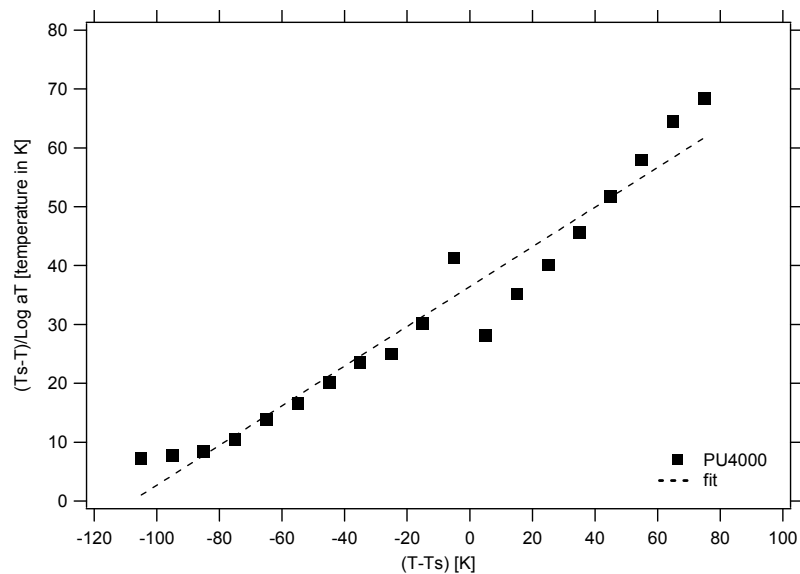


**Figure A3.3:** WLF equation at temperatures between -80 to +100°C, for PU4000.

### Appendix A3.2: Time-Temperature Superposition for PU8000

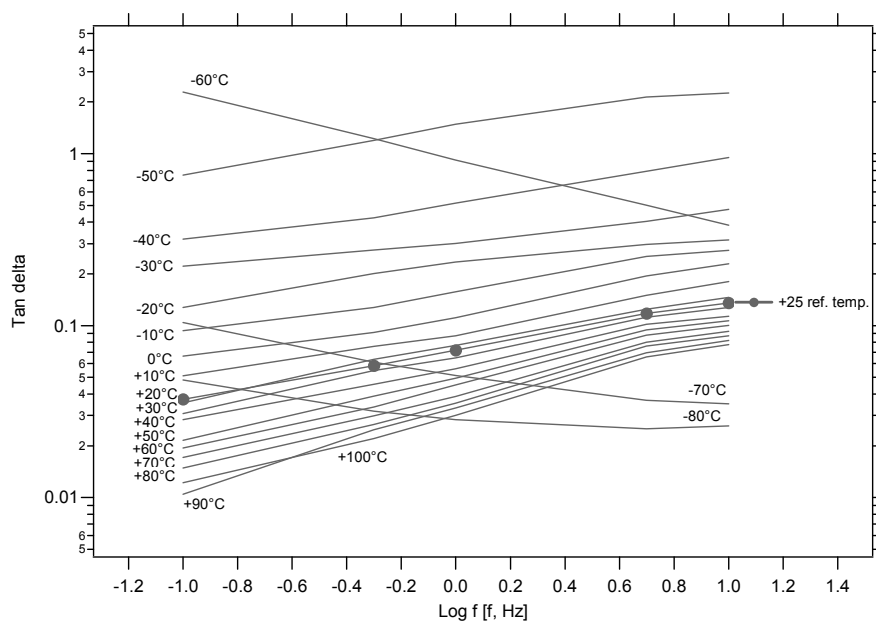


**Figure A3.4:** Variation of tan delta in function of the frequency for a range of temperatures between -80 to +100 °C, for PU8000.



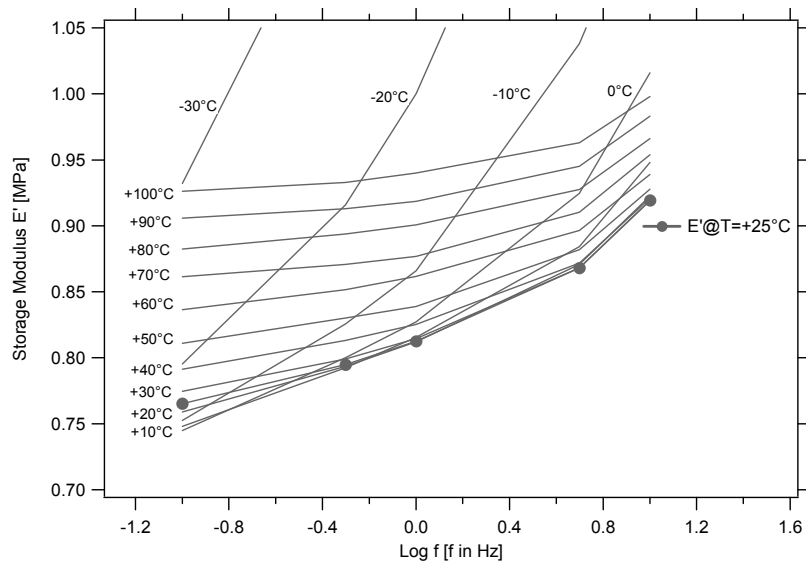


**Figure A3.5:** Variation of storage modulus in function of the frequency for PU8000. It is shown only the range between -30°C to +100°C.

The horizontal and vertical shifts are reported in Table A4.2.

**Table A3.2:** Values of Log  $a_T$ ,  $a_T$  and  $v_T$ , for each temperature, for PU8000.

Temperature [°C]	Log $a_T$	$a_T$	$v_T$
-80	12.13	$13.61 \cdot 10^{11}$	-934.76
-70	10.09	$12.30 \cdot 10^9$	-1035.82
-60	7.48	$3.06 \cdot 10^7$	-32.417
-50	5.5 1	$3.19 \cdot 10^5$	0.4633
-40	3.88	$7.5 \cdot 10^3$	0.2102
-30	2.74	$5.5 \cdot 10^2$	0.1424
-20	1.83	68.23	0.0909
-10	1.29	19.72	0.0875
0	0.81	6.53	0.0633
+10	0.41	2.55	0.0354
+20	0.099	1.26	0.0118
+25	0	1	0
+30	-0.137	0.73	-0.0140
+40	-0.366	0.43	-0.0377
+50	-0.467	0.34	-0.0573
+60	-0.568	0.27	-0.0814
+70	-0.677	0.21	-0.1021
+80	-0.772	0.17	-0.1264
+90	-0.837	0.15	-0.1491
+100	-0.916	0.12	-0.1705

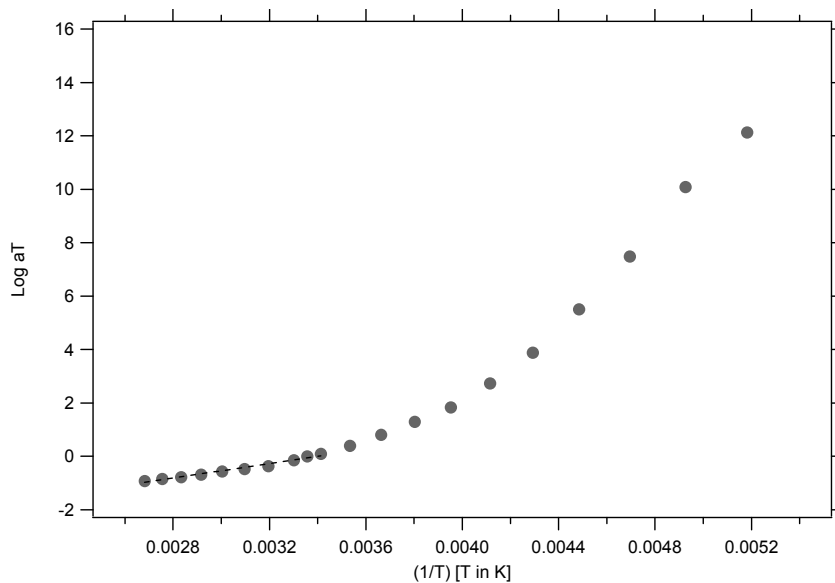


**Figure A3.6:** Log  $a_T$  versus the inverse of the temperature ( $1/T$ ), at temperatures between  $-80$  and  $+100^\circ\text{C}$ , for PU8000.

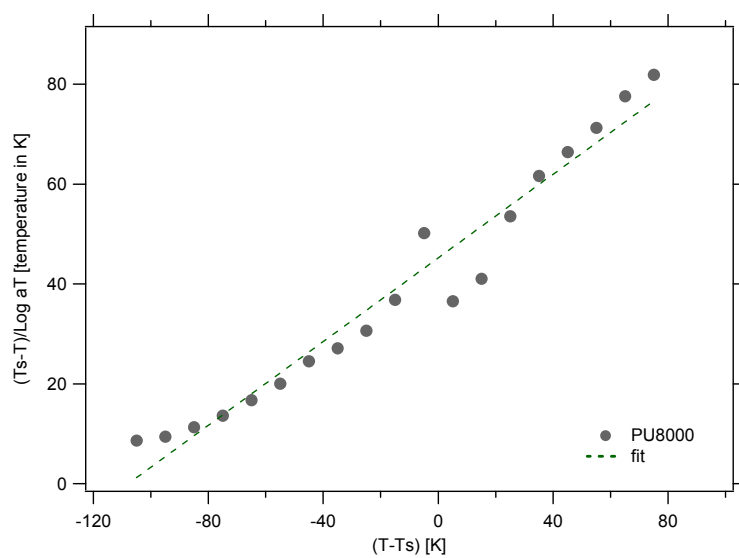


**Figure A3.7:** WLF equation at temperatures between  $-80$  to  $100^\circ\text{C}$ , for PU8000.

### Appendix A3.3: Time-Temperature Superposition for PU8000/1000.

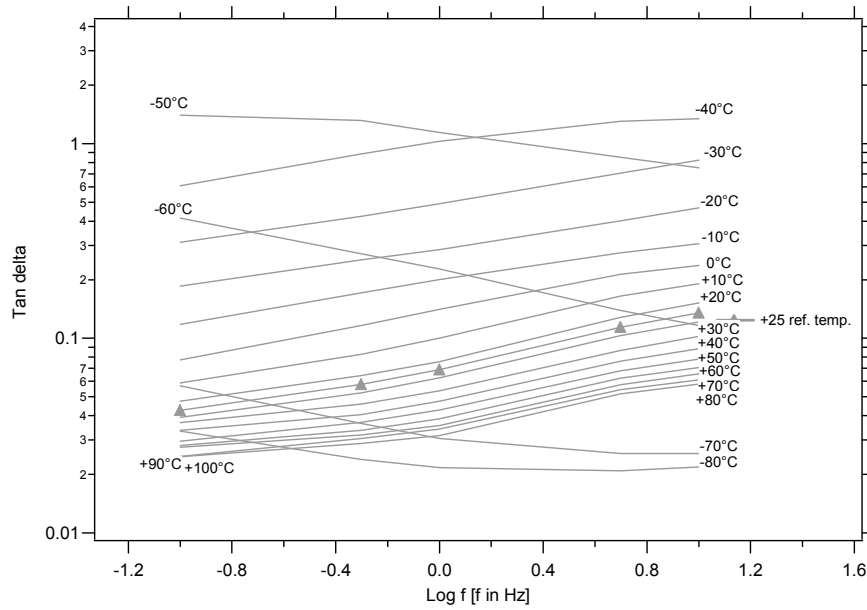


**Figure A3.8:** Variation of tan delta in function of the frequency for a range of temperatures between -80 to +100 °C, for PU8000/1000.

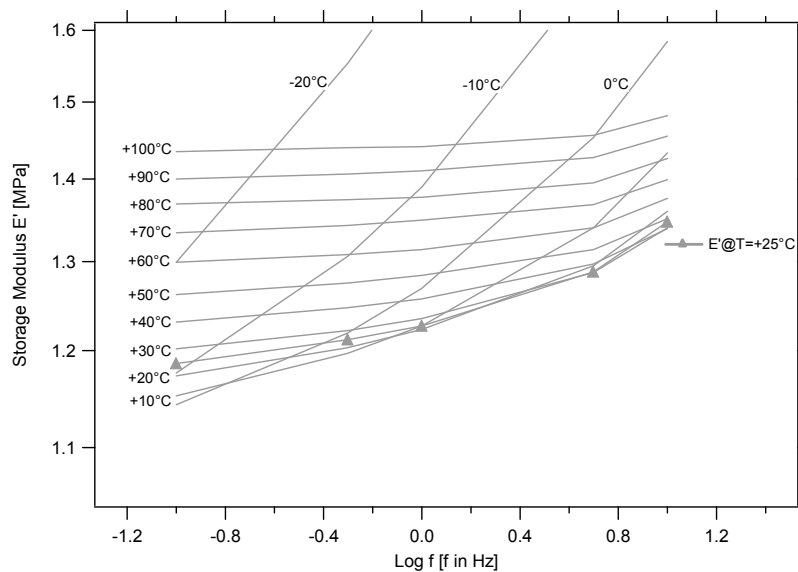


**Figure A3.9:** Variation of storage modulus in function of the frequency for PU8000/1000. It is shown only the range between -20°C to +100°C.

**Table A3.3:** Values of  $\text{Log } a_T$ ,  $a_T$  and  $v_T$ , for each temperature, for PU8000/1000.

Temperature [°C]	Log $a_T$	$a_T$	$v_T$
-80	15.34	$21.80 \cdot 10^{14}$	-561.27
-70	13.19	$15.58 \cdot 10^{12}$	-491.78
-60	10.43	$26.73 \cdot 10^9$	-294.03
-50	7.67	$46.97 \cdot 10^6$	37.42
-40	5.13	$13.42 \cdot 10^4$	0.3015
-30	3.71	$5.1 \cdot 10^3$	0.3203
-20	2.59	389.49	0.2395
-10	1.75	56.86	0.0858
0	1.15	14.17	0.1027
+10	0.646	4.43	0.0583
+20	0.202	1.59	0.0207
+25	0	1	0
+30	-0.183	0.65	-0.0206
+40	-0.466	0.34	-0.0541
+50	-0.689	0.20	-0.0878
+60	-0.862	0.14	-0.1236
+70	-0.975	0.11	-0.1607
+80	-1.099	0.08	-0.1920
+90	-1.234	0.06	-0.2278
+100	-1.312	0.05	-0.2612

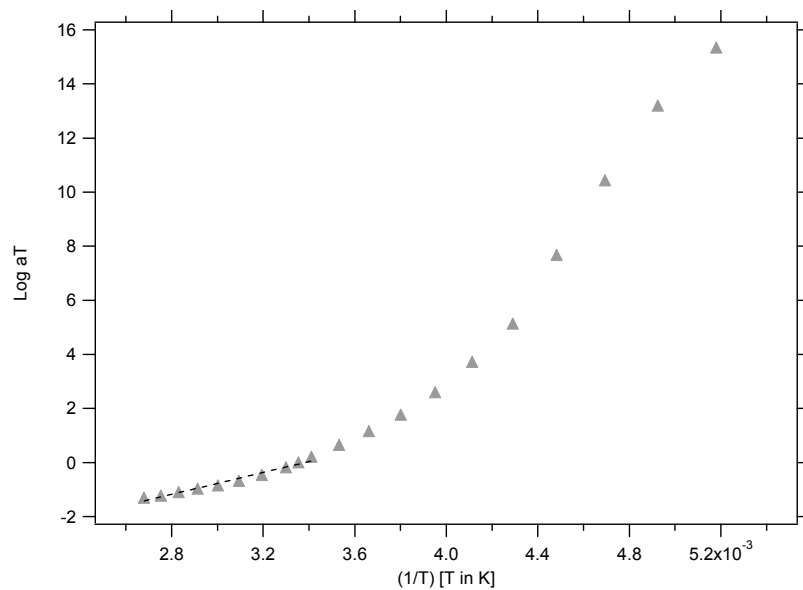


**Figure A3.10:**  $\text{Log } a_T$  versus the inverse of the temperature ( $1/T$ ), at temperatures between -80 and +100°C, for PU8000/1000.

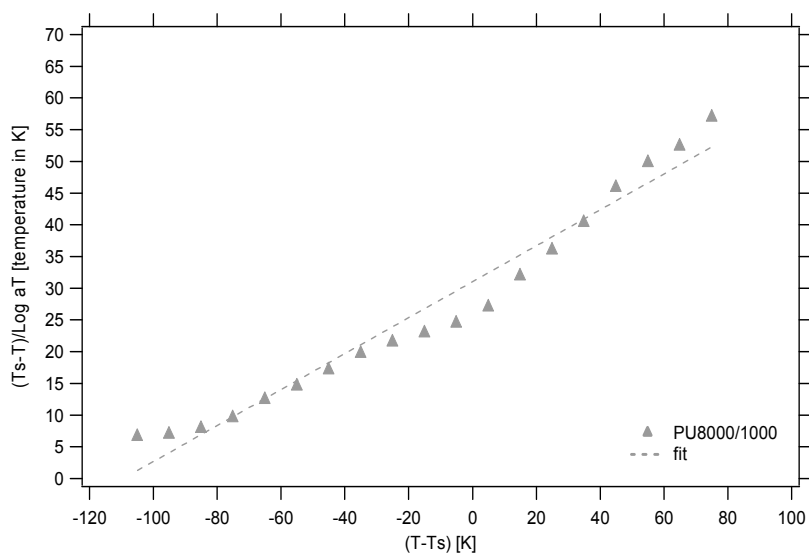


**Figure A3.11:** WLF equation at temperatures between -80 to 100°C, for PU8000/1000.

### Appendix A3.4: Fracture results

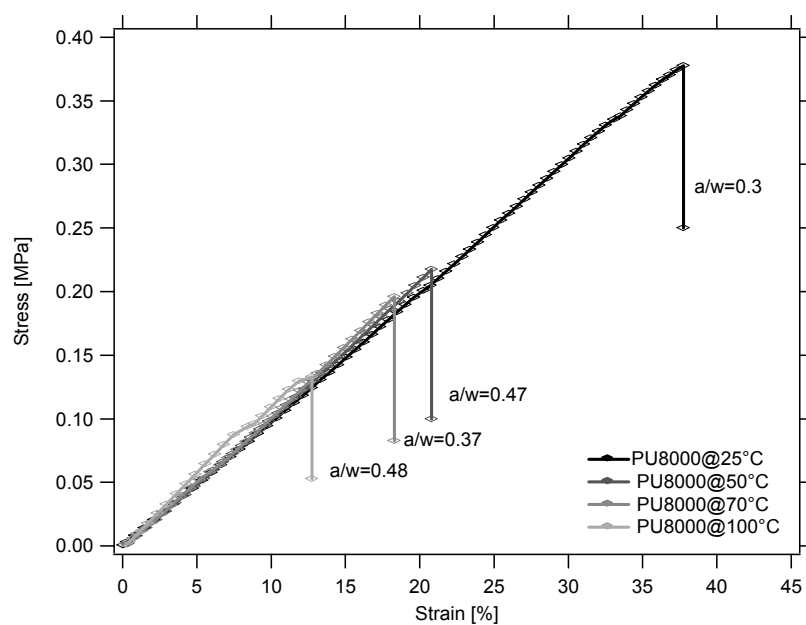


**Figure A3.12:** Fracture experiments at different temperatures for PU8000.

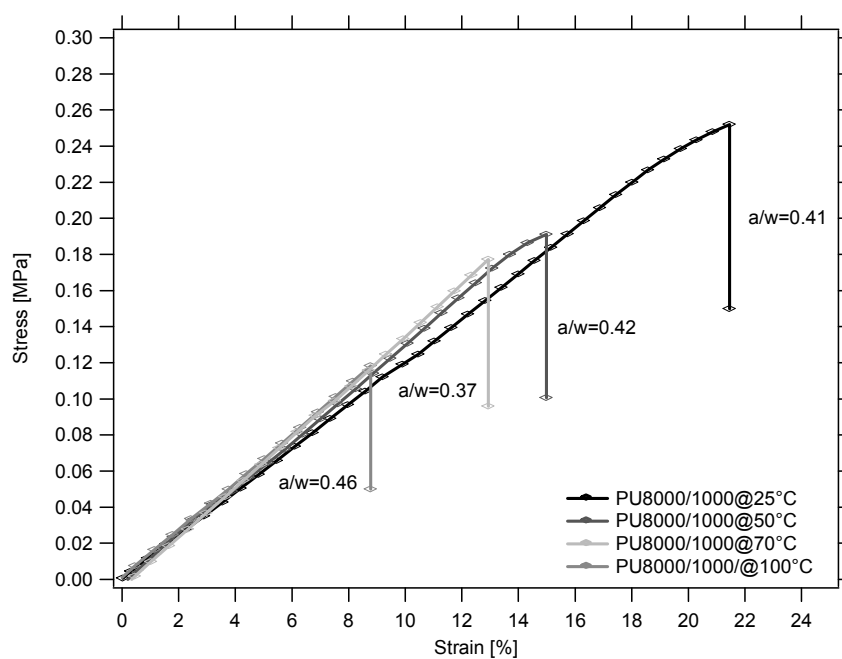


**Figure A3.13:** Fracture experiments at different temperatures for PU8000/1000.

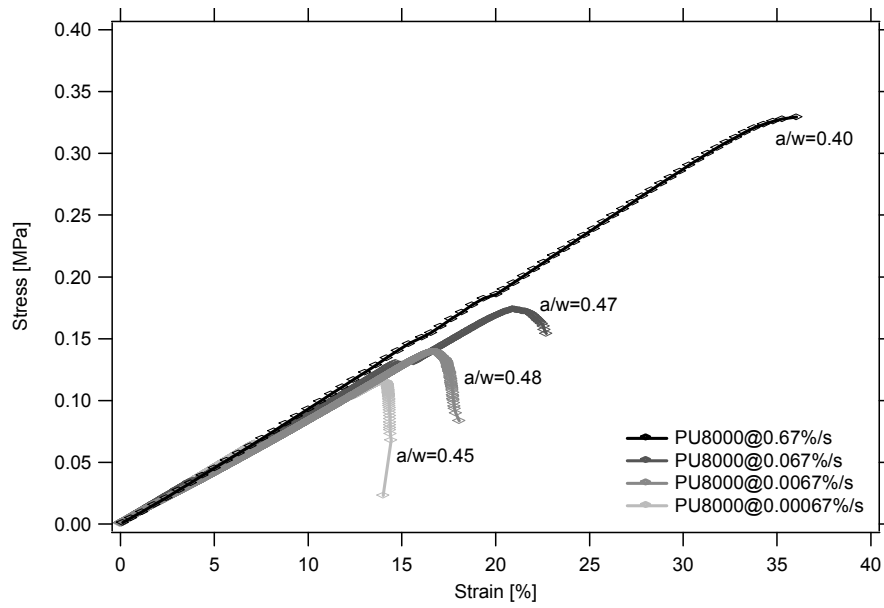


**Figure A3.14:** Fracture experiments at different speeds for PU8000

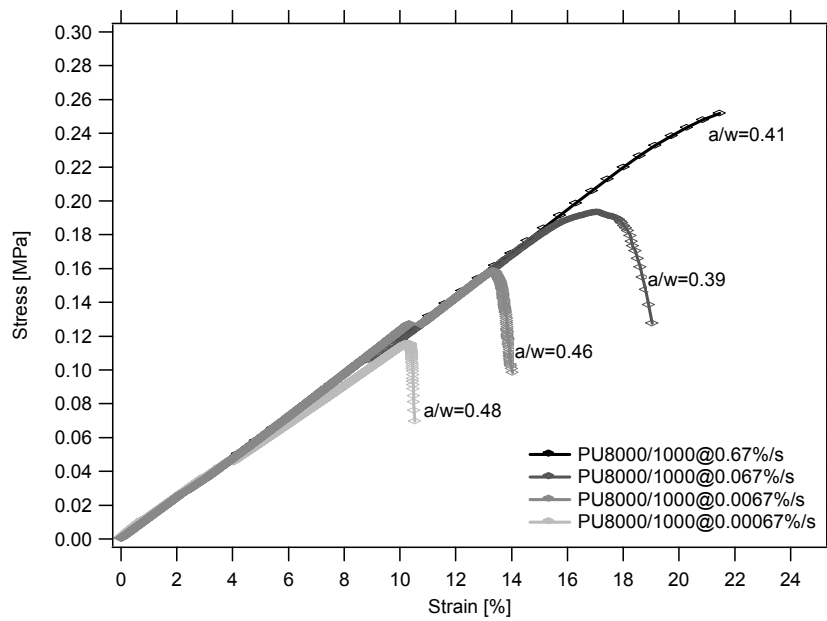


**Figure A3.15:** Fracture experiments at different speeds for PU8000/1000.

## Bibliography

- Ahagon, A. and Gent, A.N, Journal of Polymer Science: Polymer Physics Edition, 13, 1903-1911 (1975)
- Alkonis, J.J., Maxknight, W.J. and Shen, M., Introduction to polymer viscoelasticity, Wiley–Interscience/Wiley, New York (1972).
- Arruda, E.M. and Boyce, M.C., Journal of the Mechanics and Physics of Solids, 41, 2, 389-412 (1993)
- Bueche, F., Physical Properties of Polymers, Interscience, New York (1962)
- Bueche, F. and Halpin, J.C., Journal of Applied Physics, 35, 36-40 (1964).
- de Gennes, P. G. C. R. Acad. Sci. Paris,II 307, 1949-1953 (1988).
- Dickie R.A. and Smith T.L., Journal of Polymer Science, Part. A2, 7, 687-707 (1969).
- Edwards, S.F. and Vilgis, T.A., Reports on Progress in Physics, 51, 2, 243-297 (1988)
- Florez, S., Muñoz, M.E. and Santamaría, A., Macromolecules Materials Engineering, 291, 1194-1200 (2006).
- Fowlkes, C., International Journal of Fracture, 10, 99-108 (1974).
- Gent, A. N., Engineering with Rubber, USA (1992).
- Gent, A.N., Rubber Chemistry and Technology, 69, 59-61 (1996).
- Gent, A. N. *Langmuir*, 12, 4492-4496 (1996).
- Gent, A.N., Rubber Chemistry and Technology, 67, 549-558 (1994)
- Greensmith, H.W. and Thomas, A.G., Journal of Polymer Science XVIII, 189 (1955)
- Greensmith, H.W., Journal of Polymer Science, 21, 175–87 (1956).
- Greensmith, H.W., Journal of Polymer Science, 3(8), 175–82 (1960).
- Greensmith, H.W., Journal of Polymer Science, 3(8), 183–93 (1960).
- Greensmith, H.W., Journal of Applied Polymer Science, 7, 993-1002 (1963)
- Greensmith, H.W., Journal of Polymer Science, 8, 1113–28 (1964).
- Griffith, A.A., Phil. Trans. R. Soc., A221, 163-198 (1920).
- Halary, J.L. and Lauprête, F., De la macromolécule au matériau polymère, editions Belin (2006).
- Halary, J.L., Lauprête, F. and Monnerie, L., Mécanique des matériaux polymères, editions Belin (2008).
- Hamdi, A., Université des Sciences et Technologies de Lille, Laboratoire de Mécanique de Lille UMR, PhD thesis (2006)
- Hiemenz, P. C., and Timothy P. L., Polymer Chemistry. 2nd ed. Florida: Taylor & Francis Group, 486-491 (2007).
- Kawabata, S., Journal Macromolecular. Science Physics, B8(3-4), 605-630 (1973).
- Lake, G. J. and Lindley, P.B., Rubber Journal, 146 (10), 24-30 (1964).
- Lake, G.J. and Lindley, P.B., J. Appl. Polym. Sci., 9, 1233-1251 (1965).
- Lake, G.J. and Thomas, A.G., Proc. R. Soc. London, Ser. A, 300, 108 (1967).
- Lake, G.J., Rubber Chemistry and Technology, 76, 567-591 (2003).
- Mars, W.V. and A. Fatemi, A., D. Besdo, R. Schuster, J. Ihlemann (eds.), Swets and Zeitlinger, Netherlands, 213-222 (2001).



- Mars, W.V., Rubber Chemistry and Technology, 75, 1-18 (2002).
- Mars, W.V. and Fatemi, A., International Journal of Fatigue, 24, 949-961 (2002).
- Mazich, K.A., Samus, M.A., Smith, C.A. and Rossi, G., Macromolecules, 24, 10, 2766-2769 (1991).
- Miquelard-Garnier, G., Université Pierre et Marie Curie, Paris VI. PPMD-ESPCI. PhD thesis (2007)
- Mooney, M., Journal of Applied Physics, 11, 582 (1940).
- Mueller, H.K. and Knauss, W. G., Trans. Soc. Rheol., 15, 217-233 (1971)
- Mullins, L., Trans. Institute Rubber Ind., 35, 213-221 (1959)
- Mzabi, S, PhD thesis at PPMD-ESPCI, unpublished work
- Persson, B.N.J., Albohr, O., Heinrich, G. and Ueba, H., Journal of Physics: Condensed Matter, 17, 1071-1142, (2005)
- Rice, J.R., Journal of Applied Mech., 35, 379–386 (1968).
- Rivlin, R.S. and Thomas, A.G, Journal of Polymer Science, X, 3, 291-318 (1953)
- Rivlin, R.S., Phil. Trans. R. Soc. A241, 379 (1948).
- Rubinstein, M. and Panyukov, S., Macromolecules, 35, 6670-6686 (2002)
- Seitz, M.E., Martina, D., Baumberger, T., Krishnan, V.R., Hui, C.Y. and Shull, K.R., Soft Matter, 5, 447-456 (2009).
- Smith, T.L., Journal of Polymer Science, 32, 99-113 (1958).
- Smith, T.L., Society Plastics Engrs. Journal, 16, 1211 (1960)
- Thomas A.G., Journal of Polymer Science, 18, 177–88 (1955).
- Treloar, L.R.G., The Physics of Rubber elasticity, third edition, 2005.
- Ward, I.M. and Hadley, D.W., An Introduction to the Mechanical properties of solid polymers, John Wiley and Sons, England (1998).
- Young, R.J. and Lovell, P.A. Introduction to Polymers, Champman & Hall, (2nd Edition), London (1991).

# **Chapter 4**

## **Cavitation Phenomena: Experimental Methodology**

Introduction .....	151
4.1.- Literature review: selected geometry .....	151
4.2.- Experimental aspects: Cavitation samples preparation.....	155
4.2.1.- Glass surface modification.....	155
4.2.1.1.- Materials .....	155
4.2.1.2.- Procedure .....	155
4.2.2.- Metallic molds: design and surface modification .....	156
4.2.2.1.-Metallic molds: surface modification .....	157
4.2.2.1.1.- Materials .....	157
4.2.2.1.2.- Procedure .....	157
4.2.3.- Cavitation Samples' preparation – control of the geometry .....	158
4.3.- Design, construction and positioning of samples' holder .....	160
4.4.- Cavitation experiments and data treatment.....	162
4.5.- Analysis of cavitation experiments by FEM Simulation .....	165
4.5.1.- The Geometry and boundary conditions.....	165
4.5.2.- The Material behavior.....	166
4.5.3.- Calculations of the stress distribution (in linear elasticity).....	166
4.5.3.1. Radial evolution of the Hydrostatic stress.....	166
4.5.3.2.- Influence of confinement: the layer thickness .....	168
4.5.1.5.- From the Force to the local hydrostatic stress .....	169
4.6.- Cavitation experiments: FEM Simulation versus experimental results .....	171
Conclusions .....	174
Acknowledgments .....	175
Appendices A4 .....	176
Appendix A4.1: Comparison of 'h' measured by microscopy and directly in the center.....	176
Appendix A4.2 Samples'holder .....	176
Appendix A4.3: Reproducibility of the curves obtained for cavitation experiments.....	177
Appendix A4.4: Triaxiality of sphere-to-flat versus flat-to-flat.....	178
Appendix A4.5: Calibration constant calculation .....	178
Appendix A4.6: Fitting of hyperelastic model with experimental compression and tension data. ....	180
Bibliography.....	181

## Introduction

Chapter 3 described the large strain and tear behaviour of the three polyurethane model networks using a fracture mechanics approach.

The purpose of this Chapter is now to describe in detail the experimental methodology we used to investigate the failure of the elastomers by cavitation in a reproducible and reliable way. This includes the design of a new original test set-up, the development of a specific methodology for sample preparation, the experimental procedure and the raw experimental results obtained from the experiment itself and finally the data analysis method which was developed to extract the information we were looking for. The objective of the methodology was to observe the nucleation and growth of a single cavity if possible.

### 4.1.- Literature review: selected geometry

At this stage it is useful to briefly review the existing work on cavitation of rubbers. The inherent reason that rubbers are prone to failure by cavitation is the extremely high ratio between their bulk modulus  $K$  and their shear modulus  $G$ . It is therefore much less costly in elastic energy to grow a cavity by shear than to change the volume of the rubber by bulk expansion.

In practice, early theories have considered rubbers in pure hydrostatic tension in an infinite medium, while experiments have been carried out on thin rubber disks bonded to two surfaces. In this case if a tensile load is applied, due to constraints, the material is subjected to a large hydrostatic tension component and failure occurs by the mechanism called cavitation [Gent 1992].

The first documented evidence of the cavitation process is rather old [Busse 1938] and Yertzley [Yertzley 1939]. Busse bonded filled rubbers used in the automotive industry (NR) to flat metal end-pieces and applied a tensile stress while Yertzley did the same kind of experiment with neoprene. Both observed that the stress-strain curve had a marked softening and noted that the fracture surfaces after failure contained the evidence of what they called “internal cracks”.

Some years later Gent and Lindley [Gent and Lindsey 1959] used the same “poker chip” geometry (flat-to-flat) on natural rubber formulations, and the sample was also bonded to flat metal end-pieces. They prepared vulcanized rubber cylinders of 20mm in diameter and from 0.6 to 5mm in thickness (a diameter to thickness aspect ratio of  $a/h$  from 33 to 4). They changed the aspect ratio by using cylinders with different thicknesses, and under tensile load obtained that the stress at which the internal cracks form decreases as the test-piece thickness is increased from very small values, becoming substantially constant for moderately thick samples; a series of small cracks were formed in thin cylinders, uniformly distributed across the section (multiple cavitation), and in moderately thick cylinders only one or two large cracks were formed in the centre, as shown in Figure 4.1. The most important observation of that study was that the fracture strength of the poker-chip samples appeared to be a reproducible material constant proportional to the elastic modulus. This brought Gent and

Lindley to interpret their results as due to deformation (independent of initial cavity size) rather than fracture (dependent of cavity size).

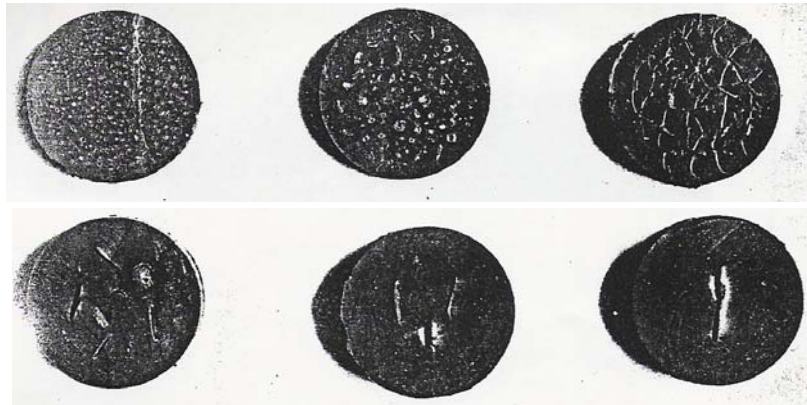


**Figure 4.1:** Central cross-sections of test-pieces of vulcanizate D, cut open after the imposition of a tensile stress of  $28 \text{ Kg/cm}^2$ . The test-piece thicknesses are: top row, left right, 0.061, 0.089, 0.137 cm; bottom, left to right, 0.180, 0.295, 0.370 cm; the diameter aspect ratio is  $a/h$  from 33 to 5.4. Taken from Gent and Lindley [Gent and Lindley 1959].

They used the theory of cavity growth of Green and Zerna [Green and Zerna 1954] to justify that the apparent yield point in the stress-strain curve appeared when the local hydrostatic pressure reached a critical value of  $5E/6$  (where  $E$  is the Young's modulus of the rubber).

This criterion of critical pressure was also confirmed by the studies of Cho and Gent [Cho and Gent 1988]; they used layers of transparent silicone rubber bonded to two steel balls (with diameters of 6.35, 9.50, 18.80 and 49.3mm) or to two parallel steel cylinders (with outer diameter of 9.55 and lengths of 12.5 to 50mm). Upon loading, cavities appeared in the rubber layers when the applied stress reached the order of the Young' modulus  $E$ . However Cho and Gent made two interesting observations: for the thinner layers (layer thickness less than 5% of sphere diameter) the cavitation stress increased markedly above the elastic modulus, and the cavity appeared over time even when the load was kept constant just below the critical value.

Experiments with rigid spherical inclusions have also been performed and reported in the literature, to characterize cavitation phenomena. Oberth and Bruenner [Oberth and Bruenner 1965], Oberth [Oberth 1967] used samples of transparent polyurethane with rigid spherical inclusions, and observed that the cavities appeared at the edge of the inclusion, due to strong triaxial stress. They performed experiments with different types of polyurethanes and found a strong correlation between the cavitation stress and the modulus. Gent and Park [Gent and Park 1984], Hall, [Hall 1951] and Petch [Petch 1953] performed also cavitation experiments with rigid inclusions and showed that the cavitation pressure depends mainly on the shape of the inclusion [Hamdi, A. 2006].

Lindsey *et al.* [Lindsey *et al.* 1963] presented some experiments on triaxial tension failure of viscoelastic materials. They used the "poker chip" geometry, and elastic transparent polyurethane rubber produced commercially. A critical aspect of their experiments was to bond the elastomer to the grips, without getting any debonding; they cut cured polyurethane sheets to bond them, by using a special adhesive, to the grips. They observed that up to a

certain applied stress (2.06MPa) very small internal bubbles appeared near the center of the disk. However all these experiments were performed at room temperature with a variety of elastomers and no particular mention of strain rate was ever made.

It is interesting to note that there is an alternative way to nucleate cavities. When gas is dissolved in the rubber under pressure and this pressure is suddenly released, bubbles (or voids) may develop and grow with time [Denecour and Gent 1968, Gent and Tompkins 1969, Gent 1992]. This is the typical situation which occurs when underwater ocean cables or rubber seals are rapidly brought to the surface and start cavitating.

These two situations are equivalent because of the incompressibility of the rubber. In both cases the formation of visible voids indicates that local fracture has occurred. Denecour and Gent [Denecour and Gent 1968] performed some model experiments in swollen transparent rubber vulcanizates, prepared from natural rubber. They dissolved gas under pressure into rubber sheets and observed upon depressurization, that up to a critical internal pressure of  $5E/6$ , bubbles formed. Also Gent and Tompkins [Gent and Tompkins 1969] observed experimentally the nucleation and growth of bubbles when the gas supersaturation pressure exceeded  $5E/6$ . They used a variety of unfilled rubber sheets made of natural rubber (NR), polyisoprene (IR), butadiene-styrene copolymer (SBR) and polybutadiene copolymer (BR).

### **The Selected geometry**

The flat-to-flat geometry (“poker chip”) for producing cavitation samples has been the most common used geometry reported in the literature.

As shown in Figure 4.2, [Gent 1992] the hydrostatic stress distribution in such poker-chip bonded block in compression or in extension, is maximal in the central part, and decreases to the edges, as shown in Figure 4.2.

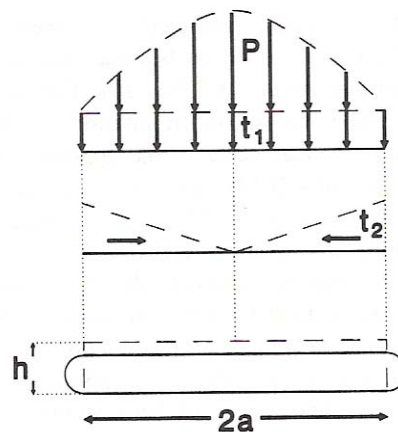


**Figure 4.2:** Stress distribution for a bonded block in compression.  $t_1$  is the tensile stress and  $t_2$  is the shear stress [Gent 1992].

The main reason to use of the poker-chip geometry is to introduce a large hydrostatic tension component in the sample. Furthermore the incompressibility of the rubbery materials, which usually have large deformations during testing, is limited to relatively small strains before failure. This provides the benefit that the infinitesimal elasticity theory can be used in the analytical work without introducing large errors [Lindsey *et al.* 1963].

Our design was guided by the dual goal to minimize multiple cavitation (possibly have a single cavity in the center) and to be able to model analytically the stress field prior to cavitation without worrying too much about boundary conditions (slippage).

Furthermore a practical problem with the flat-to-flat geometry is the difficulty to control the parallelism of the sample with the machine; if the set-up allows adjustments (as is the case when a tripod has to be used to align the flat-to-flat sample) some compliance is introduced.

A design of a different geometry such as sphere-to-flat would solve the problem of setting the parallelism. Our idea was to design a sample's geometry to nucleate a single cavity close to the centre. Then a sphere-to-flat system (see Figure 4.3) was designed to obtain a less confined material (decreasing the shear stress at the edges) than in flat-to-flat geometry, but more concentrated hydrostatic stress toward the centre of the sample, to favor growth of a single cavity in the centre.

In order to model quantitatively the stress field in the sample the degree of confinement had to be chosen in an intermediate range and we chose a ratio  $h/D = 0.027$  and  $a/h = 10$  as described in figure 4.3

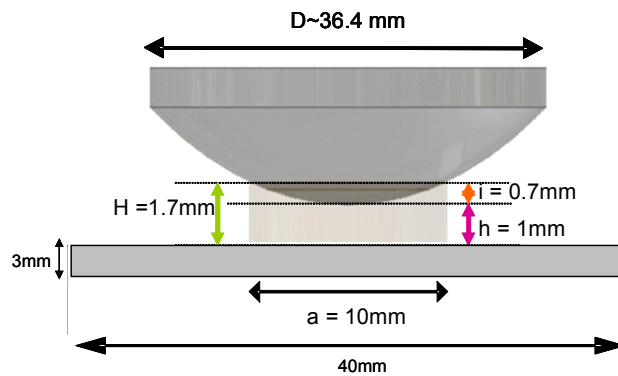


**Figure 4.3:** Sphere-flat cavitation sample geometry: The PU network is sandwiched between a glass lens and a glass plate. Side and top in situ visualization can be carried out simultaneously.

For the flat-to-flat cavitation system, approximate analytical solutions are available that give the maximum hydrostatic tension for extension and tilting deformations of bonded rubber blocks. For example, for a bonded cylinder of fairly large diameter-to-thickness ratio, the maximum hydrostatic tension is approximately twice the tensile stress applied to the cylinder [Gent 1992]. However, no analytical solution exists for the sphere-to-flat system to relate the force to the local stress field. Such a solution had to be obtained by FEM (Finite Element Method). The results of these simulations are presented in section 4.5.

## 4.2.- Experimental aspects: Cavitation samples preparation

A typical “poker-chip” system consists of two flat end-pieces and a bonded cylinder of elastomer in between. When the bonding procedure is made, precautions must be taken in order to produce a bond of sufficient strength that it will not allow the elastomer to tear away from the flat pieces before an internal failure is produced. In our case, the bonding was achieved by chemical modification of our glass substrates, and the procedure was completed during the curing of the elastomer without any additional layer of glue.

### 4.2.1.- Glass surface modification

To avoid problems of debonding during the testing (between the PU and the glass substrates) and to make sure that failure happens in the bulk of the material, for the preparation of our cavitation samples a chemical modification of the two surfaces in contact with the polyurethane elastomer was carried out in order to have covalent bonds strong enough. As mentioned in Chapter 1, one of the typical reactions of the isocyanate group can occur with an amino group; then the chemical modification of the two glass surfaces was achieved by preparing amino-terminated self-assembled monolayers to make them react with the isocyanate groups available during the curing of the polyurethane networks.

For the preparation of the sphere-to-flat geometry, we used glass plates of 40 mm in diameter and 3 mm in thickness, and plano-convex glass lenses of 18.2 mm in radius (see Figure 4.3). The materials and procedures used for the chemical modification of the glass surfaces are presented as follow.

#### 4.2.1.1.- Materials

The following materials and chemicals were used as received: (3-Aminopropyl)triethoxysilane purum  $\geq 98\%$  (Aldrich); dry toluene (Aldrich). Plano-convex lenses of BK7 for optical uses (Melles Griot), code 01LPX063: PL CX radius 18.2mm, Focale 35.0mm; Glass plates of BK7 of 40mm in diameter and 3mm in thickness. All solvents and chemicals (acetone, toluene, sulphuric acid, peroxide water) were purchased from either Aldrich or Sigma. Silanization reactions were carried out under nitrogen atmosphere (inside the glove box). All glassware used to prepare the monolayers was cleaned and dried @ 120°C.

#### 4.2.1.2.- Procedure

The glass plates and the glass lenses were modified chemically by preparing self-assembled monolayers (SAMs). Prior to monolayer formation the substrates were oxidized by immersion in piranha ( $\text{H}_2\text{SO}_4$  (96%):  $\text{H}_2\text{O}_2$  (30%): 3:1 v/v) (*Warning! Piranha solution should be handled with caution: it has been reported to detonate unexpectedly*) for 20 minutes, rinsed with Millipore water and dried with a stream of nitrogen. Amino-terminated monolayers were prepared by immersion of the clean substrates in a 4% v/v solution of (3-



Aminopropyl)triethoxysilane purum  $\geq 98\%$ , in dry toluene, inside a gloves box (nitrogen atmosphere). After  $\sim 4\text{h}$ , the substrates were rinsed with dry toluene inside the gloves box, and finally rinsed a second time with toluene (outside the gloves box) and dried under a stream of nitrogen. Fig. 4.4 presents a schematic of this procedure. The surface modification remains chemically stable under ambient conditions.

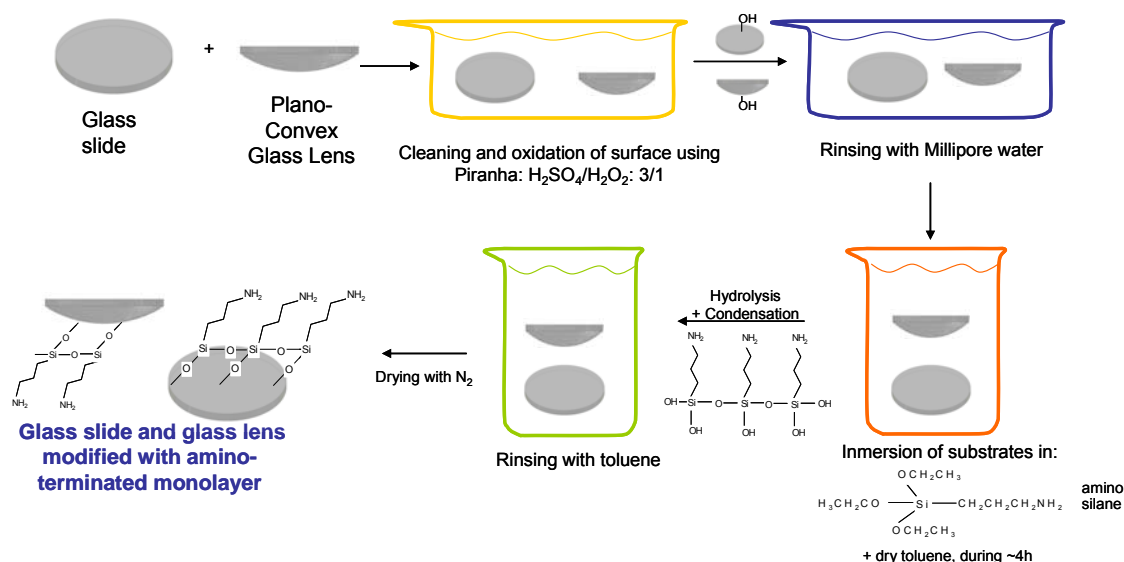


**Figure 4.4:** Schematic of glass surface modification, for cavitation samples' preparation.

#### 4.2.2.- Metallic molds: design and surface modification

With the purpose of obtaining lateral transparency of the samples, metallic molds were designed, machined in DURAL (2017) and polished. Given the radius of curvature of the lens of 18.2mm, the internal height of the mold had to measure  $H=1.7\text{mm}$ , to give a central thickness of the sample of  $h \cong 1\text{mm}$  (which gives an aspect ratio of  $a/h \cong 10$ , see Figure 4.3.). Figure 4.5 shows the design and dimensions of the metallic molds used for the cavitation samples preparation.

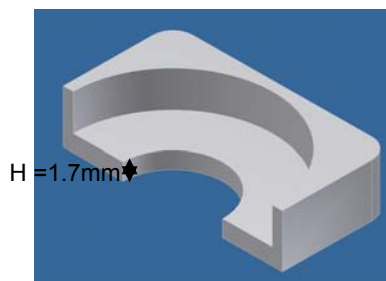
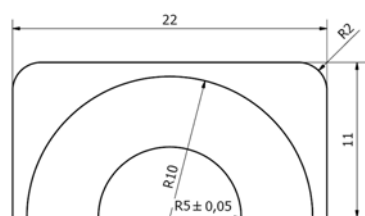


**Figure 4.5:** Schematic of the metallic molds.

#### 4.2.2.1.-Metallic molds: surface modification

The metallic molds had to be chemically modified to ensure demolding after crosslinking of the polyurethane networks. The surface modification was carried out by preparing fluoro-terminated monolayers.

##### 4.2.2.1.1.- Materials

The following chemicals were used as received: Dry toluene (Aldrich) and (Heptadecafluoro-1,1,2,2-tetrahydrodecyl) dimethylchlorosilane (ABCR). The solvents (acetone, toluene) were purchased from either Aldrich or Sigma. The silanization reactions were carried out under nitrogen atmosphere (inside the gloves box).

##### 4.2.2.1.2.- Procedure

Prior to monolayers formation, the substrates were cleaned with acetone and dried during 30min in the oven @ 120°C. The fluoro-terminated monolayers were prepared by immersion of the clean substrates in a 3% v/v solution of (Heptadecafluoro-1,1,2,2-tetrahydrodecyl) dimethylchlorosilane in dry toluene, inside a gloves box (nitrogen atmosphere). After ~4h, the substrates were rinsed with dry toluene inside the gloves box, and finally rinsed a second time with toluene (outside the gloves box) and dried under a stream of nitrogen. Figure 4.6 shows a schematic of this procedure.

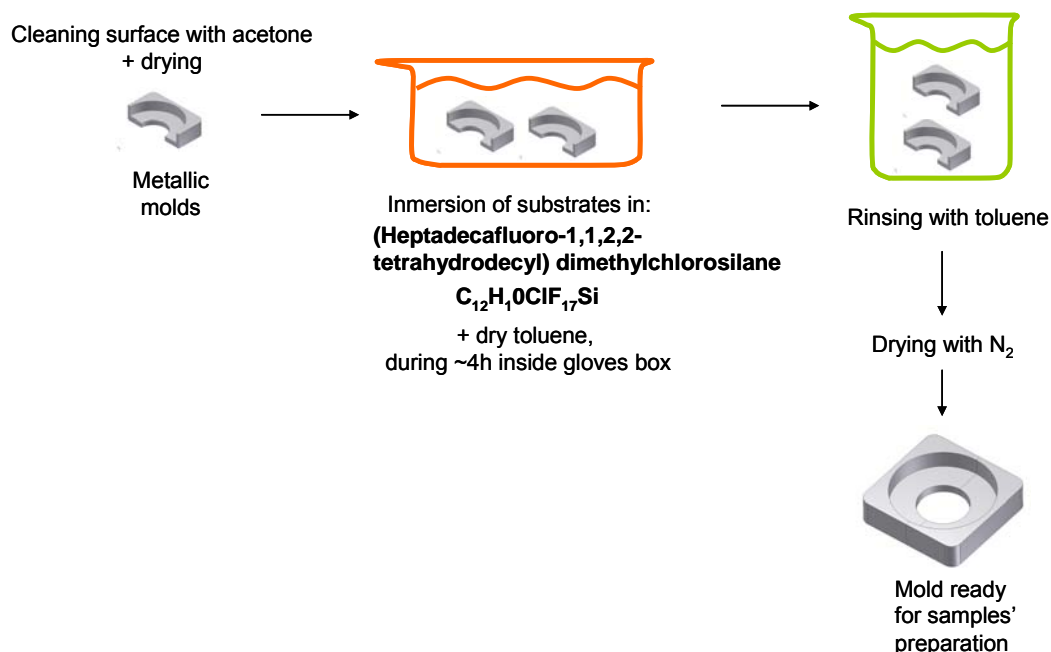


**Figure 4.6:** Schematic of the surface modification of metallic molds, for the preparation of the cavitation samples.

#### 4.2.3.- Cavitation Samples' preparation – control of the geometry

The samples' preparation was carried out under nitrogen atmosphere (inside the gloves box). Once the preparation of the three polyurethane mixtures was done (as presented in chapter 2) the cavitation samples' preparation can be carried out. The already degassed mixture was poured into the prepared cavitation samples system (glass plate + metallic mold, chemically modified) as shown in Figure 4.7. After pouring, a second degassing had to be done during ½ hour to avoid any remaining bubbles, and then the glass lens was placed on the top, being supported by the metallic mold.

The samples were then taken out of the gloves box and placed in an oven where cycles of vacuum and nitrogen were done, and finally samples were left with nitrogen in the oven. As mentioned in section 2.3, the crosslinking takes 48h @35°C (to increase viscosity in a controlled way to avoid bubbles) followed by 80h @80°C, for final network crosslinking. After curing the network, the two-pieces of the metallic mold were demolded.

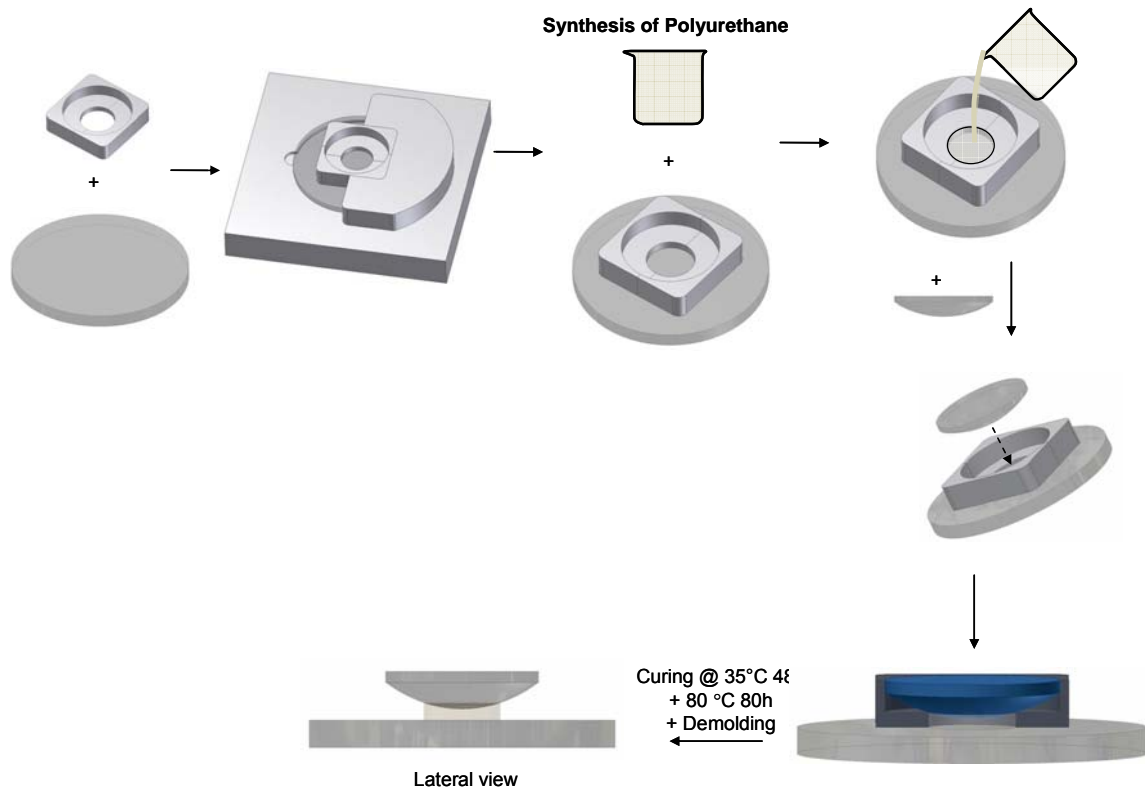


**Figure 4.7:** Schematic of the cavitation samples' preparation

The final step of the cavitation samples' preparation, before testing, was to glue the sample (the free side of the glass lens) to the probe. For all the experiments at  $T \leq 70^\circ\text{C}$  araldite cristal was used, and for experiments at  $T = 100^\circ\text{C}$  loctite<sup>®</sup> 407 was used, both transparent and with high mechanical resistance. Figure 4.8 shows an example of the cavitation sample already glued to the probe, ready for performing the cavitation experiment. The finish surface of the probe has to be as homogeneous as possible in order to ensure a neutral background for the top visualization.

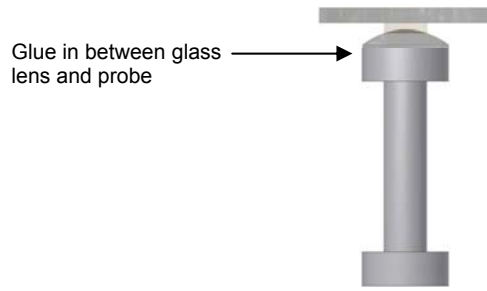


**Figure 4.8:** Example of probe and cavitation sample, ready for testing. Top view can be performed through the glass plate.

### **Geometry control**

Systematic measurement of the geometry was carried out by optical microscopy before performing the cavitation experiments. Figure 4.9 shows a picture of a cavitation sample and the corresponding dimensions. From this kind of picture, the values of ‘ $h$ ’, ‘ $H$ ’ and ‘ $a$ ’ were obtained for each sample, every time, before performing the cavitation experiment. This measurement was done with an Optical Microscope. Note that the lateral edges of the sample do not show any obvious deformation implying therefore negligible residual stresses upon curing.

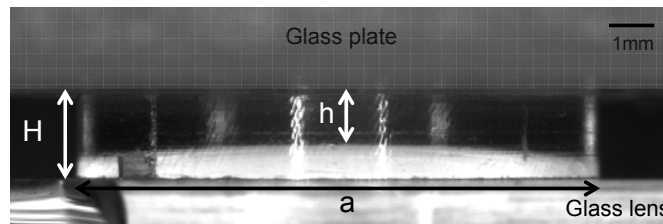


**Figure 4.9:** Picture of cavitation sample and dimensions, obtained by Optical Microscopy.

The methodology to measure the thickness of the samples was validated, to be more confident of the ‘ $h$ ’ values. Some samples called “blanks” were prepared for each network. For the “blanks” preparation the procedure to obtain the sample was the same as the one mentioned in section 4.2.3, but the glass plate and glass lens did not have any surface modification, then afterwards the complete piece of rubber could be taken out effortlessly from the mold to measure the ‘ $h$ ’ value directly on the centre of the sample with a caliper. Both dimensions were compared and very similar values were obtained for both methods (see Appendix A4.1).

### 4.3.- Design, construction and positioning of samples' holder

To perform the cavitation experiments a specific sample holder had to be designed and built. The main requirement for this was to have a quite stiff set-up with a very low compliance (with this set-up the compliance was  $10\mu\text{m}/100\text{N}$ ). Other requirements were to have a good top view of the sample and to give some flexibility to the upper and lower parts to turn to a certain angle; this, to position a second camera in front of the set-up and to have both, top and lateral, visualization. The probe was designed to be glued to the glass lens on its entire surface (as shown in Figure 4.8) to reduce the compliance of the system. Figure 4.10 presents pictures of the actual samples' holder showing the different pieces and the positioning of the sample and probe to perform the cavitation experiments. Figure 4.11 shows the positioning of the two cameras in front of the set-up. For the experiments performed under standard conditions ( $25^\circ\text{C}$ ) the heating chamber (used to control the temperature) was open, and the temperature was room temperature (measured using a thermocouple). In Appendix A4.2 are presented the samples' holder pieces and in Table A4.2 are listed the pieces.

The cavitation experiments were performed in a hydraulic MTS810 machine, and the displacement was measured with an LVDT extensometer (see details in the next section). To perform the experiments, the image acquisition from the camera were electronically connected to a computer where the visualization is done. For the data acquisition, the MTS data acquisition software and the cameras were connected to an oscilloscope to send the pulses that make possible the synchronization of images with the Force, time and displacement.

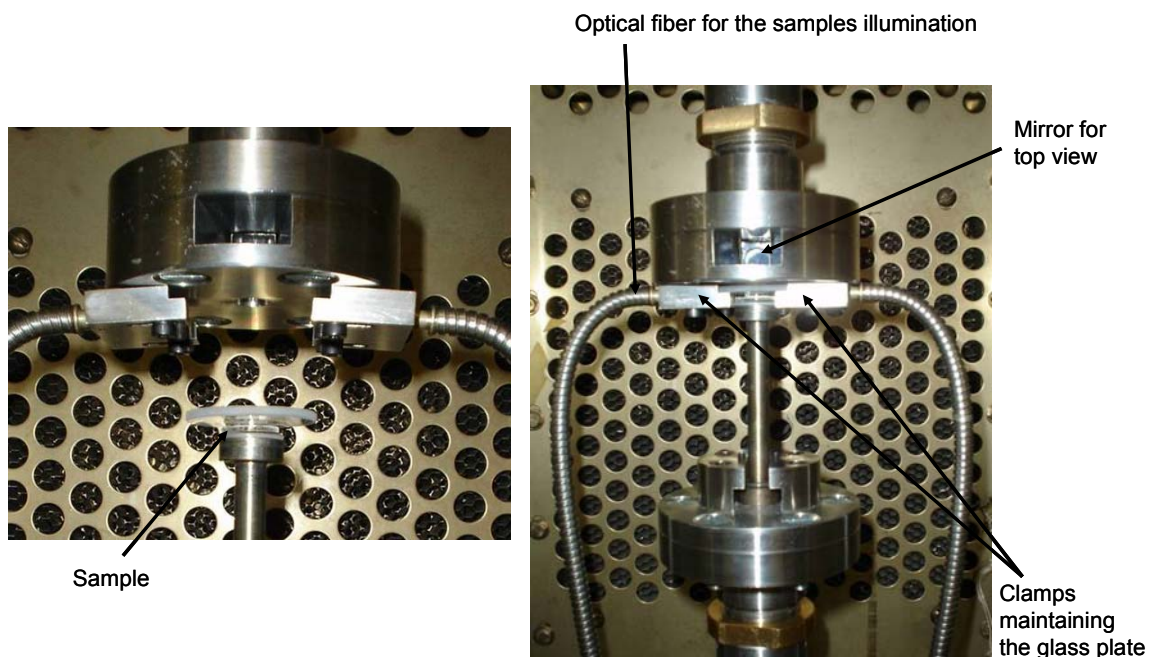


**Figure 4.10:** Samples' holder and cavitation sample positioning.



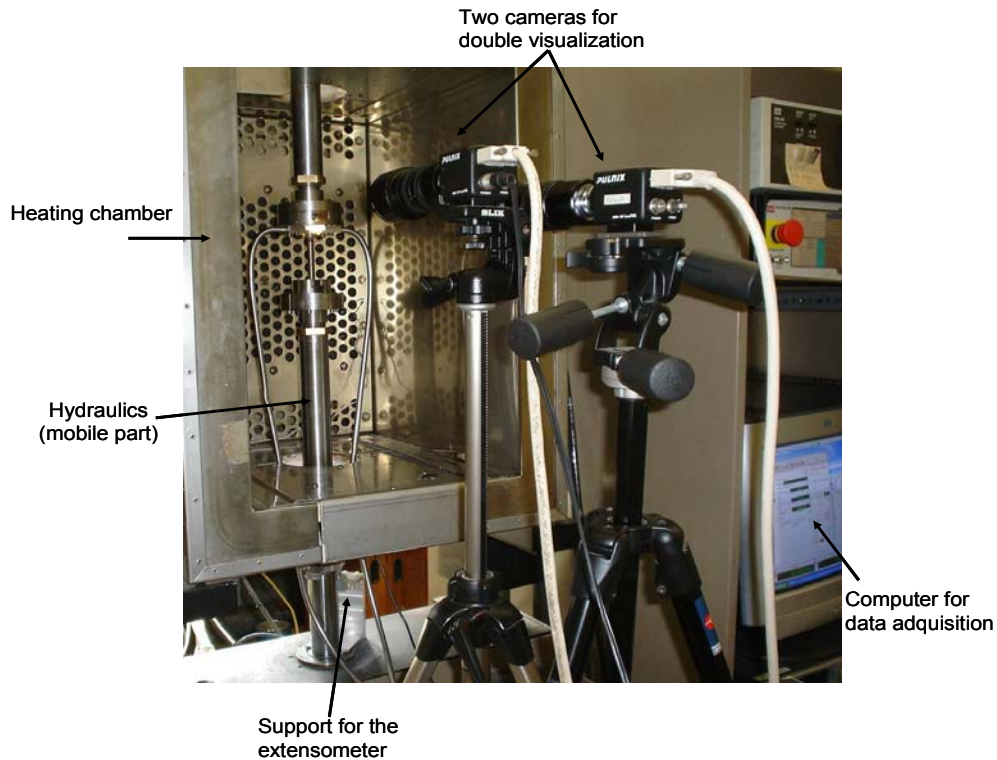


**Figure 4.11:** Example of how the cavitation experiments were performed at 25°C.

### Experimental set-up at different temperatures

To perform the experiments at different temperatures the heating chamber was maintained closed to heat up the samples, as shown in Figure 4.12.

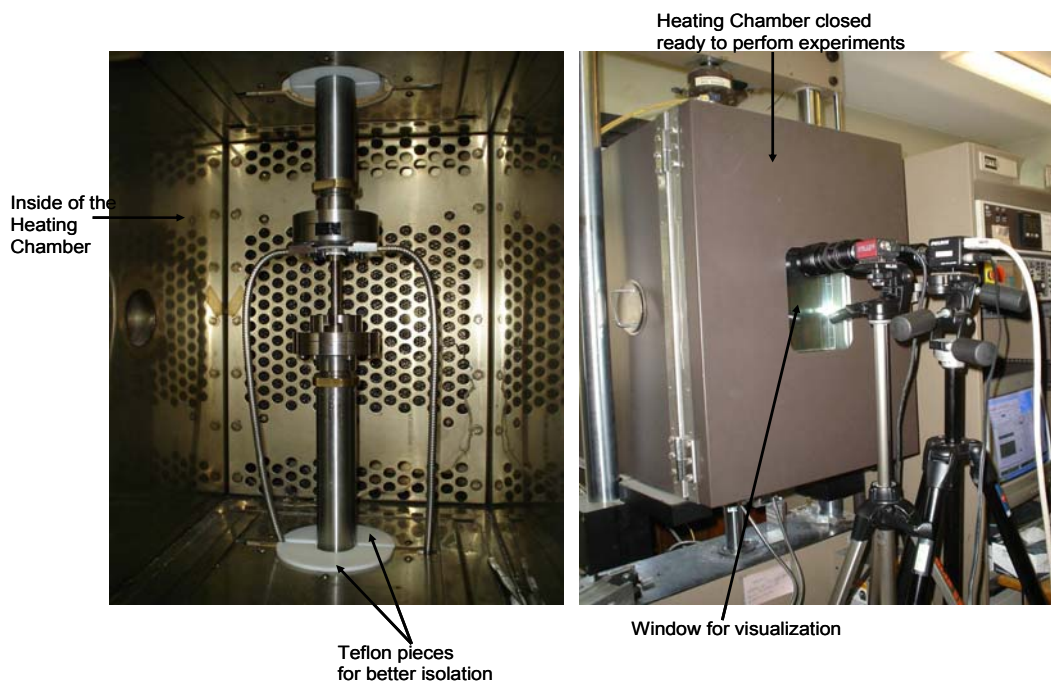


**Figure 4.12:** Heating chamber to perform cavitation experiments at higher temperatures: 50°C, 70°C and 100°C.

#### 4.4.- Cavitation experiments and data treatment

Systematic cavitation experiments were performed under standard conditions; the standard conditions were defined as  $T=25^{\circ}\text{C}$  and  $V=10\mu\text{m/s}$  (since  $h \cong 1\text{mm}$ , the initial strain rate  $\dot{\epsilon} \sim 1\%/s$ ).

The force was measured with a load cell of 2500N, with a force resolution of  $\pm 0.5\text{ N}$ . The displacement was measured by an external extensometer (LVDT 0-5mm, resolution of  $\pm 0.5\mu\text{m}$ ). The samples' holder mentioned above was used. The sample and cameras were set as shown in Figures 4.10 and 4.11 for running experiments at room temperature, and as shown in Figure 4.12 for running experiments at higher temperatures. Two cameras were used for double visualization: Marlin F-033B, standard camera (25fps) with a resolution of 656x494; and Pulnix TM-6740 CL high speed camera (200fps) with a resolution of 640x480. Figure 4.13 presents a typical curve of force versus displacement (obtained for PU8000/1000) under standard conditions. Figure 4.13 shows the curve of force versus displacement and the numbers that correspond to the synchronized image acquisition. The pictures taken from the top view are presented in Figures 4.14. The synchronized imaging allows the analysis of where the cavities appear related to the force and time, and the time is directly related to displacement.

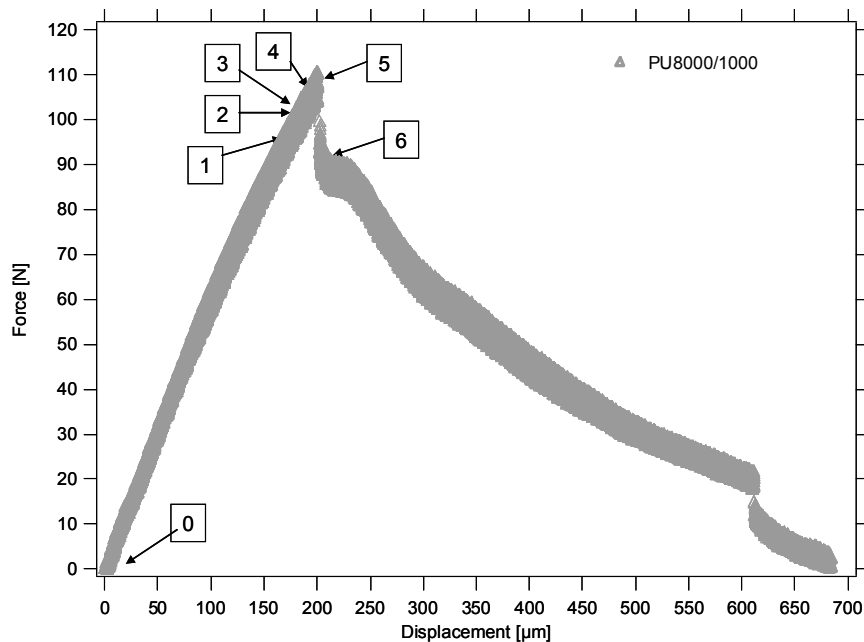


**Figure 4.13:** Typical curve obtained by cavitation experiment (PU8000/1000) under standard conditions,  $25^{\circ}\text{C}$  and  $10\mu\text{m/s}$ , and data treatment.

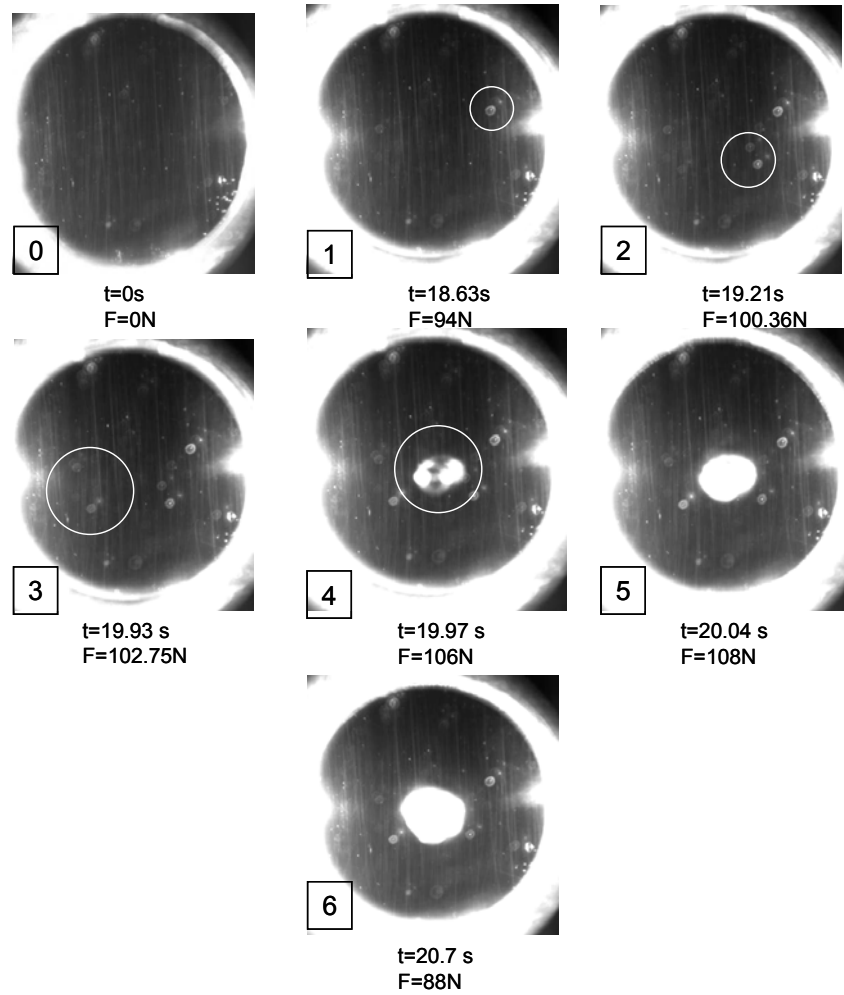


**Figure 4.14:** Images obtained from the top view (PU8000/1000) synchronized with the force versus time data acquisition. The camera acquisition rate was 25fps.

The force versus displacement curve can be generally divided in four parts (see Figure 4.15):

- A) An initial part of the curve, which can be considered as linear, that goes from zero up to certain force (increasing force) where no change is optically visible.
- B) A region (not seen for all conditions) where small cavities (seen as white spots) appear progressively and remain at a stable size. No measurable change of compliance is observed at this stage.
- C) The maximal force  $F_{max}$ , corresponding to 1 cavity growing close to the centre of the sample; followed by the fast decrease of the force;
- D) Progressive decrease of the force, which corresponds to the crack propagation.

These four ‘regions’ (A, B, C and D) are represented in Figure 4.15, as a general result. Since we were interested in the study of the nucleation of the cavitation, the main ‘region’ of interest in the force-displacement curve is the first part of the curve from zero force until the critical cavity appears and the force drops. The maximal force shown in the curve in Figures 4.13 and 4.14 (before the force drops) corresponds to a rapid expansion of a single cavity and



is used to calculate the maximal local hydrostatic stress which may then be used as a criterion to predict resistance to cavitation; the calculation is presented in the next section.

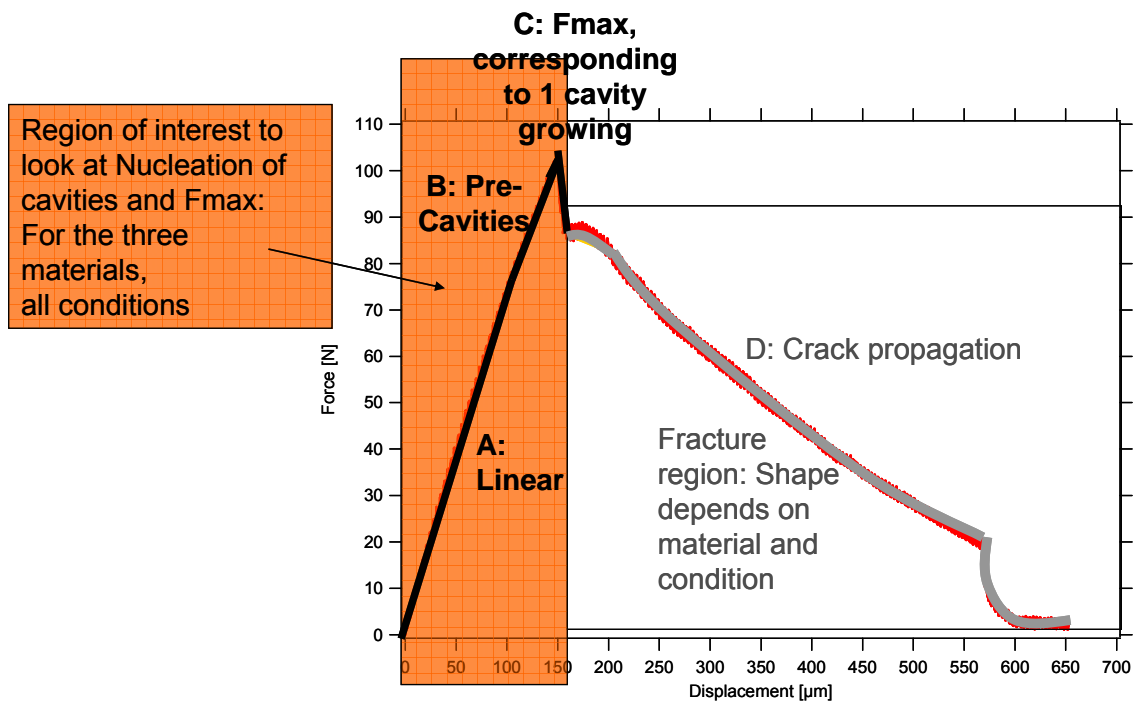


**Figure 4.15:** Description of a typical result and the data of interest.

Figure 4.16 shows the result of three cavitation samples of PU4000 and we can see that the samples are quite reproducible (see Appendix A4.3 for the curves of the other two materials).

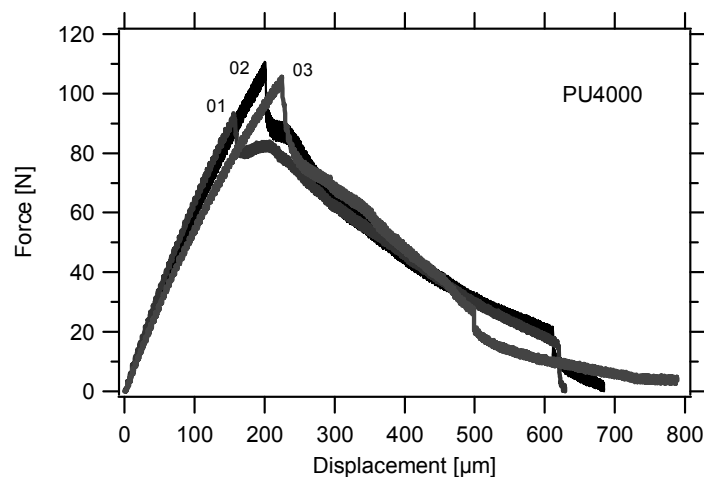


**Figure 4.16:** Example of reproducibility of the maximal force for different samples in PU4000.

The shape of the curves does change in function of the material and parameter conditions. In Chapter 5, a comparison of the cavitation resistance of the three polyurethane model networks

will be presented under standard conditions (25°C), at three higher temperatures: 50°C, 70°C and 100°C, and at two different speeds (a two decade decrease).

## 4.5.- Analysis of cavitation experiments by FEM Simulation

The simplest criterion for the growth of a cavity is that of a critical value of the local hydrostatic stress [Green and Zerna 1954, Gent and Lindley 1959, Fond 1996]. Of course and as shown in figure 4.1, the stress varies spatially and temporally in our samples during a test. In order to go from a macroscopic force measurement to a local stress value, a model has to be used for the stress field for that particular geometry.

The analytical solution for the relationship between force and local hydrostatic stress for the flat-to-flat geometry has been already reported in the literature [e.g. Gent 1992], but for the sphere-to-flat geometry the solution had to be calculated. With the purpose of obtaining the relationship between the force applied to the sphere and the hydrostatic stress numerical simulations with a Finite Element Method (FEM) were carried out at DSM Research by Jan Stolk.

### 4.5.1.- The Geometry and boundary conditions

The structure is analyzed by a FEM, in which the given geometric region or *domain* is divided in a collection of subdomains or *elements*, and over each element the governing equation is approximated by any traditional variational method. The geometry and corresponding dimensions of the sample are presented in Figure 4.17.

An axisymmetric geometry was used, which is a two dimensional half-cross section of the component with an axis of symmetry. The problem is solved in 2D.

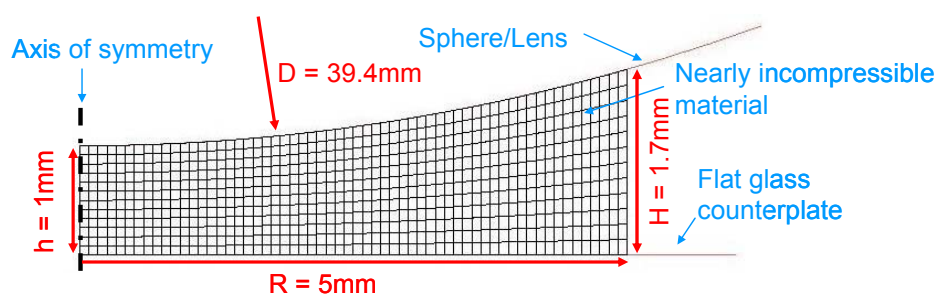


**Figure 4.17:** Geometry and finite element mesh (720 elements and 795 nodes).

The characteristics of the mesh were:

- 720 elements, 795 nodes (mesh-density determined in convergence study)
- Axisymmetric Hermann elements (Hermann elements allow simulation of nearly incompressible behaviour)
- Sphere and flat glass plate treated as rigid bodies

- Deformable material rigidly connected to rigid bodies (no relative interface motion allowed)

For this problem the following boundary conditions were specified:

- Nodes corresponding to the glass plate are fixed
- Nodes corresponding to the sphere are lifted up to 0.2 mm (which is approximately the maximal deformation up to maximal force for our materials). Note that only vertical displacement is allowed, without any horizontal accommodation.
- Nodes corresponding to the axis of symmetry are supposed to displace only vertically, in order to keep the symmetry conditions.

We used “fixed” boundary conditions. They exist when a surface of the component is firmly attached to another component or the ground. When the surface (containing the nodes) is fixed, all the DOFs (degrees of freedom) are set to zero and the node cannot move in any direction.

#### 4.5.2.- The Material behavior

Specifications of material properties for the linear analysis of an elastomer component involve the small strain basic elasticity equations, therefore:

$$K = \frac{E}{3(1-2\nu)} \quad \text{eq.4.1}$$

where K is the bulk modulus and  $\nu$  is the Poisson’s ratio.

It follows from equation 4.1 that if Poisson’s ratio is assumed to be 0.5, corresponding to an incompressible material, the bulk modulus goes to infinity. This assumption also dictates that Young’s modulus is 3 times the shear modulus  $E=3\mu$ . This is generally not exactly true for engineering elastomers, but it makes analytical solutions possible and numerical simulations much easier. When Poisson’s ratio of 0.499 and 0.5 are used, most classical finite element programs cannot analyze properly the elastomer. Then the elements used in finite element analysis need to be reformulated to accommodate this high value of Poisson’s ratio. This is usually accomplished by using an approach developed by Herrmann and Toms [Herrmann and Toms 1964] and Herrmann [Herrmann 1985] by introducing a new variational principle that includes another degree of freedom called the “mean pressure function”.

#### 4.5.3.- Calculations of the stress distribution (in linear elasticity)

##### 4.5.3.1. Radial evolution of the Hydrostatic stress

The theoretical stress distribution for bonded cylinders presents a higher stress in the central part of the sample either for flat-to-flat or sphere-to-flat (as shown in Figure 4.2). For

studying the differences between the two geometries, FEM calculations were done (the mesh for flat-to-flat geometry and the approach are shown in appendix A4.4).

Figure 4.17 presents the graphs showing the numerical comparison for an applied displacement  $\Delta u$  of 0.2 mm for our experimental geometry and the flat-flat geometry. The hydrostatic stress is defined by:

$$\sigma_{hydr} = \frac{1}{3} tr \underline{\underline{\sigma}} = \frac{1}{3} (\sigma_{11} + \sigma_{22} + \sigma_{33}) \quad \text{eq.4.2}$$

where the indices refer to the three principal directions. The hydrostatic stress as a function of the radius (i.e. position from the center) is higher in the flat-flat system in the central part of the sample resulting by a more confined conditions ( $R=5\text{mm}$ ,  $H=1\text{mm}$ ). The decay occurs away from the central axis and it is almost proportional to the decay of the sphere-to-flat geometry (Figure 4.18(a) and Figure 4.19). When the hydrostatic stress is normalized by the maximal principal stress (tensile direction), the stress triaxiality ratio  $\tau$  can be defined as:

$$\tau = \frac{\sigma_{hydr}}{\sigma_{principal, max}} \quad \text{eq. 4.3}$$

The parameter  $\tau$  can take critical values for pure shear  $\tau = 0$  ; tension  $\tau = 1/3$  and purely hydrostatic  $\tau = 1$ .

Radial evolution of  $\tau$  is shown in Figure 4.18 (b). A slight decrease from the centre is observed. The stress situation remains close to hydrostatic over most of the disc. A slightly lower stress triaxiality ratio is obtained for the sphere-flat geometry ( $\tau_{max}^{sphere-flat} = 0.921$  versus  $\tau_{max}^{flat-flat} = 0.961$ ).

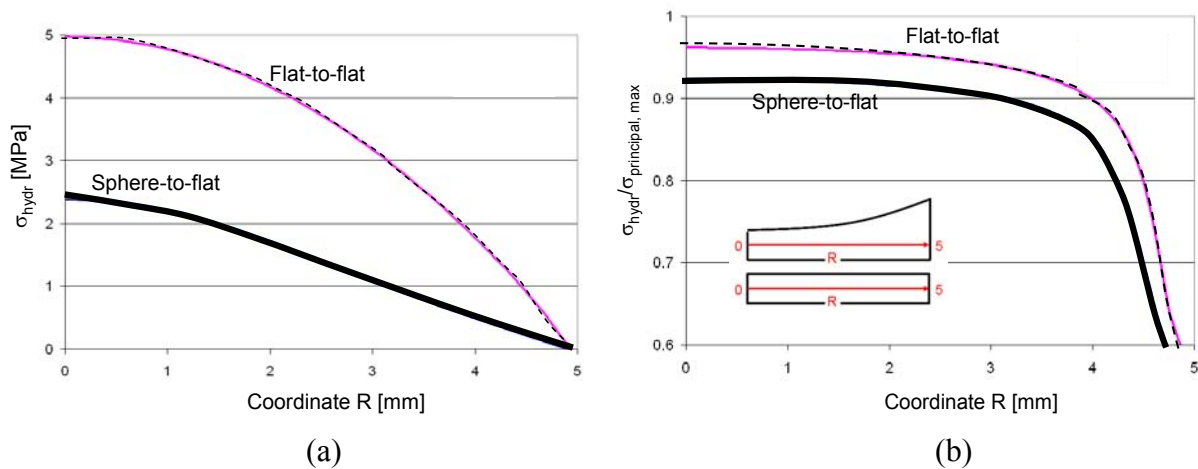


**Figure 4.18:** Triaxiality of sphere-to-flat geometry as a function of the radius of the sample, obtained by FEM ( $E=1\text{MPa}$ ,  $\nu=0.49994$ ,  $\Delta u=0.2\text{mm}$ ). As a comparison the same calculation has been done on flat-to-flat geometry ( $a=10\text{mm}$ ,  $h=1\text{mm}$ )

Regarding the question of the localization of the maximal hydrostatic stress around the central axis, Figure 4.19 shows a comparison of the localization of the maximal hydrostatic stress along the mid-plane for the sphere-to-flat and flat-to-flat geometries. The prediction shows that the hydrostatic stress is slightly more concentrated for the sphere-to-flat geometry. This higher concentration of hydrostatic stress for the sphere-to-flat geometry, together with the chosen aspect ratio  $a/h=10$  for our cavitation sample, made it possible to observe one single cavity growing in the centre of the sample.

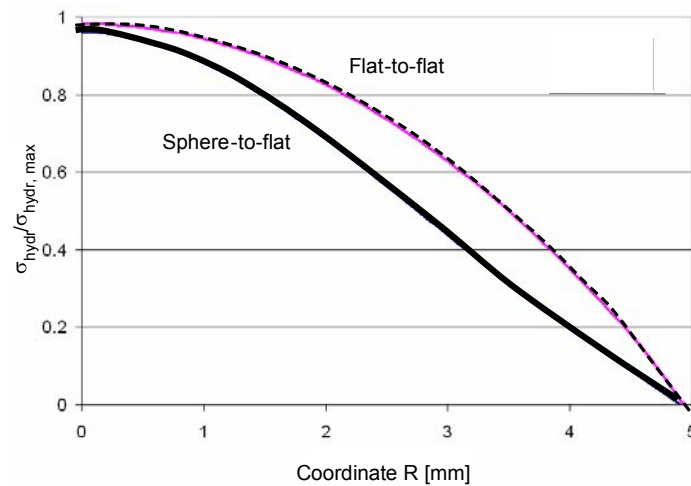


**Figure 4.19:** Prediction of the localization of the maximal hydrostatic stress in the flat-to-flat and sphere-to-flat geometries in function of the radius of the sample.

#### 4.5.3.2.- Influence of confinement: the layer thickness

Another analysis that was done by FEM for the sphere-to-flat geometry was the influence of the samples' thickness ('h'). The resulting curves of hydrostatic stress as a function of the layer thickness are shown in Figure 4.20. The hydrostatic stress at a given sphere displacement is sensitive to layer thickness as follows:

- 5% thicker layer leads to 11% reduction in hydrostatic stress
- 5% thinner layer leads to 13% increase in hydrostatic stress
- The stress situation remains close to purely hydrostatic, irrespective of the layer thickness and position along the Z-axis.

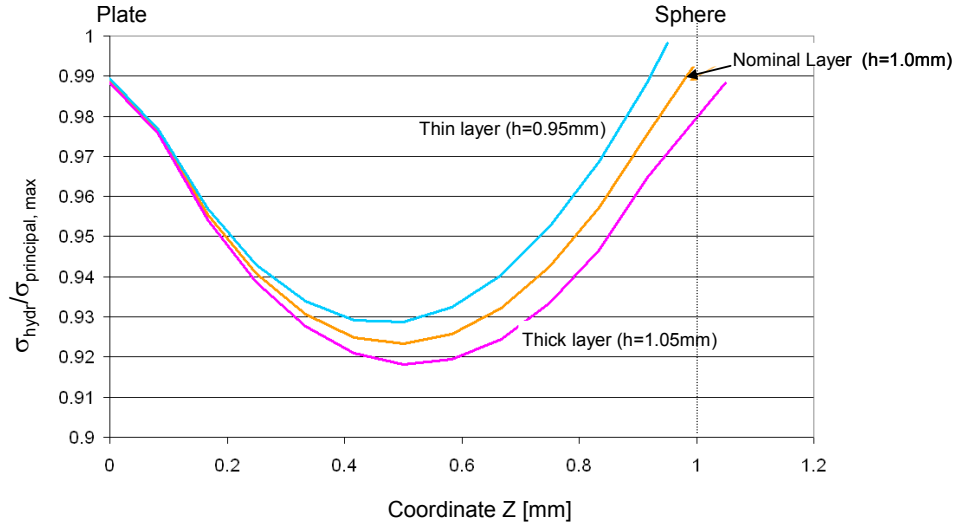


**Figure 4.20:** Numerical calculation of the variation of the hydrostatic stress for different layer thicknesses at  $\Delta u=0.2$  mm.

#### 4.5.1.5.- From the Force to the local hydrostatic stress

##### From Fmax to the maximal hydrostatic stress, $\sigma_{hydr,max}$

The criterion used to calculate the resistance to cavitation was the use of the maximal Force at which cracks grow. This corresponds to the critical state reached when one critical cavity suddenly grows in the body of the rubber, producing a drop in the extending force. This maximal force is then used to calculate the maximal hydrostatic stress,  $\sigma_{hydr,max}$ , in the center of the sample, as presented in the schematic 4.21.

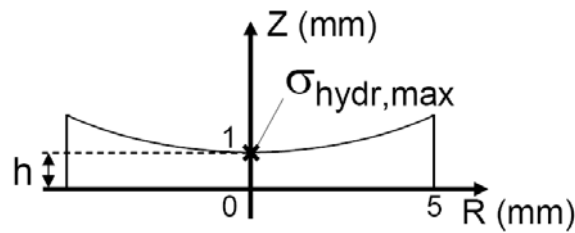


**Figure 4.21:** Schematic of the maximal hydrostatic stress in the center of the sample

To obtain the relation between the macroscopic applied force and the corresponding applied hydrostatic stress, a calibration constant  $C(v)$  was calculated by FEM simulations. The calibration constant for a given geometry was independent of the elastic modulus and dependant on Poisson's ratio. The relation between the measured force and the resulting hydrostatic stress was given by:

$$\sigma_{hydr,max} = C * F_{max} \quad \text{eq. 4.4}$$

where  $C$  is the calibration constant.

The approach was to perform the calculation for several Poisson's ratio  $0.49 \leq \nu \leq 0.49999$  and  $\Delta u = 0.2$  mm, and in all cases  $C(\nu) = \sigma_{\text{hydr,max}}/F_{\text{max}}$ . Appendix A4.5 shows the calibration curve. The calculated calibration constant was specific for this geometry.

If the geometry changes then the calibration curve will shift. In Appendix A4.5, Table A4.4 are reported the values of  $h$ ,  $F$ ,  $\sigma_{\text{hydr,max}}$  and the correspondent value of  $C(\nu)$ . The calibration factor depends only slightly on  $h$ , as 5% change in layer thickness results in only 2% change in calibration factor.

The measured value of 'h' was then used to obtain the calibration factor  $C(\nu)$ , see section 4.2.3. The maximum hydrostatic stress calculated from the peak force was not very sensitive to variations in layer thickness, as the calibration factor, unlike the compliance, was not very sensitive to layer thickness.

### **From the maximal hydrostatic stress to the local hydrostatic stress $\sigma_{\text{hydr}}$**

Using images synchronized with the force and displacement data (as the ones shown in Figure 4.13), we did some statistics to study the pre-critical cavities as a function of position from the centre of the sample, for the different testing conditions.

To define the local hydrostatic stress (i.e. as a function of the position from the sample centre) where the cavity appears, we used the FEM simulation of our geometry. Figure 4.22 presents the graph used for the determination of the stress as a function of the distance from the centre (which is the same shown in Figure 4.19 for the sphere-to-flat geometry).

Each cavitation event was localized in the bulk of the sample, mainly occurring in the vicinity of the sphere; the position from the sample centre (coordinate  $R$ ) was used in order to determine the local hydrostatic stress,  $\sigma_{\text{hydr}}$ .

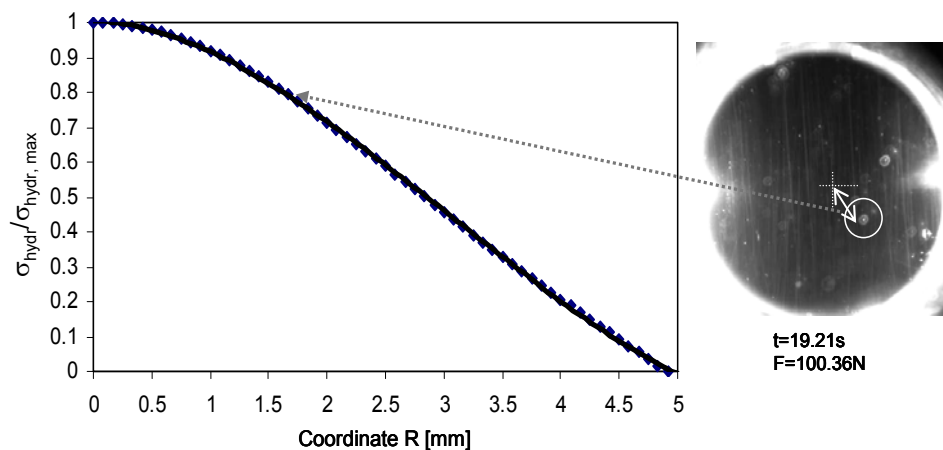


**Figure 4.22:** Calibration curve to obtain the local hydrostatic stress: normalized hydrostatic stress over the maximal hydrostatic stress (at  $R=0$ ), as a function of the position along the radial direction of the sample.

#### 4.6.- Cavitation experiments: FEM Simulation versus experimental results

As was mentioned above, the main reason to use FEM simulations was to obtain the relation between the resulting force and the local hydrostatic stress.

As an additional analysis, in this section we compared the experimental curves (Force versus displacement) obtained from the cavitation experiments with the theoretical curves calculated by FEM.

For the simulation strategy two types of calculation were carried out:

- 1) simple linear elastic model
- 2) strain hardening model (non-linear elasticity: Gent's model)

The first results obtained with a simple linear elastic model have shown quite large discrepancies with the experimental data. Calculations were carried out using the small strain Young's modulus obtained by DMA and a Poisson's ratio of 0.49994. Experimental results were seen to be stiffer than the numerical predictions, which was an unexpected result. Neither relevant variation of Young's modulus nor Poisson's ratio could explain the observed discrepancies.

In a second step, strain hardening was introduced in the calculation. The model used was a strain hardening version of the neo-Hookean model (Gent's model) as described in chapter 1.

Optimization of the parameters was done on PU4000 tensile and compression data, using the small strain Young's modulus obtained by DMA, see in Appendix A4.6. The following parameters were obtained:

$E = 1.3 \text{ MPa}$  (fixed by DMA results)

$I_m = 18$ , corresponding to a finite extensibility in a tensile test of  $\lambda_{\max}=4.5$ .

Figure 4.23 presents the experimental curves and the three simulation curves, of the PU4000 model network. The difference between experimental curves and simulation is about 20 to 30%, with the simulation predicting a lower stiffness than the experimental curves. Having experimental results stiffer than the numerical predictions was an unexpected result; then several questions about the experiments were double checked and answered.



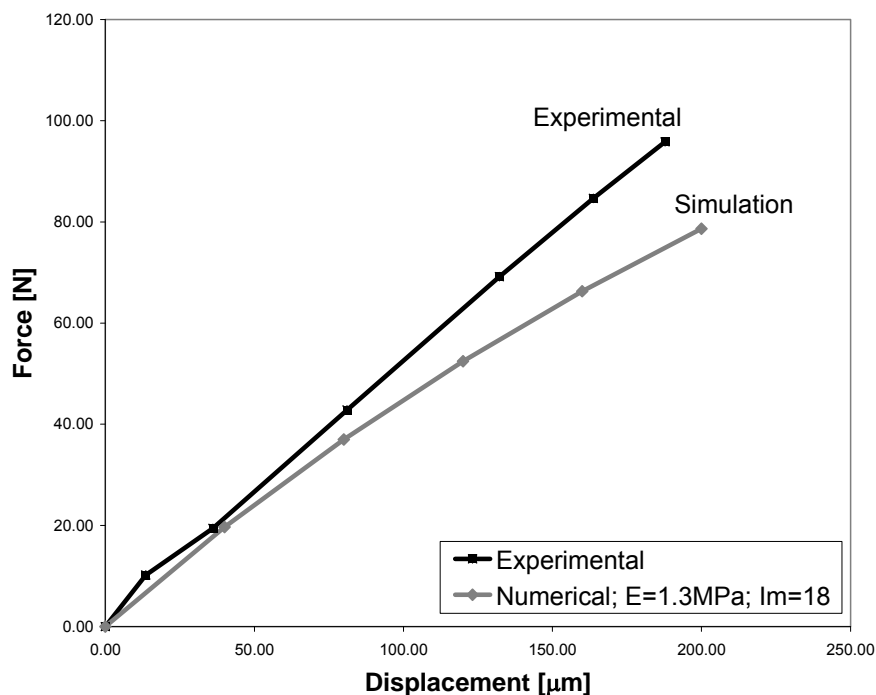


**Figure 4.23:** Fitting of the cavitation PU4000 data using Gent's model.

To look at possible explanations of these differences we checked several aspects:

1) Geometrical effects: Such as the radius of the glass lenses and the measurement of 'h'. The radius of the glass lens was confirmed by profilometry, and the result was  $R=18.2\text{mm}$ , which is the same reported by the provider. Comparing the geometry of demolded blanks with that of the mold we found an identical shape, confirming the absence of residual stresses. The measurement of 'h', was verified by two techniques.

2) Material properties, such as difference in modulus between the films used for the DMA measurements and cavitation samples. Because the films used to carry out DMA and the cavitation samples were cured in slightly different conditions as mentioned in Chapter 3 ('open' environment versus completely confined environment, in the oven) the question about a possible difference in curing between films and cavitation samples came out. Swelling results did not show significant differences. However in order to have also a mechanical experiment to answer this particular point, two kind of compression samples were prepared, one under completely confined environment (same as cavitation samples) and another one in an 'open' environment. Both results were compared, and the differences in modulus between 'closed' and 'open' environments, for the three materials, were less than 10%. Such difference was expected considering that polyurethanes' preparation is very sensitive to the environment and our curing times are relatively long. However, this difference is too small to explain the gap between simulation and experimental results.

3) Residual (extra) polyurethane on the edges of the samples on the glass lens that remains after demolding could change the resistance of the material during cavitation testing. Regarding this question, a simulation was done considering this extra material, and the result was that the influence of having this extra material was negligible.

Then, we concluded that the difference between the simulation and the experimental data comes from another factor that we did not take into account. Because our study is dealing with the same geometry, we have been mainly focused on comparative analysis. In any case such difference of 20-30% between experimental results and simulation can be considered acceptable.

## Conclusions

The objective of this chapter was to describe the experimental methodology developed to study cavitation.

### On the chosen geometry

- Even if the so called “poker chip” (flat-to-flat) geometry has been the most used geometry reported in the literature, some practical aspects such as the control on the parallelism are difficult to set. Then mainly for practical reasons we chose the sphere-to-flat geometry for the cavitation sample’s preparation, which gives less confinement but slight higher concentration of the hydrostatic stress to the centre of the sample. The chosen aspect ratio  $a/h = 10/1$  together with the higher concentration of the stress to the centre for this geometry, allowed us to observe most of the time one single cavity very close to the centre of the sample.
- To ensure good and strong interfacial bonds between the glass and the polyurethane, the top and bottom surfaces of the mold were chemically modified with amino-terminated monolayers, which guarantee that failure occurs in the bulk of the polyurethane.
- Lateral transparency of the cavitation samples was achieved by using metallic molds.

### On the very low compliance of the cavitation testing

- A new samples’ holder was designed and built to perform the cavitations experiments. We obtained a quite stiff set-up in which the compliance was very low ( $0.1\mu\text{m}/\text{N}$  or  $10^7 \text{ N/m}$ ). This set-up was specially designed to have a good top view of the sample through one camera positioned in front of the machine and a good lateral visualization with a second camera.

### On the analysis of the cavitation experiments

- Thanks to the synchronization of the data acquisition and video imaging, it was possible to obtain the curves of force versus displacement for each sample and to know where and when the cavities appeared (all the experimental results are presented in Chapter 5). Because the main interest of this Thesis was to look at the nucleation of cavitation our study was focused on the first part of the curve force versus displacement passing through three main ‘regions’: the ‘linear’ initial part of the curve, the pre-critical cavities region which appears from certain force and remain stable, until the critical cavity appears at the maximal force, the maximal force, corresponding to 1 cavity growing close to the centre of the sample; and there was a fourth region which was not analyzed, corresponding to the crack propagation.

- High reproducibility in the curves of force versus displacement was obtained, when comparing several samples of the same material and same condition.

#### On the analysis of the cavitation experiment by simulation

- Simulations using Finite Element Method (FEM) were performed and the relation between the force applied to the sphere and the local hydrostatic stress was obtained. For this, a calibration factor was calculated for our specific geometry, independent of the elastic modulus and dependant on the Poisson's ratio. The combination of the calibration constant and the simulation of the radial stress distribution made it possible to calculate a reasonably accurate value of the local stress for cavity appearing in the sample before or at the peak force.
- The comparison of the experimental stress-strain curve with simulation results, done by using the Gent's model, gave differences of ~20-30% between the experimental data and the simulation, for the three networks. After double checking all the possible causes, we concluded that a geometric factor that was not properly taken into account was probably causing the difference but that such a difference for the compliance between experimental results and simulation can be considered relatively low and does not affect greatly the stress values.

#### **Acknowledgments**

In this chapter we would like to thank Jan Stolk from DSM for FEM calculations, and Lucien Laiarinandrasana (ENSMP) for helpful discussions.

Ludovic Olanier for the design and building of the samples'holder, metallic molds, and teflon molds.

## Appendices A4

### Appendix A4.1: Comparison of ‘h’ measured by microscopy and directly in the center

**Table A4.1:** Comparison of measured thicknesses ‘h’ by microscopy and directly measured in the center

Material	‘h’ obtained by microscopy [mm]	‘h’ obtained by direct measure in the center [mm]
PU4000	1.027	1.03 ; 1.02 ; 1.04
PU8000	1.0	1.01 ; 1.00 ; 1.02
PU8000/1000	1.16	1.15 ; 1.16 ; 1.14

### Appendix A.4.2 Samples’holder

*Figure A4.1 presents the samples’ holder pieces and in Table A4.1 are listed the pieces.*

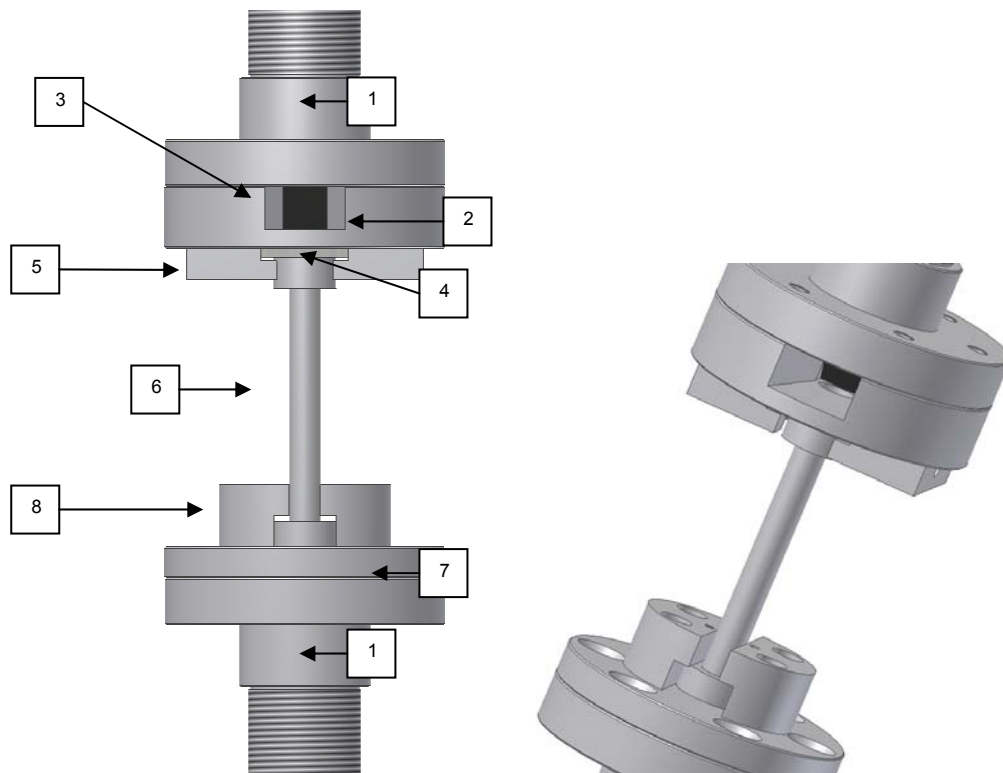


**Figure A4.1:** Schematics of the design of the samples’ holder

**Table A4.2:** List of pieces corresponding to each part of the samples' holder

Number	Piece description
1	base adaptor
2	high support
3	support mirror and mirror
4	Sample
5	Clamps
6	Probe
7	Base
8	T-piece

The set up works as follow:

The probe with the sample (4+6) is placed on the central part of the base (7), and it is fixed by screws that are on the T-piece (8). The bottom part, which is the mobile part connected to the hydraulics, moves up until it touches the upper part (2), and the clamps (5) are brought to the center and the sample is fixed by using screws. The optical fiber is placed in the lateral holes, left in the clamps for illumination of the sample; and the extensometer is fixed to the bottom part of the hydraulics, below the bottom base adaptor (1). Finally, the two cameras are set up in front of the samples' holder for obtaining the best possible imaging from the top view trough the mirror (3) and from the lateral view.

#### Appendix A4.3: Reproducibility of the curves obtained for cavitation experiments

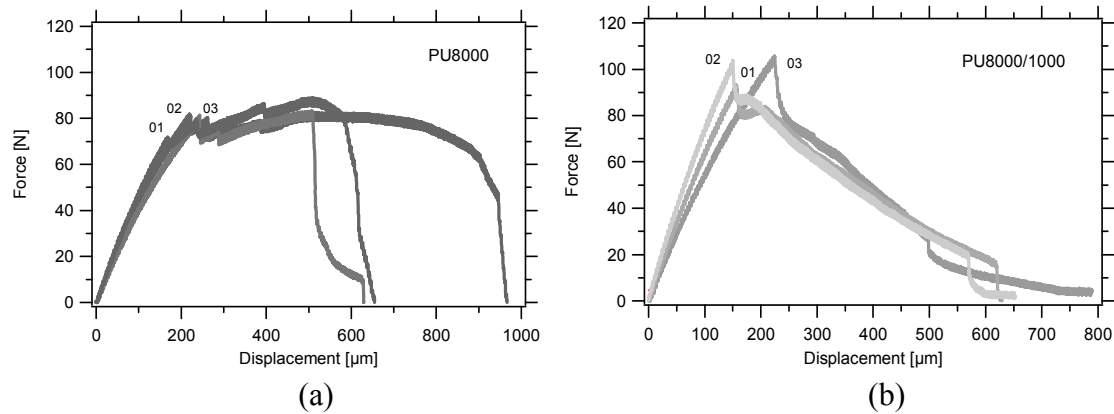
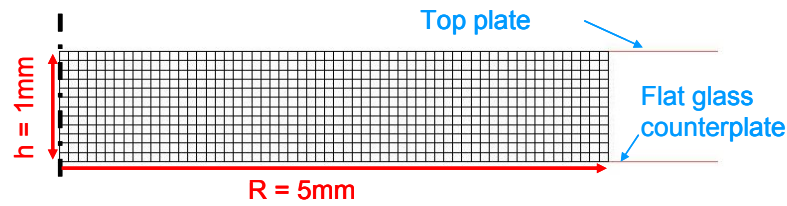


**Figure A4.2:** Reproducibility of the maximal force for different samples in (a) PU8000 and (b) PU8000/1000

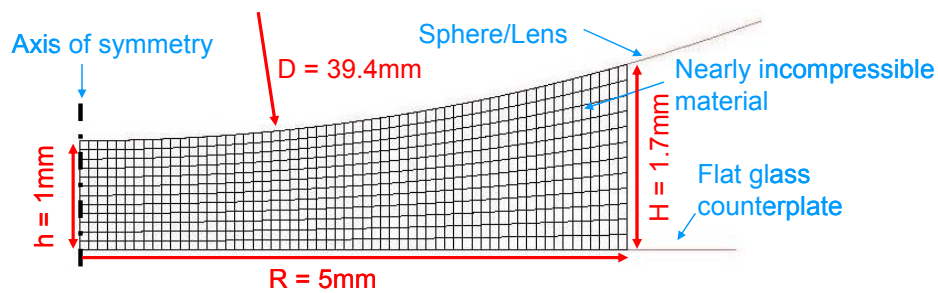
#### Appendix A4.4: Triaxiality of sphere-to-flat versus flat-to-flat

Approach:

- Use sphere-to-flat model and build new axisymmetric model for flat-to-flat geometry
- Material properties:  $E = 1 \text{ MPa}$ ,  $\nu = 0.49994$
- Lift sphere (in case of sphere-to-flat) or top plate (in case of flat-to-flat) by  $\Delta u = 0.2 \text{ mm}$
- Calculate hydrostatic stress distribution and force on sphere, and the response of the top plate



**FEM model for flat-to-flat geometry**



**FEM model for sphere-to-flat geometry**

#### Appendix A4.5: Calibration constant calculation

For typical values of  $\nu$  (0.499-0.49999) the calibration constant is virtually constant, meaning that also the hydrostatic stress is virtually constant

**Table A4.3:** Variation of Poisson's ratio versus calibration constant

Poisson's ratio	Calibration constant [MPa/N]
0.49	0.0279
0.4925	0.0287
0.495	0.0297
0.4975	0.0307
0.499	0.0313
0.4995	0.0315
0.4999	0.0317
0.49994	0.0317
0.49999	0.0317

By FEM, for different thicknesses 'h' values lower than 1.2 mm and higher than 0.8 mm, calibration factors were calculated, and the results are reported in Table A4.3. Then for a given value of thickness a calibration factor was obtained and using equation 4.2, the hydrostatic stress can be calculated.

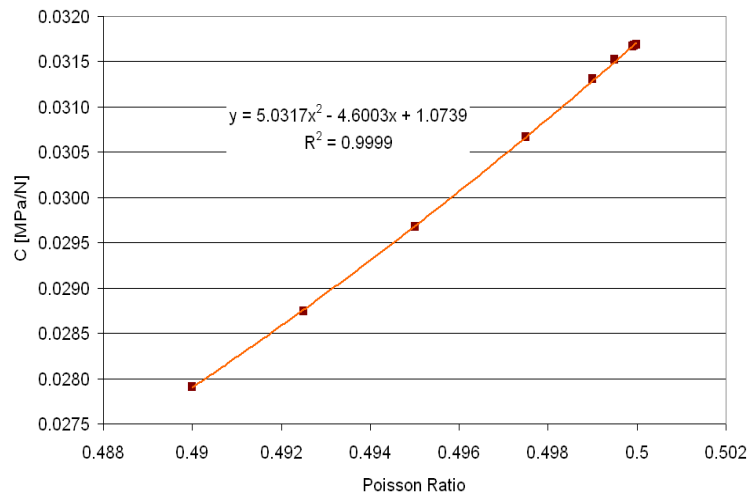


**Figure A4.3:** Calibration constant versus Poisson's ratio.



**Table A4.4:** Dependence of the calibration factor on the samples' thickness.

<b>h [mm]</b>	<b>F [N]</b>	<b><math>\sigma_{\text{hydr, max}}</math> [MPa]</b>	<b>Calibration factor [MPa/N]</b>
0.80	121.7	4.202	0.0345
0.85	108.1	3.647	0.0337
0.90	96.6	3.189	0.0330
0.95	86.7	2.808	0.0324
1.00	78.3	2.483	0.0317
1.05	71.0	2.209	0.0311
1.10	64.7	1.982	0.0306
1.15	59.3	17.84	0.0301
1.20	54.4	1.610	0.0296

**Appendix A.4.6: Fitting of hyperelastic model with experimental compression and tension data.**

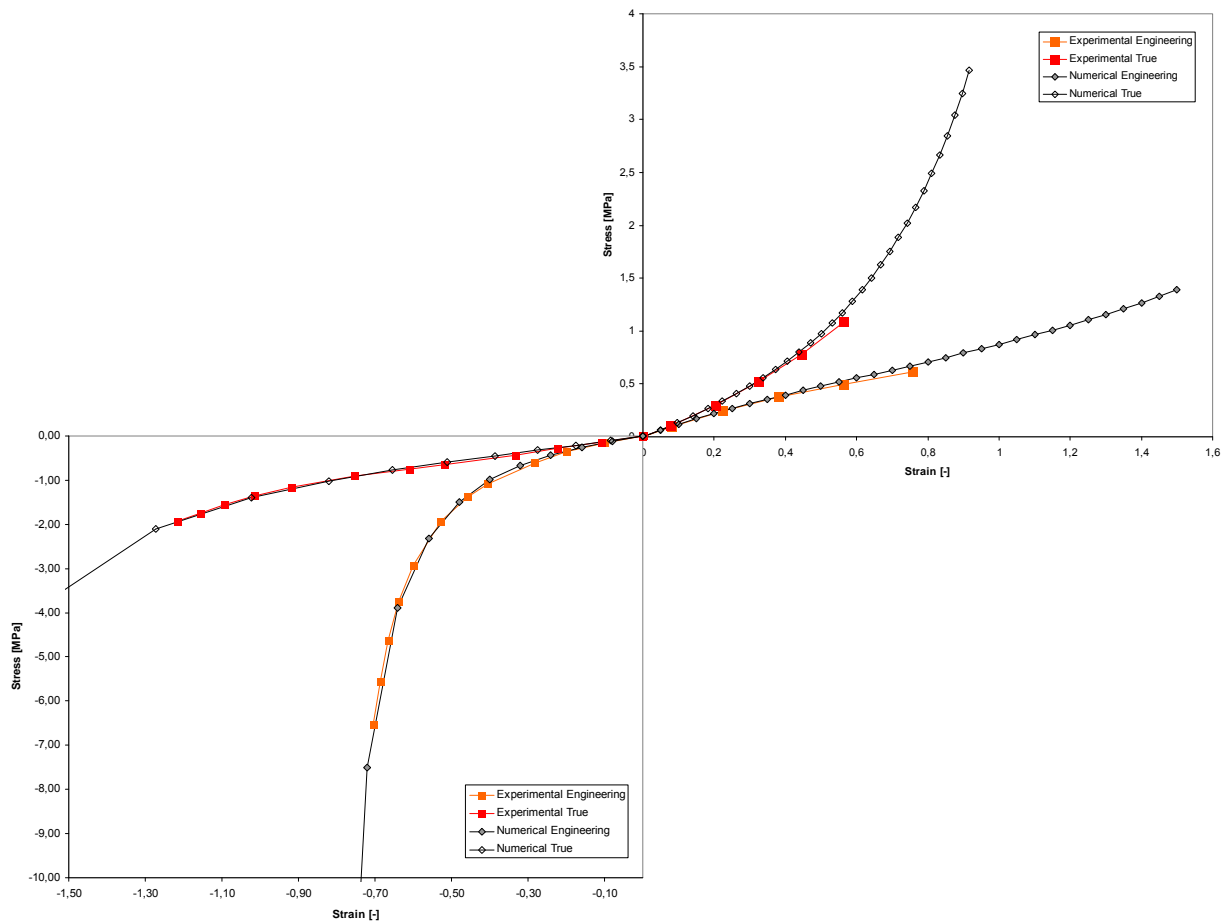


**Figure A4.4:** Fit of hyperelastic model (Gent's model) with experimental data for tension and compression, PU4000. ( $E=1.3\text{MPa}$  ;  $I_m=18$ ).

## Bibliography

- Busse W.F., Physics of rubber as related to the automobile, *Journal of Applied Physics*, 9, 438-451 (1938)
- Cho, K. and Gent, A.N., *Journal of Materials Science*, 23, 141-144 (1988)
- Denecour, R.L. and Gent, A.N., *Journal of Polymer Science Part A-2*, 6, 1853-1861 (1968)
- Fond, C., Lobbrecht, A., Schirrer, R., *Int. Journal of Fracture*, 77, 141-159 (1996).
- Gent A.N. and Lindley P.B., *Proc. Roy. Soc. A*249, 195-205 (1959).
- Gent A.N. and Tompkins, D.A., *J. Appl. Phys.*, 40, 2520, (1969)
- Gent, A. N., *Engineering with Rubber, USA*, 1992.
- Gent, A.N. and Park, B., *Journal of Polymer Science*, 19, 1947-1956 (1984).
- Green A.E. and Zerna W., *Theoretical elasticity*, Oxford Univ. Press, London (1954).
- Hall, E.O., *Proc. Physics Society, London*, 64B, 747 (1951).
- Hamdi A., *Université des Sciences et Technologies de Lille, Laboratoire de mecanique de Lille UMR, PhD thesis* (2006)
- Herrmann, L.R. and Toms, R.M., *J. Appl. Mech. Trans. ASME*, 85, 140-141 (1964).
- Herrmann, L.R., *AIAA J.*, 3 (10), 1896-1900 (1985).
- Lindsey, G.H., Schapery, R.A., Williams, M.L. and Zak, A.R., *Report of the California Institute of Technology, Aerospace Research Laboratories, USA Air Force* (1963).
- Oberth, A.E. and Bruenner, R.S., *Trans. of the Society of Rheology*, 9(2), 165-185 (1965)
- Oberth, A.E., *Rubber Chemistry and Technology*, 40, 1337-1363 (1967)
- Petch, N.J., *Journal Iron Steel Institute, London*, 174, 174 (1953)
- Yerzley, F.L. *Adhesion of Neoprene to metal, Ind. and Eng. Chem.*, 31, 950-956 (1939).



# **Chapter 5**

## **Cavitation Phenomena: Experimental Mechanisms**

Introduction .....	185
5.1.- Experimental cavitation results at standard conditions (room temperature) .....	186
5.1.1. General trends: Shape of the curve and Maximal hydrostatic stress.....	186
5.1.1.1. PU4000.....	186
5.1.1.2. PU8000.....	189
5.1.1.3.- PU8000/1000 .....	191
5.1.1.4.- Comparative analysis: maximal hydrostatic stresses and critical cavity formation .....	193
5.1.2.- Critical cavity growth - Crack propagation (Region B).....	196
5.1.3.- Morphology of the fracture surfaces.....	197
5.2.- Cavitation results at different temperatures .....	199
5.2.1.- Experimental part and results at different temperatures .....	199
5.2.1.1.- General trends .....	199
5.2.1.2.- Critical cavity size and crack propagation .....	204
5.2.1.3.- Fracture morphology.....	204
5.3.- Cavitation results at different strain rates .....	206
5.3.1.- Experimental part and results at different strain rates .....	206
5.3.1.1.- General trends .....	206
5.2.1.2.- Critical cavity size and crack propagation .....	209
5.2.1.3.- Fracture morphology.....	210
5.4.- Pre-critical cavities analysis.....	211
5.4.1.-Lateral profile: Volume change .....	211
5.4.2.- Conditions of pre-critical cavity formation.....	212
5.4.2.1.- Pre-critical cavities analysis at standard conditions.....	214
5.4.2.2.-Pre-critical analysis at high temperature.....	215
5.4.2.3.-Pre-critical analysis at low strain rate .....	216
Conclusions .....	219
Acknowledgments .....	220
Appendices A5 .....	221
Appendix A5.1: Cavitation results at standard conditions .....	221
Appendix A5.2: Cavitation results at different temperatures.....	223
Appendix A5.3: Cavitation results at different strain rates .....	226
Bibliography.....	227

## Introduction

Chapter 4 described in detail the experimental methodology to investigate the failure of the three polyurethane model networks by cavitation. As mentioned in Chapter 4, the phenomenon of cavitation in elastomers has been previously observed and studied by several groups [Busse 1938, Yerzley 1939, Gent and Lindley 1959, Cho and Gent 1988, Oberth and Bruenner 1965, Oberth 1967, Gent and Park 1984, Hall 1951, Petch 1953, Lindsey *et al.* 1963, Denecour and Gent 1968, Gent and Tompkins 1969, Hamdi 2006, Bayraktar 2008] mostly using rubber-metal bonded disks of large diameter-to-height ( $a/h$ ) ratios.

However, all these experiments were performed at room temperature with different types of elastomers. To the best of our knowledge none of the cavitation experiments reported in the literature examined the effect of parameters such as strain rate or temperature.

Additionally, none of the experimental cavitation studied before have really focused on the events occurring before the stiffness drops macroscopically so that the physical mechanism of nucleation of the cavities is not fully understood. The first abrupt drop in stiffness has usually been considered as the signature of cavitation events.

In an effort to answer this question we designed and performed well controlled cavitation experiments on fully transparent elastomers at different loading rates and temperatures. An optical real time visualization of the damage events inside the elastomers during the loading was designed specifically to capture the early growth stages of the cavities (as presented in chapter 4).

With the purpose of establishing a relationship between the molecular architecture of the polymer networks and their resistance to cavitation, we studied and compared three polyurethane model networks, PU4000, PU8000 and PU8000/1000. An important practical question motivating this thesis and addressed in this chapter was if we could prepare a tough material with a high resistance to cavitation.

Several aspects have been examined:

- 1) The use of the local maximal hydrostatic stress to predict cavitation resistance;
- 2) The effect of changing material and experimental parameters on the shape of the curves force versus displacement;
- 3) The effects of the temperature and the possible thermal activation of the process;
- 4) The effects of the strain rate on the cavitation and the role played by the viscoelasticity;
- 5) The crack propagation once the critical cavity has appeared.
- 6) The morphology of the fracture surfaces after complete fracture, and
- 7) A qualitative study of pre-critical cavities has been made.

Chapter 4 described the experimental setup and argued that the reason to use a sphere-to-flat geometry was to avoid multicavitation and in this chapter our choice of geometry is confirmed. In this Chapter we present all the experimental cavitation results. For each

experimental condition, five tests for each polyurethane model network were carried out. The results presented in this chapter are an average of the three most representative tests, for each condition and each material.

Figure 5.1 recalls figure 4.15 in which the different stages of the process were represented on the curve force versus displacement. Since the cavitation criterion reported in the literature [Green and Zerna 1954, Gent and Lindley 1959, Fond 1996] is related to a critical value of the local hydrostatic stress for the growth of a cavity, in the first part of this chapter (sections 5.1, 5.2 and 5.3) we analyze the curve force versus displacement from the peak, that corresponds to the maximal force (and maximal hydrostatic stress) to the later stages related to the crack propagation. In the last section of this chapter (section 5.4) we analyse the left side of the curve force versus displacement, in which pre-critical cavities are observed and a qualitative analysis is carried out.

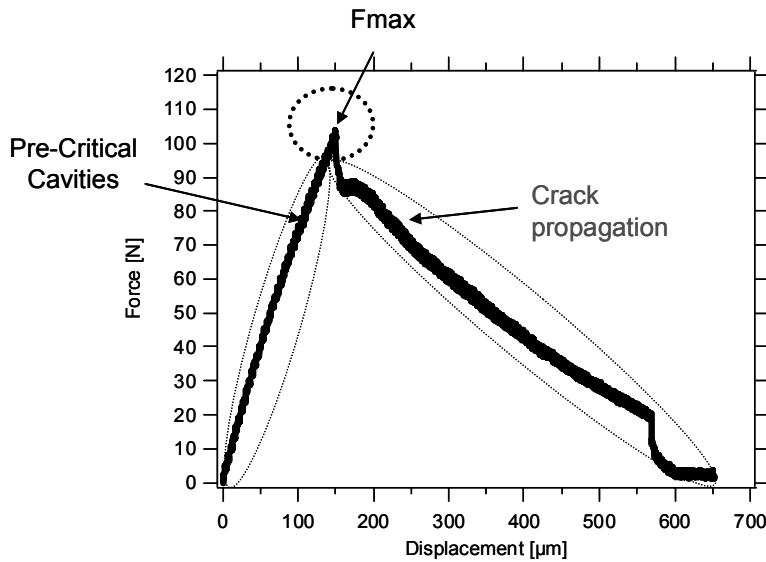


**Figure 5.1:** Parts of the force versus displacement curve analyzed in this chapter in the experimental cavitation results.  $F_{\max}$ =critical crack growing.

## 5.1.- Experimental cavitation results at standard conditions (room temperature - $\dot{\epsilon} \sim 10^{-2} .s^{-1}$ )

Using the cavitation samples prepared as mentioned in chapter 4, experiments under standard conditions, defined as  $T=25^{\circ}C$  and  $V=10\mu m/s$  (initial strain rate  $\sim 1\%/s$ ), were carried out to compare the different polyurethane model networks.

### 5.1.1. General trends: Shape of the curve and Maximal hydrostatic stress

#### 5.1.1.1. PU4000

Figure 5.2 shows a representative experimental curve of force versus displacement obtained for PU4000 at standard conditions. The maximal force that corresponds to the critical cavity

growing occurs at around  $\sim 15\%$  strain; this relatively low strain shows the fragility of the sample. The numbers in the figure corresponds to the synchronized imaging acquisition of force as a function of time (and displacement). Every number is associated to one image and one event happening in the sample during the tensile experiment. The corresponding pictures taken from the top view and from the lateral view for PU4000, are presented in Figures 5.3 and 5.4, respectively. Figure 5.3 presents the time and position of the cavities observed during the data acquisition (camera rate 25fps). We observe that only one single cavity appears just before the maximal force is reached and then grows from the center to the edges. However in the early stages, the shape of the growing cavity as seen from the combined top and side projection is far from spherical and grows perpendicular to the tensile direction (Figure 5.3 and 5.4 (2, 3)) then in the direction of traction (compare Figure 5.4 (4 and 5)) and finally becomes circular in the top view (Figure 5.3 (5, 6)). During the growing of the cavity, after maximal force, the force drops first very fast and then slower until zero force (complete fracture). As one would expect, the observed images and the video clearly point out a fracture process rather than any reversible deformation.

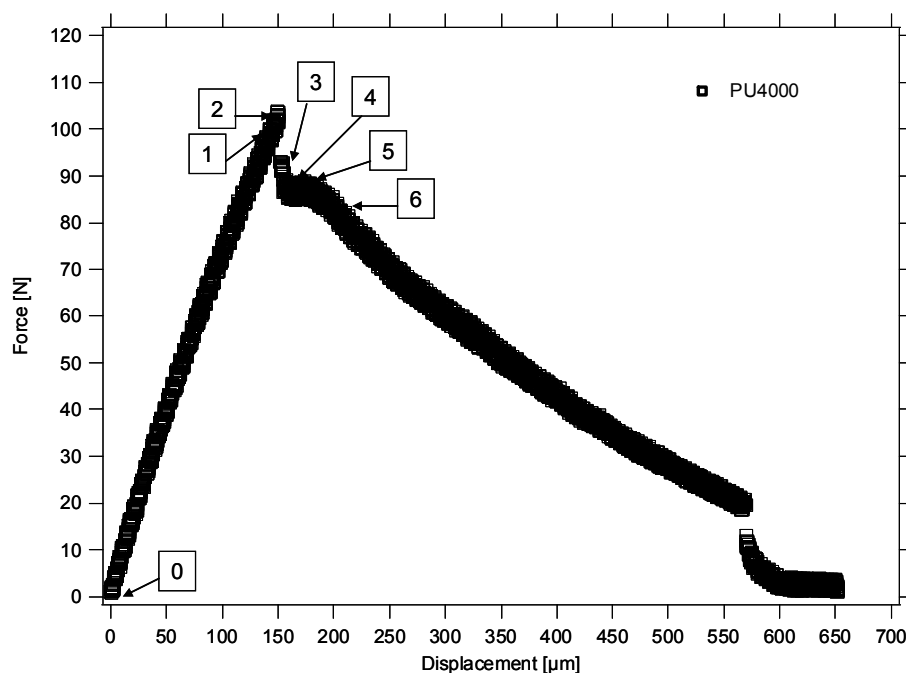


**Figure 5.2:** Typical curve of PU4000 at standard conditions (25°C and 10 $\mu\text{m/s}$ ) obtained during the cavitation experiment.

Figures 5.3 and 5.4, show for PU4000 only one critical cavity growing. This is typically what was observed for the PU4000. Figure 5.4 shows the lateral view for PU4000. We observe that the critical cavity appears in the centre of the sample, close to the glass lens surface where hydrostatic stress is seen to be maximum.



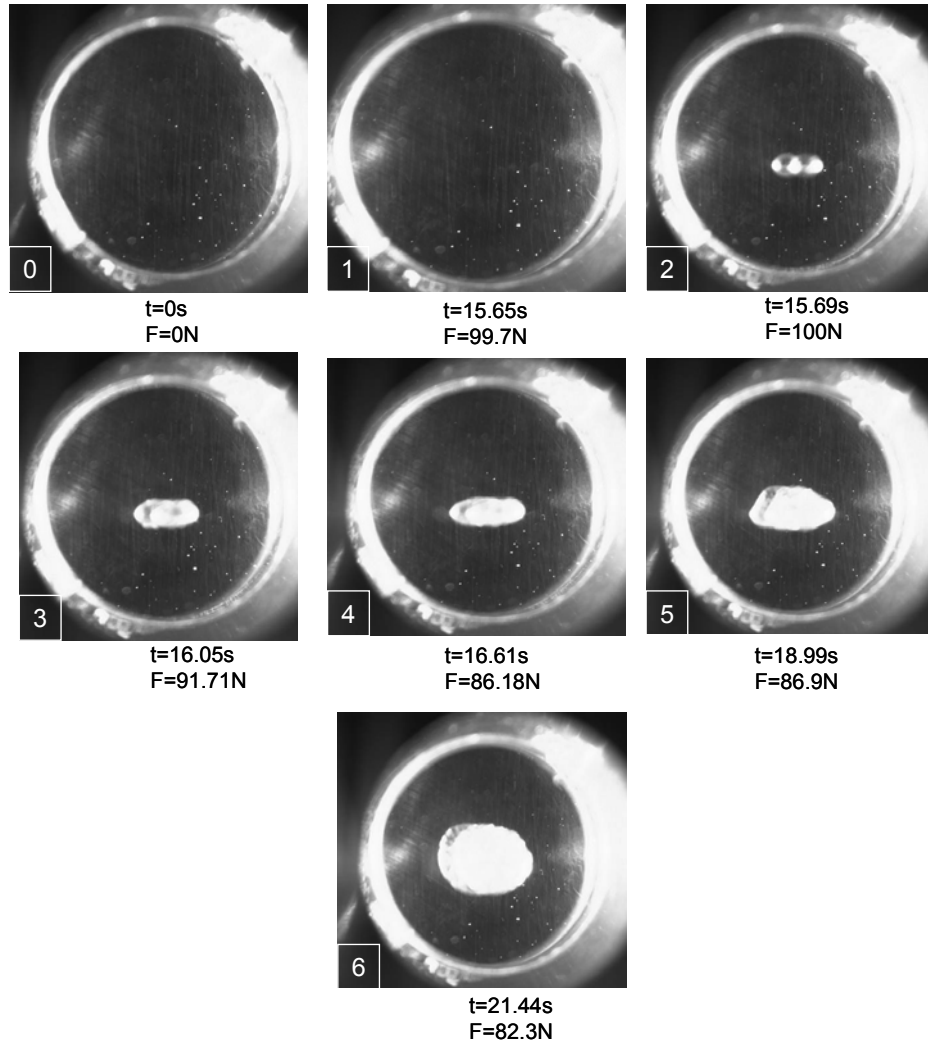


**Figure 5.3:** Images of PU4000 obtained from the top view @ 25fps and synchronized with the force versus displacement data acquisition, at standard conditions. Note that picture 1 and 2 are two consecutive images. Cavity size in picture 2 is around 1mm.

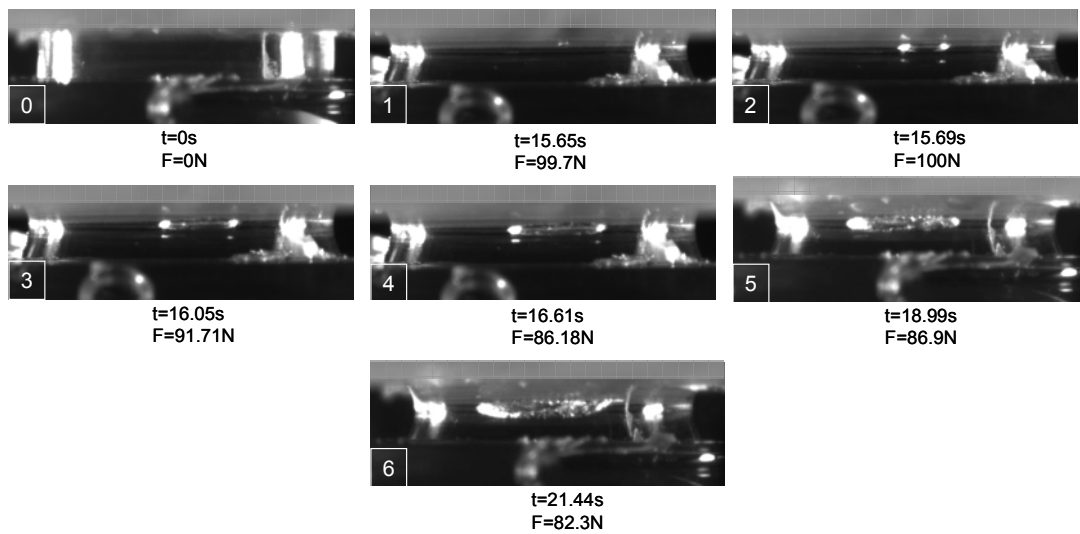


**Figure 5.4:** Images of PU4000 obtained from the lateral view @ 26.36fps and synchronized with the force versus displacement data acquisition, at standard conditions.

### 5.1.1.2. PU8000

The cavitation behaviour of PU4000 was compared with PU8000, to analyze the effect of having two different molecular structures with two different crosslink densities, close to and above the average molecular weight between entanglements ( $M_e \sim 3000 \text{ g/mol}$ ). Figure 5.5, presents a typical curve of force versus displacement obtained for PU8000 at standard conditions. Qualitatively, significant differences between the curve of PU4000 and PU8000 were observed.

In PU8000, the first peak is reached at a lower force than for PU4000 (see Appendix A5.1) and occurred at a mean strain around 20%. The shape of the curves are different, with more than one well defined peak so that the final drop of the force (before complete fracture) occurs at much higher mean strain, above 50% (see Figure 5.11).

The reason why the curve of PU8000 shows more than one peak is that more than one cavity is growing in the sample: each peak corresponds to one cavity growing, see Figures 5.6 and 5.7. When the first large cavity reaches a size where growth nearly stops or at least slows down to the point that the macroscopic force increases, then a second macroscopic cavity grows. For the PU4000 elastomer, a single growing large cavity was always observed while for PU8000 at least two large cavities appeared before the final ruin of the sample. PU8000 has stable crack propagation, where the force increases still during propagation, showing higher crack propagation resistance than the other two materials.

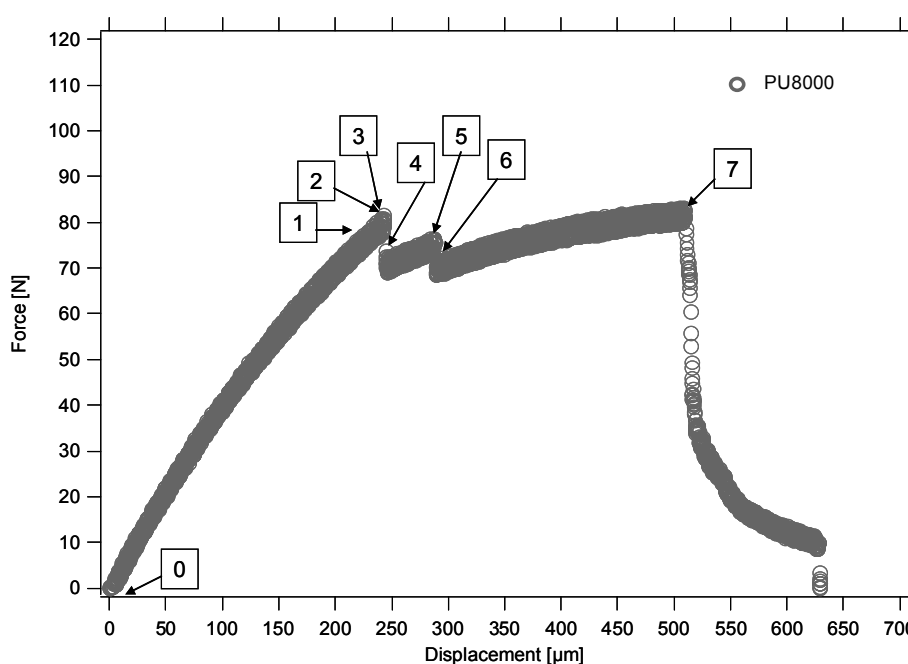


**Figure 5.5:** Typical curve of PU8000 at standard conditions (25°C and 10 $\mu\text{m/s}$ ) obtained during the cavitation experiment.

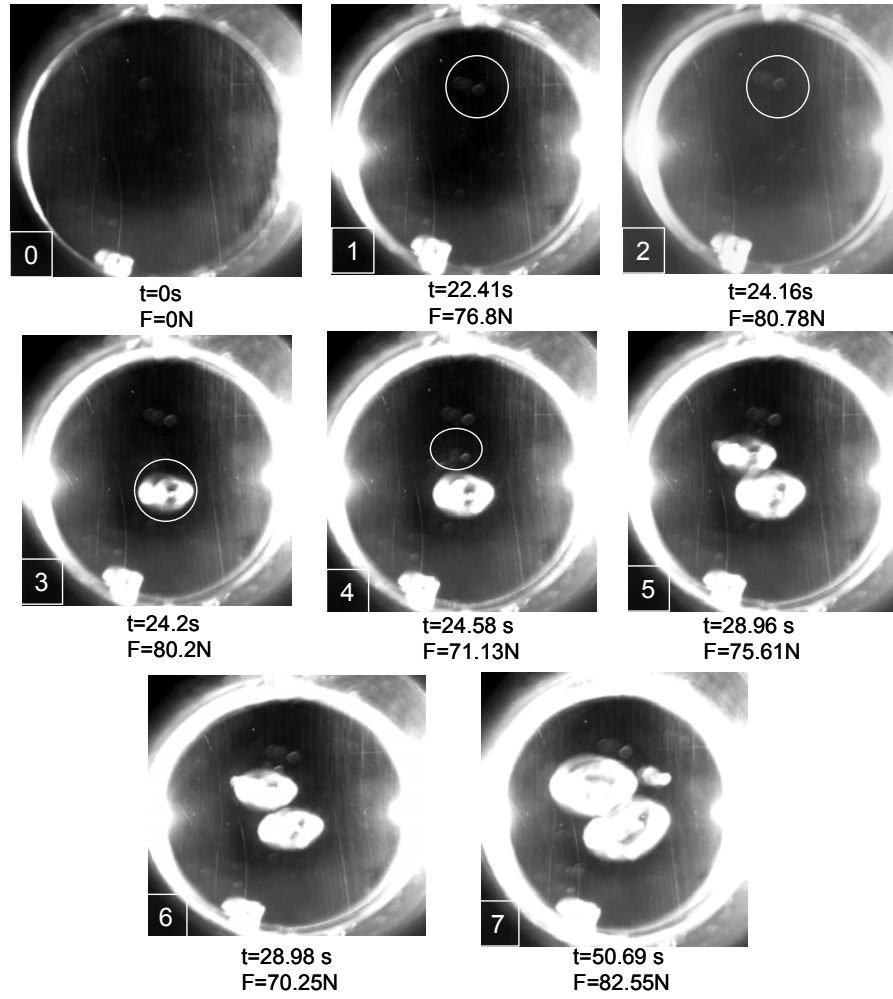


**Figure 5.6:** Images of PU8000 obtained from the top view @ 25fps and synchronized with the force versus displacement data acquisition, at standard conditions. Note that picture 2 and 3 are two consecutive images. Cavity diameter in picture 3 is around 1.4mm.

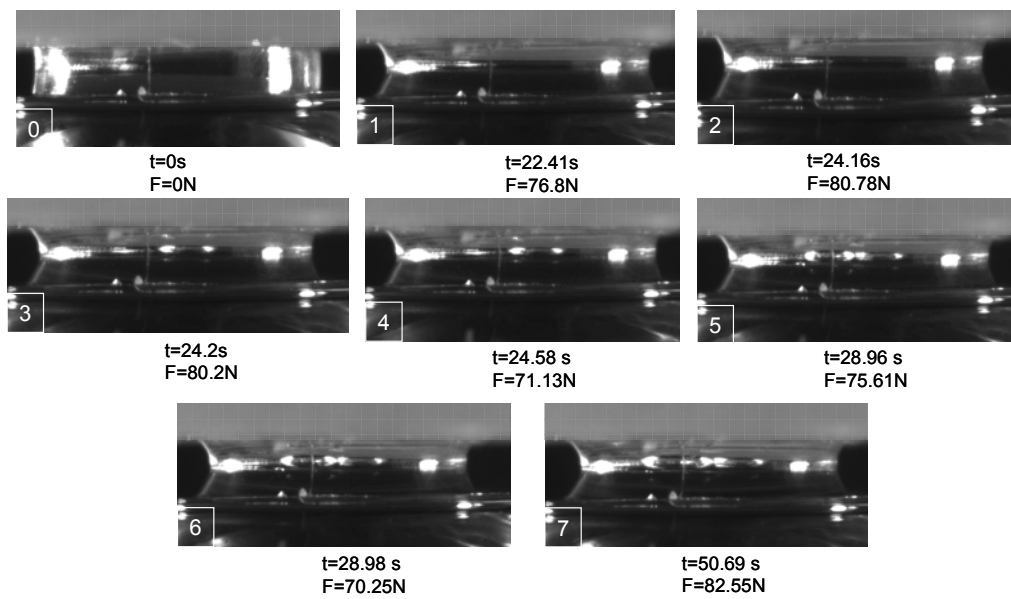


**Figure 5.7:** Images of PU8000 obtained from the lateral view @ 26.36fps and synchronized with the force versus displacement data acquisition, at standard conditions.

### 5.1.1.3-. PU8000/1000

The cavitation behaviour of PU8000 in the cavitation experiments was compared with PU8000/1000, to investigate the effect of adding short chains (PPG1000) to long chains (PPG8000). Figure 5.8 presents a typical curve of force versus displacement obtained for PU8000/1000 at standard conditions. Figures 5.9 and 5.10 present the top view and the lateral view, respectively. Several pre-critical cavities were observed (small cavities seen as white spots). They appear and remain stable and only one cavity grew very close to the centre of the sample, similar to the situation for the PU4000. We also observe that the shape of the curve is similar to that of the PU4000, but the force is slightly higher (see Appendix A5.1) as well and the fracture of the sample occurs at around 17% average strain.

One single cavity was seen to grow close to the centre of the sample when the maximal force is reached. The fracture was brittle with non-controlled crack propagation in all cases for the three materials.

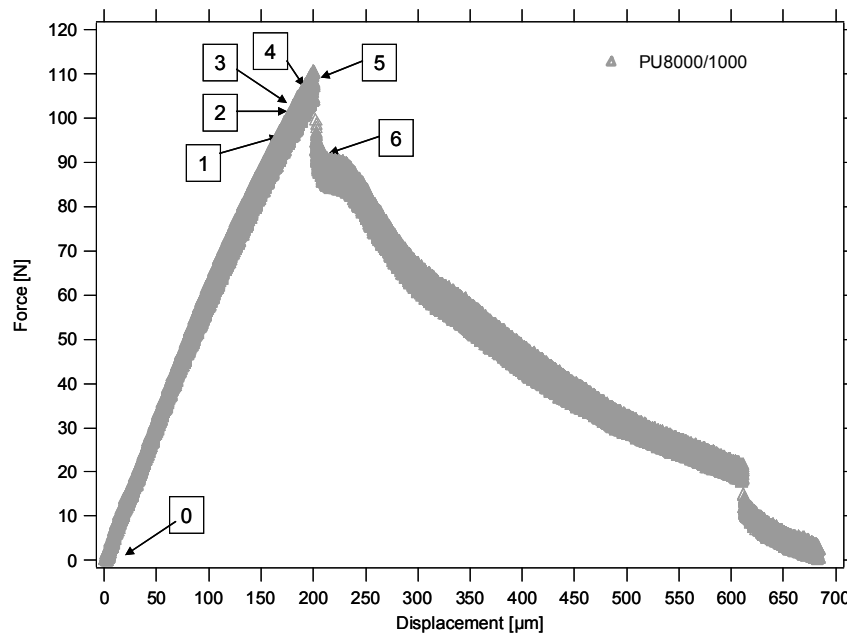


**Figure 5.8:** Typical curve of PU8000/1000 at standard conditions (25°C and 10μm/s) obtained during the cavitation experiment.

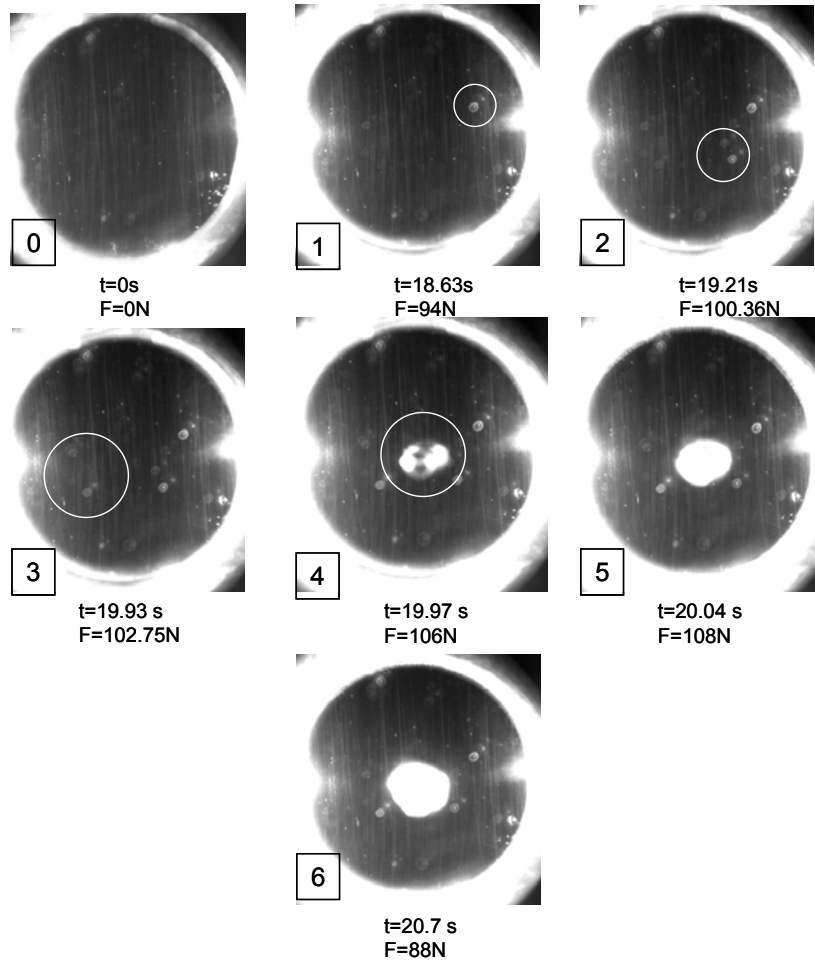


**Figure 5.9:** Images of PU8000/1000 obtained from the top view @ 25fps and synchronized with the force versus displacement data acquisition, at standard conditions. Note that picture 3 and 4 are two consecutive images. Cavity diameter in Picture 4 is around 1.2mm.

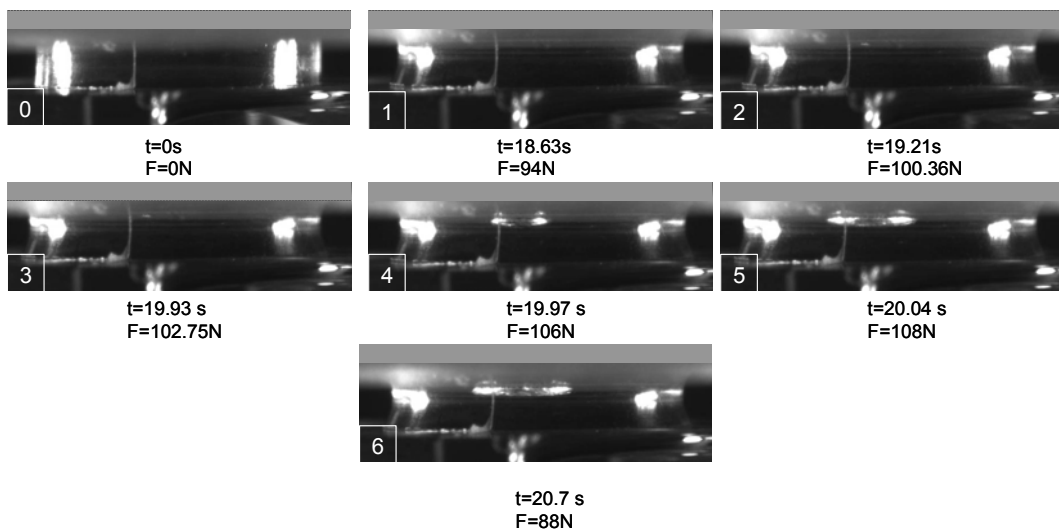


**Figure 5.10:** Images of PU8000/1000 obtained from the lateral view @ 26.36fps and synchronized with the force versus displacement data acquisition, at standard conditions.

#### 5.1.1.4.- Comparative analysis: maximal hydrostatic stresses and critical cavity formation

##### Shape of the force-displacement response

Figure 5.11 shows a comparison of the cavitation curves obtained at standard conditions for the polyurethane model networks. We observe that the three curves are non-linear, and the stiffness of the materials clearly scales with the modulus (as presented in chapter 2 and 3). In a very confined geometry the stiffness of the cavitation curves becomes less dependent on the shear modulus of the materials and more on the bulk modulus and on the boundary conditions (which are nearly identical for the three materials), but since our geometry sphere-to-flat the material is less confined we do observe that the stiffness depends on the shear modulus.

As mentioned in chapter 3 the three polyurethane model networks are rather brittle and have relatively low  $G_{IC}$  at standard conditions. This brittleness is also reflected in the cavitation results, since the maximal force that corresponds to the critical cavity growing occurs at relatively low strain for the three polyurethane model networks. When comparing the materials we do observe that the effect of adding 20% wt. of PPG1000 to PPG8000 cancels the effect of having long chains (with entanglements) in terms of maximum extension at fracture, giving a bimodal network (PU8000/1000) with similar behavior as the monomodal PU4000.

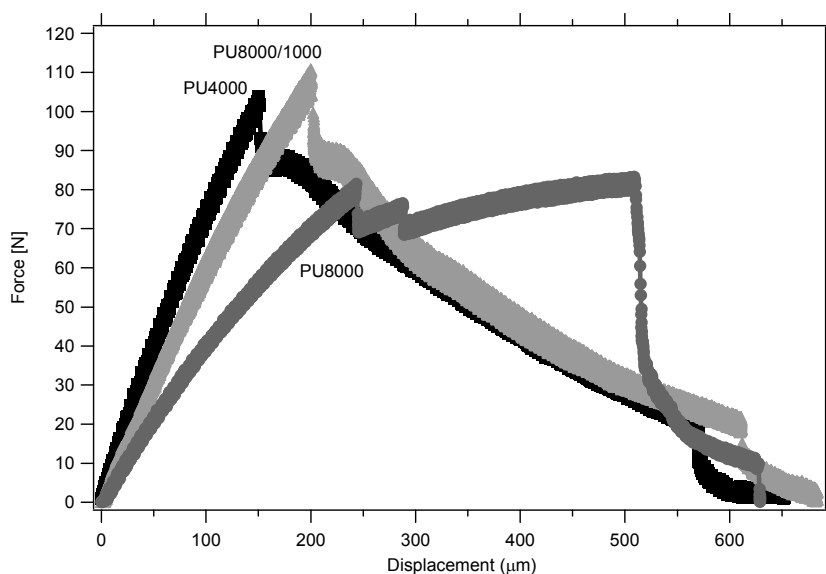


**Figure 5.11:** Comparison of cavitation curves for the three polyurethane model networks at standard conditions.

##### Maximal hydrostatic stress

Table 5.1 presents the average maximal hydrostatic stress obtained at standard conditions, for the three polyurethane model networks. The methodology to go from the maximal force (unique peak for PU4000 and PU8000/1000 and first peak for PU8000) to the maximal

hydrostatic stress was presented in Chapter 4. Incidentally, we observe that the critical hydrostatic stresses obtained at standard conditions are almost five times the fracture strength of the materials in uniaxial tension (Figure 3.4).

The cavitation phenomenon was experimentally observed by Gent and Lindley [Gent and Lindley 1959] in rubber disks. They observed that the stress at which the cracks form was highly reproducible, as we did. They used the nonlinear theory of elasticity to explain the unstable cavity growth in elastomers in which when a critical value of the negative pressure is reached then any cavity in the rubber will grow to infinite size. There were several problems with this simple theoretical approach and in particular Gent assumed reversible deformation and not fracture, and ignored the surface tension. Williams and Schapery [Williams and Schapery 1965] predicted the same result with a critical stored energy criterion. It is interesting to note that both models used a critical constant pressure inside the cavity and an infinite medium, which are not the experimental situations.

Yet, they found experimentally that the critical stress for cavitation was directly proportional to the Young's modulus of the rubber. Table 5.1 shows that PU4000 has higher maximal hydrostatic stress than PU8000/1000 followed by PU8000. This ranking scales well with the modulus of the materials; however, when the hydrostatic stress is normalized by using the modulus of the material the scaling is inverted. In other words the cavitation stress scales with the modulus but is not directly proportional to it. Figure 5.12 puts graphically in evidence this dependence on the modulus.

**Table 5.1:** Maximal hydrostatic stress  $\sigma_{\text{hydro, max}}$ , and hydrostatic stress normalized by the Young' modulus, for the three polyurethane model networks, at standard conditions.

<b>Material</b>	<b>E [MPa]</b>	<b><math>\sigma_{\text{hydro, max}}</math> [MPa]</b>	<b><math>\sigma/E</math></b>
<b>PU4000</b>	$1.3 \pm 0.08$	$3.25 \pm 0.13$	2.50
<b>PU8000</b>	$0.8 \pm 0.06$	$2.45 \pm 0.08$	3.06
<b>PU8000/1000</b>	$1.2 \pm 0.07$	$3.09 \pm 0.15$	2.58

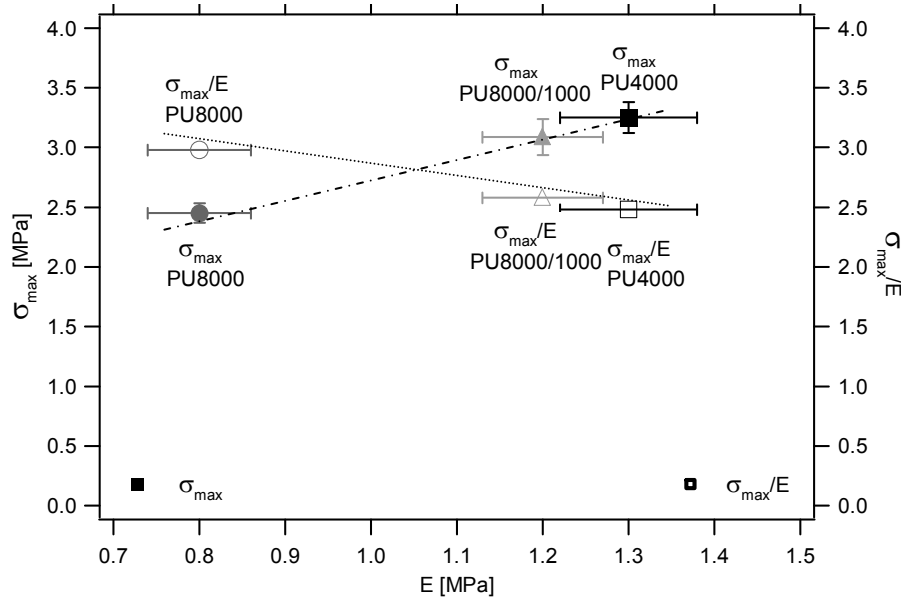


**Figure 5.12:** Maximal hydrostatic stress  $\sigma_{\text{hydro, max}}$ , and hydrostatic stress normalized by the Young' modulus, for the three polyurethane model networks, at standard conditions.

### Critical cavity formation

Our experimental results have shown sequences of images that have been synchronized with force and time (as explained in chapter 4). For our cameras acquisition rate the time elapsed between two consecutive frames was 0.04s, then the average rate at which the critical cavity grows initially can be estimated. Figure 5.13 shows three region of critical cavity growth.

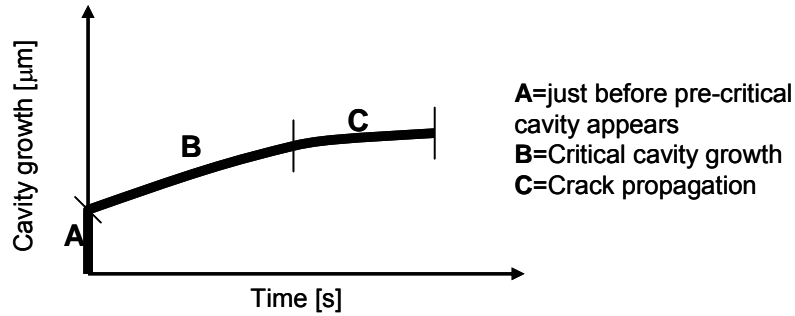


**Figure 5.13:** Schematic of critical cavity growth.

In the region A the crack growth is very fast and is calculated between two consecutive images from which nothing can be seen and the critical cavity appears. Once the critical cavity is visible and starts growing the process is still uncontrolled but slower (region B), and in the later stages of the crack propagation (region C) the growth rate of the cavity slows down further and is now controlled by the applied crosshead displacement rate until complete fracture occurs.

In region A, we observed that once the critical cavity appears the process is quite rapid. A small cavity that looks first grey and then white, burst and grows. The transition from not



visible critical cavity to a visible critical cavity with a certain size takes place a time shorter than the time between two successive frames, i.e. in less than 40 ms. The size of the first observable cavity and the estimated growth rates is shown in Table 5.2.

**Table 5.2:** Initial size and growth rate of the critical cavity at standard conditions.

<b>Material</b>	<b>Initial size [mm]</b>	<b>Growth rate [mm/s]</b>
<b>PU4000</b>	1 x 0.5	26
<b>PU8000</b>	1.4 x 0.7	36
<b>PU8000/1000</b>	1.2 x 0.7	31

Such big visible and measurable initial sizes mean that we are seeing cavities growth and not the cavities nucleation. It is expected that a much smaller pre-critical cavity existed before the critical cavity appeared but it was not visible to us. The camera speed and resolution, limit the visualization of the actual initial defect from which the fracture grows.

### **5.1.2.- Critical cavity growth - Crack propagation (Region B)**

The shape of the cavity and the growing rate depends on the material. From top view, the critical cavity grows in two directions, ‘size I’ corresponds to the longer size and ‘size II’ corresponds to the perpendicular direction to I.

Figure 5.14 presents an example of the curves of the critical cavity growing as a function of time (see Appendix A5.1 for reproducibility). We observe that PU4000 has one side ‘size I’ growing faster than the other side ‘size II’, which means an initial growing with oval shape which afterwards become circular (or with radial shape).

For PU8000/1000 we observed either an initial oval shape followed by circular shape, or a circular shape growing from the beginning, and for PU8000 the growing cavity was always circular. For PU8000 the growth rate of the critical cavities was lower than for PU4000 and PU8000/1000. Note that the graphs of Figure 5.14 correspond to region B in Figure 5.13.

As the displacement is increased the critical cavity propagates along a principal normal stress trajectory until the two pieces are completely apart. Figure 5.15 shows a typical picture of the fracture surfaces; we observe that the initial damage occurs in the central region of the sample, meaning that the cavity/cavities were in the bulk of the material and never at the elastomer/glass interface. Such cases were rare and the results were discarded.

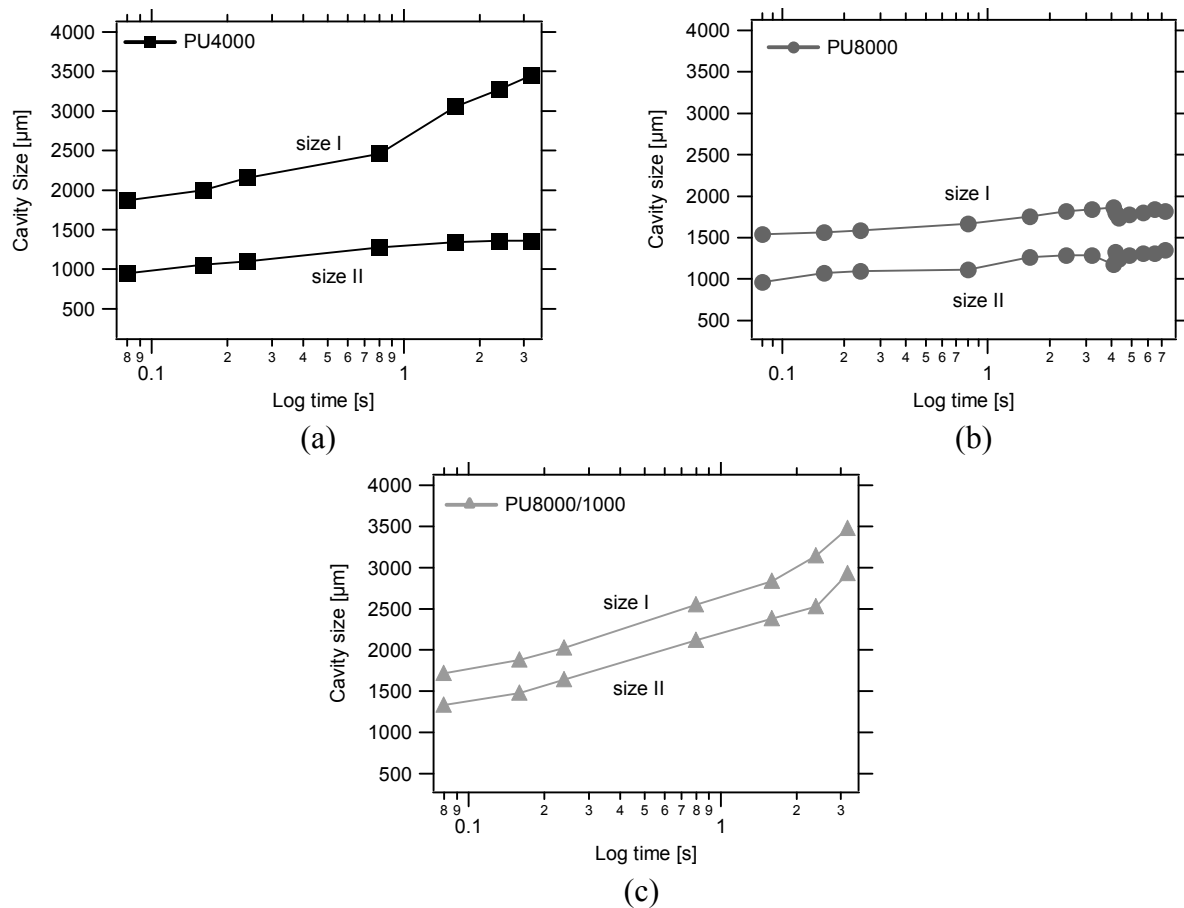


**Figure 5.14:** Critical cavity growth for: (a) PU4000, (b) PU8000 and (c) PU8000/1000, at standard conditions.



**Figure 5.15:** Lateral view of a cavitation sample just after complete fracture.

### 5.1.3.- Morphology of the fracture surfaces

Once the samples were completely fractured, the fracture surface were observed by optical microscopy. Figure 5.16 shows the fractured surface of a PU4000 sample (PU8000/1000 fractured surface looks very similar, see Appendix A5.1). Most of the surface is very rough, which is related to the velocity of propagation [Lindsey 1966, Knauss 1965], being that slower process gives rougher surface. On the left side we observe that the fracture initiation was very close to the centre of the sample and that a crack of  $\sim 1.5$ -2mm long was first formed. By focusing closer on the fracture (right side of the figure) we observe that the surface of the crack is inclined at an angle of approximately  $\sim 45^\circ$ -  $90^\circ$ , and that it forms a ‘step’. The

change in surface is abrupt, indicating a rapid change from slow to fast mode. These observations are consistent with the real time observations showing first a fast growth of a crack close to the center of the sample followed by a controlled fracture propagating outwards. A similar morphology was observed for PU8000/1000.

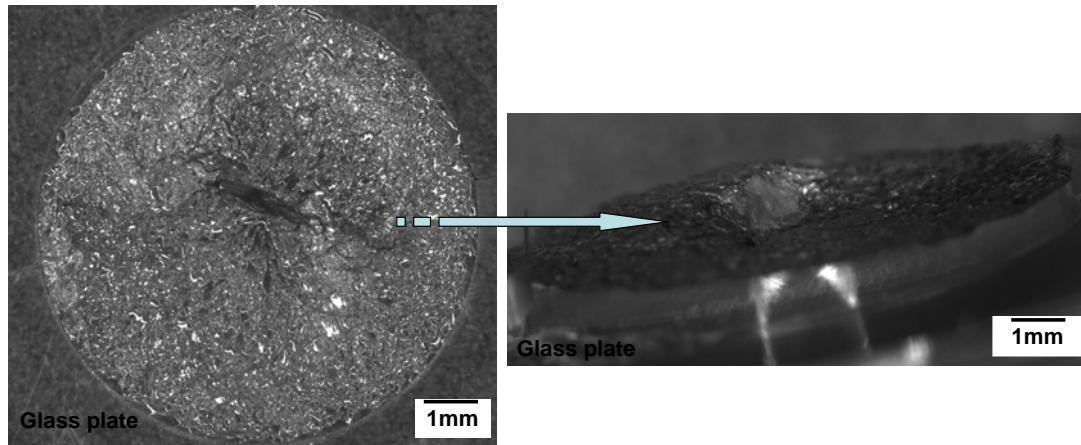


**Figure 5.16:** Typical optical microscopy fractured surface of PU4000 after cavitation, at standard conditions. Similar fracture surface is observed for PU8000/1000.

Figure 5.17 shows the fractured surface of a PU8000 sample. We observe that the traces of 3-4 oyster-shaped cavities are visible. Because cavity growth stops due to the toughness of the material, the stress keeps increasing as the material is deformed and several cavities can grow one after the other. The second nucleation of failure is typically less catastrophic and smaller in size. The fracture surface is virtually planar, consequently what had appeared to be a bubble growing while the fracture was being observed is believed to have actually been a penny-shaped crack in the plane normal to the tensile direction. Probably the fracture nucleates from a specific point (or in this case several points) where an initial defect in the material exists.

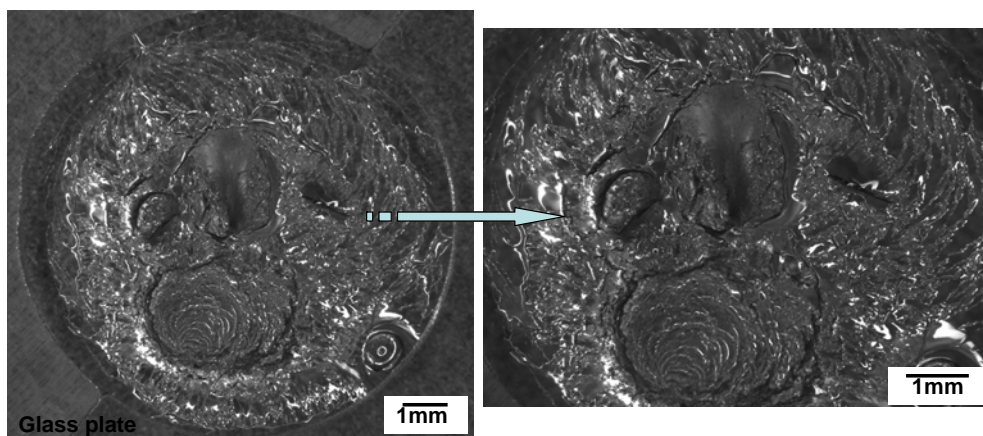


**Figure 5.17:** Optical microscopy fractured surface of PU8000 after cavitation, at standard conditions.

## 5.2.- Cavitation results at different temperatures

With the purpose of evaluating the effect of the possible thermal activation on the cavitation process, experiments at different temperatures were carried out for the three polyurethane model networks. This section presents the main results. All the comparisons are done with the cavitation results that were obtained at ‘standard conditions’.

### 5.2.1.- Experimental part and results at different temperatures

#### 5.2.1.1.- General trends

To perform these cavitation experiments the same initial speed used at standard conditions was maintained which was  $10\mu\text{m/s}$  (initial strain rate  $\sim 1\%/s$ ) but the temperature was varied. To perform the experiments at different temperatures the heating chamber in the MTS machine was maintained closed to heat up the samples (as presented in section 4.3). The effect on the behaviour of the materials at three additional higher temperatures was evaluated:  $50^\circ\text{C}$ ,  $70^\circ\text{C}$  and  $100^\circ\text{C}$ .

Figure 5.18 shows typical curves of force versus displacement at standard conditions  $25^\circ\text{C}$  and at  $100^\circ\text{C}$ . The curves and the values of force at  $25^\circ\text{C}$ ,  $50^\circ\text{C}$ ,  $70^\circ\text{C}$  and  $100^\circ\text{C}$ , for the three materials are presented in Appendix A5.2. We observe that when the temperature is increased ( $100^\circ\text{C}$ ) the critical force is reached at lower values than at standard conditions ( $25^\circ\text{C}$ ) and the shape of the curves changes. The propagation regime becomes much faster and less controlled as the temperature is increased.

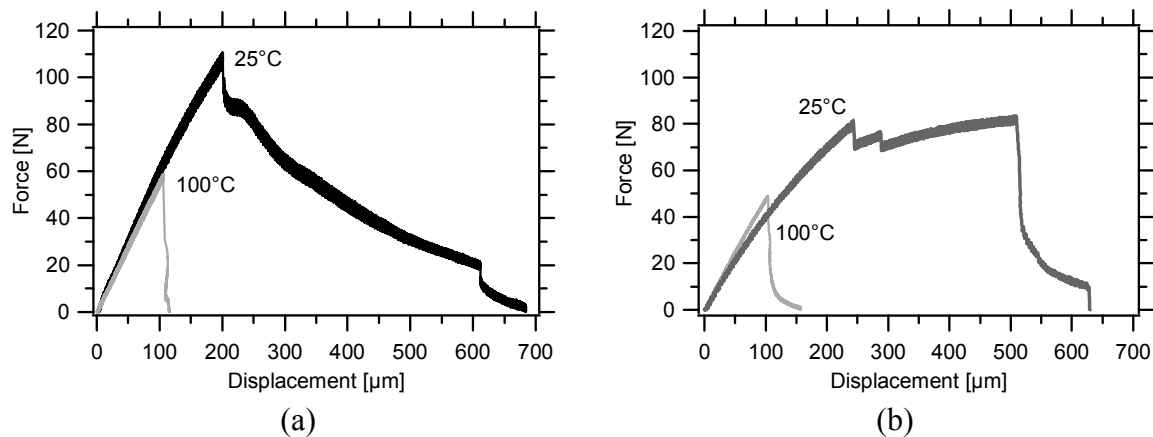


**Figure 5.18:** Typical cavitation curves showing a lower critical force at higher temperatures. Comparison at  $10\mu\text{m/s}$ ,  $25^\circ\text{C}$  and  $100^\circ\text{C}$  for: (a) PU4000 and PU8000/1000; (b) PU8000.

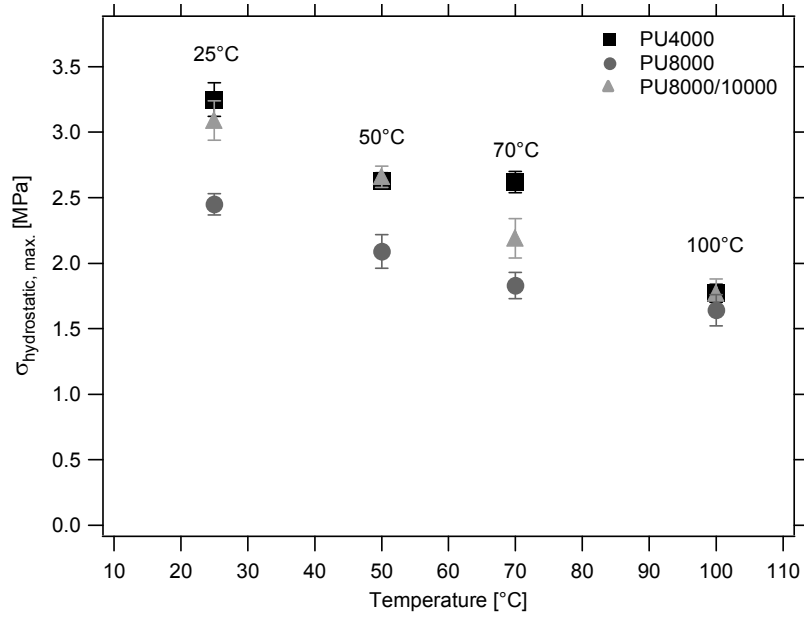
Table 5.3 presents the calculated values of maximal hydrostatic stress for the different temperatures and the three materials. The values of maximal force and displacement are reported in Appendix A5.2. Figure 5.19 shows graphically the maximal hydrostatic stress as a function of temperature and we observe that for higher temperatures the hydrostatic stress decreases for the three polyurethane networks. The fracture results in chapter 3 reported that

at higher temperature the fracture toughness decreases significantly. Higher stiffness when the temperature is increased is due to the thermoelasticity of the elastomers, and was already observed by DMA in chapter 2 and in the fracture experiments described in chapter 3. Since we observe the same effect of the temperature on the fracture and cavitation results, we can say that the temperature in the cavitation experiments acts on the toughness of the material: showing that an increase of the temperature leads to a decrease in the toughness of the material, even in confined conditions.

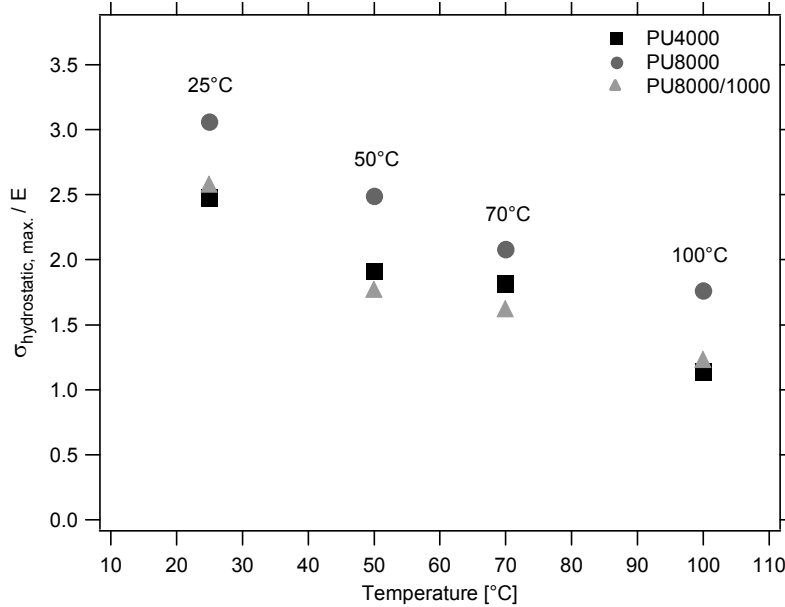
When the three polyurethane model networks are compared at different temperatures, we observe that, at all the temperatures, the order of resistance to cavitation from higher to lower is  $\text{PU4000} \geq \text{PU8000/1000} > \text{PU8000}$  which scales with the respective modulus of the materials at different temperatures (as stated by Gent and Lindley). However, when the maximal hydrostatic stress is normalized by the modulus, we observe (see Figure 5.20) that the order is inversed showing PU8000 higher cavitation resistance related to its modulus than PU4000 and PU8000/1000, at all the temperatures.

**Table 5.3:** Modulus, maximal hydrostatic stress  $\sigma_{\text{hydro, max}}$ , and hydrostatic stress normalized by the modulus for the three polyurethane model networks, at different temperatures.

Materials	Temperature [°C]	E [MPa]	$\sigma_{\text{hydro, max}}$ [MPa]	$\sigma_{\text{max}} / E$
<b>PU4000</b>	25	$1.3 \pm 0.08$	$3.25 \pm 0.13$	2.50
	50	$1.38 \pm 0.07$	$2.63 \pm 0.06$	1.91
	70	$1.45 \pm 0.09$	$2.62 \pm 0.08$	1.81
	100	$1.55 \pm 0.04$	$1.77 \pm 0.07$	1.14
<b>PU8000</b>	25	$0.8 \pm 0.06$	$2.45 \pm 0.08$	3.06
	50	$0.84 \pm 0.03$	$2.09 \pm 0.13$	2.49
	70	$0.88 \pm 0.04$	$1.83 \pm 0.10$	2.08
	100	$0.93 \pm 0.04$	$1.64 \pm 0.12$	1.76
<b>PU8000/1000</b>	25	$1.2 \pm 0.07$	$3.09 \pm 0.15$	2.58
	50	$1.28 \pm 0.04$	$2.66 \pm 0.08$	1.77
	70	$1.35 \pm 0.06$	$2.19 \pm 0.15$	1.62
	100	$1.44 \pm 0.05$	$1.77 \pm 0.11$	1.23



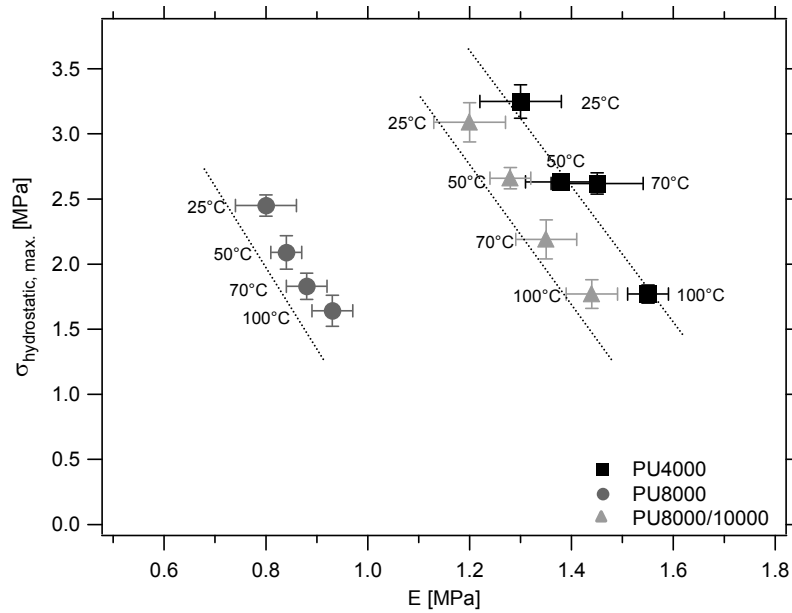
**Figure 5.19:** Maximal hydrostatic stress  $\sigma_{\text{hydrostatic, max.}}$ , as a function of the temperatures 25°, 50°C, 70° and 100°C, and 10 $\mu\text{m/s}$ .



**Figure 5.20:** Maximal hydrostatic stress  $\sigma_{\text{hydro, max}}$  normalized by the modulus, as a function of the temperatures 25°C, 50°C, 70°C and 100°C, and 10 $\mu\text{m/s}$ .

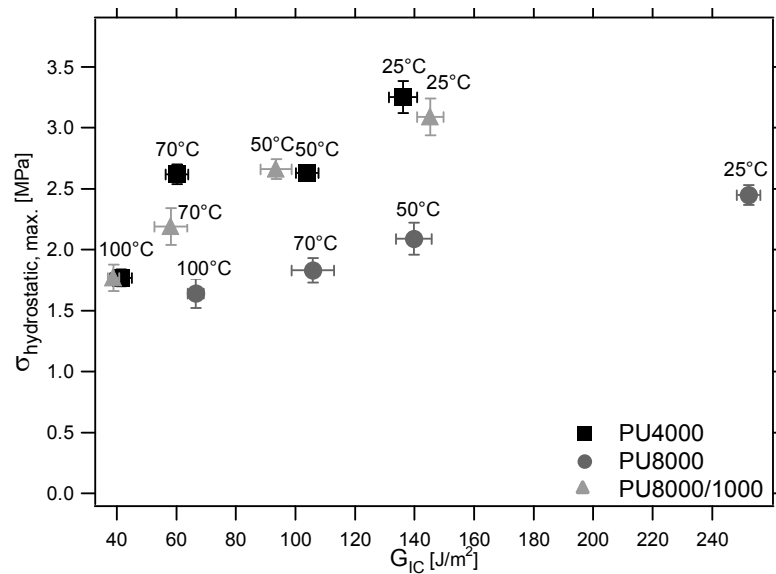
Now as mentioned before, Gent and Lindley [Gent and Lindley 1959] proposed that the critical stress for cavitation was a linear function of the Young's modulus of the rubber, but if we graph our cavitation results at different temperatures as a function of the modulus of the material (see Figure 5.21) we observe that for the three polyurethanes networks while the modulus increases as the temperature increases, the hydrostatic stress decreases and this result goes clearly in the opposite direction as Gent and Lindley's statement. This interesting result provides some clues on the mechanism. Any mechanism purely based on reversible non linear elastic behavior will be unable to capture such a behavior since nonlinear elastic properties

are weakly dependent on the temperature and the modulus of entropic origin increases with temperature.



**Figure 5.21:** Maximal hydrostatic stress  $\sigma_{\text{hydro, max}}$  in function of the modulus at different temperatures 25°, 50°C, 70° and 100°C, and 10 $\mu\text{m/s}$ .

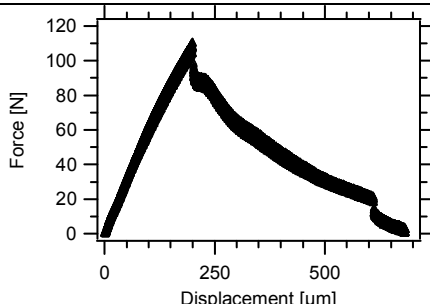
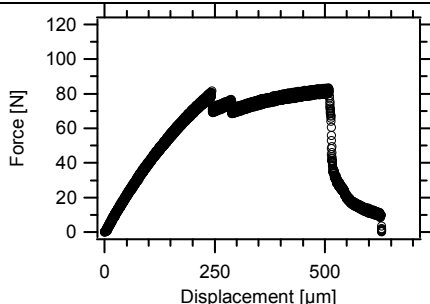
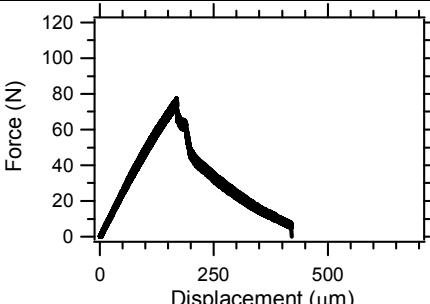
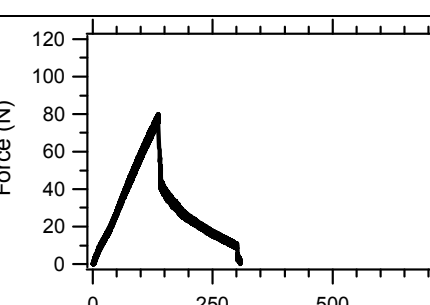
It is therefore interesting to represent the maximal hydrostatic stress as a function of the fracture energy measured in mode I with DEN samples. Figure 5.22 shows that clearly for a given material the resistance to cavitation increases with toughness, which is a new result, but also shows that the elastomer with higher moduli display a higher resistance to fracture in confined conditions as well, stressing the need for a model incorporating both parameters.



**Figure 5.22:** Maximal hydrostatic stress as a function of the critical fracture energy, at different temperatures for the three polyurethane model networks.

Once the critical cavity has appeared the fracture process occurs very fast and in an uncontrolled way. The shape of the curves of force versus displacement changes at the different temperatures for the three polyurethane networks. Table 5.4 presents a summary of the typical changes of the force-displacement curves when the temperature increases for each material. We observe that at higher temperatures than 25°C once the maximal force is reached the force drops sharply and very rapidly.

**Table 5.4:** Typical change of the shape of the cavitation curves for the three polyurethane model networks, at different temperatures.

	Materials		
Curves	PU4000	PU8000	PU8000/1000
	@25 °C		@25 °C
		@25 °C	
		@50 °C @70 °C	
	@50 °C @70 °C @100 °C	@100 °C	@50 °C @70 °C @100 °C



### 5.2.1.2.- Critical cavity size and crack propagation

In general the cavitation process and the growing of the critical cavity occur faster and at lower forces at higher temperatures than at standard conditions. Table 5.5 shows the initial size of the critical cavity (initial size on the region B in Figure 5.13) at 25°C and at 100°C, the measures were roughly calculated but a comparison can be made. We observe that at higher temperatures a smaller critical cavity appears than at standard conditions, for the three materials, but the cavity becomes bigger very fast (Figure 5.23). Additionally, one can see that apparently the initial size of the critical cavity is larger for PU8000 than for the other two materials, at 25°C and higher temperatures. Note that the actual initial defect from which the fracture grows was probably much smaller for both conditions, for the three materials.

**Table 5.5:** Approximate initial critical cavity size at standard conditions 25°C and at 100°C. The critical cavity grows in two directions, the ‘size I’ corresponds to the longer size and ‘size II’ corresponds to the perpendicular cavity size.

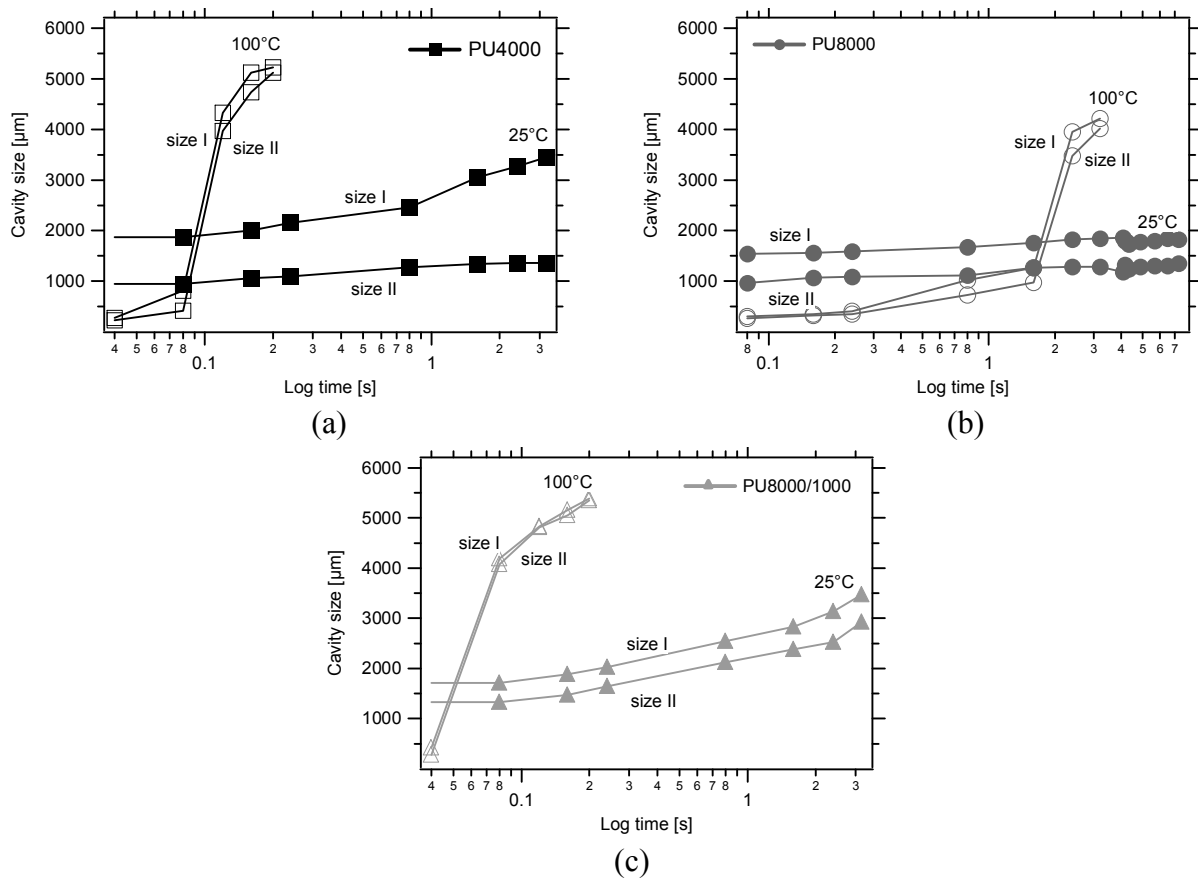
Material	Size I @25°C [mm]	Size II @25°C [mm]	Size I @100°C [mm]	Size II @100°C [mm]
PU4000	1.0 ± 0.28	0.49 ± 0.15	0.27 ± 0.05	0.17 ± 0.04
PU8000	1.4 ± 0.06	0.72 ± 0.26	0.34 ± 0.03	0.28 ± 0.04
PI8000/1000	1.2 ± 0.13	0.71 ± 0.17	0.33 ± 0.03	0.24 ± 0.03

Figure 5.23 shows a comparison of the critical cavity growing as a function of time for standard conditions 25°C and at the highest temperature 100°C. Note that the graphs in Figure 5.23 correspond to region B in Figure 5.13. Upon appearance of the critical cavity the process of cavity growth occurs much faster at higher temperatures than at standard conditions and the fastest fracture process occur at the highest temperature 100°C, for the three polyurethane networks (see Appendix A5.2 for reproducibility).

Compared to standard conditions, at higher temperatures only one critical cavity appears and, from top view, the cavity is circular (symmetric radial growth) for the three materials, since both size I and II growth rates are similar.

### 5.2.1.3.- Fracture morphology

Figure 5.24 presents the micrographs of the fracture surface of PU4000 and PU8000/1000. We observe that at higher temperatures the surfaces display a mirror-like area in the center of the sample which is characteristic of a very fast crack growth encountered typically for brittle fracture. Figure 5.25 shows the fracture surface of PU8000, for higher temperatures ((a) 50°C, 70°C and (b) 100°C). When the materials are compared at higher temperatures, we observe that PU4000 and PU8000/1000 present more damaged surface than PU8000 after cavitation.



**Figure 5.23:** Cavity growth as a function of the time for two temperatures 25°C and 100°C, (strain rate 10μm/s ~ 1%/s) for: (a) PU4000, (b) PU8000 and (c) PU8000/1000.

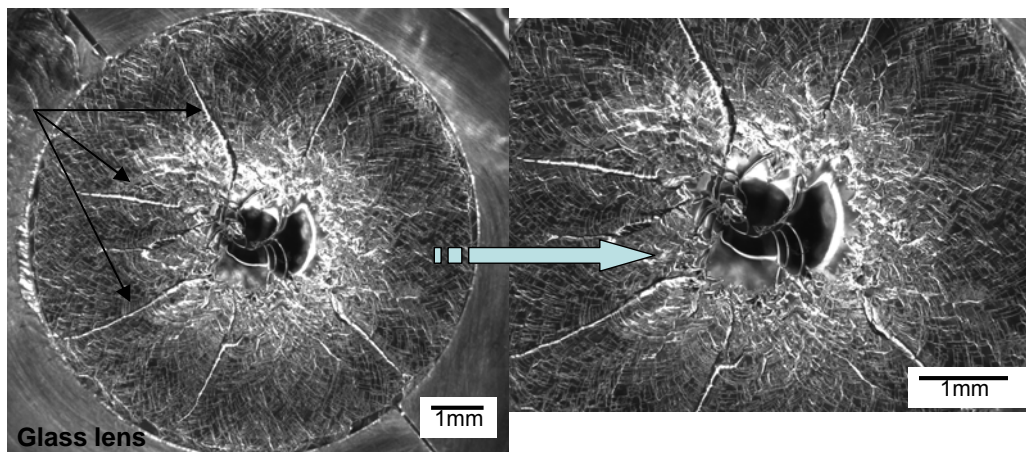


**Figure 5.24:** Typical optical microscopy images of the fractured surface of PU4000 after cavitation at 50, 70°C and 100°C. Similar fracture surface is observed for PU8000/1000. Arrows point out radial cracks.

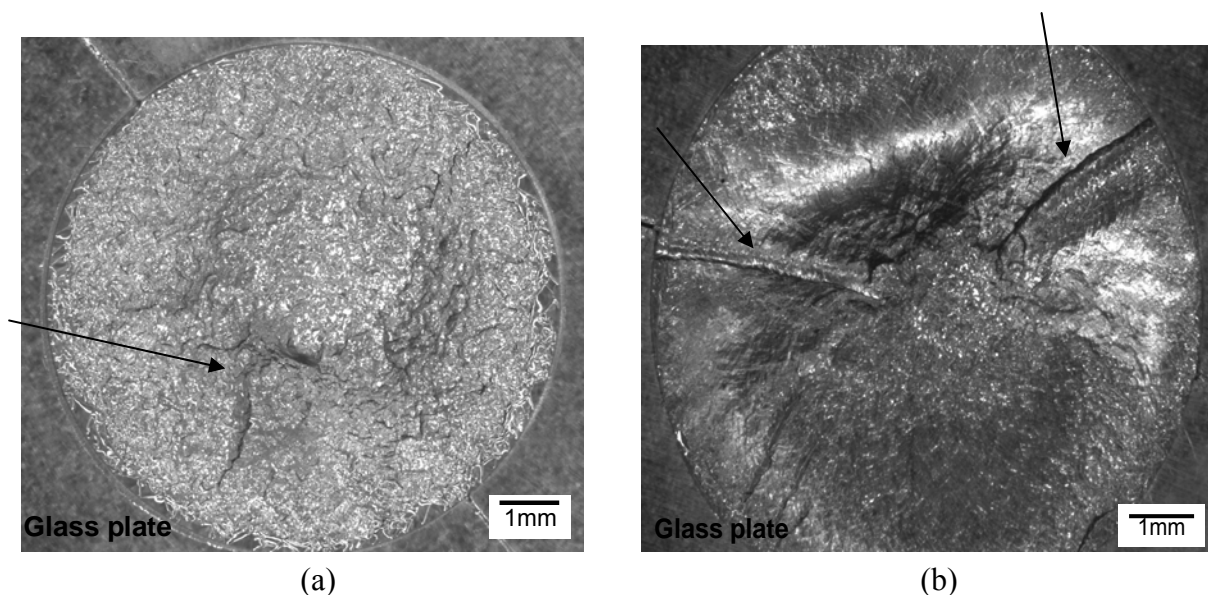


**Figure 5.25:** Typical optical microscopy images of the fractured surface of PU8000 after cavitation at (a) 50°C and 70°C, and (b) 100°C. Arrows point out radial cracks.

Our cavitation results obtained at higher temperatures are in agreement with our fracture results reported in chapter 3, where the fracture toughness  $G_{IC}$  of the materials decreases as the temperature increases as presented in Figure 5.22. Fragile and very fast fractures are observed at higher temperatures for the three polyurethane model networks.

### 5.3.- Cavitation results at different strain rates

With the purpose of evaluating the effect of the viscoelastic properties on fracture and therefore on the cavitation process, experiments at a slow average strain rate, two decades below than at standard conditions, were carried out, for the three polyurethane model networks. This section presents the main results.

#### 5.3.1.- Experimental part and results at different strain rates

The samples preparation was already reported in chapter 4. These cavitation experiments were carried out at 25°C and we used a crosshead velocity of 0.1  $\mu\text{m/s}$  (strain rate  $\sim 0.01\%/s$ ).

##### 5.3.1.1.- General trends

Figure 5.26 shows typical curves of force versus displacement at standard conditions 10  $\mu\text{m/s}$  and at 0.1  $\mu\text{m/s}$ . We observe that at lower strain rates, the maximal force is reached at lower values (see Appendix A5.3) than at standard conditions. Table 5.6 reports the results obtained for the maximal hydrostatic stress at both speeds, for the three polyurethane networks. The storage modulus of the three materials is almost the same at both speeds as presented in section 3.2 for the time-temperature superposition.

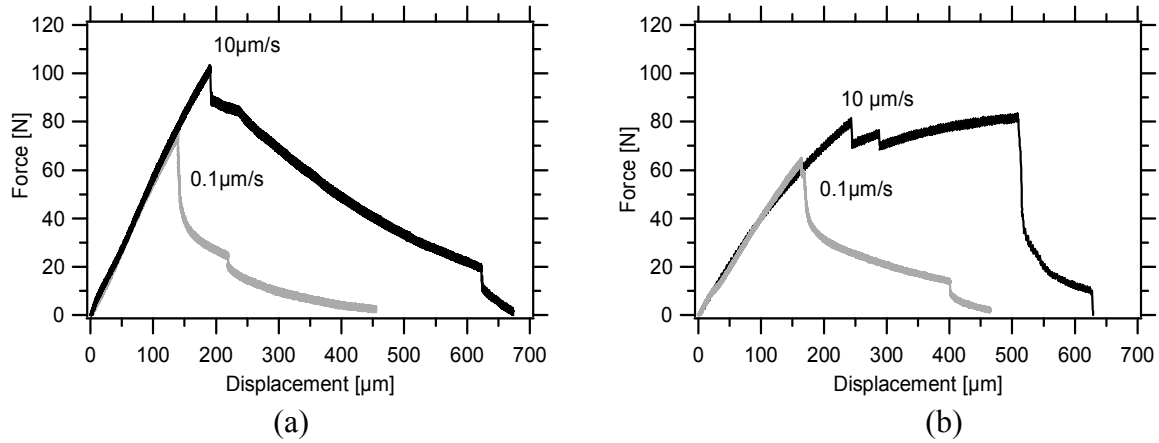


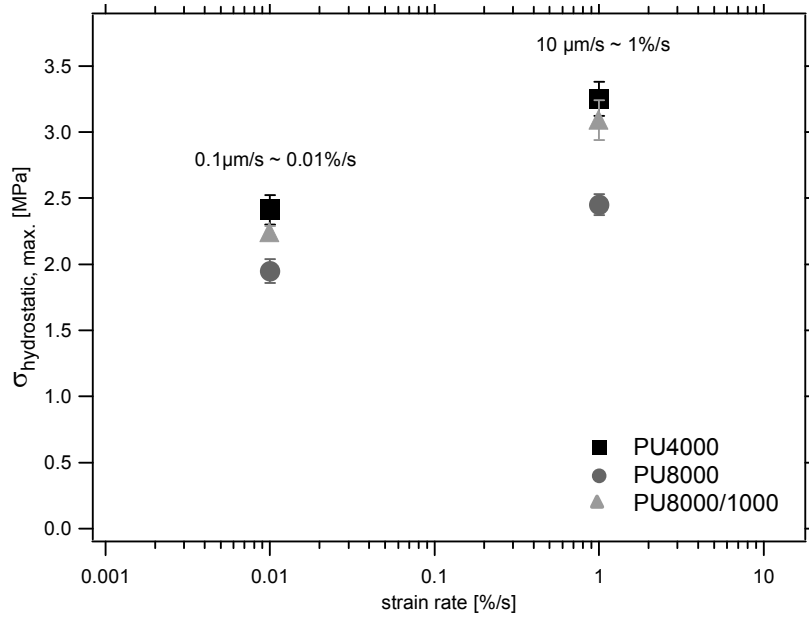
**Figure 5.26:** Typical cavitation curves showing lower critical force at lower speed. Comparison at 10  $\mu\text{m/s}$  and 0.1  $\mu\text{m/s}$  for: (a) PU4000 and PU8000/1000, and (b) PU8000.

**Table 5.6:** Modulus, maximal hydrostatic stress  $\sigma_{\text{hydro, max}}$ , and hydrostatic stress normalized by the modulus, at two speeds 10  $\mu\text{m/s}$  and 0.1  $\mu\text{m/s}$ , for the three polyurethane model networks.

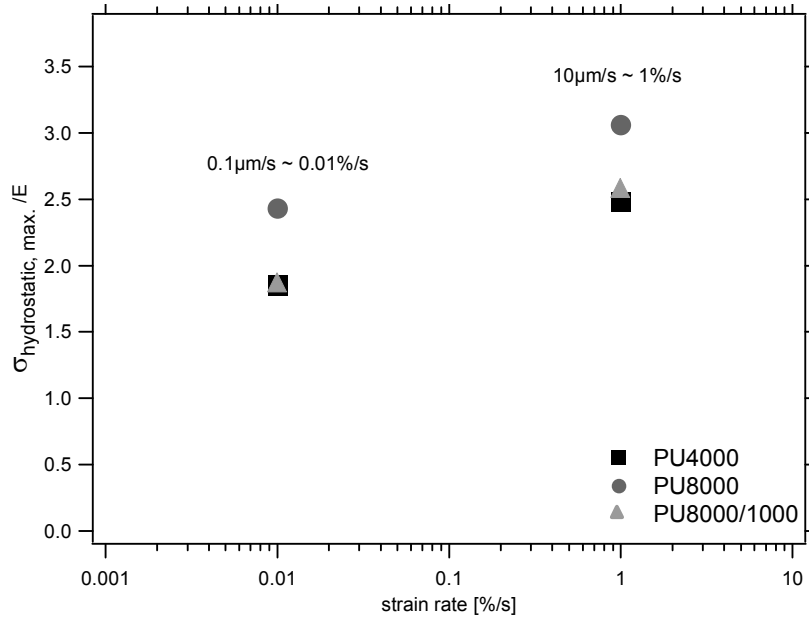
Materials	E [MPa]	@10 $\mu\text{m/s}$	@10 $\mu\text{m/s}$	@0.1 $\mu\text{m/s}$	@0.1 $\mu\text{m/s}$
		$\sigma_{\text{hydro, max}}$ [Mpa]	$\sigma_{\text{max}} / E$	$\sigma_{\text{hydro, max}}$ [MPa]	$\sigma_{\text{max}} / E$
<b>PU4000</b>	$1.3 \pm 0.08$	$3.25 \pm 0.13$	2.50	$2.41 \pm 0.11$	1.85
<b>PU8000</b>	$0.8 \pm 0.06$	$2.45 \pm 0.08$	3.06	$1.95 \pm 0.09$	2.43
<b>PU8000/1000</b>	$1.2 \pm 0.07$	$3.09 \pm 0.15$	2.58	$2.24 \pm 0.05$	1.87

Figure 5.27 shows graphically the maximal hydrostatic stress as a function of the crosshead speed. We observe that for lower strain rate the hydrostatic stress decreases for the three polyurethane networks. This shows that when a material is loaded during a longer time, lower forces are needed to fracture the material. Superficially, this rate effect on the cavitation results goes in the same direction as the fracture results reported in chapter 3, in which at lower strain rates a lower fracture toughness  $G_{\text{IC}}$  is measured. Rate dependence effects suggest that dissipative mechanisms are present also in the cavitation mechanisms and that time temperature equivalence may be obtained. However, as presented in chapter 3 only a qualitative time-temperature dependence is observed for the three polyurethane networks, since quantitatively, a very different time temperature equivalence is obtained from linear viscoelastic master curves and from fracture results.

When the cavitation results of the three polyurethane networks at different speeds are compared we observe that the rate dependence effect is roughly equivalent for all materials. Figure 5.28 shows the hydrostatic stress normalized by the modulus for the three polyurethane model networks at standard conditions (10  $\mu\text{m/s}$ ) and two decades below (0.1  $\mu\text{m/s}$ ). At both strain rates PU8000 is more cavitation resistant than the other two materials as already observed for the tests at different temperatures.



**Figure 5.27:** Maximal hydrostatic stress  $\sigma_{\text{hydrostatic, max.}}$  as a function of the speeds  $10\mu\text{m/s}$  (strain rate  $\sim 1\%/s$ ) and  $0.1\mu\text{m/s}$  (strain rate  $\sim 0.01\%/s$ ), and  $25^\circ\text{C}$  for the three polyurethane model networks.



**Figure 5.28:** Maximal hydrostatic stress  $\sigma_{\text{hydro, max}}$  normalized by the modulus, as a function of the speeds  $10\mu\text{m/s}$  (strain rate  $\sim 1\%/s$ ) and  $0.1\mu\text{m/s}$  (strain rate  $\sim 0.01\%/s$ ), and  $25^\circ\text{C}$  for the three polyurethane model networks.

If the maximal hydrostatic stress is plotted against the modulus we observe that the hydrostatic stress scales with the modulus for the three polyurethane networks at  $0.1\mu\text{m/s}$  (see Figure 5.29).

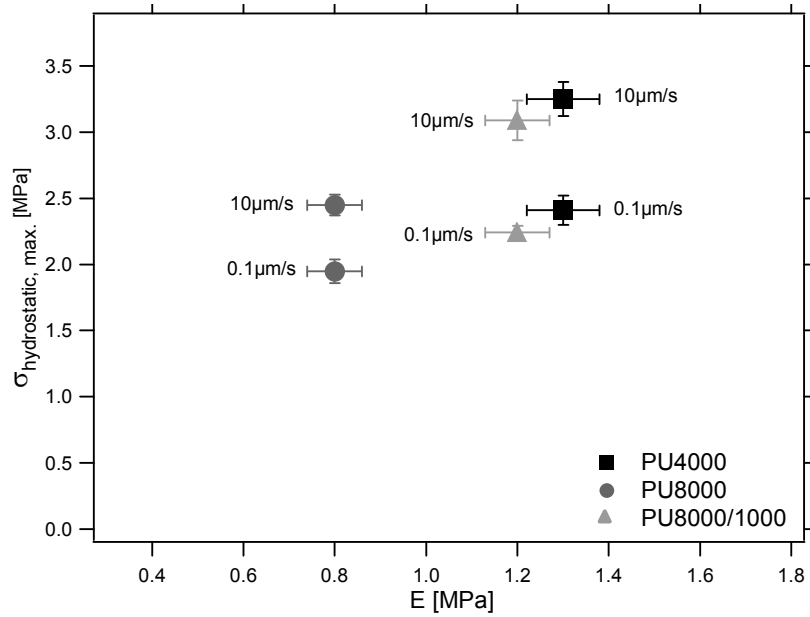


**Figure 5.29:** Maximal hydrostatic stress  $\sigma_{\text{hydro, max}}$  as a function of the modulus at two speeds  $10\mu\text{m/s}$  (strain rate  $\sim 1\%/s$ ) and  $0.1\mu\text{m/s}$  (strain rate  $\sim 0.01\%/s$ ), and  $25^\circ\text{C}$  for the three polyurethane model networks.

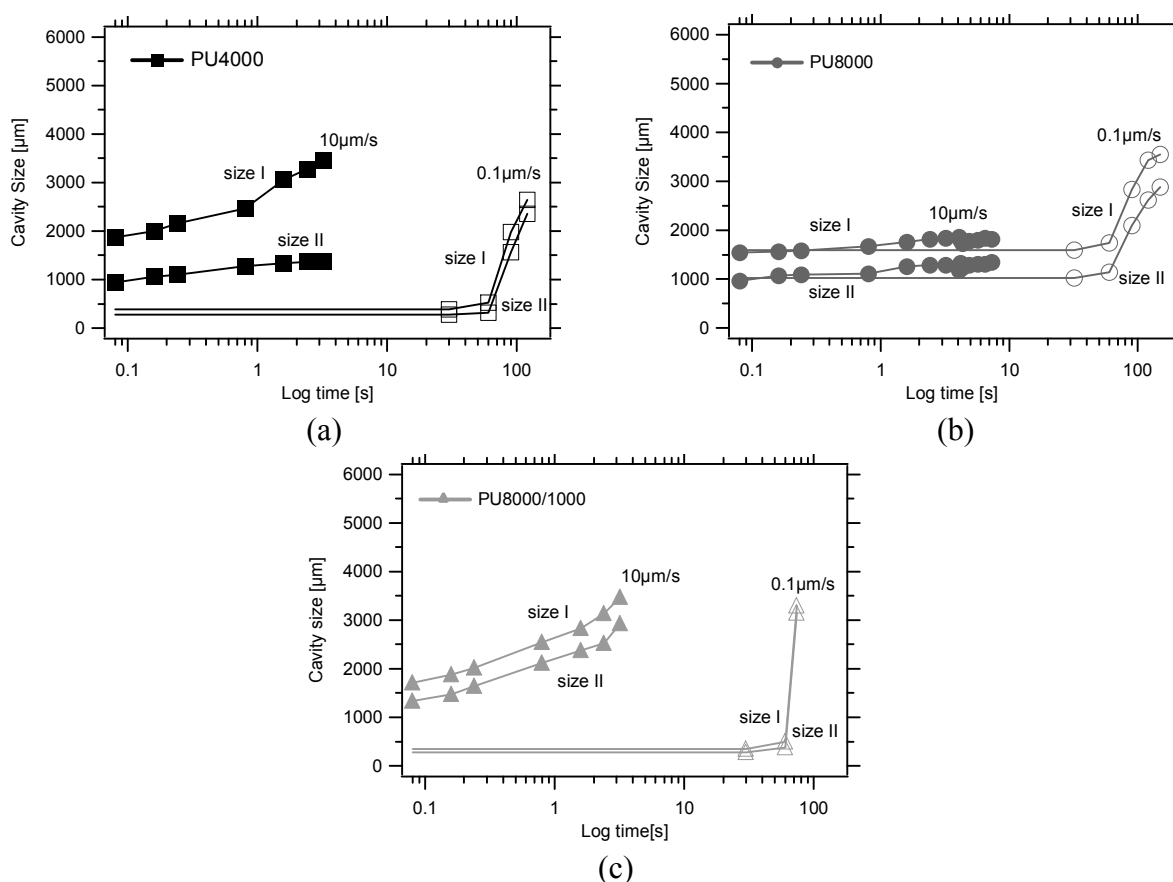
#### 5.2.1.2.- Critical cavity size and crack propagation

Table 5.7 shows the size of the critical cavity when it is first measurable (region A), at  $10\mu\text{m/s}$  and at  $0.1\mu\text{m/s}$ . The measurements were roughly estimated, but we observe that at lower speed the critical cavity is smaller and more symmetric than when it appears at standard conditions, for the three materials. The visible critical cavity size at low strain rate measures approximately  $\sim 0.28\text{ mm} \times 0.24\text{ mm}$  for PU4000,  $0.47\text{ mm} \times 0.36\text{ mm}$  for PU8000 and  $0.35\text{ mm} \times 0.28\text{ mm}$  for PU8000/1000; after the fracture surface has been formed, the crack grows. However, since the time elapsed between two consecutive frames was the same at both speeds (25 fps, i.e. 40 ms) the average rate at which the cavity grows initially can be estimated to be different roughly by a factor of 2. Note that, as for the experiments done at different temperatures, the actual nucleus from which the fracture grows was probably much smaller for both conditions, for the three materials.

Figure 5.30 (see Appendix A5.3 for reproducibility) shows in a log scale that, at low strain rate, once the critical cavity has appeared it grows slowly up to a second critical size and then the growth rate increases; however direct visual comparisons between the growth rates at low and high average strain rate are biased by the use of the log scale. The initial size of the critical cavity is slightly bigger for PU8000 than for the other two materials, at standard conditions and at low strain rate. The cavity growing is circular at low speed since both sizes I and II are parallel. At low speed, there is only one critical cavity growing for the three polyurethanes networks.

**Table 5.7:** Approximate initial critical cavity size at standard conditions 10 $\mu\text{m/s}$  and at 0.1 $\mu\text{m/s}$ .

Material	Size I @10 $\mu\text{m/s}$ [mm]	Size II @10 $\mu\text{m/s}$ [mm]	Size I @0.1 $\mu\text{m/s}$ [mm]	Size II @0.1 $\mu\text{m/s}$ [mm]
PU4000	$1.0 \pm 0.28$	$0.49 \pm 0.15$	$0.28 \pm 0.04$	$0.24 \pm 0.03$
PU8000	$1.4 \pm 0.06$	$0.72 \pm 0.26$	$0.47 \pm 0.08$	$0.36 \pm 0.06$
PI8000/1000	$1.2 \pm 0.13$	$0.71 \pm 0.17$	$0.35 \pm 0.08$	$0.28 \pm 0.06$



**Figure 5.30:** Cavity growing as a function of the time for two speeds 10 $\mu\text{m/s}$  and 0.1 $\mu\text{m/s}$ , and 25°C for: (a) PU4000, (b) PU8000 and (c) PU8000/1000.

### 5.2.1.3.- Fracture morphology

Figure 5.31 (a) presents the fracture surfaces after the tests at low speed for PU4000 and PU8000/1000 and Figure 5.31 (b) for PU8000. No evidence of the critical cavity can be observed. Apparently, the three polyurethane networks present a more fragile fracture when the speed is at standard conditions (10  $\mu\text{m/s}$ ) where the crack growth is faster, compared with the fracture after cavitation at low strain rate (0.1  $\mu\text{m/s}$ ).

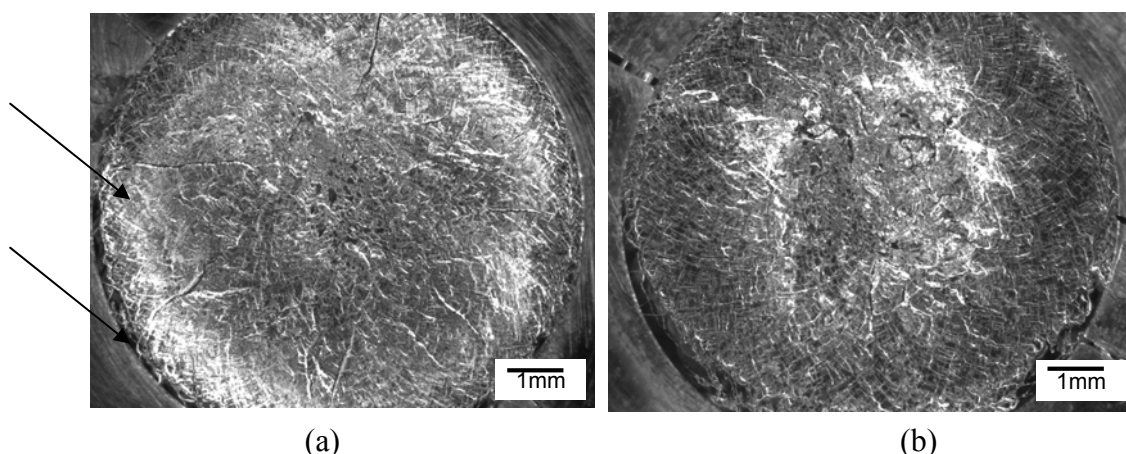


**Figure 5.31:** Typical optical microscopy images of the fractured surface after cavitation at  $0.1\mu\text{m/s}$  of (a) PU4000 and PU8000/1000, and (b) PU8000. Arrows point out radial cracks.

## 5.4.- Pre-critical cavities analysis

Until this point of the chapter, the discussion has been focused on the fracture process. On the unstable cavity growing, once a critical hydrostatic stress has been reached. We studied changes in the force-displacement curves upon fracture, the growth rate of the critical cavity and the fracture surfaces, for the three polyurethane model networks at different experimental conditions. Here, rises the question if the maximal force ( $F_{\text{max}}$ ) is the really the right criterion to study the nucleation of cavitation. The appearance of pre-critical cavities before catastrophic fracture occurs implies the existence of two separate criteria: one for the brittle expansion of the critical cavity and one for the growth (crack propagation). In this section we present an analysis that to-date has not been reported in the literature, the analysis of the pre-critical cavities.

### 5.4.1.-Lateral profile: Volume change

Since the elastomers are considered incompressible or quasi-incompressible, non volume change is expected in the materials when submitted to certain amount of loading stress, unless the material has developed internal voids. In fact, a variation of the volume of these materials is an indication that pre-critical cavity/cavities have nucleated in it.

Measures of the variation of volume were done for the three polyurethane model networks by using the lateral profiles obtained from the side projection. For each polyurethane three samples were studied. By using around fifteen (15) measurements of force and displacement, before the critical cavity starts growing, the volume change was calculated. For the images analysis a programme was developed in the lab.

Figure 5.32 presents the typical graphs obtained for the variation of volume as a function of the displacement for (a) PU4000, (b) PU8000 and (c) PU8000/1000 ; the arrow points out where the critical cavity appears (whether it stays stable or not before crack growth). Note that at the beginning of the analysis the variation of the volume is almost zero. Later, there is



a change of the slope of the curve of force versus displacement, which shows a volume change. We observe for the three polyurethane model networks a total volume change of  $\Delta V/V_0 \leq 2.5\%$ , this maximum volume change is reached at the maximum force and displacement before the critical cavity grows for the three materials. We could not appreciate a clear difference in volume change for the three polyurethane networks.

Despite the possible uncertainties that this measurement has, the results obtained show a tendency that was reproducible for the different samples. This change in volume obtained experimentally at the first stages of the cavitation experiments suggests that pre-critical cavities has been formed, even before they are visible to us on the camera.

An analysis on the visible pre-critical cavities is presented in the next sections.

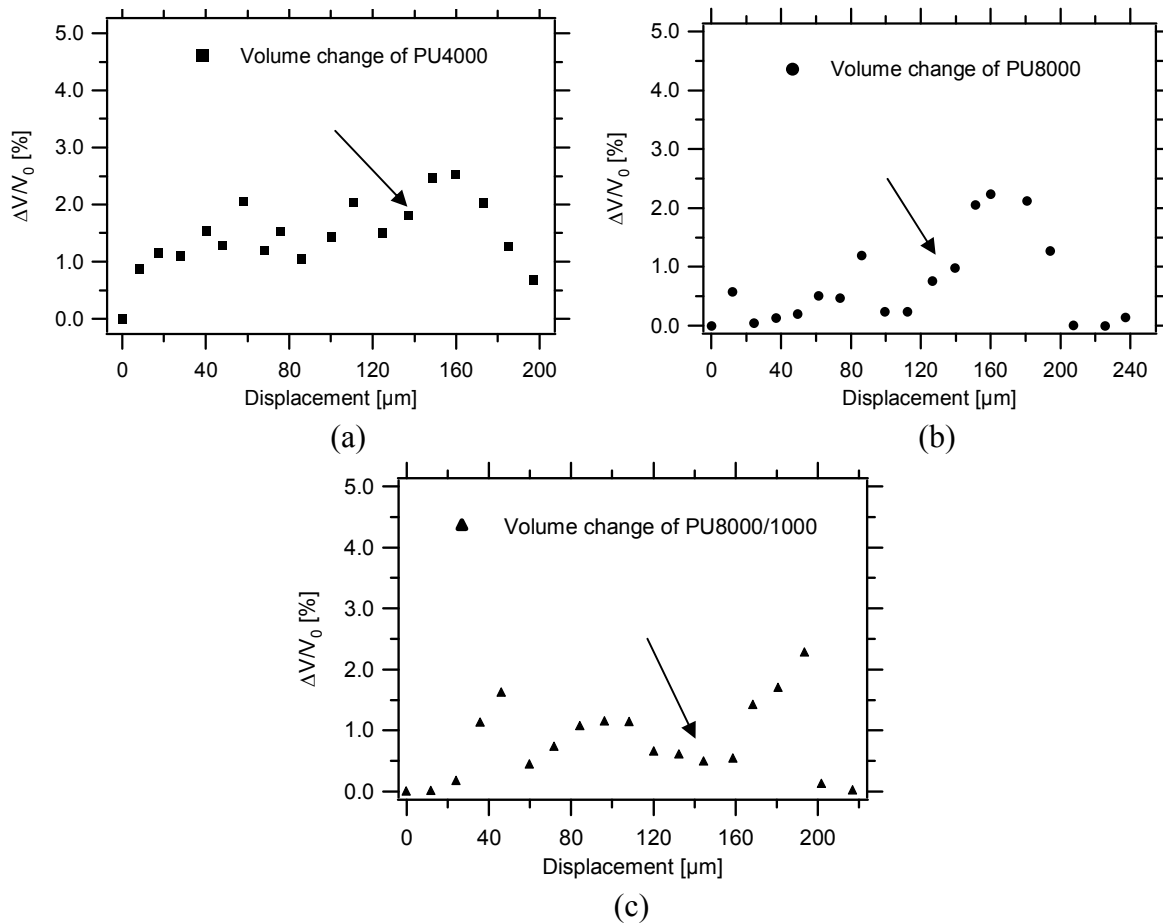


**Figure 5.32:** Volume change in function of the displacement for (a) PU4000; (B) PU8000; and (c) PU8000/1000. The arrow shows where the critical cavity appears.

#### 5.4.2.- Conditions of pre-critical cavity formation

In order to better understand the mechanism of cavitation, and since our samples and cavitation system allowed us to visualize pre-critical cavities and to follow them in time, we did analyze the visible pre-critical cavities on different experimental conditions.

The formation of relatively small stable white spots was observed and we made an analysis of these “pre-critical cavities”. In this section, the conditions of pre-critical cavity formation

have been analyzed in terms of number of events and time of appearance for different materials and conditions. . In chapter 6, a statistical analysis is proposed, looking at position distributions and probabilities of events.

In this section we focus on the first part of the force versus displacement curve (the left side in Figure 5.1). Figure 5.33 presents an example of how the analysis is carried out for each sample and condition.

The procedure is based on the videos and the synchronized force versus time curves, the corresponding image where one event happens (a cavity appears) is taken with the timing and force at which it appeared, then by using the image, the distance of the cavity from the center of the sample is measured and the hydrostatic stress value is calculated. Since the hydrostatic stress has a stress distribution which is maximal in the central part, and decreases to the edges (see Figure 4.2), the maximal hydrostatic stress has to be normalized as a function of the position along the radial direction (see Figure 4.22) as introduced in chapter 4.

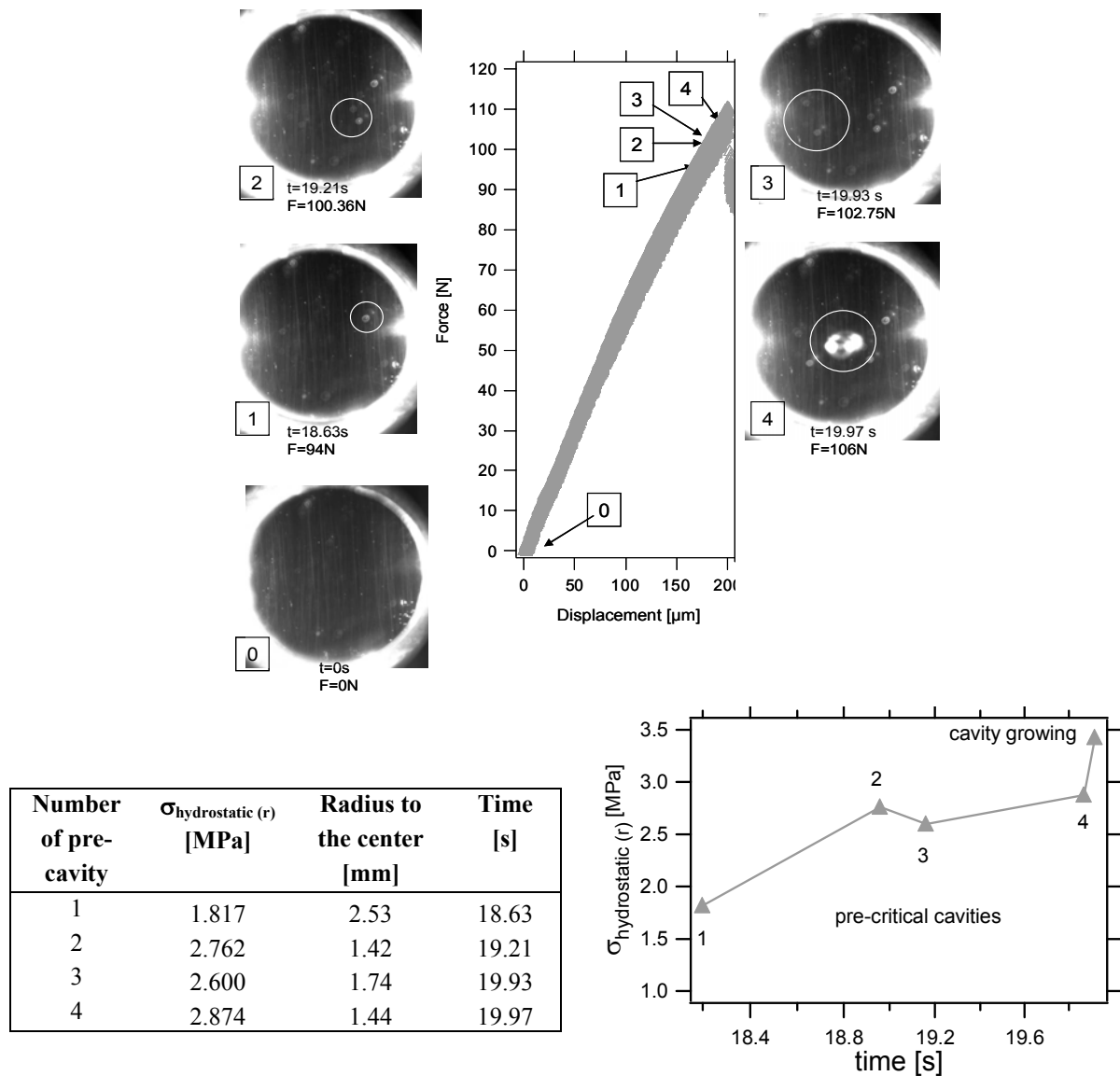


**Figure 5.33:** Example of pre-critical cavities analysis. Point 4 corresponds to the critical cavity appearance and the point after is the critical cavity growth.

### 5.4.2.1.- Pre-critical cavities analysis at standard conditions

Figure 5.34 presents the local hydrostatic as a function of the time for the three polyurethane model networks, at standard conditions. Three samples were analyzed, for each condition. The typical size of a visible pre-critical cavity was  $\sim 200\text{-}300\mu\text{m}$ .

We observe that at standard conditions few visible pre-critical cavities ( $\sim 4\text{-}5$  cavities) appear in PU4000 and in PU8000/1000 in centre region of the sample, but they stay stable and only one cavity, which was already there or not, is the one growing (the critical cavity). For PU8000 less pre-critical cavities are observed ( $\sim 2$  cavities) before the critical cavity appears and growth. We can see, qualitatively, that PU4000 and PU8000/1000 present more ‘dispersion’ in the stress values than PU8000, more detailed analysis is done in chapter 6.

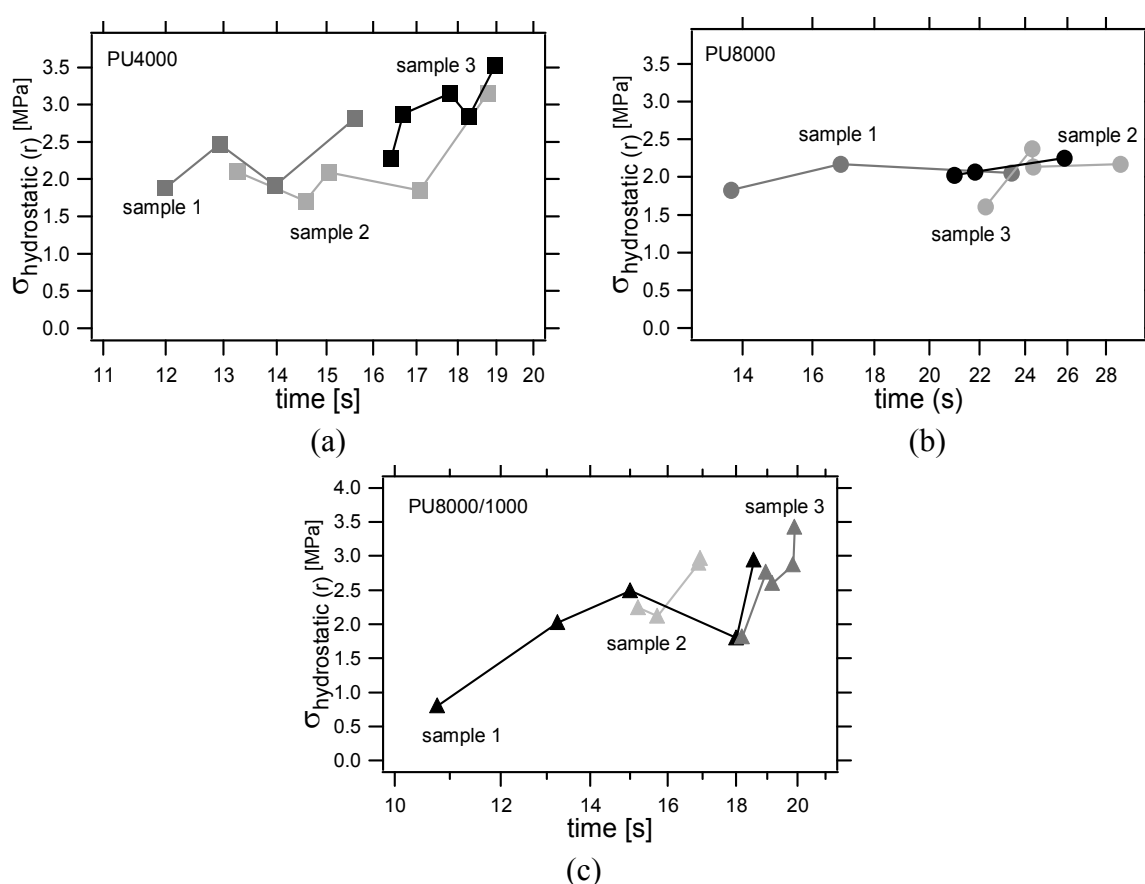


**Figure 5.34:** Local Hydrostatic stress as a function of the time at standard conditions, for: (a) PU4000, (b) PU8000, and (c) PU8000/1000.

The fact that we do observe pre-critical cavities which appear and remain stable and do not grow means that some pre-critical cavities are able to grow in the material as a consequence of the hydrostatic stress but due to the surface tension, only one or few cavities are able to expand. This also makes reasonable to assume that each defect acts independently. The pre-critical cavities appear much less frequently in PU8000 implying that either the initial defects are smaller or they grow more slowly under stress. When comparing the networks with short

and long chains (unentangled and entangled) it is clear that the entanglements toughen the material which stabilizes the crack growth even in confined conditions.

#### 5.4.2.2.-Pre-critical analysis at high temperature

When the temperature is increased less pre-critical cavities are observed for the three polyurethane model networks. Here, we only present the data for 100°C (the highest temperature we used) and the results are compared with standard conditions. Figure 5.35 presents the local hydrostatic stress of the sample as a function of the time for the three polyurethane model networks, at 100°C. We observe that at higher temperatures only 2-3 pre-cavities (less than at standard conditions) appear before the critical cavity appears for PU4000. For PU8000/1000, and for PU8000 only one critical cavity appears. Probably due to the increase in temperature the cavities are less stable and once they appear the material is prone to catastrophic failure.

Figure 5.36 presents the local hydrostatic stress as a function of time for the three materials at 100°C compared to 25°C. The graph shows clearly the effect of the temperature in the materials regarding the amount of cavities, the decrease of the stress and faster cavitation process. The cavitation behaviour of samples at 50°C and 70°C is just in between the two extremes (25°C and 100°C).

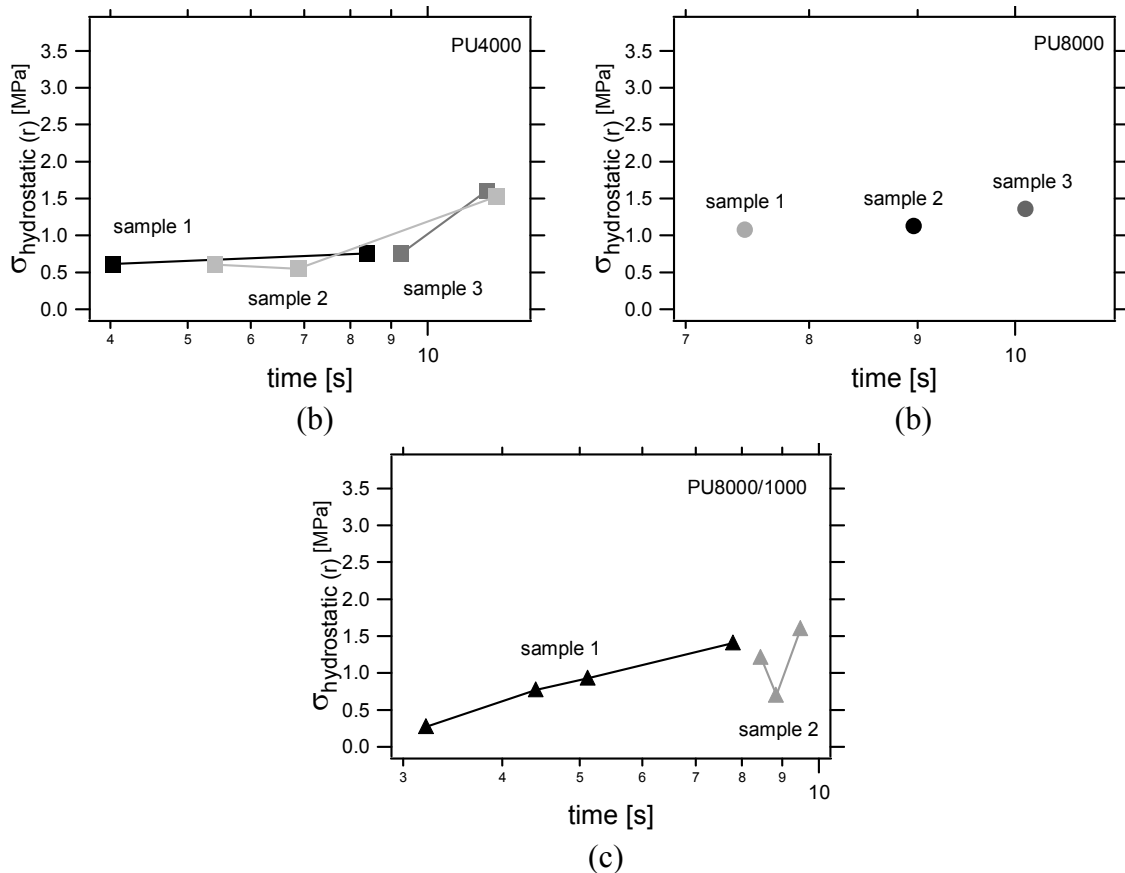


**Figure 5.35:** Local Hydrostatic stress as a function of the time at 100°C, for: (a) PU4000, (b) PU8000, and (c) PU8000/1000.

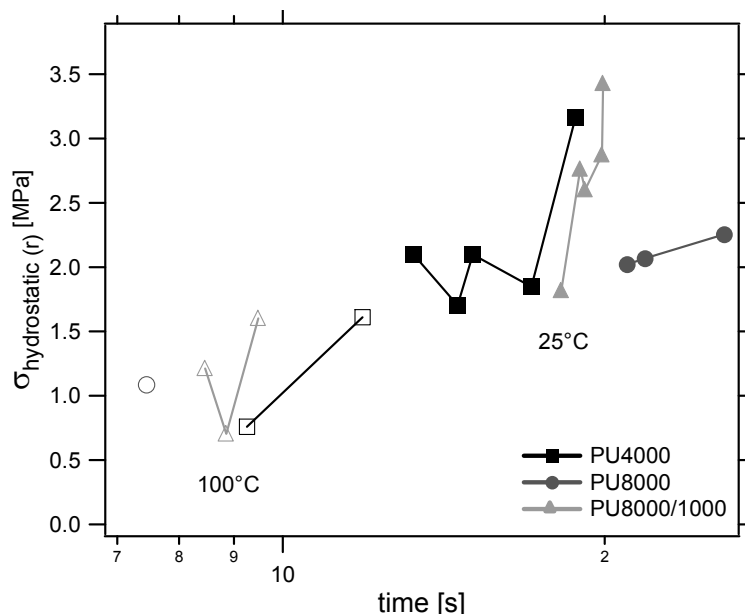


**Figure 5.36:** Local Hydrostatic stress as a function of the time for the three polyurethane model networks, at 25°C and 100°C.

#### 5.4.2.3.-Pre-critical analysis at low strain rate

When the speed of the cavitation experiment is decreased some changes are observed regarding the appearance of pre-critical cavities. The same trend is observed for the three networks, at lower speed pre-critical cavities appear earlier and stay stable for a longer time until the critical cavity grows, see. Figure 5.37.

For PU4000, the number of pre-critical cavities highly increases with a decrease in strain rate: we observe about 8 pre-critical cavities at 0.1 $\mu\text{m/s}$  while at 10 $\mu\text{m/s}$  showed only 4-5 pre-cavities before the growing of the critical cavity. For the sample PU4000 it was observed the more marked influence of the strain rate, being the amount of pre-critical cavities that appear at low strain rate around twice the amount that appear at standard conditions.

For PU8000 and PU8000/1000 at 0.1 $\mu\text{m/s}$  the amount of pre-critical cavities that appear did almost not change with respect to the amount of pre-critical cavities observed at standard conditions. When comparing the networks with short and long chains (unentangled and entangled) it is clear that the entanglements toughen the material which stabilizes the crack growth even when the material is submitted longer time to stresses.

Figure 5.38 presents the stress as a function of time for the three materials at 0.1 $\mu\text{m/s}$  compared to standard conditions. The graph shows the effect of the strain rate in the materials where at 0.1 $\mu\text{m/s}$  the stress is lower and the pre-cavities stay longer time stable even if they appear at lower forces.

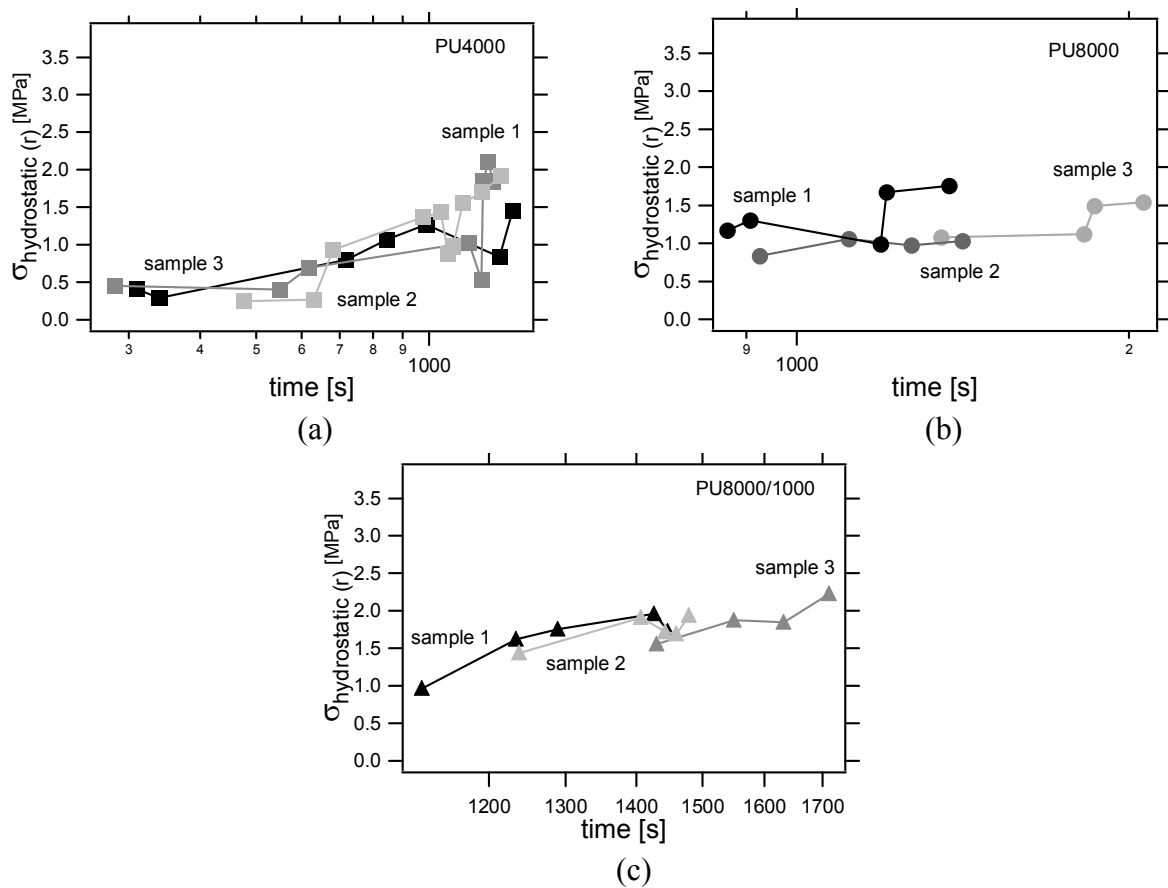


**Figure 5.37:** Local Hydrostatic stress as a function of the time at  $0.1 \mu\text{m/s}$ , for: (a) PU4000, (b) PU8000, and (c) PU8000/1000.

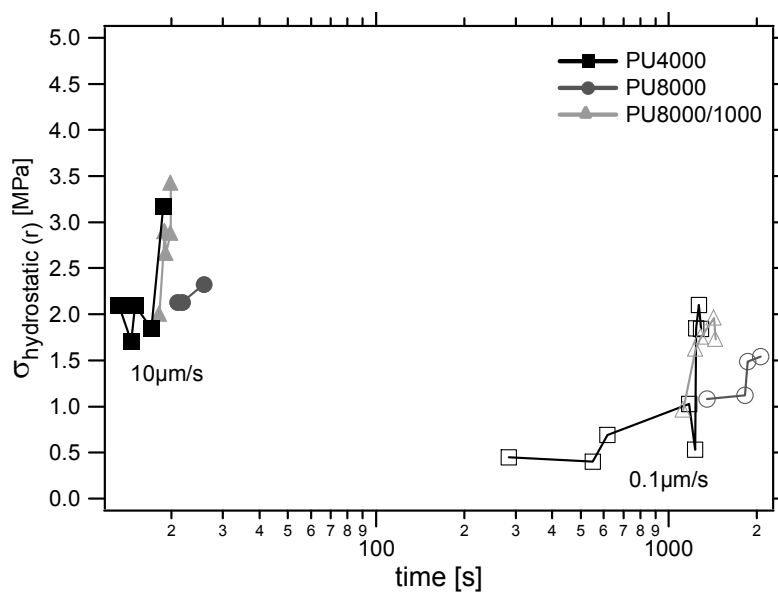


**Figure 5.38:** Local Hydrostatic stress normalized as a function of the time for the three polyurethane model networks, at  $10 \mu\text{m/s}$  and  $0.1 \mu\text{m/s}$ .

### Summarizing the pre-cavities analysis at different experimental conditions

Figure 5.39 presents a comparison of the three materials at standard conditions, at higher temperature 100°C and at low speed 0.1μm/s. Here, only one sample of each material and condition is presented to make the comparison. When the experimental conditions are at higher temperature and low speed we observe lower hydrostatic stresses than at standard conditions. We observe that at higher temperature, only few pre-critical cavities appear, the hydrostatic stress is lower than at standard conditions and the cavitation process is faster than at standard conditions. At low strain rate, we observe for PU4000 more pre-critical cavities appear than at standard condition, however, for PU8000 and PU8000/1000 the amount of pre-critical cavities is more or less the same than at standard conditions. At low strain rate, the hydrostatic stress is lower than at standard conditions and the cavitation process takes longer time while the cavities appear at lower forces. Table 5.8 summarizes the mean number of pre-critical cavities for the different conditions.

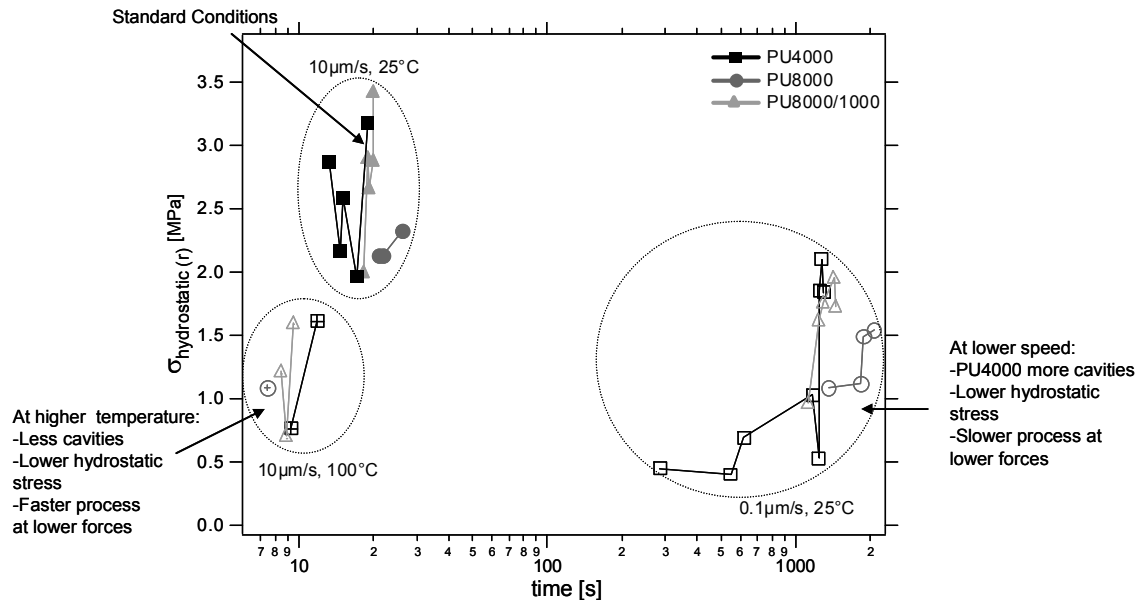


**Figure 5.39:** Local Hydrostatic stress as a function of the time at high temperature and low speed, for the different conditions.

**Table 5.8:** Mean number of pre-critical cavities for the different conditions.

Mean number of pre-critical cavities	Standard conditions 25°C – 10μm/s	High Temperature T=100°C – 10μm/s	Low strain rate T=25°C – 0.1μm/s
<b>PU4000</b>	4-5	2-3	8
<b>PU8000</b>	2-3	1	2-3
<b>PI8000/1000</b>	4-5	2-3	4-5

## Conclusions

### On the physics of the problem

- The critical cavity for the three materials appears very close to the centre of the sample when the maximal force is almost reached.
- The appearance of stable pre-critical cavities before catastrophic fracture occurs implies the existence of two separate criteria: one for the nucleation and one for the cavity growth.
- The temperature change acts mostly on the toughness but the time acts mostly on the pre-critical cavity formation. Both effects must be important.
- For the different experimental conditions investigated (i.e. temperature and strain rate), no direct scaling of the hydrostatic stress with the modulus has been observed. On the other hand the cavitation stress appears to scale better with the fracture energy  $G_{Ic}$  of the material in mode I.

### On the materials properties

- The presence of pre-critical cavities depends very markedly on the material and on the conditions (maximum for low rate and minimum for high temperature). This implies that the toughness **does not** control the appearance of these cavities (since  $G_{Ic}$  decreases both with rate and temperature but the pre-cavities do very differently).
- The indications are that a softer material containing trapped entanglements (PU8000) as well as homogeneous crosslinks (PU8000/1000) can give a relatively high resistance to cavitation. PU8000/1000 has a cavitation strength higher than PU4000 and the pre-critical nucleation at low rate is less pronounced than for the PU4000.
- However, the presence of short chains in the bimodal network completely kills the entanglement effect in terms of toughness  $G_{Ic}$  but does not kill it in terms of slow growth in view that pre-critical cavities grow less for PU8000/1000 than for the 4000 at low rates.

*The cavitation strength depends for use on Temperature, hydrostatic stress  $\sigma$  and time and a general function maybe a predictor.* In the next chapter pre-existing cavitation models are presented and our experimental results are tried to fit them. A new fitting method is proposed by using our experimental results.



## **Acknowledgments**

In this chapter we would like to thank Fabrice Monti for the programme about the calculations of the volume change.

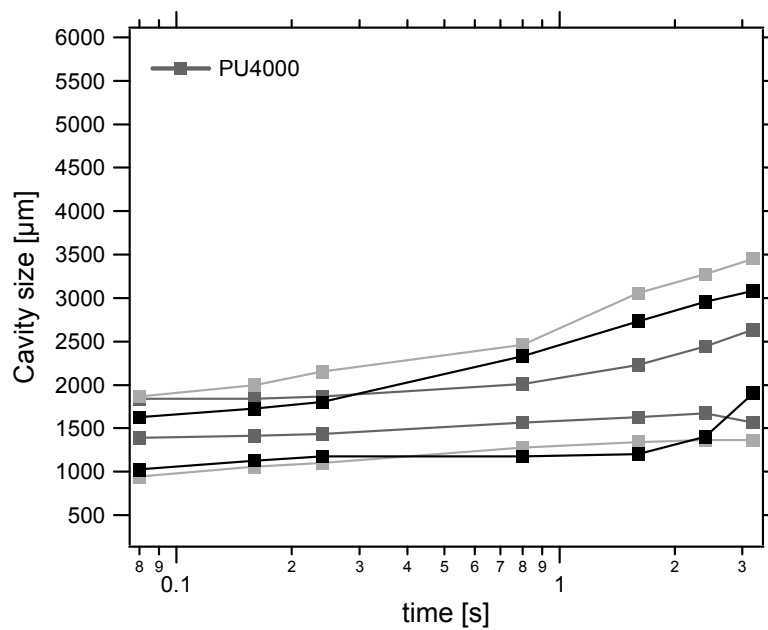
## Appendices A5

### Appendix A5.1: Cavitation results at standard conditions

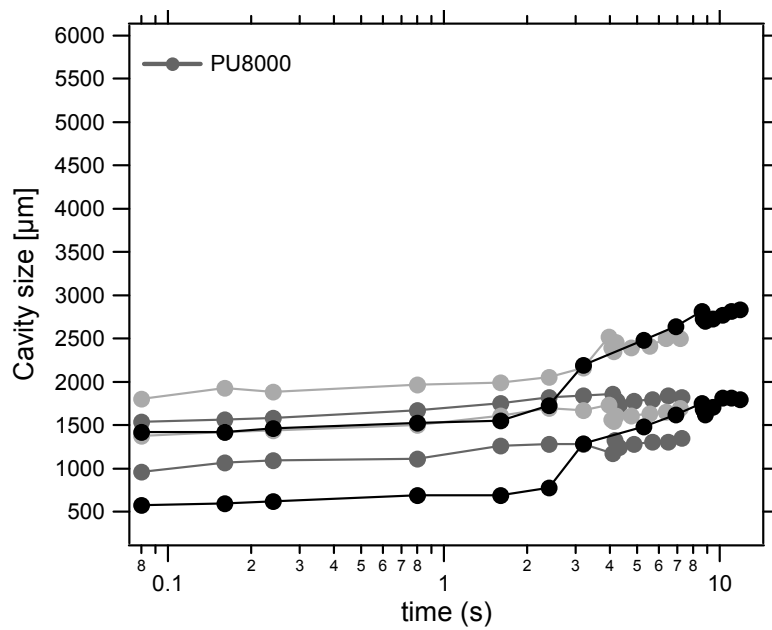
**Table A5.1:** Maximal Force  $F_{\max}$ , maximal displacement  $\Delta\mu$  and maximal hydrostatic stress  $\sigma_{\text{hydro, max}}$ , reported for PU4000, PU8000 and PU8000/1000, at standard conditions.

Material	E [MPa]	$F_{\max}$ [N]	$\Delta\mu_{\max}$ [ $\mu\text{m}$ ]	$\sigma_{\text{hydro, max}}$ [MPa]	$\sigma/E$
<b>PU4000</b>	$1.3 \pm 0.08$	$103.5 \pm 3.4$	$177 \pm 8$	$3.25 \pm 0.13$	2.50
<b>PU8000</b>	$0.8 \pm 0.06$	$78.5 \pm 2.5$	$221 \pm 11$	$2.45 \pm 0.08$	3.06
<b>PU8000/1000</b>	$1.2 \pm 0.07$	$98.7 \pm 3.5$	$214 \pm 7$	$3.09 \pm 0.15$	2.58

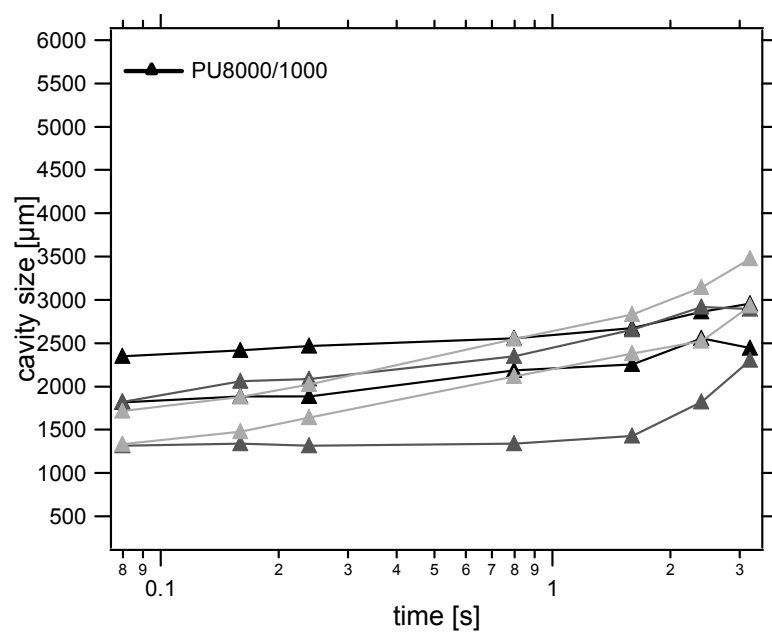
The cavity growth for three samples of each material at standard conditions is presented in Figure A5.1, A5.2 and A5.3.



**Figure A5.1:** Cavity growth for three samples of PU4000 at standard conditions.

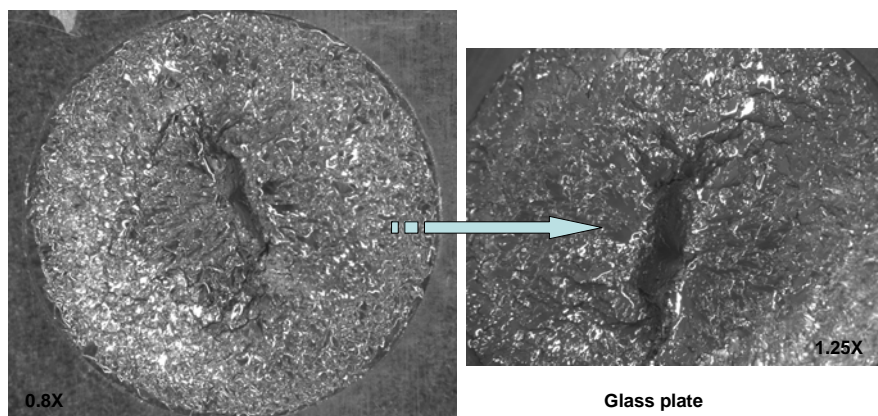


**Figure A5.2:** Cavity growth for three samples of PU8000 at standard conditions.



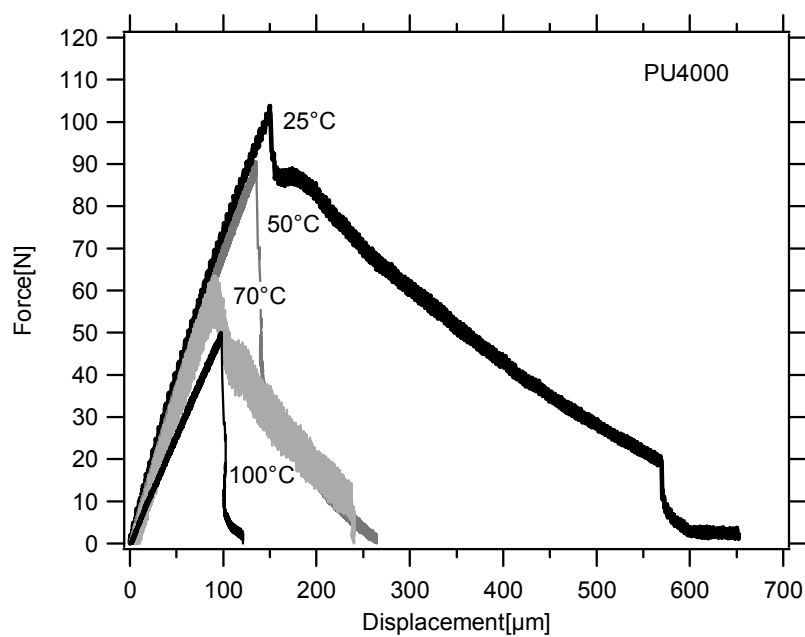
**Figure A5.3:** Cavity growth for three samples of PU8000/1000 at standard conditions.

Figure A5.4 shows the fractured surface of a PU8000/1000 sample after performing the cavitation experiment.



**Figure A5.4:** Optical microscopy fractured surface of PU8000/1000 after cavitation at standard conditions.

#### Appendix A5.2: Cavitation results at different temperatures



**Figure A5.5:** Cavitation results for PU4000 at different temperatures

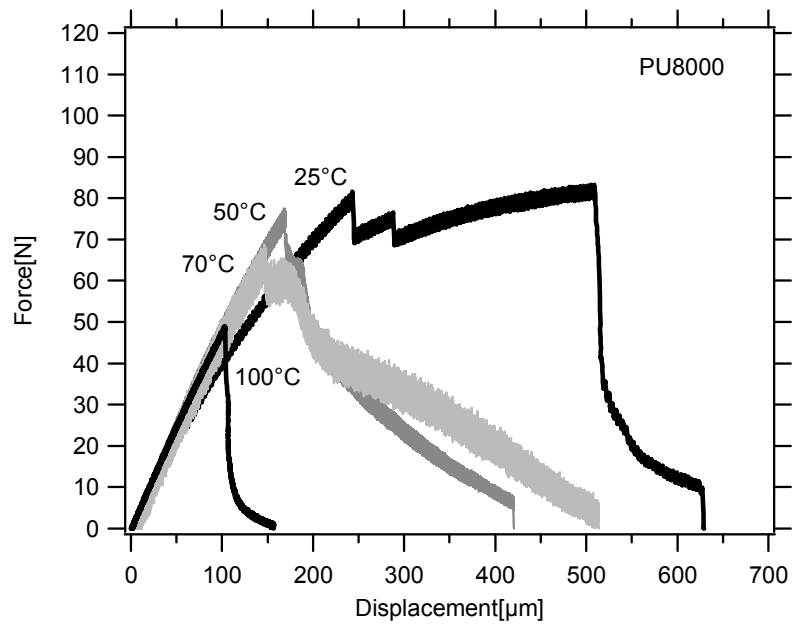


**Figure A5.6:** Cavitation results for PU8000 at different temperatures

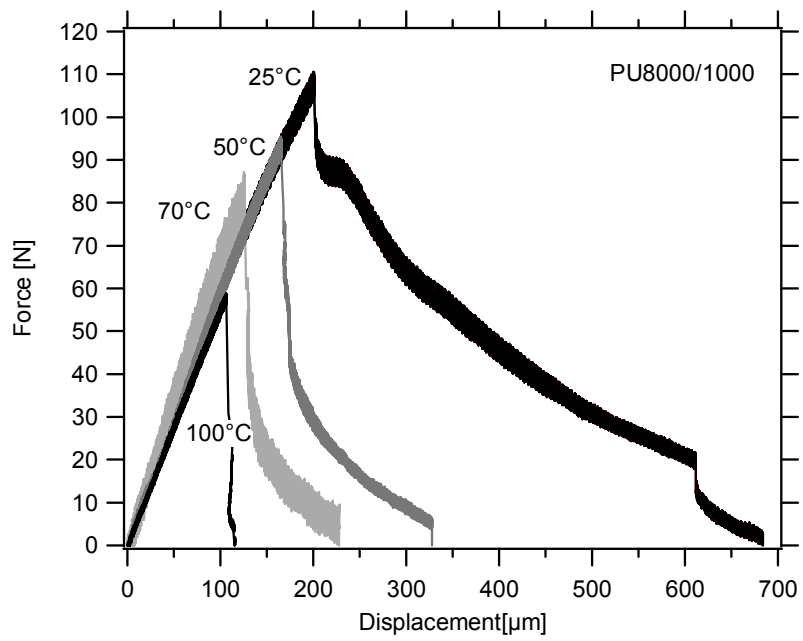


**Figure A5.7:** Cavitation results for PU8000/1000 at different temperatures

**Table A5.2:** Maximal Force  $F_{\max}$ , maximal displacement  $\Delta\mu$  and maximal hydrostatic stress  $\sigma_{\text{hydro, max}}$ , reported for the three polyurethane model networks, at different temperatures.

Materials	E [MPa]	Temp. [°C]	$F_{\max}$ [N]	$\Delta\mu_{\max}$ [ $\mu\text{m}$ ]	$\sigma_{\text{hydro, max}}$ [MPa]	$\sigma_{\max}/E$
<b>PU4000</b>	$1.3 \pm 0.08$	25	$103.5 \pm 3.4$	$177 \pm 8$	$3.25 \pm 0.13$	2.50
	$1.38 \pm 0.07$	50	$82.67 \pm 1.5$	$131 \pm 6$	$2.63 \pm 0.06$	1.91
	$1.45 \pm 0.09$	70	$83.5 \pm 2.5$	$121 \pm 3$	$2.62 \pm 0.08$	1.81
	$1.55 \pm 0.04$	100	$57.7 \pm 3.5$	$112 \pm 5$	$1.77 \pm 0.07$	1.14
<b>PU8000</b>	$0.8 \pm 0.06$	25	$78.5 \pm 2.5$	$221 \pm 11$	$2.45 \pm 0.08$	3.06
	$0.84 \pm 0.03$	50	$65.1 \pm 6.9$	$146 \pm 7$	$2.09 \pm 0.13$	2.49
	$0.88 \pm 0.04$	70	$58.1 \pm 3.4$	$144 \pm 5$	$1.83 \pm 0.10$	2.08
	$0.93 \pm 0.04$	100	$51.2 \pm 3.9$	$116 \pm 6$	$1.64 \pm 0.12$	1.76
<b>PU8000/1000</b>	$1.2 \pm 0.07$	25	$98.7 \pm 3.5$	$214 \pm 7$	$3.09 \pm 0.15$	2.58
	$1.28 \pm 0.04$	50	$84.5 \pm 1.4$	$141 \pm 5$	$2.66 \pm 0.08$	1.77
	$1.35 \pm 0.06$	70	$70.1 \pm 4.2$	$130 \pm 5$	$2.19 \pm 0.15$	1.62
	$1.44 \pm 0.05$	100	$57.1 \pm 3.4$	$97 \pm 8$	$1.77 \pm 0.11$	1.23

The cavity growth for two samples of each material at 100°C is presented in Figure A5.8.

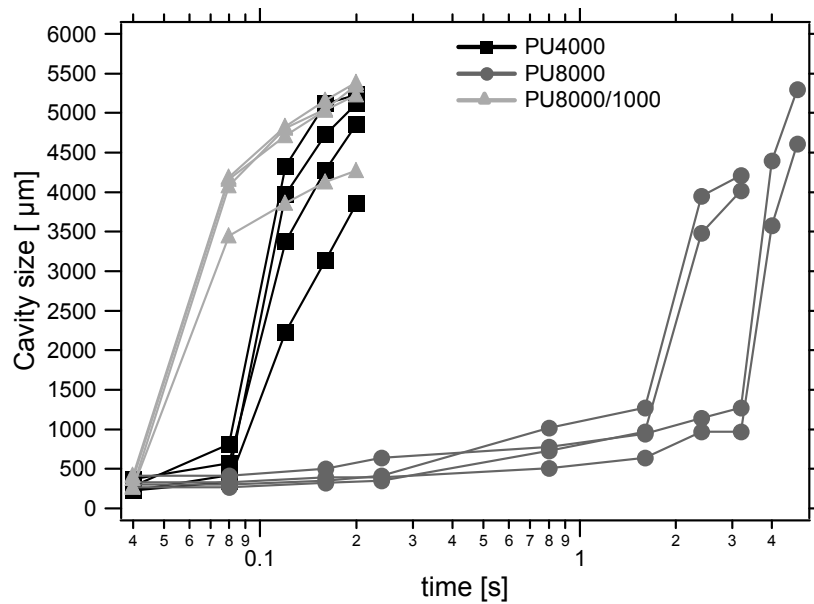


**Figure A5.8:** Cavity growth for PU4000, PU8000 and PU8000/1000 at 100°C.

### Appendix A5.3: Cavitation results at different strain rates

**Table A5.2:** Modulus, maximal hydrostatic stress  $\sigma_{\text{hydro, max}}$ , and hydrostatic stress normalized by the modulus, reported for three polyurethane model networks at different speeds

Materials	E [MPa]	Speed [ $\mu\text{m/s}$ ]	$F_{\text{max}}$ [N]	$\Delta\mu_{\text{max}}$ [ $\mu\text{m}$ ]	$\sigma_{\text{hydro, max}}$ [MPa]	$\sigma_{\text{max}}/E$
PU4000	$1.3 \pm 0.08$	10	$103.5 \pm 3.4$	$177 \pm 8$	$3.25 \pm 0.13$	2.50
	$1.3 \pm 0.08$	0.1	$90.6 \pm 4.5$	$143 \pm 5$	$2.41 \pm 0.11$	1.85
PU8000	$0.8 \pm 0.06$	10	$78.5 \pm 2.5$	$221 \pm 11$	$2.45 \pm 0.08$	3.06
	$0.8 \pm 0.06$	0.1	$61.1 \pm 1.5$	$189 \pm 13$	$1.95 \pm 0.09$	2.44
PU8000/1000	$1.2 \pm 0.07$	10	$98.7 \pm 3.5$	$214 \pm 7$	$3.09 \pm 0.15$	2.58
	$1.2 \pm 0.07$	0.1	$83.2 \pm 3.6$	$151 \pm 10$	$2.24 \pm 0.05$	1.87

The cavity growth for two samples of each material at 0.1  $\mu\text{m/s}$  is presented in Figure A5.9.

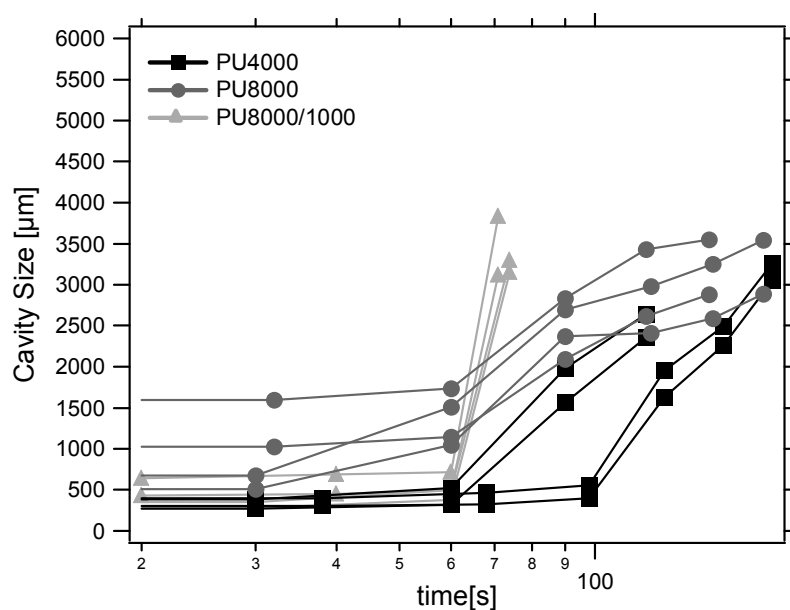


**Figure A5.9:** Cavity growth for PU4000, PU8000 and PU8000/1000 at 0.1  $\mu\text{m/s}$ .

## Bibliography

- Busse W.F., Physics of rubber as related to the automobile, *Journal of Applied Physics*, 9, 438-451 (1938).
- Bayraktar, E., Isac, N., Bessri, K. and Bathias, G., *Fatigue and Fracture of Engineering Materials & Structures*, 31, 2, 184-196 (2008).
- Cho, K. and Gent, A.N., *Journal of Materials Science*, 23, 141-144 (1988)
- Denecour, R.L. and Gent, A.N., *Journal of Polymer Science Part A-2*, 6, 1853-1861 (1968)
- Fond, C., Lobbrecht, A., Schirrer, R., *Int. Journal of Fracture*, 77, 141-159 (1996).
- Gent A.N. and Lindley P.B., *Proc. Roy. Soc. A*249, 195-205 (1959).
- Gent A.N. and Tompkins, D.A., *J.Appl. Phy.*, 40, 2520, (1969)
- Gent, A. N., *Engineering with Rubber*, USA, 1992.
- Gent, A.N. and Park, B., *Journal of Polymer Science*, 19, 1947-1956 (1984).
- Green A.E. and Zerna W., *Theoretical elasticity*, Oxford Univ. Press, London (1954).
- Hall, E.O., *Proc. Physics Society*, London, 64B, 747 (1951).
- Knauss, W.G., *Report of the California Institute of Technology.- Preprint International Conference on Fracture*, Sendai, Japan, Sept. (1965).
- Lindsey, G.H., Schapery, R.A., Williams, M.L. and Zak, A.R., *Report of the California Institute of Technology, Aerospace Research Laboratories, USA Air Force* (1963).
- Lindsey, G.H., *Hydrostatic Tensile Fracture of Polyurethane Elastomers. California Institute of Technology, USA. PhD Thesis* (1966).
- Oberth, A.E. and Bruenner, R.S., *Trans. of the Society of Rheology*, 9(2), 165-185 (1965)
- Oberth, A.E., *Rubber Chemistry and Technology*, 40, 1337-1363 (1967)
- Petch, N.J., *Journal Iron Steel Institute*, London, 174, 174 (1953)
- Yerzley, F.L. *Adhesion of Neoprene to metal*, *Ind. and Eng. Chem.*, 31, 950-956 (1939).
- Williams M. L. and Schapery R.A., *Int. J. Fract. Mech.*, 1, 64-72 (1965).





# **Chapter 6**

## **Cavitation Models and Analysis**

Introduction .....	231
6.1.- State-of-the-art .....	231
6.1.1.- Prediction of the resistance to cavitation based on the stress field and the elastic instability: Simple Deformation .....	231
6.1.2.- Cavitation resistance prediction considering the surface energy .....	233
6.1.3.- Prediction of the cavitation resistance based on the expansion by fracture.....	235
6.2.- Model-experiment comparisons: Temperature dependence .....	238
6.2.1.- Simple deformation cavitation model .....	238
6.2.2.- Expansion by Fracture: Linear Elastic Fracture Mechanics (LEFM).....	239
6.2.3.- Non-linear Model: Strain hardening .....	240
6.2.3.1.- Fit of our experimental results with the nonlinear fracture model.....	244
6.3.- Model-experiment comparisons: Speed dependence .....	248
6.3.1.- Fitting of the experimental results at different speeds .....	248
6.4.- Statistics: Number of pre-critical cavities and position distribution.....	250
6.4.1.- Cumulative probability of cavitation .....	250
6.4.2.- Spatial distribution of pre-critical cavities .....	251
Conclusions .....	255
Acknowledgements .....	256
Appendices A6 .....	257
Appendix A6.1: FEM simulation for a penny-shaped crack in an infinite material subjected to internal pressure. ....	257
Appendix A6.2: FEM simulation .....	258
Bibliography .....	260

## Introduction

Chapter 3 presented the mechanical properties of the three polyurethane model networks including the fracture toughness, and Chapter 5 presented the results of the cavitation experiments. As described in Chapter 5 this is the first time that a complete study of fracture toughness in mode I and a study of the resistance to cavitation under very confined conditions is carried out on the same materials. This chapter discusses the results in view of the pre-existing theoretical models to predict cavitation resistance. All analytical models describe the expansion of a preexisting cavity in an infinite medium under a symmetric hydrostatic loading. We start from older models considering expansion by deformation only, to go toward fracture models and to more recent models in which the limiting extensibility and the initial cavity size are taken into account. We compare our experimental data obtained with a finite size sample and confined conditions and propose possible explanations for the discrepancies between our experimental data and the model predictions.

### 6.1.- State-of-the-art

It is useful to briefly review now the most important existing cavitation models on rubbers. Although the notion of cavitation, which comes from liquids, implies the nucleation of a cavity from a previously homogeneous material, most mechanical descriptions of cavitation are actually cavity expansion models. They can be roughly divided in two categories: reversible expansion by deformation and irreversible expansion by fracture.

#### 6.1.1.- Prediction of the resistance to cavitation based on the stress field and the elastic instability: Simple Deformation

The earliest cited theoretical work on cavity expansion by deformation in rubbers was reported by Green and Zerna [Green and Zerna 1954] and later by Gent and Lindley [Gent and Lindley 1959]. They proposed that, for a cavity expanding in an infinite medium of neo-Hookean material, the relation between the extension ratio  $\lambda$  of the circumference in the inner surface and the inflating constant pressure  $P$  in the cavity takes the form:

$$P = \frac{E}{6} \left( 5 - \frac{4}{\lambda} - \frac{1}{\lambda^4} \right) \quad \text{eq. 6.1}$$

Figure 6.1 shows the schematic of the problem of internal pressure in a cavity that, in incompressible materials, is equivalent to an applied far-field constant true triaxial stress.

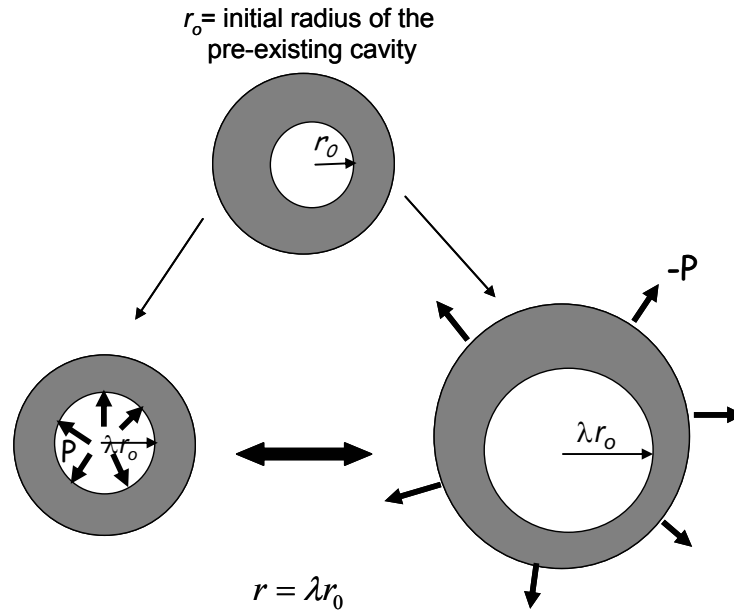


**Figure 6.1:** Schematic of the problem of internal pressure in a cavity, which is equivalent in incompressible materials. Left-down: Sketch of inflated spherical cavity. Right-down: Spherical cavity in a material under far-field triaxial tension of  $-P$ .

Equation 6.1 shows immediately that for such a material, the hydrostatic stress applied to a sphere can not exceed a critical value  $P_c$  given by:

$$P_c = \frac{5}{2}\mu \quad \Leftrightarrow \quad P_c = \frac{5}{6}E \quad \text{eq. 6.2}$$

where  $P_c$  is the critical hydrostatic stress ( $P_c = \sigma_{\text{hydrostatic, max}}$ ) corresponding to unstable inflation; and  $\mu$  and  $E$  are the shear and Young's moduli of the material measured at low strain, respectively.

Based on these theoretical predictions Gent and Lindley [Gent and Lindley 1959] associated the critical hydrostatic stress measured in a poker-chip tensile test to the onset of cavitation. They found that the cracking stress ( $S' = P_c$ ) was generally higher for stiffer vulcanizates rubbers and reported that the cracking stress depended linearly on the Young's modulus  $E$  of the rubber. The cavitation models based on simple deformation [Green and Zerna 1954, Gent and Lindley 1959] assume that the results are independent of the initial size of cavity since the cavity is in an infinite medium and grows by deformation without surface tension. The cavity grows under a constant internal pressure and the deformation is reversible. Their results were interpreted by them as suggesting that probably, during the materials processing, some gas bubbles were trapped.

In 1982, Ball [Ball 1982] proposed the first mathematical analysis of the phenomenon of nucleation of a cavity from a homogeneous material in non-linear elasticity. Using a

minimization of potential energy argument, he investigated a class of singular solutions to the equations of nonlinear elasticity in which a spherical cavity forms at the center of a ball of isotropic material placed in tension by means of surface tractions or displacements. The existence of such solutions depends on the properties of the strain energy function  $W$  for large strains. He justified theoretically that for a neo-Hookean material a hydrostatic pressure of  $5E/6$  was needed to nucleate a cavity. This theoretical analysis was later used by several authors [Chou-Wang and Horgan 1989, Horgan and Pence 1989, Horgan and Abeyaratne 1986, Polignone and Horgan 1993]. Hou and Abeyaratne [Hou and Abeyaratne 1992] generalized the Ball's model to an infinite media submitted to triaxial loading under arbitrary stress boundary conditions [Fond 2001, Hamdi 2006].

The criterion of a critical pressure  $P_c=5E/6$  for cavitation was confirmed experimentally by several authors such as Cho and Gent [Cho and Gent 1988], Kakavas and Chang [Kakavas and Chang 1992], Pond [Pond 1993], Oberth and Bruenner [Oberth and Bruenner 1965], Oberth [Oberth 1967], Gent and Park [Gent and Park 1984], Denecour and Gent [Denecour and Gent 1968], Gent and Tompkins [Gent and Tompkins 1969]. However, some experimental results had already shown that  $P_c$  could be higher than  $5E/6$  in certain conditions and that there certainly was a missing element in the model.

#### 6.1.2.- Cavitation resistance prediction considering the surface energy

In 1969, Gent and Tompkins [Gent and Tompkins 1969] treated theoretically the expansion of an existing cavity in a neo-Hookean medium, in a relatively simple way. They obtained that the surface tension tends to close the very small cavities (needing pressures of 1000 atm. for holes of 10 Å radius) and they concluded that higher stresses should be necessary to cause the growth of microvoids, taking into account the surface energy, which provides an additional restraint upon expansion. The surface tension can be regarded as an internal negative pressure ( $P_i$ ) by:

$$P_i = \frac{2\gamma}{r} = \frac{2\gamma}{\lambda r_0} \quad \text{eq. 6.3}$$

where  $\gamma$  is the surface tension of the rubber,  $r$  is the radius of the cavity,  $r_0$  is the initial radius of the cavity, and  $\lambda=r/r_0$  is the stretch ratio under equibiaxial tension in the inner surface [Fond 2001]. Gent and Tompkins, assumed that the surface of the cavity has a surface energy  $\gamma$  of the same kind as in simple liquids and they considered then that the inflation pressure of a cavity consists of both elastic and surface energy term resulting in the following prediction.:

$$P = \frac{E}{6} \left( 5 - \frac{4}{\lambda} - \frac{1}{\lambda^4} \right) + \frac{2\gamma}{\lambda r_0} \quad \text{eq. 6.4}$$

Figure 6.2 presents the results of the model of Gent and Tompkins (on the left) and a sketch of the effect of the surface tension  $\gamma$  on the cavity growth, related as an internal pressure ( $P_i$ ) (on the right); the present radius of the cavity noted by 'a' is equal to 'r'.

Gent and Tompkins [Gent and Tompkins 1969] studied the case of a spherical cavity in an incompressible neo-Hookean material, and calculated the hydrostatic stress to be applied to an infinite medium containing a spherical cavity to increase its size.

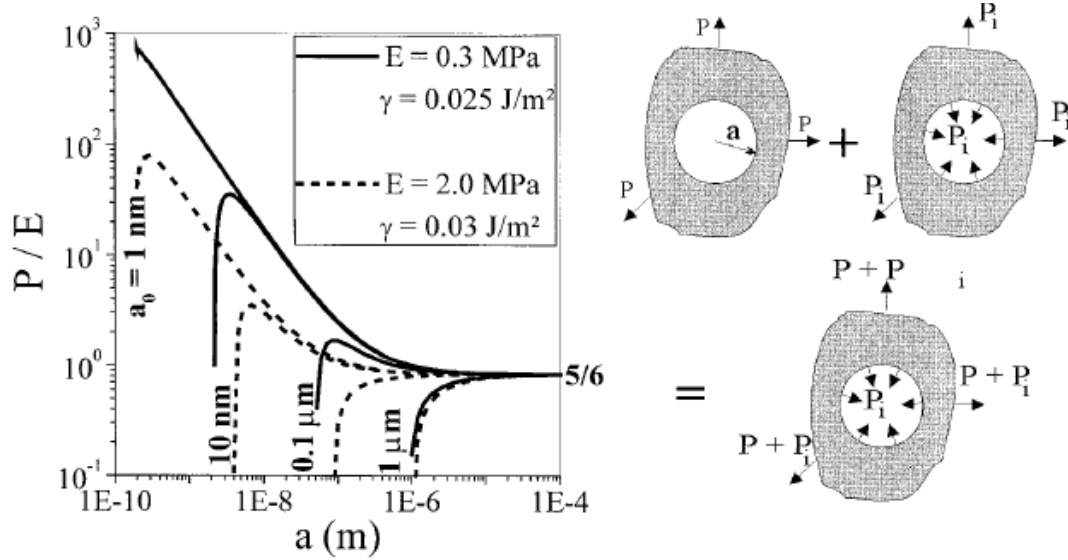


**Figure 6.2:** Model of Gent and Tompkins taking into account the surface tension of the rubber (taken from Fond [Fond 2001]). Present radius of the cavity = 'a' = 'r'.  $P_c > 5E/6$ .

It is interesting to see what is the typical size of the cavity where surface tension becomes important since it is given by  $\gamma/E$ . For our materials this leads to  $r_\gamma$  of the order of 50 nm. Therefore of the materials contains cavities (or cracks) larger than 50 nm the effect of surface tension can be neglected. Since we do not expect our materials to be exempt of defects at that length scale, we will neglect surface tension on the following.

Gent and Tompkins [Gent and Tompkins 1969] and also William and Schapery [William and Schapery 1965] developed a model considering the inflation pressure of a cavity, by considering both elastic and surface energy terms. The parameters taken into account in these models are the modulus  $E$  of the incompressible material, the surface tension  $\gamma$  and the initial size of the cavity  $r_0$ . However, these models still consider a reversible deformation and do not take into account the limiting extension of any real rubber under equibiaxial tension, which will cause fracture of bonds if the cavity stretches macroscopically beyond the limiting extensibility of the network chains. This important remark leads us now to consider a different type of models.

### 6.1.3.- Prediction of the cavitation resistance based on the expansion by fracture

As discussed in chapter 1, the bases of fracture criteria were laid by Griffith in 1921 [Griffith 1920]. He stated that a critical amount of mechanical energy has to be released to propagate a tear  $G > G_c$  (released elastic energy  $G$  higher than the critical fracture energy  $G_c$ ); therefore, the cavity growth is explained in terms of a critical fracture energy  $G_c$ .

Apart from Williams and Schapery's model [William and Schapery 1965] which was not really a fracture model, the first model considering explicitly expansion by fracture was proposed by Gent and Wang [Gent and Wang 1991] and then slightly modified by Diani [Diani 2001] who also developed criteria of irreversible expansion of cavities, based on energy approaches. In 1991, Gent and Wang [Gent and Wang 1991] proposed a model that was inspired by that of Williams and Schapery [William and Schapery 1965] and studied the conditions of propagation of a pressurized penny-shaped crack within a highly elastic material. They found that the critical internal pressure  $P_c$  depended strongly of the initial size of the crack.

This last conclusion differs from earlier results where only expansion of a cavity in a neo-Hookean material was considered, in which sufficiently large cracks would tear open at  $P_c = 5E/6$ , independently of the crack size [Gent and Lindley 1959, Oberth and Bruenner 1965, Denecour and Gent 1968, Gent and Tompkins 1969, Gent and Park 1984, Cho and Gent 1988]. However, this criterion remains useful as a guide for crack having initial radii in an intermediate range,  $r_0 = 0.5\mu\text{m}$  to  $1\text{mm}$ .

Gent and Wang (G-W) [Gent and Wang 1991] calculated values of  $P_c$  for a range of initial crack sizes, using a critical energy release rate criterion for fracture. In this fracture model [Gent and Wang 1991] the main parameters that play an important role in cavitation are:

- Materials parameters: Modulus ( $E$ ), Fracture energy ( $G_c$ ) and the nonlinear elastic properties of the material, including strain hardening due to finite chain extensibility.
- the initial crack size  $r_0$ .
- System parameters (loading): Hydrostatic stress ( $P$ )).

The insight of the model of Gent and Wang [Gent and Wang 1991] is that it is possible to calculate the normalized pressure  $P/E$  as a function of the normalized energy release rate  $G/E r_0$  by calculating both as a function of  $\lambda$ , i.e.:

$$G = E r_0 f(\lambda) \quad \text{eq. 6.5}$$

$$P = E f(\lambda) \quad \text{eq. 6.6}$$



Since the adimensional parameters are normalized by E, there is only one solution for a neo-Hookean material given as

$$\frac{G}{Er_0} = \frac{2}{3} \left( 1 + \lambda^2 - \frac{2}{\lambda} \right) \quad \text{eq. 6.7a}$$

$$\frac{P}{E} = \frac{1}{6} \left( 5 - \frac{4}{\lambda} - \frac{1}{\lambda^4} \right) \quad \text{eq. 6.7b}$$

Plotting 6.8 as a function of 6.7 for any given value of  $\lambda$  gives then the desired prediction of P/E as a function of G/Er<sub>0</sub>.

If the material constitutive equation contains additional parameters, the details of the P/E vs. G/Er<sub>0</sub> curve will depend on these additional parameters. It is particular noteworthy that for materials with a finite extensibility, the energy release rate is no longer unbounded at P/E = 5/6 and a solution for G/Er<sub>0</sub> can be found for higher pressures, as measured experimentally. The difficulty of the G-W approach is however the accurate calculation of G for a penny-shaped crack. The solution given in equation 6.1 assumes that the crack can expand to a cavity of same diameter without external work, which is obviously incorrect. This leads to a wrong prediction of G for low values of P where G should be proportional to (P/E)<sup>2</sup>. The reader is referred to the paper of Lin and Hui [Lin and Hui 2004] for a more complete discussion of the different models.

In 2004, Lin and Hui [Lin and Hui 2004] proposed a numerical method (Finite Element Method FEM) to calculate G exactly for small penny-shaped cracks in an infinite medium. Lin and Hui [Lin and Hui 2004] used three different materials behaviour: a power law material model, a Mooney-Rivlin material, and a material model proposed by Gent [Gent 1996] which takes into account that the molecular structure will fail at a limiting stretch ratio. Lin and Hui [Lin and Hui 2004] compared their results to the results of Gent and Wang [Gent and Wang 1991] and Williams and Schapery [William and Schapery 1965] as presented in Figure 6.4.

Based on the results obtained by Lin and Hui, the linear fracture theory provides a reasonably approximation to the energy release rate, even at intermediate deformations. A nonlinear analytical approximation is also proposed for a neo-Hookean material.

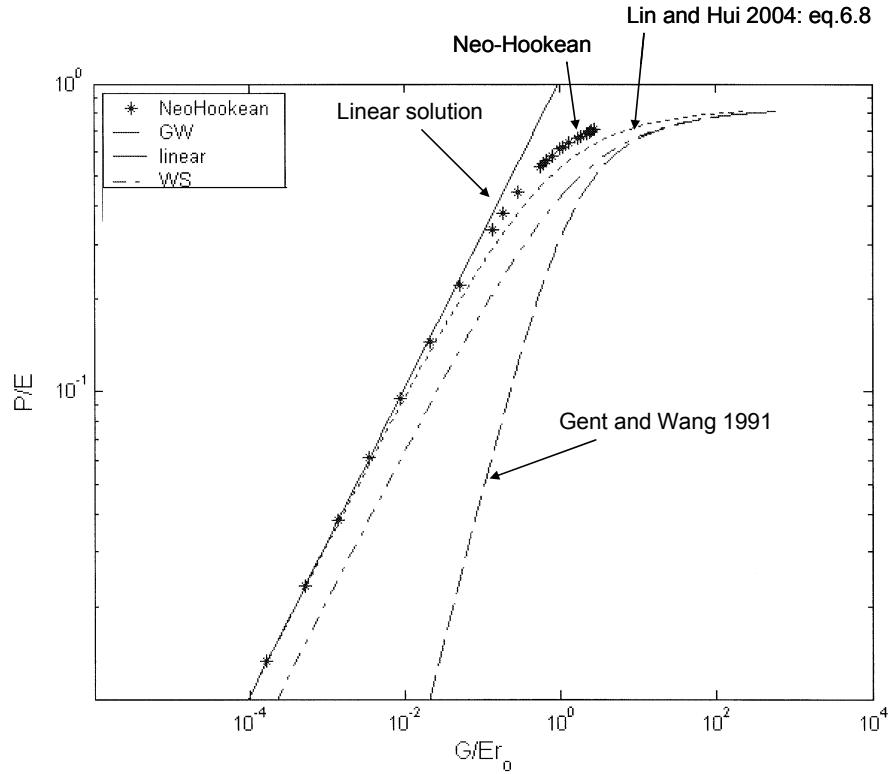


**Figure 6.3:** Normalized pressure versus the normalized energy release rate (taken from Lin and Hui 2004).

The resulting approximation equation (22) reported by Lin and Hui [Lin and Hui 2004] presented in the graph (Figure 6.3) is given in equation 6.8:

$$G \cong \frac{4Er_0}{9\pi} \left( 2\lambda^2 + \frac{1}{\lambda^4} - 3 \right) \quad \text{eq. 6.8}$$

This equation relates the energy release rate  $G$  of a circular crack loaded by internal pressure to the volume of the deformed cavity. This numerical result gives an error of the order of 100 percent for the energy release rate prediction. The expression is valid for incompressible hyperelastic materials. The plotted results of Williams and Schapery seem to be a better approximation of the energy release rate than Gent's; however, Williams and Schapery's theory overestimate the energy release rate by about 200 percent and the values of  $\lambda$  (not plotted here) are unphysical for low deformations.

Since the G-W's model [Gent and Wang 1991] overestimates the value of the energy release rate  $G$ , then if the Griffith criterion is used to predict fracture initiation, the Gent's result underestimates (by about one order of magnitude) the critical hydrostatic stress  $P_c$  for crack initiation, while for large cavities the  $P_c$  values are abnormally low.

However, Gent and Wang's model [Gent and Wang 1991] is simple to implement and the finite extensibility can be built into the model. Then, by using Gent and Wang's original idea [Gent and Wang 1991] but the Lin and Hui's methodology [Lin and Hui 2004] we tried to fit our experimental data to the G-W model, as presented in the next sections.

## 6.2.- Model-experiment comparisons: Temperature dependence

First, it is useful to summarize the results of chapter 5, on the maximal hydrostatic stress normalized by the Young's modulus. Figure 6.4 shows that for all three networks at different temperatures, the softer network PU8000 is tougher and more cavitation resistant relative to its modulus, followed by PU8000/1000 and PU4000. The question is how can these results be explained theoretically?.

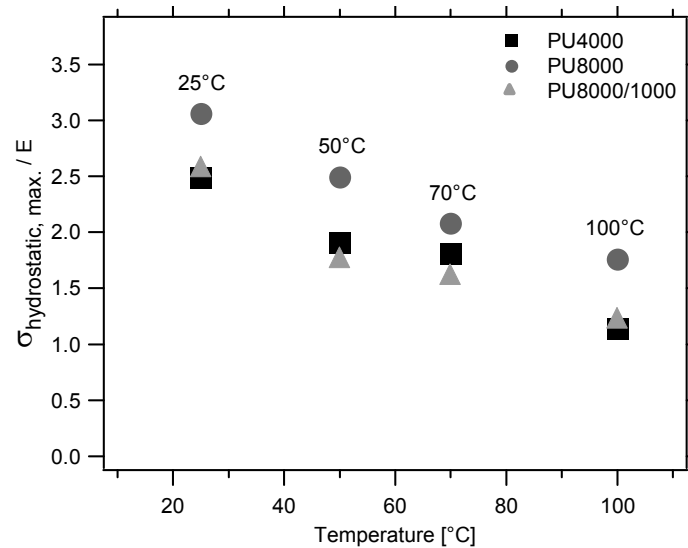


**Figure 6.4:** Maximal hydrostatic stress  $\sigma_{\text{hydro, max}}$  normalized by the modulus, for the three polyurethane model networks as a function of the temperatures 25°C, 50°C, 70°C and 100°C, and 10μm/s.

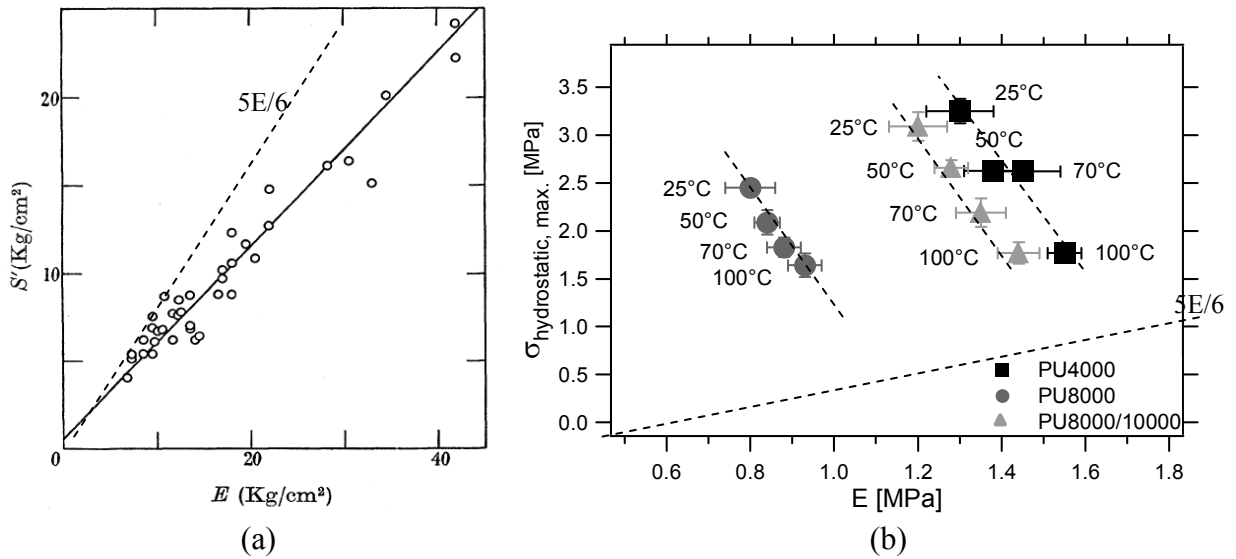
### 6.2.1.- Simple deformation cavitation model

Figure 6.5 (b) shows the maximal hydrostatic stress  $\sigma_{\text{hydro, max}}$  as a function of the modulus for the three polyurethane model networks for different temperatures. Figure 6.5 (b) shows clearly that for a given network the maximal hydrostatic stress  $\sigma_{\text{hydro, max}}$  decreases while the modulus increases due to thermoelasticity, in blatant contradiction with Gent and Lindley's results(Figure 6.5 (a)). Yet comparing different networks as Gent did, the cavitation stress does seem to increase with modulus. How to reconcile these contradictory observations?

We also observe in Figure 6.5 (b) that for our experimental results for the three polyurethane model networks the maximal hydrostatic stress  $\sigma_{\text{hydrostatic, max}}$  at different temperatures is significantly higher than the predicted criterion of critical pressure  $P_c = 5E/6$ . Based on these results this simple criterion is inadequate to interpret the crack growth initiation of our experimental data.

The simple deformation model was developed for neo-Hookean materials, considering that the cavity was in an infinite medium growing by deformation at constant applied true stress

no surface tension. This is clearly unrealistic and in the next section models taking into account the surface tension are mentioned.



**Figure 6.5:** Comparison of maximal hydrostatic stress  $\sigma_{\text{hydro, max}}$  as a function of the modulus for (a) Vulcanizates (taken from Gent and Lindley 1959), and (b) the three polyurethane model networks at different temperatures 25°, 50°C, 70° and 100°C, and 10 $\mu\text{m/s}$ .

### 6.2.2.- Expansion by Fracture: Linear Elastic Fracture Mechanics (LEFM)

The Griffith's fracture criterion [Griffith 1920], states that the crack growth occurs when the energy release rate 'G' reaches the critical value  $G_c$  ( $G \geq G_c$ ) also called fracture energy which is in principle a material constant, depending only on the mode of loading (mode I opening, II shear and III, transverse shear). Because the energy release rate depends on the initial flaw size, a given material can have different fracture stresses for the same value of  $G_c$ . In our geometry and although the size and shape of flaws initially present is unknown, we assume that a penny-shaped crack with initial radius  $r_0$  much smaller than the sample size exists. Then, within the framework of linear elasticity the dependence of the fracture energy G on the initial crack radius  $r_0$  is given by [Lin and Hui 2004]:

$$G \cong \frac{P^2}{E} r_0 \phi_{\text{geometry}} \quad \text{eq. 6.9}$$

where  $\phi$  is a dimensionless function that involves the geometry, E is the Young's modulus of the hyperelastic material at small strains, and P is the hydrostatic stress. The hydrostatic stress P becomes  $P_c$  ( $P_c = \sigma_{\text{hydrostatic, max}}$ ) when the maximal hydrostatic stress is reached, and G becomes  $G_c$  when the critical fracture energy value is reached. Equation 6.9 is valid at very low applied pressure, when the energy release rate G must be given by the small strain theory. The geometry used to perform fracture experiments, as presented in chapter 3, is different than the confined geometry used to perform the cavitation experiments. Yet we can check

whether  $P_c^2/E$  scales with  $G_{Ic}$  measured in DENT tests. Figure 6.6 shows clearly that for the same material at different temperatures the relationship between  $P_c^2/E$  and  $G_{Ic}$  is approximately linear. If now we try to fit all the materials in one single line we observe that it is not possible. This means that either  $r_0$  (proportional to  $G$  based on equation 6.9) is different for each material or the fracture energy  $G$  as calculated by equation 6.9 is not good because the Linear Elastic Fracture Mechanics (LEFM) does not take into the limiting extension of the chains (strain hardening).

Anyway, as presented by Lin and Hui [Lin and Hui 2004] the simple model of the linear fracture theory provides a reasonably approximation to the fracture energy  $G$ , but this model by itself is not enough to predict the cavitation phenomenon and to fit our experimental data into a cavitation model.

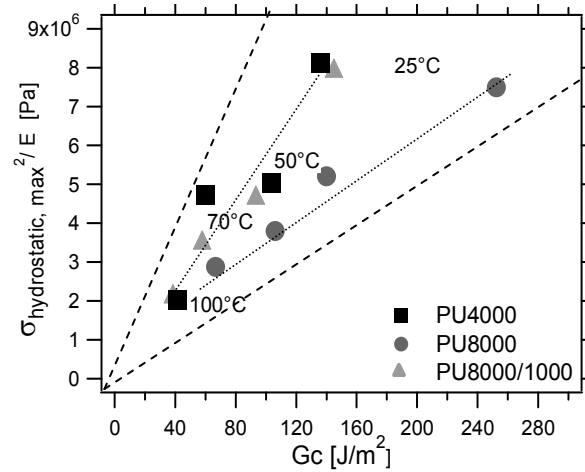


**Figure 6.6:** Expansion by fracture using Linear Elastic Fracture Mechanics (LEFM). Relation between  $P^2/E$  and  $G_c$  for the three polyurethane model networks at different temperatures.

### 6.2.3.- Non-linear Model: Strain hardening

Here we present the Gent and Wang's method details [Gent and Wang 1991] and the Lin and Hui method's details [Lin and Hui 2004], and we show our predicted curves and the fittings. Both methods calculate  $G/Er_0$  as a function of  $\lambda$ , but the methods to calculate it differ.

#### The Gent and Wang's method to calculate $G$ :

In the Gent and Wang's model [Gent and Wang 1991]  $G$  is calculated by assuming from the start that a planar circular crack of radius  $r_0$  under hydrostatic stress can expand to an initial spherical cavity of the same radius  $r_0$  without any work. This is then the reference configuration and  $G$  is calculated by comparing the strainenergy of two cavities of different initial radii expanded to the same volume. Figure 6.7 illustrates schematically the Gent's

procedure. Figure 6.7 (a) shows the deformation of a crack into a spherical void of the same radius with no applied pressure (stress free). The spherical void of radius  $r_0$  is then inflated into a spherical cavity of radius  $R_0$  (see Figure (1b)). Next, the same infinite solid with larger circular crack ( $r_0+dr_0$ ) repeats the same process illustrated in Figure 6.7(a) and (b), and fluid is pumped into the interior of the larger spherical cavity in such a way that the final volume of the cavities are the same (see Figure 6.7 (c) and (d)), the elastic strain energy at the end of the process is given by  $W(r_0+dr_0)$ . The difference between  $W(r_0)$  and  $W(r_0+dr_0)$  divided by  $dr_0$  is the the energy release rate  $G$ . With the procedure outlined here this difference can be obtained analytically for a neo-Hookean material and the result is equation 6.7a.

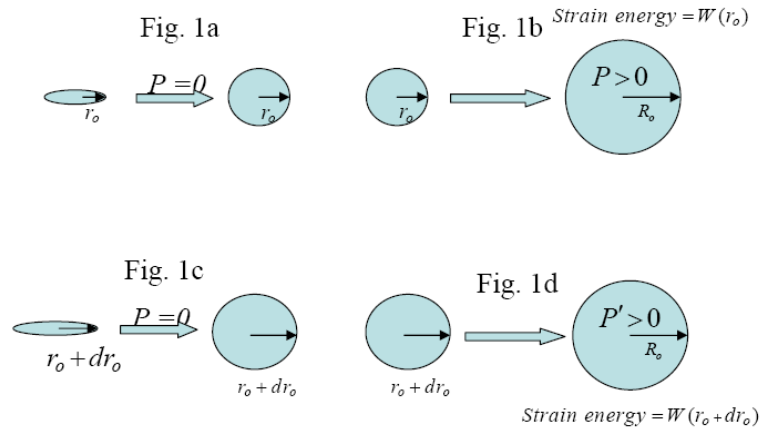


**Figure 6.7:** Gent and Wang's procedure [Gent and Wang 1991] to compute the energy release rate of a penny-shaped crack (taken from Lin and Hui 2005).

The advantage of this methodology is that if the constitutive equation is not too complicated the equivalent of equations 6.7 can be obtained analytically and a prediction can then be easily made. However, [Lin and Hui 2004] the approximation made by Gent and Wang in calculating  $G$  grossly overestimates  $G$  and does not extrapolate of the correct solution in the linear regime (as presented in Figure 6.3). Alternatively if the Griffith criterion is used to predict fracture initiation, the Gent's result underestimates the critical hydrostatic stress  $P_c$  for crack initiation.

### **The Lin and Hui's method to calculate $G$ :**

Lin and Hui [Lin and Hui 2004] compute  $G$  by simulating a volume controlled expansion test with a finite element method. Using the definition of fracture energy,

$$G = \frac{1}{2\pi r_0} \left. \frac{\partial W}{\partial r_0} \right|_V \quad \text{eq. 6.10}$$

where

$$W = \int_0^V P(V') dV' \quad \text{eq. 6.11}$$

where W is the strain energy of the system, P is the hydrostatic stress and V is the volume. is

To compute  $\left. \frac{\partial W}{\partial r_0} \right|_V$

$$W = PV - \int_0^P V(r_0, P') dP' = PV - r_0^3 \int_0^P \Omega(P' / E) dP' \quad \text{eq. 6.12}$$

where  $\Omega$  is a dimensionless function, E the (initial) tensile modulus of the material. Then the fracture energy or energy release rate is obtained:

$$G = \frac{3r_0}{2\pi} \int_0^P \Omega(P' / E) dP' \quad \text{eq. 6.13}$$

Equation 6.14 is a useful form of the fracture energy since the volume of the deformed crack at any applied load can be computed numerically. The details of the numerical methods are given in Appendix A6.

The question that arises is how we can compare the fracture models with experimental data?. We can divide the procedure into three main steps.

Step 1: To compute G ( $r_0$ , P) for a given material with equation 6.15, we need the characterization of the elastic properties in the nonlinear regime and a reasonable constitutive equation needs then to be used to fit the tree materials. We use the constitutive equation proposed by Seitz *et al.* [Seitz *et al.* 2008]. The strain energy function is given by:

$$U = \frac{E}{6} J_* \left( \exp \left( \frac{J_1}{J_*} \right) - 1 \right) \quad \text{and} \quad J_1 = \lambda_x^2 + \lambda_y^2 + \lambda_z^2 - 3 \quad \text{eq. 6.14}$$

and the uniaxial compression prediction is given by:

$$\sigma_N = \frac{E}{3} \left( \lambda_y - \frac{1}{\lambda_y^2} \right) \exp \left( \frac{J_1}{J_*} \right) \quad \text{and} \quad J_1 = \lambda_y^2 + \frac{2}{\lambda_y} - 3 \quad \text{eq. 6.15}$$

If equation 6.17 is fitted to the data, two parameters are obtained: the initial modulus E and the strain hardening parameter  $J_*$ . This is done for our materials in chapter 3.

Step 2: The normalized energy release rate needs to be calculated analytically (with the Gent method) or numerically (with the Hui method) as a function of  $\lambda$  to obtain the curve of equation 6.5 for each material. Then an hypothesis needs to be made for the value of  $G$  and  $r_0$  to obtain a critical value of  $\lambda = \lambda_c$  where fracture occurs.

$$\frac{G_c}{Er_0} = f(\lambda_c) \quad \text{eq. 6.16}$$

Step 3: The inflation pressure necessary to grow the bubble to the critical  $\lambda_c$  can now be calculated with equation which again can be calculated analytically or numerically:

$$\frac{P_c}{E} = g(\lambda_c) \quad \text{eq. 6.17}$$

The outcome is a prediction for:  $\frac{P_c}{E}$  as a function of  $\frac{G_c}{E * r_0}$

The use of the three steps mentioned before gives predictions of  $P/E$  as a function of  $G_c/Er_0$  as presented in Figure 6.8.

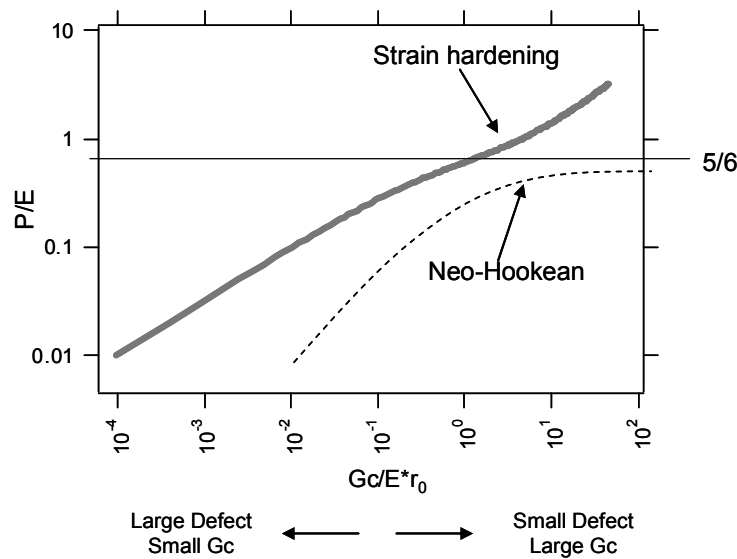


**Figure 6.8:** Typical curve predicted with the Gent and Wang's methodology [Gent and Wang 1991]:  $P_c/E$  vs.  $G_c/Er_0$ .

Now, the original insight of the model of Gent and Wang [Gent and Wang 1991] was to propose a methodology for a finite strain version of the Griffith argument. Lin and Hui proposed a numerical way to calculate  $G$  which does not require any approximation or new analytical calculations when the constitutive equation is changed.



For the purpose of this thesis, L. Rong in the research group of C.Y. Hui (at Cornell University), did a FEM calculation of  $G$  as a function of  $P$  and  $r_0$  for the three materials of our study as described by equation 6.15. The outcome of this FEM calculation is represented as:  $P/E$  vs.  $G/Er_0$  in figure 6.9.

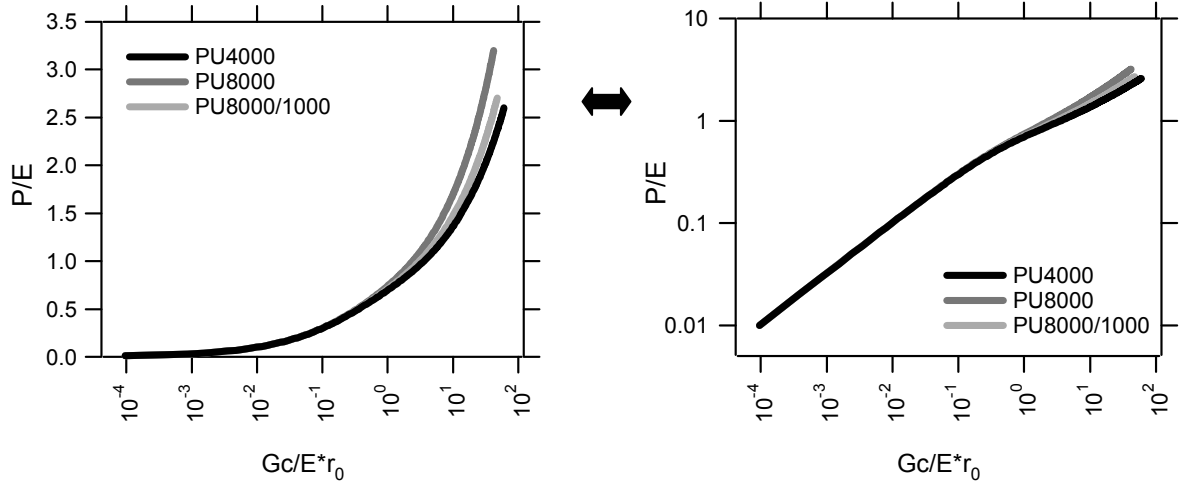


**Figure 6.9:** Predicted curves  $P/E$  vs.  $G/Er_0$  obtained by FEM, for the three polyurethane model networks. Left:  $P/E$  in linear scale, and Right:  $P/E$  in log scale.

Since in the exponential fit of the compression data we obtained for PU4000 and PU8000/1000 that the strain hardening was less pronounced than for PU8000, and since we had doubts about the validity of the data for the two most brittle networks, we decided to use PU8000 as the standard curve for our polyurethanes to check the theoretical prediction of the fracture model.

#### 6.2.3.1.- Fit of our experimental results with the nonlinear fracture model

The average maximum hydrostatic stress for the three polyurethane model networks was obtained experimentally from the maximum force of the force displacement curve while the Young's modulus was obtained in chapter 2. Hence  $P_c/E$  is well defined for each material and temperature. According to the nonlinear fracture model, this value of  $P_c/E$  should correspond to a value of  $G_c/Er_0$ . The 'adjustable' parameters are  $G_c$  and  $r_0$ , where  $G_c$  can either be a threshold value in the Lake-Thomas sense  $G_0$  (an intrinsic fracture resistance which does not take into account dissipation), or an experimentally determined value  $G_{IC}$  (in mode I by DENT) which then can vary with strain rate and temperature.

Figure 6.10 presents the PU8000 curve and our experimental data at different temperatures for the three polyurethane model networks. In the x-axis only  $G_c/E$  is used without using any specific  $r_0$ .

Figure 6.10(a) shows the experimental data using  $G_0 \cong G_c$  at highest temperature and Figure 6.10(b) shows the experimental data using  $G_c$  at different temperatures. We observe that when  $G_0$  is used all points for the same material fall on the same vertical line. Comparing figure

6.10a and figure 6.9a, it is clear that the only vertical part of the theoretical curve falls around  $G_c/Er_0 \sim 10$ . Given that our values of  $G_c$  are around  $100 \text{ J/m}^2$  and the moduli are around 1 MPa this suggests values of  $r_0$  around  $10 \text{ }\mu\text{m}$ .

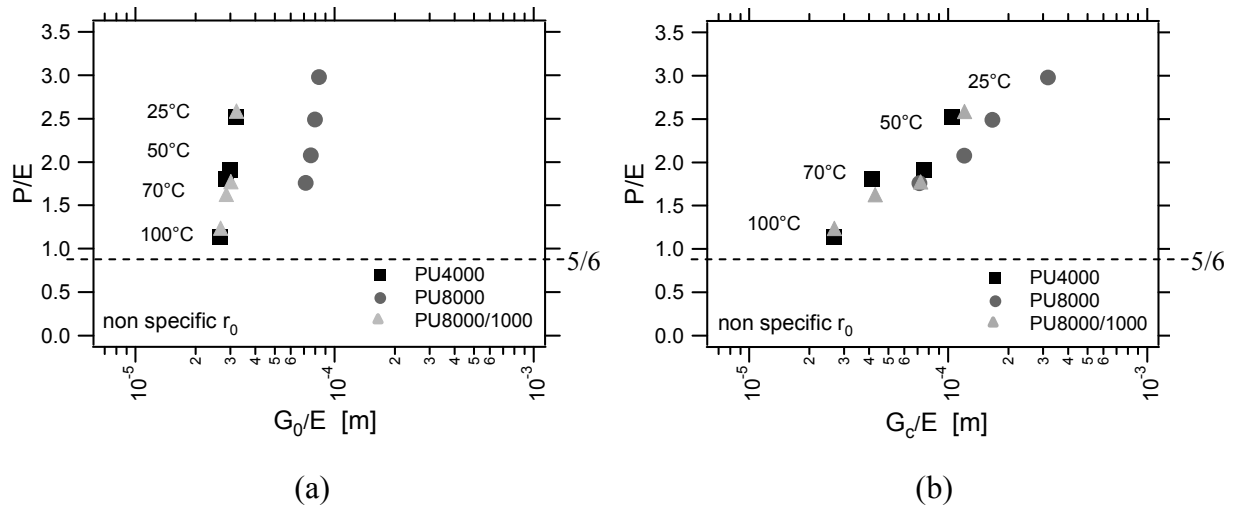


**Figure 6.10:** Fitting of our experimental data to the theoretical predicted curves, for the three polyurethane model networks: (a) using  $G_0 \cong G_c$  at highest temperature, and (b) using  $G_c$  at different temperatures. None  $r_0$  value was used.

Indeed, if one arbitrary  $r_0$  (i.e.  $r_0 = 5 \text{ }\mu\text{m} = 5 \cdot 10^{-6} \text{ m}$ ) is used for all the temperatures and the three polyurethane model networks, then the experimental points are moved close to the theoretical curve (see Figure 6.11 (a) and (b)). When the fracture energy threshold is chosen as  $G_0 \cong G_{Ic}(\text{DENT})$  at  $T = 100^\circ\text{C}$  (Figure 6.11(a)) the data can clearly not fit the model..

However, when  $G_c$  is taken as  $G_{Ic}(\text{DENT})$  at the temperature where the cavitation tests were carried out (Figure 6.11(b)), we observe that the points fit much better to the theoretical curve, particularly knowing that only the theoretical curve for the PU8000 is precisely known and shown in the figure.

This interesting result suggests that the cavitation resistance is controlled not only by  $E$  but also by  $G_c$ . However the question that arises here is why the data fits the model for all the temperatures and for the three polyurethane model networks when using the same initial crack  $r_0$ .

In other words while there is probably an initial size distribution of defects, the temperature dependence is controlled by the fracture toughness  $G_c$  and not by the distribution of initial sizes of the cavity  $r_0$  which would have given a much broader distribution of values of fracture stress..

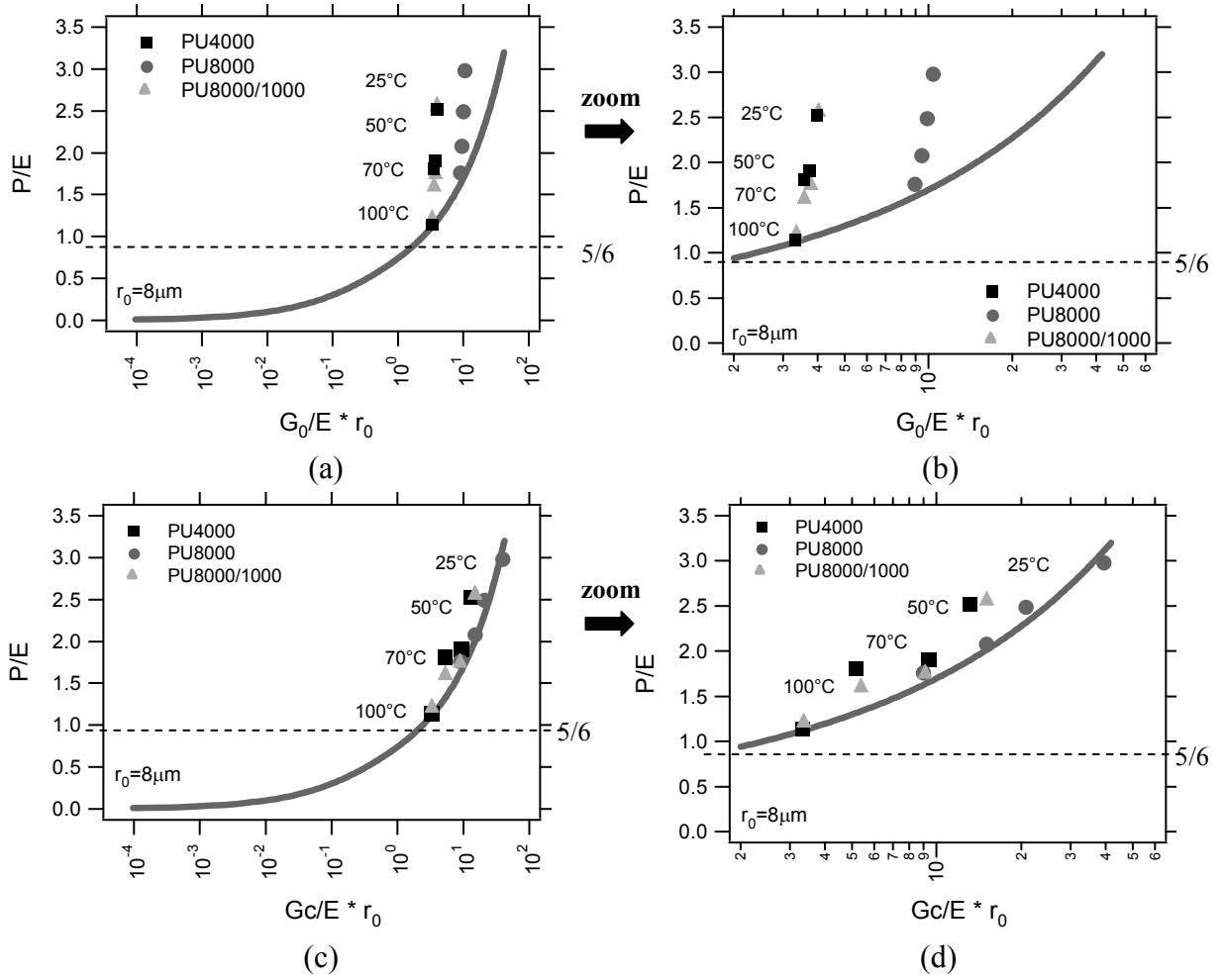


**Figure 6.11:** Fitting of our experimental data to the theoretical predicted curves using  $r_0 = 8 \mu\text{m} = 8 \cdot 10^{-6}\text{m}$ , for the three polyurethane model networks: (a) using  $G_0 \cong G_c$  at highest temperature, (b) zoom using  $G_0 \cong G_c$  at highest temperature, (c) using  $G_c$  at different temperatures, and (d) zoom, using  $G_c$  at different temperatures.

### Alternative Proposal: thermally activated microscopic cavitation model

Although the conclusion that the resistance to cavitation is controlled by  $G_c$  is reasonable, it may not be the only possible one. We made a qualitative analysis, and we argue that the initial crack size  $r_0$  is different at different temperatures and we propose that a given subcritical crack with a given initial size (an initial defect) will grow due to thermal activation.

The idea behind this model is that if a pre-crack grows (see Figure 6.12) by random but irreversible bond fracture under stress until a critical size where fracture mechanics applies, then at early stages thermal activation and subcritical crack growth may be the dominant (nucleation mechanism) and the Eyring model may be used [Guarino *et al.* 1999].

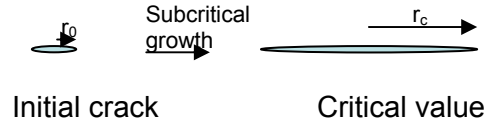


**Figure 6.12:** Pre-crack thermally activated.

The equation governing the crack growth would be the Eyring equation, where the first term  $\left(-\frac{\Delta H}{RT}\right)$  corresponds to the thermally activated part and the second term  $\left(\frac{\sigma V_a}{RT}\right)$  corresponds to the activation due to stress. Then the probability of a molecular fracture event at the crack tip would be proportional to  $\exp\left(-\frac{\Delta H}{RT}\right) \sinh\left(\frac{\sigma V_a}{RT}\right)$  and as a result the subcritical crack growth rate  $dr/dt$  could scale as;

$$\frac{dr}{dt} = \dot{r}_0 \exp\left(-\frac{\Delta H}{RT}\right) \sinh\left(\frac{\sigma V_a}{RT}\right) \quad \text{eq. 6.18}$$

In other words if each irreversible step of crack growth in the subcritical regime is thermally and stress activated, then the crack would grow faster for higher temperatures and slower for lower temperatures. Since in our cavitation experiments we are applying loading ramps at a constant strain rate we expect the samples loaded at high temperature to reach a critical crack size (by subcritical crack growth) for macroscopic growth, faster, i.e. at lower stresses. This effectively corresponds to adjusting  $r_0$  rather than  $G_c$  to adjust the model to the data (see Figure 6.13). The different  $r_0$  obtained at different temperatures (for PU8000) fitted into the curve are:  $7.7\mu\text{m}$ ,  $8.6\mu\text{m}$ ,  $8.8\mu\text{m}$ ,  $9.9\mu\text{m}$ , at  $25^\circ\text{C}$ ,  $50^\circ\text{C}$ ,  $70^\circ\text{C}$  and  $100^\circ\text{C}$ .

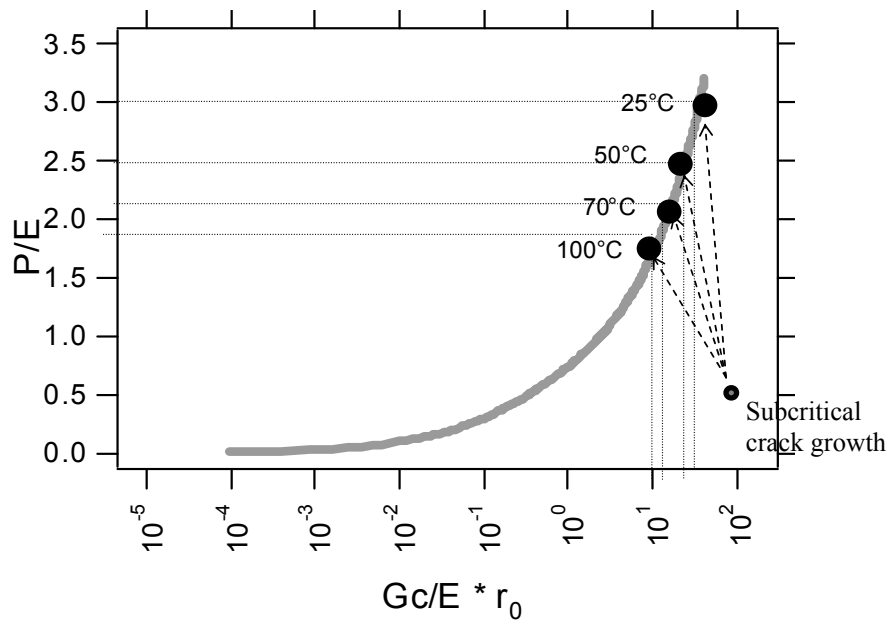


**Figure 6.13:** Sub-critical crack growth: Thermally activated.

At this stage it is difficult to decide which behaviour is the most likely to dominate the response of the material and we need to consider further results.

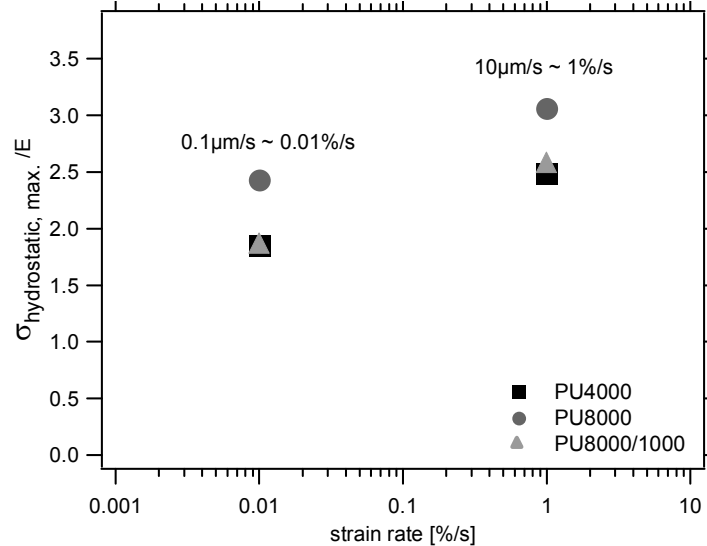
### 6.3.- Model-experiment comparisons: Speed dependence

Since the thermal activation hypothesis implies that the probability of nucleation of a macroscopic cavity increases with time we have carried out experiment at the same temperature but at different strain rates.

Figure 6.14 shows the normalized fracture stress as a function of macroscopic strain rate ( $v/h$ ). For all 3 networks the fracture stress increases with strain rate and for both rates the PU800 has a higher cavitation threshold than the other two materials.

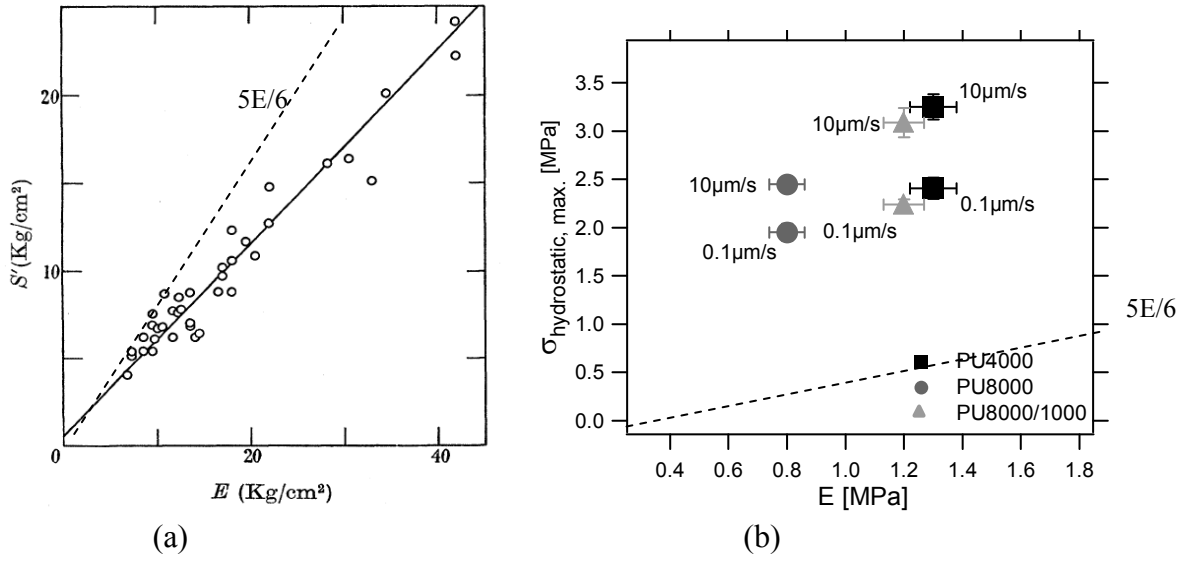
#### 6.3.1.- Fitting of the experimental results at different speeds

Figure 6.15b shows that the rate of strain rate is important for the fracture resistance, yet the rate at which the cavity expands from the video images remains the same as discussed in 5.2.1.2. This implies somehow that a time dependence of the nucleation of cavitation process exists and none of the cavity growth models by fracture or expansion take the time dependence into account.



**Figure 6.14:** Maximal hydrostatic stress  $\sigma_{\text{hydro, max}}$  normalized by the modulus, for the three polyurethane model networks: as a function of the crosshead speeds  $10\mu\text{m/s}$  (strain rate  $\sim 1\%/s$ ) and  $0.1\mu\text{m/s}$  (strain rate  $\sim 0.01\%/s$ ), and  $25^\circ\text{C}$ .

We also observe in Figure 6.15 (b) that for our experimental results for the three polyurethane model networks the maximal hydrostatic stress  $\sigma_{\text{hydrostatic, max}}$  at different speeds is significantly higher than the predicted criterion of critical pressure  $P_c = 5E/6$ .



**Figure 6.15:** Comparison of maximal hydrostatic stress  $\sigma_{\text{hydro, max}}$  as a function of the modulus for (a) Vulcanizates (taken from Gent and Lindley 1959); (b) the three polyurethane model networks at two speeds 10  $\mu\text{m/s}$  (strain rate  $\sim 1\%/s$ ) and 0.1  $\mu\text{m/s}$  (strain rate  $\sim 0.01\%/s$ ), and 25°C.

To compare the experimental results at different speeds with the fracture model, there is an important consideration to make. As mentioned in section 6.2, the different speeds of the cavitation experiments were 10  $\mu\text{m/s}$  (strain rate  $\sim 1\%/s$ ) and 0.1  $\mu\text{m/s}$  (strain rate  $\sim 0.01\%/s$ ). We carried out  $G_{\text{Ic}}$  (DEN geometry) tests at 25°C, strain rate 0.67%/s (at standard conditions) which can be used for both speeds of the cavitation experiments.

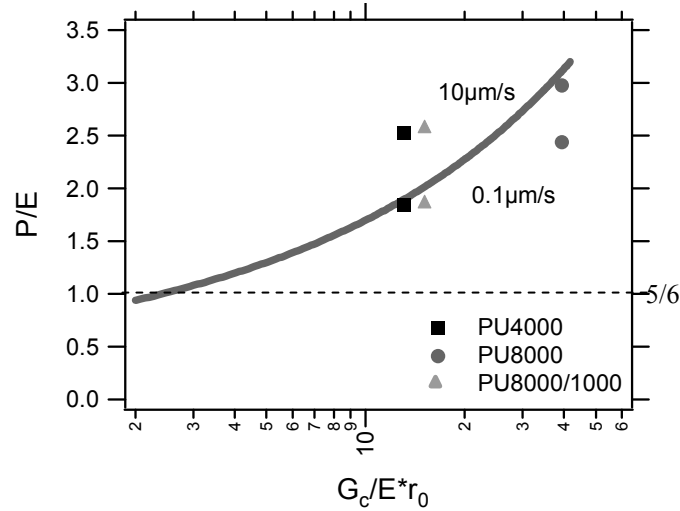


**Figure 6.16:** Fitting of our experimental data to the theoretical predicted curves using  $r_0 = 8 \mu\text{m} = 8 \cdot 10^{-6}\text{m}$ , for the three polyurethane model networks: using  $G_c$  at 25°C.

However the initial cavity growth rate is approximate between 10-30mm/s) for the three polyurethane model networks, at both speeds 10  $\mu\text{m/s}$  and at 0.1  $\mu\text{m/s}$ . Since the cavity growth is approximately the same for both cavitation rates (very fast independently of the pulling

rate), then the  $G_c$  can not be an ‘adjustable’ parameter when changing the speed. Then, what may control the rate dependence is the initial cavity size  $r_0$ . Slow strain rates favour subcritical crack growth by loading the material over much longer periods of time. As a result the stress required to grow a macroscopic crack decreases with strain rate. Figure 6.16 shows data and model using one arbitrary  $r_0$  (i.e.  $r_0 = 5 \mu\text{m} = 5 \cdot 10^{-6}\text{m}$ ) and the same  $G_c$  (the fast strain rate  $G_c$  for both speeds). It is clear that the model fits very poorly the data obtained at two strain rates suggesting here much more clearly that a probabilistic view of the cavitation process is necessary to make lifetime predictions.

## 6.4.- Statistics: Number of pre-critical cavities and position distribution

At the end of chapter 5 we presented experimental evidence demonstrating that small cavities (called pre-critical) appear in certain conditions before catastrophic fracture occurs. The number, position and time of appearance of these pre-critical cavities can be analyzed further.

### 6.4.1.- Cumulative probability of cavitation

Some statistics, by using the cumulative probability of all the pre-critical cavities observed for each material and condition, was done. Three samples of each material and condition were used to calculate the cumulative probability of cavitation at a given hydrostatic stress depending on the experimental conditions. This was an interesting form of looking at the position distribution (dispersion) of the pre-critical cavities in the samples and to compare this dispersion for the three polyurethane model networks, and additionally to demonstrate (in a different form than in the graphs presented in the preceding chapter) the amount of pre-critical cavities present per condition and material.

Supposing that for a given test condition (i.e. network, strain rate, temperature), the  $N$  pre-critical cavities are independant events. Then the  $N$  events can be ordered by ascendant hydrostatic stress  $\sigma_{j,\text{hydrostatic}}$  ( $i=1, 2, \dots, N$ ). For each experimental hydrostatic stress, a cumulative probability  $P_i$  of cavitation is associated. As it is done in Weibull’s treatments [Weibull 1951], the cumulative probability can be defined by:

$$P_i = \frac{i}{N+1} \quad \text{eq. 6.19}$$

Figure 6.17 shows the cumulative probability of cavitation as a function of hydrostatic stress. As defined in the model, an increasing hydrostatic stress leads to a higher probability of pre-critical cavities appearance. In these graphs, for a given experimental condition, the slope traduces the distribution of events (i.e. distribution of defect size).

Figure 6.17 (a) shows the cumulative probability for PU4000, and we observe that significantly more pre-critical cavities appear at low strain rate than at high temperature, while the position distribution of the pre-critical cavities in the sample is similar (similar

slope); this position distribution (slope) is also similar for the pre-critical cavities at standard conditions, but at higher hydrostatic stresses.

Figure 6.17 (b) shows the cumulative probability for PU8000. We observe that more or less the same amount of pre-critical cavities at low strain rates and at standard conditions are present, while fewer amounts of pre-critical cavities are present at higher temperatures. The distribution of the pre-critical cavities seems to be similar (similar slope) for all conditions. However, for higher temperature, it is difficult to conclude (more experimental data would be necessary). We also observe that the hydrostatic stresses are lower at lower strain rate and higher temperature than at standard conditions.

Figure 6.17 (c) shows the cumulative probability for PU8000/1000. Here, the amount of pre-critical cavities is nearly the same at lower strain rate and at standard conditions, while less amount of pre-critical cavities appear at higher temperature. The position distribution of the pre-critical cavities in the sample is similar (similar slope) at low strain rate and high temperature, while apparently there is a higher dispersion of pre-critical cavities at standard conditions.

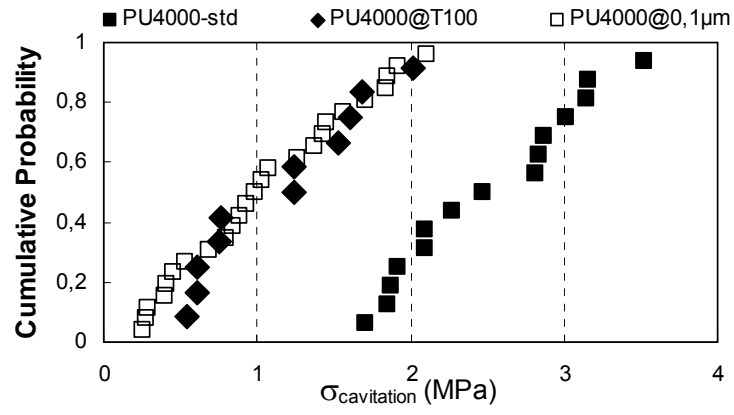
In general, for the three conditions is shown a higher dispersion of the pre-critical cavities for PU4000 and PU8000/1000 than for PU8000.

#### **6.4.2.- Spatial distribution of pre-critical cavities**

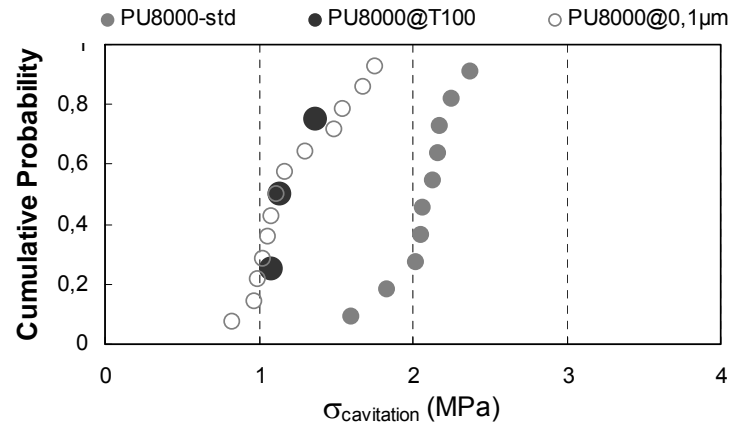
Focusing the analysis on the number of pre-critical cavities as a function of the position in the sample (radius), Figure 6.18 shows the data when the numbers of pre-critical cavities that appears are classified from the center of the sample (0mm) to the edge of the sample (5mm). Figures 6.18 (a), (b) and (c) show the number of pre-critical cavities as a function of the radius (from the center to the edges) at standard conditions, high temperature and low strain rate, respectively, for the three polyurethane model networks.

We observe that most of the cavities appear very close to the center of the sample (less than 2mm from the center of the cavitation sample) where the hydrostatic stress is maximal and this happens for the three experimental conditions. With these graphs we re-validate the choice of our cavitation sample geometry sphere-to-flat, as a good geometry to avoid multicavitation and big dispersion of the cavities everywhere in the sample. We observe that most of the cavities appeared very close to the center and almost no cavities appeared at further distances than ~3.5 mm from the center of the sample.

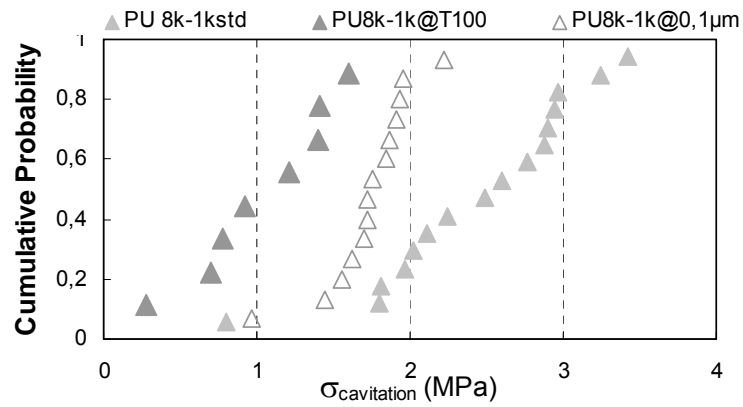




(a)



(b)



(c)

**Figure 6.17:** Cumulative Probability of cavitation: Pre-critical cavities analysis for (a) PU4000, (b) PU8000, and (c) PU8000/1000. Note that the cavitation stress  $\sigma_{\text{cavitation}}$ , corresponds to the local hydrostatic stress.

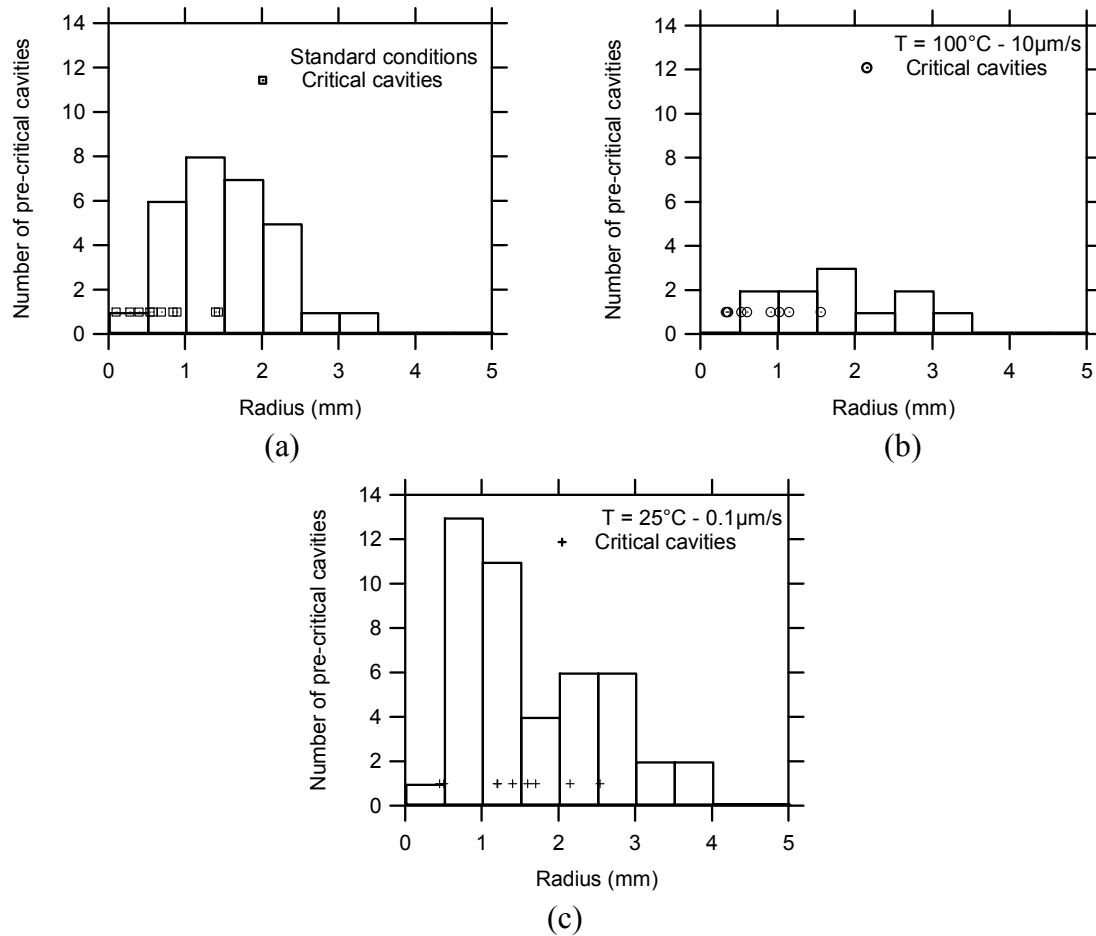


**Figure 6.18:** Number of pre-critical cavities as a function of the position along the radial direction of the sample at (a) standard conditions, (b) high temperature 100°C and (c) low speed 0.1 μm/s.

### Summary of the statistic analysis of pre-critical cavities

The presence of pre-critical cavities depends clearly very markedly on the material and on the conditions. More pre-critical cavities appear at a lower strain rate (i.e. PU4000) and very few pre-critical cavities appear at high temperature.

The three materials behave quite differently concerning their sensitivity to these two mechanisms: The indications are that a softer material containing trapped entanglements (PU8000) as well as homogeneous crosslinks (PU8000/1000) can give a relatively high resistance to the nucleation of these precritical cavities. Interestingly PU8000/1000 has a cavitation strength higher than PU4000 and the pre-critical nucleation rate at low strain rate is clearly less pronounced than for the PU4000.

Since the fracture toughness  $G_c$  decreases both with rate and temperature but the pre-critical cavities do differently, this implies that the toughness does not control by itself the appearance of these cavities.

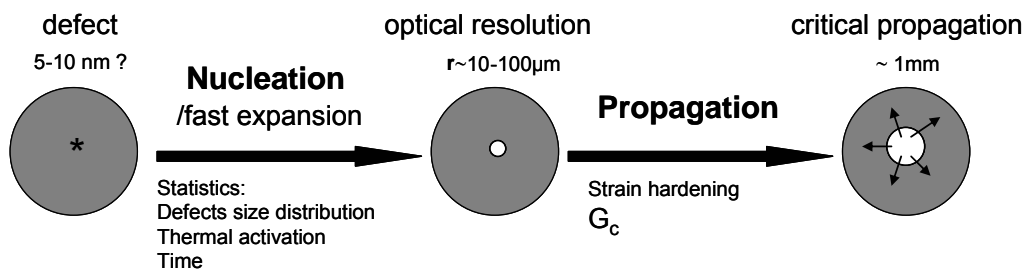
These results shed an interesting light on the whole initial problem and reveal some interesting and previously hidden differences between the materials. First, concerning the

effect of loading conditions, for all materials the increase in temperature results in less precritical cavities appearing (or even none for the PU8000) before catastrophic fracture. On the other hand reducing the strain rate has exactly the opposite effect, i.e. increasing the rate of nucleation of precritical cavities. These points reveal the existence of two separate “cavitation” mechanisms. A nucleation mechanism which is sensitive to time more than temperature, and a fracture mechanism which is accelerated by temperature more than time.

We can conclude that the change in strain rate acts mostly on the cavities nucleation while the temperature change acts probably mostly on the toughness. As a result both effects must be considered to predict the cavitation resistance.

## Conclusions

- The simple deformation model [Gent and Lindley 1959] considered that the cavity was in an infinite medium growing by deformation at constant applied true stress and with no surface tension. This model predicting a cavitation strength increasing linearly with the modulus  $E$  does not fit at all the experimental results for a given material at different temperatures.
- The linear model of fracture provides a reasonable approximation to the energy release rate  $G$ , but this approximation was not enough to predict quantitatively the differences between materials. The limited extensibility of the chains in the network, i.e. the strain hardening of the materials and the initial cavity size  $r_0$  has also to be included in the predictive models for resistance to cavitation.
- The temperature dependence of the cavitation strength for a given elastomer is clearly not controlled by the modulus alone but also by the fracture toughness  $G_c$ .
- However when we compare our tested model networks at different strain rates by using the existing models to predict cavitation, we obtain that  $E$  and  $G_c$  alone are not good general predictors of the cavitation strength, then the critical size of the cavity at which fracture occurs has to be taken into account. This implies that subcritical crack growth occurs before catastrophic fracture.
- Since the fracture toughness  $G_c$  decreases both with rate and temperature but the pre-critical cavities do differently, this implies that the toughness does not control by itself the appearance of these cavities. We can conclude that the change in strain rate acts mostly on the cavities nucleation while the temperature change acts mostly on the toughness. Then both effects must be considered to predict the cavitation resistance.
- The appearance of pre-critical cavities before catastrophic failure implies the existence of two separate criteria, one for nucleation and one for propagation:



The cavitation strength depends on the hydrostatic stress  $\sigma_{\text{hydrostatic, max.}}$ , the temperature and the time, then the Gent and Wang's model is so far the best general idea to predict cavitation

resistance. However, to obtain a good estimate of the energy release rate  $G$ , it was necessary to implement a FEM model by using Hui's methodology.

### **Acknowledgements**

In this chapter we would like to thank Professor C.Y. Hui in the department of Theoretical and Applied Mechanics at Cornell University in Ithaca, USA for interesting comments and suggestions, as well as his PhD student L. Rong for the penny-shaped crack FEM simulation.

## Appendices A6

### Appendix A6.1: FEM simulation for a penny-shaped crack in an infinite material subjected to internal pressure.

#### Problem definition

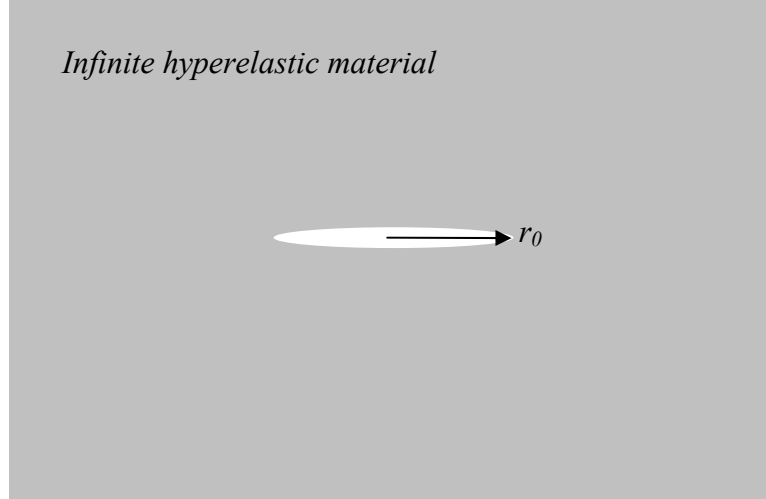


**Figure A6.1:** Schematic of the crack. This is a cross section of an axisymmetric object.

Figure A6.1 shows a circular crack in an infinite media with Young's modulus  $E$ . Initially the crack has a radius of  $r_0$ . Suppose we apply internal pressure  $P$  to the crack (this is equivalent to applying a uniform pressure field  $P$  at infinity). The aim is to find out how the energy release rate  $G$  varies with internal pressure. According to the previous paper by Y.Y Lin and C.Y. Hui [Lin and Hui 2005], one can calculate the energy release rate using the following formula:

$$G = \frac{3}{2\pi r_0^2} \int_0^P V(P') dP' \quad \text{eq. A6.1}$$

where  $V(P')$  is the deformed volume of the crack subjected to the internal pressure of  $P'$ . We introduce the normalization as following:

$$\bar{G} = G / Er_0, \quad \bar{P} = P / E, \quad \Omega = V / r_0^3 \quad \text{eq. A6.2}$$

Therefore, equation A6.1 becomes:

$$\bar{G} = \frac{3}{2\pi} \int_0^{\bar{P}} \Omega(\bar{P}') d\bar{P}' \quad \text{eq.A6.3}$$

The reason we use equation A6.1 or A6.3 to determine energy release rate is because it only requires the volume of deformed crack instead of the local stress field near the crack tip (for example, through J-integral). It is easier to obtain the displacement field than the stress field with FEM method and the result for displacement field is also more accurate.

### **Appendix A6.2: FEM simulation**

We used ABAQUS<sup>TM</sup> to implement the FEM simulation. By symmetry, only a quarter of the cross section is needed in the calculation. The mesh and boundary conditions are shown in Figure A6.2. We increase the pressure with a fixed increment  $\Delta P = 0.01E$  and obtain the crack face profile for each pressure step. From the crack face profile, we calculate the deformed crack volume in Matlab and use equation A6.3 to calculate the energy release rate.

Because of large deformation, elements near the crack tip are highly distorted. Such distortions are avoided using a remeshing technique. Basically, one extracts the geometry from the previous step and applies a new mesh to it. The stress field from the previous calculation is mapped to the new mesh using interpolation via an ABAQUS subroutine, MAP SOLUTION.

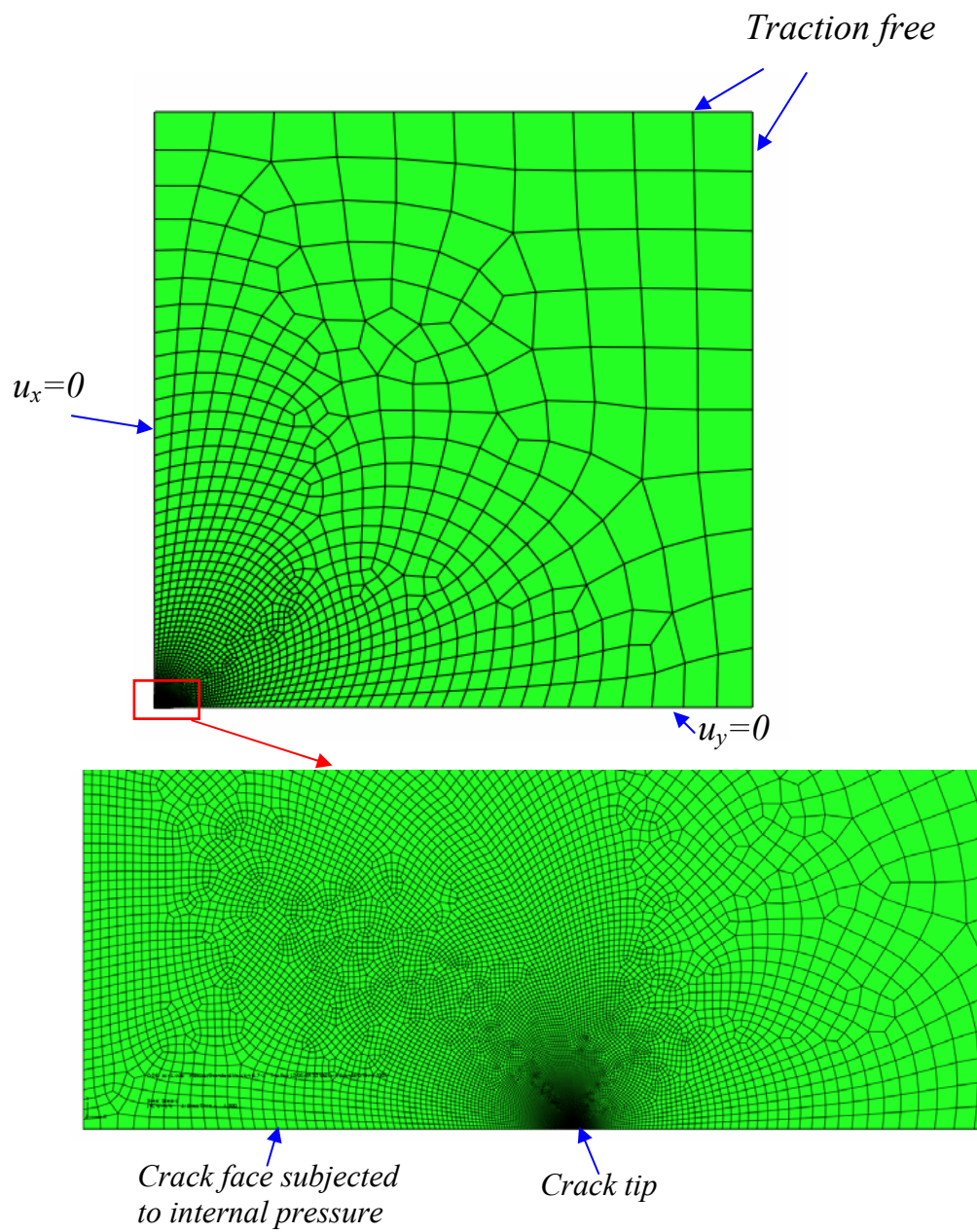


**Figure A6.2:** Mesh and boundary conditions in FEM simulation



## Bibliography

- Ball J.M., Phil. Transactions of the Royal Society of London, A306, 1496, 557-611 (1982).
- Busse W.F., Physics of rubber as related to the automobile, Journal of Applied Physics, 9, 438-451 (1938).
- Chiche, A.J., Dollhofer, J. and Creton, C., European Physical Journal E, 17, 389-401 (2005).
- Cho, K. and Gent, A.N., Journal of Materials Science, 23, 141-144 (1988).
- Chou-Wang, M.S. and Horgan, C.O., International Journal of Solids Struct., 25(11), 1239-1254 (1989).
- Denecour, R.L. and Gent, A.N., Journal of Polymer Science Part A-2, 6, 1853-1861 (1968).
- Diani, J., International Journal of Fracture, 112(2), 151-161 (2001).
- Fond, C., Lobbrecht, A., Schirrer, R., Int. Journal of Fracture, 77, 141-159 (1996).
- Fond, C. Journal of Polymer Science: Part B: Polymer Physics, 39, 2081-2096 (2001).
- Gent A.N. and Lindley P.B., Proc. Roy. Soc. A249, 195-205 (1959).
- Gent A.N. and Tompkins, D.A., J.Appl. Phy., 40, 2520, (1969)
- Gent, A. N., Engineering with Rubber, USA (1992).
- Gent, A. N. and Wang, C., Journal of Materials Science, 26, 3392 (1991).
- Gent, A.N. and Park, B., Journal of Polymer Science, 19, 1947-1956 (1984).
- Gent, A.N., Rubber Chemistry and Technology, 69, 59-61 (1996).
- Green A.E. and Zerna W., Theoretical elasticity, Oxford Univ. Press, London (1954).
- Griffith, H.S., Phil. Transactions of the Royal Society of London, A221, 163 (1920).
- Guarino, A., Ciliberto, S. and Garcimartin, A., Europhys. Lett. 47, 456-461 (1999).
- Hall, E.O., Proc. Physics Society, London, 64B, 747 (1951).
- Hamdi A., Université des Sciences et Technologies de Lille, Laboratoire de mecanique de Lille UMR, PhD thesis (2006)
- Herrmann, L.R. and Toms, R.M., J. Appl. Mech. Trans. ASME, 85, 140-141 (1964).
- Herrmann, L.R., AIAA J., 3 (10), 1896-1900 (1985).
- Horgan, C.O. and Pence, T.J., Journal of Elasticity, 21, 61-82 (1989).
- Horgan, C.O. and Abeyaratne, R., Journal of Elasticity, 16, 189-200 (1986).
- Hou, H.S. and Abeyaratne, R., Journal of Mechanics Phys. Solids, 40(3), 571-592 (1992).
- Kakavas, P.A. and Chang, W.V., Journal of Applied Polymer Science, 42, 1997 (1992).
- Lin, Y.Y. and Hui, C.Y., International Journal of Fracture, 126, 205-221 (2004).
- Lindsey, G.H., Schapery, R.A., Williams, M.L. and Zak, A.R., Report of the California Institute of Technology, Aerospace Research Laboratories, USA Air Force (1963).
- Lindsey, G.H., Journal of Applied Physics, 38 (12), 4843-4852 (1967).
- Oberth, A.E. and Bruenner, R.S., Trans. of the Society of Rheology, 9(2), 165-185 (1965)
- Oberth, A.E., Rubber Chemistry and Technology, 40, 1337-1363 (1967)
- Petch, N.J., Journal Iron Steel Institute, London, 174, 174 (1953).
- Polignone, D.A. and Horgan, C.O., Journal of Elasticity, 33, 27-65 (1993a).
- Pond, T.J., Journal of Natural Rubber Res., 8(2), 83-101 (1993).
- Seitz, M.E., Martina, D., Baumberger, T., Krishnan, V.R., Hui, C.Y. and Shull, K.R., Soft Matter, 5, 447-456 (2009).

Yerzley, F.L. Adhesion of Neoprene to metal, Ind. and Eng. Chem., 31, 950-956 (1939).  
Weibull W., Journal of Applied Mechanics, 18, 293 (1951).  
William M.L. and Schapery R.A., Int. Journal of Fracture Mechanics, 1, 64-72 (1965).



## General Conclusions

In this thesis we studied the fracture by cavitation of model polyurethane elastomers. The main objective was to establish the role played by the composition and crosslinking structure of elastomers on their resistance to cavitation under a predominantly hydrostatic pressure. To accomplish our objective we worked with three polyurethane model networks prepared from triisocyanate and diols (PPGs) of various molecular weights.

The specific sphere-to-flat geometry for the cavitation sample allowed us to observe most of the time one single critical cavity very close to the centre of the sample. The transparency of the samples, the synchronized visualization and data acquisition in the cavitation experiments, and the double visualization (from the top and lateral) let us visualize the early stages of the appearance of pre-critical cavities as well as the critical cavity.

Despite the difficulty in obtaining purified products and the reactivity of the isocyanate, we developed a protocol of purification of the three poly(ethylene) glycols and the polyisocyanate (reagents) to have a good control on the stoichiometry of the reactions. A systematic and in-depth characterization of the reagents showed that the precursor chains were monodisperse, and the molecular weights were very close to the values given by the manufacturers. Using a fully uncatalyzed two-stage curing procedure, we have been able to synthesize reproducible polyurethane model networks with well defined molecular structures and to prepare these networks in different types of molds without any problems of bubbles, macroscopic heterogeneities or degradations due to oxidation. Three different kinds of polyurethanes model networks were prepared with the idea of establishing comparisons among them regarding the molecular structure and the mechanical properties.

The networks obtained had very low sol fractions, and a very elastic behavior above room temperature implying a very high degree of perfection. The stoichiometric ratio used to obtain the networks was very close to the theoretical one. The low level of defects of the networks was confirmed by the clear thermoelastic behavior dominated mainly by entropic elasticity and by the multiple quantum NMR result, showing very homogeneous and defect-free network architecture for the three networks.

Based on the DMA results and on the rubber elasticity theory, all three polyurethane model networks showed a deformation behavior between the affine and phantom models. The storage modulus of the networks increases from PU8000 < PU8000/1000 < PU4000. On the other hand the PU8000 is more dissipative than the other two materials above 20°C but has a lower  $T_g$  and a lower density. The comparison between the value of  $M_c$  obtained from the chemistry and that obtained from the elastic modulus suggested that the PU8000 contains both entanglements and crosslinks. This was not the case at all for the PU4000 and may be partially true for the PU8000/1000.

The tensile tests showed that the three model networks were brittle rubbers, as expected for very elastic materials. The Mooney plot revealed a low level of softening in all the three samples, except for the PU8000 where a fit to the Rubinstein-Panyukov model implied ~20% of contribution of entanglements to the modulus.

Compression experiments showed that the three model networks strain harden. By using an ‘exponential’ model’ (two parameters) both tensile and compression data could be fitted well, implying that our lubricated compression experiments were carried out properly. However the fitted finite extensibility of the three networks scaled, surprisingly, with the modulus. Although there was no direct evidence from the hysteresis it is possible that some damage to the two most brittle materials may have caused this counterintuitive result.

The fracture energies  $G_{Ic}$ , decrease significantly with increasing temperature and decreasing strain rate. These results were not expected for such elastic materials, implying that significant viscoelastic dissipation is active at the crack tip. The PU8000 was tougher than the two other networks at all temperatures, qualitatively consistent with the higher level of viscoelastic dissipation at high strain rate observed for PU8000 and PU8000/1000 than for PU4000. The lowest values of  $G_{Ic}$  measured (at high temperature or at very low strain rate) were probably close to threshold values and hence representative of the fracture of the network strands without much contribution of viscoelasticity.

For the cavitation experiments we chose the sphere-to-flat geometry for the cavitation sample’s preparation, mainly for practical reasons. This geometry gives less confinement but a slightly higher concentration of the hydrostatic stress toward the centre of the sample than the flat-to-flat geometry. The chosen aspect ratio  $a/h = 10/1$  together with the higher concentration of the stress to the centre for this geometry, allowed us to observe most of the time one single cavity very close to the centre of the sample.

A new samples’ holder was designed and built to perform the cavitations experiments. We obtained a quite stiff set-up in which the compliance was very low. This set-up was specially designed to have a good top view of the sample through one camera positioned in front of the machine and a good lateral visualization with a second camera. Thanks to the synchronization of the data acquisition and video imaging, it was possible to obtain the curves of force versus displacement for each sample and to know where and when the cavities appeared. Because the main interest of this Thesis was to look at the nucleation of cavitation our study was focused on the first part of the curve force versus displacement passing through three main ‘regions’:

- 1) the ‘linear’ initial part of the curve,
- 2) the region of appearance of the pre-critical cavities, which appears above a certain force and remain stable,
- 3) The critical cavity appearing and growing at the maximal force close to the centre of the sample. A high reproducibility in the curves of force versus displacement was obtained.

Simulations using a Finite Element Method (FEM) were performed to obtain the relation between the force applied to the sphere and the local hydrostatic stress. For this, a calibration factor was calculated for our specific geometry, independent of the elastic modulus and dependant on the Poisson's ratio and slightly on confinement. The combination of the calibration constant and the simulation of the radial stress distribution made it possible to calculate a reasonably accurate value of the local stress for cavity appearing in the sample before or at the peak force.

For a given elastomer the local hydrostatic stress at the peak force decreased markedly with increasing test temperature in contradiction with predictions from models based on cavity growth by deformation since thermoelasticity causes the elastomer to become stiffer with increasing temperature. On the other hand at a given temperature the cavitation stress increased with the modulus of the material in agreement with previous studies.

This apparent contradiction can be predicted by a modified version of the Gent and Wang model for cavity growth by irreversible fracture. Incorporating the strain hardening in the constitutive equation and the mode I fracture toughness in the model a reasonable prediction of  $P/E$  as a function of  $G_c/r_0E$  could be obtained. However the prediction worked quantitatively by assuming that the fracture energy measured in tension is relevant and that the initial defect size  $r_0$  is the same for all elastomers. This suggested that fracture energy and modulus are sufficient to predict fracture of an elastomer in a confined geometry.

For a given elastomer the local hydrostatic stress at the peak force decreased with decreasing strain rate. Since the growth rate of the critical cavity was roughly the same for both strain rates, this difference could not be explained by a difference in  $G_c$ . The most likely explanation is then the thermally activated subcritical growth of cracks in the material. A longer time under stress causing the growth of subcritical defects to a larger size, leading to fracture at lower average stresses.

This thermal activation of the nucleation process was confirmed by the appearance of stable pre-critical cavities before catastrophic fracture. The density of pre-critical cavities depended very markedly on the material and on the conditions (maximum for low rate and minimum for high temperature). This implied that the toughness does not control the appearance of these cavities (since  $G_{Ic}$  decreases both with rate and temperature but the pre-cavities do very differently). The temperature change acted mostly on the toughness but the time acts mostly on the nucleation. Both effects are important but toughness maybe dominant at high strain rates while resistance to subcritical crack growth may be important at low strain rates.

Comparing the networks with short and long chains (unentangled and entangled) it was clear that the entanglements toughen the material which stabilizes the crack growth even in confined conditions. Pre-critical cavities appeared much less frequently implying that either the initial defects were smaller or they grew more slowly under stress.

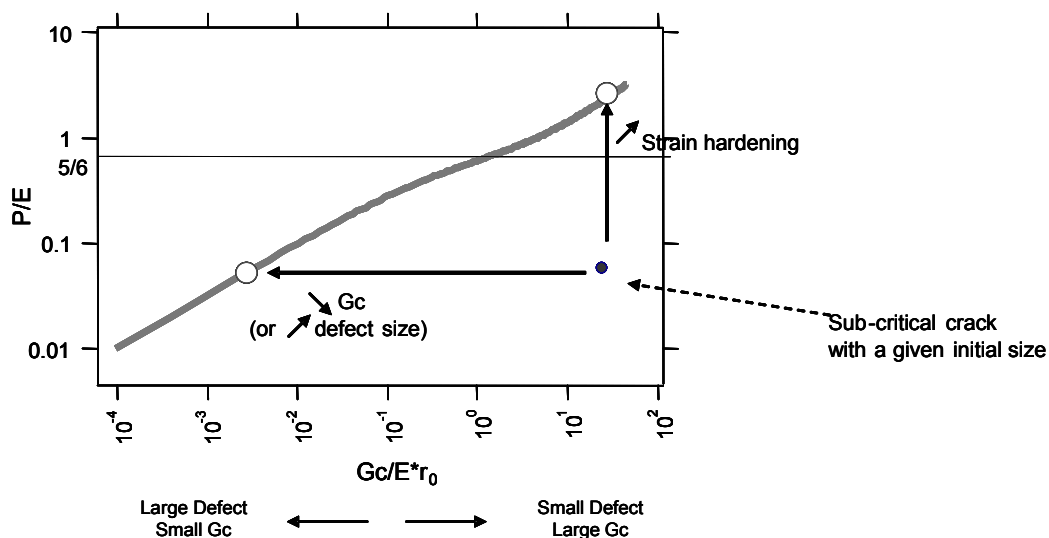
The indications were that a softer material containing trapped entanglements (PU8000) as well as homogeneous crosslinks (PU8000/1000) can give a higher resistance to cavitation compared to its modulus (PU8000) or toughness (PU8000/1000). PU8000/1000 had a cavitation strength higher than PU4000 and the pre-critical nucleation at low rate was less pronounced than for the PU4000.

The comparison between the long chains and a true bimodal network did not really reach its objective since the material remains very homogeneous (no clustering). However, the presence of short chains completely kills the entanglement effect in terms of toughness  $G_{Ic}$  but does not kill it in terms of slow growth in view that pre-critical cavities grow less for PU8000/1000 than for the 4000 at low rates.

### **Final remark**

An important practical question addressed in the thesis is the identification of guidelines for the design of a soft material with high resistance to cavitation. The schematic below show that based on the cavitation models and on our experimental results, to have a material more resistant to cavitation, a pronounced strain hardening combined with a high fracture toughness (or low defect size) is ideal.

From our three polyurethane model networks, these requirements are best fulfilled by PU8000. Additionally, since the fracture toughness  $G_c$  decreases both with rate and temperature but the pre-critical cavities do differently, this implies that the fracture energy  $G_{Ic}$  does not control by itself the appearance of these cavities. We can conclude that the change in strain rate acts mostly on the probability of nucleation of the cavities while the temperature change acts mostly on the toughness. However both effects are present and must be considered to predict the cavitation resistance.



*In conclusion for all elastomers the probability to nucleate and then grow a cavity depends on stress, time and temperature. While the temperature dependence seems to be predictable and rather universal, the stress and time dependence depends markedly on the chemistry of the material and cannot be reduced to the modulus. We have shown clearly that entanglements play a major role in increasing the resistance to cavitation and the fracture toughness of unfilled elastomers, suggesting that sparse but regular crosslinking is a good strategy.*





# Résumé en Français

## **1.- Introduction**

Les élastomères réticulés sont des polymères quasi-incompressibles qui, sous des conditions de chargement fortement triaxiales en tension, s'endommagent par nucléation et croissance de cavités. Expérimentalement, la cavitation des élastomères a été observée dans la littérature il y a un certain nombre d'années déjà, mais depuis très peu d'études expérimentales systématiques ont été menées. Et notamment, un aspect clé qui n'a pas été étudié expérimentalement est le rôle de la résistance à la rupture des élastomères sur la croissance des cavités. Différents modèles théoriques ont été proposés dans la littérature, les modèles initialement proposés se sont concentrés sur les mécanismes de déformation d'une cavité pré-existante ; ce n'est qu'en 1991, que Gent propose un nouveau modèle intégrant l'expansion de cavité avec la notion de taille de défaut et de rupture [Gent et Wang 1991]. Plus tard, Lin et al. revisitent et améliorent ce dernier modèle en effectuant un calcul éléments finis (E.F.) plus rigoureux [Lin et Hui 2004].

Nous avons étudié la fracture par cavitation dans des élastomères modèles de polyuréthane (PU) à base de polyéthers. Nous avons synthétisé, dans des conditions bien contrôlées, trois réseaux dits « modèles » de polyuréthane (PU) avec des masses molaires de chaînes entre points de réticulation inférieures ou supérieures à la masse molaire moyenne entre enchevêtrements de ce type de PU ( $M_e \sim 3000 \text{ g/mol}$ ).

L'objectif principal de cette thèse a été de déterminer le rôle joué par l'architecture macromoléculaire du réseau sur les propriétés élastiques non linéaires, la résistance à la rupture ainsi que la résistance à la cavitation sous chargement hydrostatique. Nous avons développé un dispositif original permettant de suivre la nucléation et la croissance de cavités sous chargement hydrostatique, à la résolution optique près, en temps réel, et synchronisé avec les données mécaniques. Les mécanismes observés et les valeurs de résistance à la cavitation suggèrent un rôle important de la dissipation viscoélastique ou de la croissance de défauts de taille sous-critique thermiquement activée.

## **2.- Partie expérimentale**

### **2.1.- Synthèse :**

Nous avons synthétisé, dans des conditions contrôlées des élastomères modèles de Polyuréthane, avec une chimie basée sur un triisocyanate (le tris (4-isocyanatophenyl) – thiophosphate) et des chaînes de PolyPropylène Glycols (PPG). Les trois réseaux modèles sont composés de trois types de PPG isomoléculaires ( $4000 \text{ g/mol}$ ,  $8000 \text{ g/mol}$  et  $1000 \text{ g/mol}$ ). En utilisant ces composants ont été synthétisés : deux réseaux homogènes avec des masses molaires entre les points de réticulation respectivement de  $4000$  et de  $8000 \text{ g/mol}$ , ainsi qu'un réseau hétérogène avec une fraction molaire de  $1/3$  de polyol de  $8000 \text{ g/mol}$  et  $2/3$  de polyol de  $1000 \text{ g/mol}$ . La synthèse est réalisée en absence d'eau (dans une boîte à gants), après un protocole précis de purification des réactifs qui a été optimisé. La réticulation a été effectuée

en conditions anhydres à 35°C pendant 48h puis à 80°C pendant 80 heures pour tous les réseaux. Les élastomères obtenus sont non chargés et parfaitement transparents.

## **2.2.- Caractérisations physico-chimie et essais mécaniques**

Une caractérisation physico-chimie fine des réactifs et des réseaux a été réalisée en utilisant des techniques telles que : RMN, FTIR, fractions solubles. Les propriétés mécaniques des trois réseaux modèles ont été analysées en menant des essais de traction, de compression, de rupture ainsi que des essais multifréquences en DMA afin de s'intéresser à la dissipation viscoélastique de ces réseaux.

Les modules élastiques ont été caractérisés par DMA pour chaque réseau et les propriétés à rupture des différents systèmes ont été testées sur des éprouvettes entaillées en géométrie DENT (« Double Edge Notched Tension »).

Pour étudier les mécanismes de cavitation, une variation sur l'essai de « poker-chip » a été développé. L'échantillon de PU est pris en « sandwich » entre deux plaques de verre. Les essais de cavitation ont été effectués avec une machine d'essai de traction MTS 810 avec un porte échantillon conçu au laboratoire. Le dispositif permet d'appliquer un état de contrainte hydrostatique au centre de l'échantillon et de suivre, par transparence, les mécanismes de formation de cavités. Chaque essai a été filmé par une caméra sur le côté et une, au dessus, afin d'observer en temps réel et de façon synchronisée le processus de cavitation et de rupture ayant lieu pendant l'essai de traction.

## **3.- Résultats et discussion**

### ***Module élastique aux petites déformations – température de transition vitreuse***

Les réseaux obtenus ont des fractions solubles très basses (en dessous de 3%), et un comportement très élastique au-dessus de la température ambiante, impliquant un très haut degré de perfection. Le faible niveau de défauts des réseaux (chaînes pendantes, boucles, etc.) a été confirmé par le comportement thermo-élastique observé à faible niveau de déformation et confirme un comportement dominé principalement par l'entropie. D'après les résultats de DMA et la théorie d'élasticité caoutchoutique, les trois réseaux modèles de polyuréthane révèlent un module élastique aux petites déformations encadré entre les modèles affine et fantôme.

Dans le Tableau 1, figurent les modules de conservation  $E'$  et les  $\tan \delta$  obtenus en DMA à température ambiante et à 1Hz pour les trois systèmes. Les modules de conservation,  $E'$  des réseaux augmentent de PU8000 < PU8000/1000 < PU4000. D'autre part, le PU8000 avec une température de transition plus basse, est plus dissipatif que les autres deux matériaux au-dessus de 20°C. La comparaison entre la valeur de masse molaire moyenne entre points de réticulation,  $M_c$  obtenue théoriquement par la stoechiométrie et la caractérisation physico-chimique et celle obtenue via le module élastique, suggère que le PU8000 contienne des

enchevêtrements. Ceci n'est pas le cas pour le PU4000 et n'est que peut être partiellement vrai pour le PU8000/1000.

**Tableau 1:** Températures de transition vitreuse,  $T_{\alpha}$ , valeurs des modules et du  $\tan \delta$  obtenu par DMA à 1 hertz.

Matériaux	$T_{\alpha}$ (°C)	$E'$ [MPa] @25°C	$\tan \delta$ @25°C
<b>PU4000</b>	$-54.1 \pm 0.5$	$1.3 \pm 0.08$	$0.041 \pm 0.005$
<b>PU8000</b>	$-59.8 \pm 0.5$	$0.8 \pm 0.06$	$0.067 \pm 0.006$
<b>PU8000/1000</b>	$-56.4 \pm 0.4$	$1.2 \pm 0.07$	$0.057 \pm 0.004$

### *Comportement dissipatif et mécanique non-linéaire*

Les propriétés mécaniques, d'intérêt principal pour notre étude, ont été les propriétés viscoélastiques linéaires, les propriétés aux grandes déformations pour caractériser l'effet des enchevêtrements et de l'extensibilité limite des chaînes, ainsi que les propriétés de fracture.

La dissipation viscoélastique des trois réseaux de polyuréthane a été obtenue par des expériences multifréquences de DMA et les courbes maîtresses de module de conservation et de  $\tan \delta$  ont été construites. Ces résultats ont été liés aux résultats de fracture.

L'analyse de la rupture a été menée sur des éprouvettes entaillées en faisant varier la vitesse de déformation et la température pour obtenir le taux de restitution d'énergie critique ( $G_{Ic}$ ), qui est un paramètre « matériau ». En diminuant la vitesse de déformation et augmentant la température, la valeur seuil de l'énergie de rupture (minimale)  $G_0$  a été obtenue expérimentalement. Le taux de restitution d'énergie critique ( $G_{Ic}$ ) obtenu pour les différents matériaux et conditions a été utilisé pour interpréter les résultats de cavitation à la lumière des modèles déjà existants.

### *Mécanismes de cavitation dans les réseaux modèles*

Pour suivre la cavitation, un dispositif original a été développé afin de visualiser et de quantifier les premiers stades de l'endommagement: la nucléation et la croissance des cavités (Figure 1). L'échantillon est moulé entre une lentille en verre hémisphérique et une plaque de verre. Les deux verres ont été préalablement traités avec un aminosilane pour pouvoir former des liaisons covalentes entre le PU et la paroi de verre et obtenir une condition de parfaite adhésion entre l'élastomère et le substrat en verre (non glissement à la paroi). Une géométrie sphère-plan a été choisie, avec un confinement modéré ( $a/h=10$ ). Les paramètres «  $h$  » et «  $a$  » ont été mesurés avant chaque essai, mais étaient en général respectivement de l'ordre de 1 mm et 10 mm.



**Figure 1:** Géométrie expérimentale pour l'essai de cavitation. L'échantillon PU est entre la lentille hémisphérique en verre et la plaque de verre.

La Figure 2 présente une courbe Force-Déplacement typique d'un essai de cavitation. Les Figure 3 et 4 présentent les observations associées, respectivement en vue de dessus et en vue latérale.

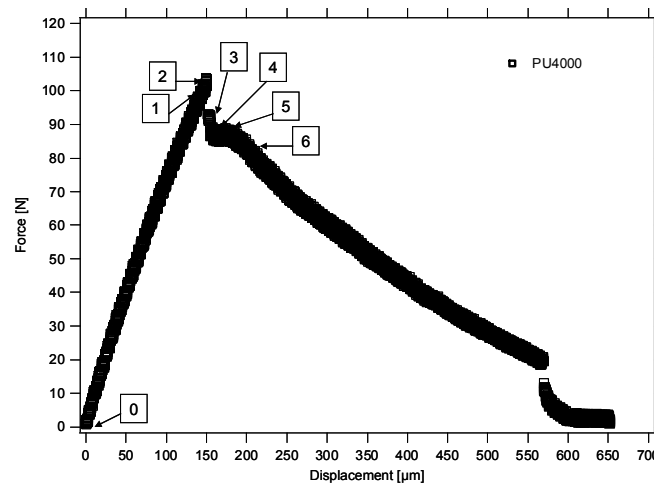


**Figure 2 :** Force vs déplacement d'un essai typique de cavitation.

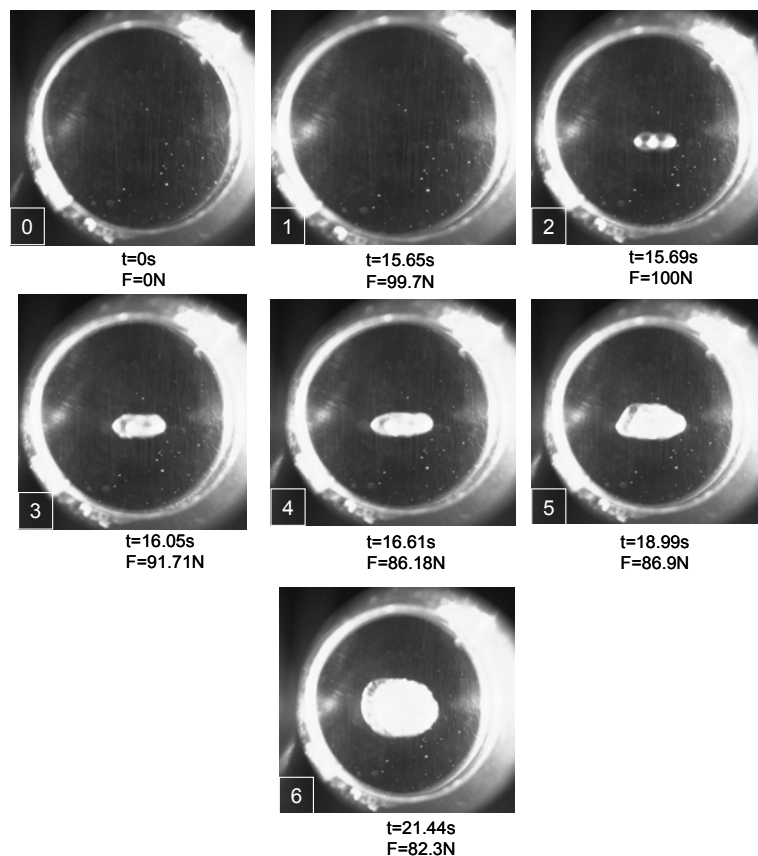


**Figure 3 :** Essai typique de cavitation (Vue de dessus). Les images correspondent aux temps et forces notés sur la courbe Force-Déplacement.

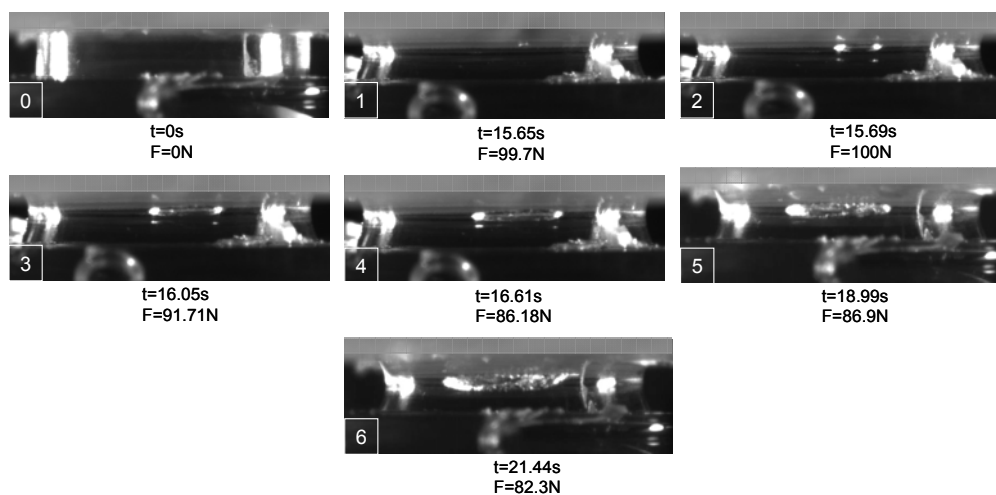


**Figure 4 :** Force vs déplacement d'un essai typique de cavitation (Vue latérale). Les images correspondent aux temps et forces notés sur la courbe Force-Déplacement de la figure 3.

Dans le but d'établir une relation entre l'architecture moléculaire des réseaux de polymère et leur résistance à la cavitation, nous avons étudié et avons comparé les trois réseaux modèles de polyuréthane : PU4000, PU8000 et PU8000/1000.

Plusieurs aspects ont été examinés :

- 1) L'usage de la contrainte maximale hydrostatique pour prédire la résistance à la cavitation ;
- 2) L'effet de changer les paramètres expérimentaux sur la forme des courbes force vs déplacement ;
- 3) L'effet de la température et l'activation thermique possible du processus ;
- 4) L'effet de la vitesse de chargement sur la cavitation en raison de la viscoélasticité des matériaux ;
- 5) La vitesse de croissance après l'apparition de la cavité critique ;
- 6) L'observation des faciès de rupture après la cavitation, et
- 7) Une étude qualitative de cavités pré-critiques a été faite.

Les essais de cavitation ainsi que les essais de rupture ont été réalisés à quatre températures différentes et à quatre vitesses de traverse différentes. Les résultats montrent que le module élastique du matériau augmente avec la température (Figure 5) alors que la contrainte critique de cavitation diminue, en désaccord avec les résultats prédits par Gent [Gent et Lindley 1959]. Contrairement à ce modèle d'instabilité élastique communément utilisé, nos résultats montrent que l'expansion critique de la cavité n'est pas directement pilotée par le module, mais également par l'énergie de rupture,  $G_c$ , par le durcissement dû à l'extensibilité finie des chaînes du réseau ainsi que des propriétés complexes telles que les mécanismes dissipatifs. Ce résultat suggère que la rupture de l'élastomère en conditions non confinées, affecte la résistance à la cavitation, ou qu'il y a une croissance significative d'une cavité sous-critique par activation thermique avant que la rupture finale ne soit observée.

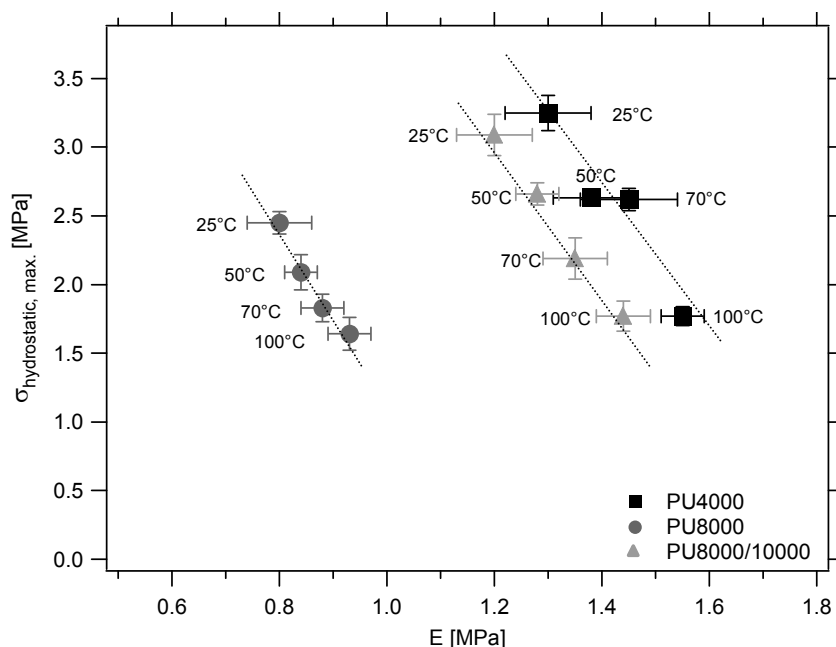


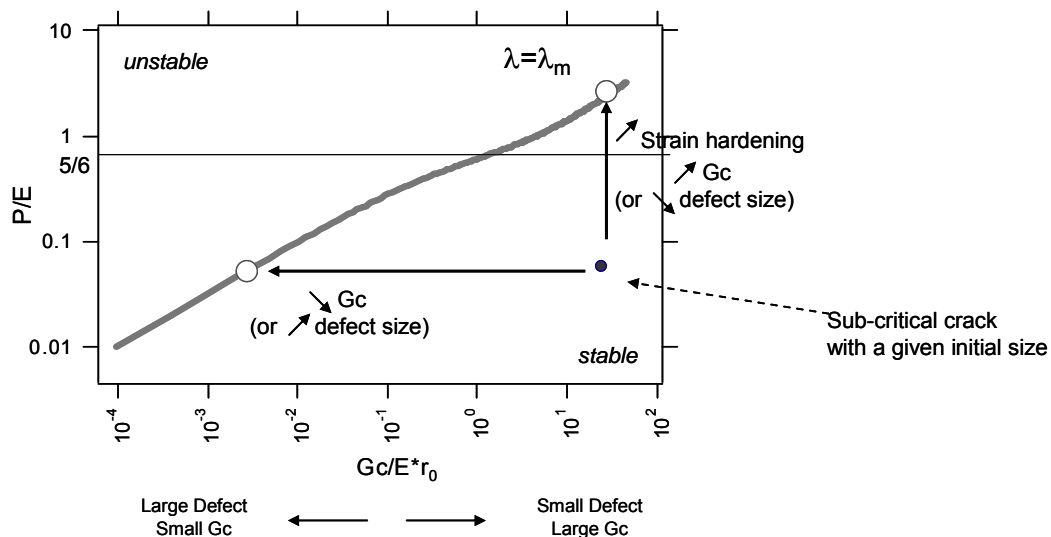
**Figure 5:** Contrainte hydrostatique locale de cavitation  $\sigma_{\text{hydro, max}}$  en fonction du module à différentes températures : 25°, 50°C, 70° et 100°C, et 10 $\mu\text{m/s}$ .



Par ailleurs, nous avons observé l'apparition des cavités pré-critiques avant la fracture catastrophique ; ce qui semble mettre en évidence l'existence de deux critères : l'un, propre au processus de nucléation, principalement piloté par des mécanismes statistiques (défauts, temps, température, etc.); et l'autre, lié à la croissance de la cavité en milieu confiné contrôlé par  $G_{IC}$ , et par le comportement aux grandes déformations. Enfin, la présence d'enchevêtrements dans l'architecture du réseau macromoléculaire s'est avérée clairement bénéfique pour stabiliser la croissance de cavités et donc pour renforcer la résistance à la cavitation.

A la question, comment rendre un réseau élastomère plus résistant à la cavitation ? ; nos résultats expérimentaux permettent de répondre. Afin d'augmenter la résistance à la cavitation, le matériau doit avoir un durcissement prononcé (« strain hardening ») combiné avec une grande résistance à la rupture ( $G_{IC}$  grand ou bien une petite taille de défaut).

Sur les trois réseaux modèles de polyuréthane, ces conditions sont mieux remplies par l'échantillon PU8000.



#### 4.-Conclusion

Nous avons enfin conclu que, en général, pour les élastomères la probabilité d'avoir nucléation et croissance d'une cavité dépend de la contrainte hydrostatique appliquée, du temps et de la température. Alors que la dépendance en température semble être plutôt déterministe, en jouant principalement sur la résistance à la propagation de la rupture ; la dépendance en temps et au niveau de contrainte hydrostatique appliqué dépend nettement de l'architecture macromoléculaire du matériau et ne peut pas être réduite au simple module élastique. Nous avons clairement montré que les enchevêtrements jouent un rôle majeur dans l'augmentation de la résistance à la cavitation et de la rupture des élastomères non chargés.

## 5. Références

- Gent A.N. and Lindley P.B., Proc. Roy. Soc. A249, 195-205 (1959).  
Gent A.N. and Tompkins, D.A., J.Appl. Phy., 40, 2520, (1969)  
Gent, A. N. and Wang, C., Journal of Materials Science, 26, 3392 (1991).  
Lin, Y.Y. and Hui, C.Y., International Journal of Fracture, 126, 205-221 (2004).



## General Bibliography

- Abder-Rahim, D. « Synthèse in situ de microparticules polyuréthane par addition interfaciale dans un monomère epoxide ». Chapter II. PhD Thesis INSA de Lyon, (2001).
- Ahagon, A. and Gent, A.N, Journal of Polymer Science: Polymer Physics Edition, 13, 1903-1911 (1975)
- Alkonis, J.J. , Maxknight, W.J. and Shen, M., Introduction to polymer viscoelasticity, Wiley–Interscience/Wiley, New York (1972).
- Anderson T.L., Fracture Mechanics: Fundamentals and Applications, CRC Press, Boston (1995).
- Andrady, A.L. and Sefcik, M.D., Journal of Polymer Science: Polymer Physics Ed., 21, 2453 (1983)
- Andrady, A.L., Llorente, M. A. and Mark, J. E., Polymer Bulletin, 28, 103-108 (1992).
- Andrews, E. H., Proc. Phys. Soc. 77, 483 (1961).
- Arruda, E.M. and Boyce, M.C., Journal of the Mechanics and Physics of Solids, 41, 2, 389-412 (1993).
- Baker, J.W., Holdsworth, J.B, Journal of Chemical Society, 713–726, (1947).
- Ball J.M., Phil. Transactions of the Royal Society of London, A306, 1496, 557-611 (1982).
- Bayer data sheets ACCLAIM series (4000 and 8000g/mol), and Arch Chemical data sheets (1000g/mol).
- Bayraktar, E., Isac, N., Bessri, K. and Bathias, G., Fatigue and Fracture of Engineering Materials & Structures, 31, 2, 184-196 (2008).
- Beshah, K., Mark, J.E., Ackerman, J.L., Himstedt, A., Journal of polymer science. Polymer physics edition, 24, n°6, 1207-1225 (1986).
- Bos, H. L. and Nusselder J. J. H., Polymer, 35, 13: 2793-2799 (1994).
- Boulares A., Tessier M. and Marechal E., Journal of Macromolecular Science-Pure Appl. Chem., A35 (6): 933-953 (1998)
- Bueche, F. and Halpin, J.C., Journal of Applied Physics, 35, 36-40 (1964).
- Bueche, F., Physical Properties of Polymers, Interscience, New York (1962)
- Busse W.F., Physics of rubber as related to the automobile, Journal of Applied Physics, 9, 438-451 (1938)
- Chiche, A.J., Dollhofer, J. and Creton, C., European Physical Journal E, 17, 389-401 (2005).
- Cho, K. and Gent, A.N., Journal of Materials Science, 23, 141-144 (1988)
- Chou-Wang, M.S. and Horgan, C.O., International Journal of Solids Struct., 25(11), 1239-1254 (1989).
- de Gennes, P. G. C. R. Acad. Sci. Paris,II, 307, 1949-1953 (1988).
- Denecour, R.L. and Gent, A.N., Journal of Polymer Science Part A-2, 6, 1853-1861 (1968).
- Diani, J., International Journal of Fracture, 112(2), 151-161 (2001).
- Dickie R.A. and Smith T.L., Journal of Polymer Science, Part. A2, 7, 687-707 (1969).
- Edwards, S. F. and Vilgis, T., Polymer, 27, 483-492 (1986).
- Edwards, S.F. and Vilgis, T.A., Reports on Progress in Physics, 51, 2, 243-297 (1988).
- Erman, B. and Mark, J.E., Oxford University Press, New York (1997)

Evans, M.G. and Polanyi M., Trans. Faraday Society, 31, 875 (1935).

Eyring, H., Journal of Chemistry Physics, 3, 107 (1935).

Farben, I.G., German Patent 728.981, (1937)

Florez, S., Muñoz, M.E. and Santamaría, A., Macromolecules Materials Engineering, 291, 1194-1200 (2006).

Flory, P. J., Principles of polymer chemistry. Cornell University Press, Ithaca, NY. 1953.

Flory, P.J. and Rehner, J., Journal of Chemistry Physics, 11, 512 (1943).

Flory, P.J., Chem.Rev, 35, 51 (1944)

Flory, P.J., Polymer Journal, 17, 1, 1-12 (1985).

Fond, C. Journal of Polymer Science: Part B: Polymer Physics, 39, 2081-2096 (2001).

Fond, C., Lobbrecht, A., Schirrer, R., Int. Journal of Fracture, 77, 141-159 (1996).

Fowlkes, C., International Journal of Fracture, 10, 99-108 (1974).

Garrido, L., Mark, J.E., Ackerman, J.L., Kinsey, R.A., . ; KINSEY R. A., Journal of polymer science. Part B. Polymer physics, 26, n<sup>o</sup>11, 2367-2377 (1988).

Geede ULF. W., Polymer Physics, Kluwer Academic Publishers, 3<sup>rd</sup> edition (1999).

Gent A.N. and Tompkins, D.A., Journal of Applied Physics, 40, 2520, (1969)

Gent, A. N. and Wang, C., Journal of Materials Science, 26, 3392 (1991).

Gent, A. N. Engineering with Rubber, Hanser Publishers, USA (1992).

Gent, A. N. Rubber Chemistry and Technology, 69, 59-61 (1996).

Gent, A.N. and Lindley, P.B., Proc. Royal Society London, Ser. A, 249, 195 (1959)

Gent, A.N. and Meinecke, E.A., Polymer Engineering Science, 10, 48 (1970).

Gent, A.N. and Thomas, A.G., Journal of Polymer Science, 28, 265 (1958).

Gent, A.N. and Wang, C., Journal of Materials Science, 26, 3392 (1991).

Gent, A.N. and Park, B., Journal of Polymer Science, 19, 1947-1956 (1984).

Gent, A.N., Henry, R.L. and Roxbury, M.L., Journal of Applied Mechanics, 41, 855 (1974).

Gent, A.N., Rubber Chemistry and Technology, 67, 549-558 (1994)

Gent, A.N., Rubber Chemistry and Technology, 69, 59-61 (1996)

Goldwasser, J.M. and Adolph, H.G., Polymer Engineering Science, 26, 1510 (1986)

Gough, J., Mem. lit. Philosophical Society Manchester, 1, 288 (1805).

Green A.E. and Zerna W., Theoretical elasticity, Oxford Univ. Press, London (1954).

Greensmith, H.W. and Thomas, A.G., Journal of Polymer Science XVIII, 189 (1955)

Greensmith, H.W., Journal of Applied Polymer Science, 7, 993-1002 (1963)

Greensmith, H.W., Journal of Polymer Science, 21, 175-87 (1956).

Greensmith, H.W., Journal of Polymer Science, 3(8), 175-82 (1960).

Greensmith, H.W., Journal of Polymer Science, 8, 1113-28 (1964).

Griffith, H.S., Phil. Transactions of the Royal Society of London, A221, 163 (1920).

Griffiths, P. R. and De Haseth, J. A., Fourier Transform Infrared Spectrometry (Chemical Analysis: A Series of Monographs on Analytical Chemistry and Its Applications), Wiley-Interscience, 2 edition (2007).

Guarino, A., Ciliberto, S. and Garcimartin, A., Europhys. Lett. 47, 456-461 (1999).

Halary, J.L. and Lauprêtre, F., De la macromolécule au matériau polymère, éditions Belin (2006).

- Halary, J.L., Lauprête, F. and Monnerie, L., *Mécanique des matériaux polymères*, editions Belin (2008).
- Hall, E.O., Proc. Physics Society, London, 64B, 747 (1951)
- Hall, E.O., Proc. Physics Society, London, 64B, 747 (1951).
- Hamdi A., Université des Sciences et Technologies de Lille, Laboratoire de mecanique de Lille UMR, PhD thesis (2006)
- Herrmann, L.R. and Toms, R.M., J. Appl. Mech. Trans. ASME, 85, 140-141 (1964).
- Herrmann, L.R., AIAA J., 3 (10), 1896-1900 (1985).
- Hiemenz, P. C., and Timothy P. L., *Polymer Chemistry*. 2nd ed. Florida: Taylor & Francis Group, 486-491 (2007).
- Higgs, P.L. and Ball, R.C., Journal of Physics (Paris), 49, 1785 (1988).
- Horgan, C.O. and Abeyaratne, R., Journal of Elasticity, 16, 189-200 (1986).
- Horgan, C.O. and Pence, T.J., Journal of Elasticity, 21, 61-82 (1989).
- Hou, H.S. and Abeyaratne, R., Journal of Mechanics Phys. Solids, 40(3), 571-592 (1992).  
[http://scholar.lib.vt.edu/theses/available/etd-04122002-012440/unrestricted/chapter\\_4.pdf](http://scholar.lib.vt.edu/theses/available/etd-04122002-012440/unrestricted/chapter_4.pdf)  
[http://scholar.lib.vt.edu/theses/available/etd-04122002-012440/unrestricted/chapter\\_2.pdf](http://scholar.lib.vt.edu/theses/available/etd-04122002-012440/unrestricted/chapter_2.pdf)
- James, H. M. and Guth, E., Journal of Polymer Science, 4, 153-182 (1943).
- Joule, J.P., Phil. Trans. Royal Society, 149, 91 (1859).
- Kakavas, P.A. and Chang, W.V., Journal of Applied Polymer Science, 42, 1997 (1992).
- Kawabata, S., Journal Macromolecular. Science Physics, B8(3-4), 605-630 (1973).
- Kloczkowski, A., Mark, J. E. and Erman, B. Macromolecules, 24, 3266 (1991).
- Knott, J.F., *Fundamentals of Fracture Mechanics* (1973).
- Lake, G. J. and Lindley, P.B., Rubber Journal, 146 (10), 24-30 (1964).
- Lake, G. J., Lindley, P. B. and Thomas, A. G., Proc. Int. Conf Fract., 2nd, Brighton, Chapman and Hall, London, p. 493 (1969).
- Lake, G.J. and Lindley, P.B., J. Appl. Polym. Sci., 9, 1233-1251 (1965).
- Lake, G.J. and Thomas, A.G., Proc. R. Soc. London, Ser. A, 300, 108 (1967).
- Lake, G.J., Rubber Chemistry and Technology, 76, 567-591 (2003).
- Lawn B., *Fracture of Brittle Solids*, Cambridge University Press, 2nd edition (1993).
- Lin, Y.Y. and Hui, C.Y., International Journal of Fracture, 126, 205-221 (2004).
- Lindsey, G.H., Journal of Applied Physics, 38 (12), 4843-4852 (1967).
- Lindsey, G.H., Schapery, R.A., Williams, M.L. and Zak, A.R., Report of the California Institute of Technology, Aerospace Research Laboratories, USA Air Force (1963).
- Love, J.C., Estroff, L.A., Kriebel, J.K., Nuzzo, R.G. and Whitesides, G.M., Chemical Review, 105, 1103-1169 (2005).
- Marchessaultt, R., Bluhm, E. Rirem Gharapetianan, H., Pudupadr, D., Sundarakaj, I., Can J. Chem. 63. (1985)
- Marek W. Urban, *Attenuated Total Reflectance Spectroscopy of Polymers: Theory and Practice*, Oxford University Press (1996).
- Mark, J. E. and Erman, B., *Rubberlike Elasticity: A Molecular Primer*; Wiley-Interscience: New York (1988).
- Mark, J. E. Macromolecules Rev. 11, 135 (1976).

- Mark, J.E., Br. Polymer Journal, 17, 144 (1985).
- Mark, J.E., Macromolecules Sym., 77, 201 (2003)
- Mars, W.V. and A. Fatemi, A., D. Besdo, R. Schuster, J. Ihlemann (eds.), Swets and Zeitlinger, Netherlands, 213-222 (2001).
- Mars, W.V. and Fatemi, A., International Journal of Fatigue, 24, 949-961 (2002).
- Mars, W.V., Rubber Chemistry and Technology, 75, 1-18 (2002).
- Mazich, K.A., Samus, M.A., Smith, C.A. and Rossi, G., Macromolecules, 24, 10, 2766-2769 (1991).
- Menard, K.P., Dynamic Mechanical Analysis: A Practical Introduction, CRC-Press; 1 edition (1997)
- Miquelard-Garnier, G., Université Pierre et Marie Curie, Paris VI. PPMD-ESPCI. PhD thesis (2007)
- Mooney, M., Journal of Applied Physics, 11, 582 (1940).
- Mueller, H.K. and Knauss, W. G., Trans. Soc. Rheol., 15, 217-233 (1971)
- Mullins, L., Trans. Institute Rubber Ind., 35, 213-221 (1959)
- Mzabi, S, PhD thesis at PPMD-ESPCI, unpublished work
- O'Sickey, M. J. PhD thesis, 2002. University Library Virginia Tech, Chapter 2 and 4
- Oberth, A.E. and Bruenner, R.S., Trans. of the Society of Rheology, 9(2), 165-185 (1965)
- Oberth, A.E., Rubber Chemistry and Technology, 40, 1337-1363 (1967)
- Oclin, S. "A Molecular Printboard on Glass", PhD thesis, University of Twente, The Netherlands, (2004).
- Odian, G., Principles of polymerization, Wiley, New York, 1981.
- Oertel, G., Polyurethane Handbook. New York: Macmillen Publishing Co., Inc (1985).
- Pasch, H. and Schrepp, W., MALDI-TOF Mass Spectrometry of Synthetic Polymers, Springer; 1 edition (2003)
- Pavia, D. L. and Lampman, G. M., Introduction to Spectroscopy, Brooks Cole; 3 edition (2000).
- Persson, B.N.J., Albohr, O., Heinrich, G. and Ueba, H., Journal of Physics: Condensed Matter, 17, 1071-1142, (2005)
- Petch, N.J., Journal Iron Steel Institute, London, 174, 174 (1953)
- Petrovic, Z. S. and MacKnight, W. J., Bull.Slovenian Chem.Soc., 36(4), 405-422 (1989).
- Petrovic, Z. S., MacKnight, W. J., Koningsveld, R. and Dusek, K., Macromolecules 20, 1088 (1987).
- Polanyi, J.C., Science, 236 (4802), 680-690 (1987).
- Polignone, D.A. and Horgan, C.O., Journal of Elasticity, 33, 27-65 (1993a).
- Polymer Handbook, Brandrup, J. and Immergut, E.A. ; Wiley-Interscience : New York, p IV (1975).
- Pond, T.J., Journal of Natural Rubber Res., 8(2), 83-101 (1993).
- Randall, D.; Lee, Steve, The Polyurethanes Book. New York: Wiley. (2002).
- Rice, J.R., Journal of Applied Mech., 35, 379-386 (1968).
- Rivlin, R.S. and Thomas, A.G, Journal of Polymer Science, 10, 3, 291-318 (1953)

- Rivlin, R.S. in Eirich, F.R., Ed., *Rheology, Theory and Applications*, Vol. 1, Academic Press, New York, Chapter 10, (1956).
- Rivlin, R.S., *Phil. Trans. R. Soc. A*241, 379 (1948).
- Rubinstein, M. and Colby, R.H., *Polymer Physics*, Oxford University Press, USA (2003).
- Rubinstein, M. and Panyukov, S., *Macromolecules*, 35, 6670-6686 (2002).
- Saalwächter K., *Progr. NMR Spectrosc.*, 57, 1–35 (2007).
- Saalwächter K., Sommer, J-U., *Macromolecular Rapid Communications*, 28, 1455-1465 (2007).
- Saalwächter K., Ziegler, P., Spyckerelle, O., Haidar, B., Vidal, A., Sommer, J.-U., *J. Chem. Phys.*, 119, 3468 (2003).
- Schwartz, D.K., *Annu. Review of Physical Chemistry*. 52, 107 (2001).
- Seader, J. D. and Henley E. J., *Separation Process Principles*, Wiley; 2 edition ( 2005)
- Seitz, M.E., Martina, D., Baumberger, T., Krishnan, V.R., Hui, C.Y. and Shull, K.R., *Soft Matter*, 5, 447-456 (2009).
- Sepe, M., *Dynamical Mechanical Analysis for plastics engineering*, Dickten & Masch Manufacturing, Wisconsin, USA (1998).
- Smith, B. C., *Fundamentals of Fourier Transform Infrared Spectroscopy*, CRC, 1 edition (1995).
- Smith, T.L., *Journal of Polymer Science*, 32, 99-113 (1958).
- Smith, T.L., *Society Plastics Engrs. Journal*, 16, 1211 (1960)
- Steeman, P.A.M. & Nusselder, J.J.H., *Polymer Gels and Networks*, 3: 159-177 (1995).
- Sullivan, T. P. and Huck, W. T. S., *Eur. Journal of Organic Chemistry*, 17-29, (2003).
- Takeuchi, H, and Cohen, C., *Macromolecules*, 32, 6792. (1999).
- Techniques de l'ingenieur: Berthier, J. C., Polyurethane PUR*, AM 3 425 v2.
- Termonia, Y., in: S.M. Aharoni, Eds., *Plenum Press*, New York, p.201 (1992)
- Thomas A.G., *Journal of Polymer Science*, 18, 177–88 (1955).
- Thomas, A. G. “The Development of Fracture Mechanics for Elastomers,” Goodyear Medal paper presented to the American Chemical Society Rubber Division Meeting, Chicago, April 1994; *RUBBER CHEM. TECHNOL.* 67, G50 (1994).
- Thomas, A. G., *Journal of Applied Polymer Science*, 3, 168 (1960).
- Thomas, A. G., *Journal of Polymer Science*, 18, 177 (1955).
- Treloar, L.R.G., *The Physics of Rubber elasticity*, Oxford Classic Texts, third edition (2005).
- Ulrich, H., *Chemistry and Technology of Isocyanates*. New York: John Wiley & Sons, Inc (1996).
- Urayama, K., Kawamura, T., Kohjiya, S., *Polymer* 50, 347-356 (2009)
- Urayama, K., *Polymer Journal*, 40, 8, 669–678 (2008).
- Vos, J., G., Forster, R. J., Keyes, T. E., *Interfacial Supramolecular Assemblies*. Wiley, John & Sons, Incorporated, 88-94 (2003).
- Wall, F.T., *Journal of Chemistry Physics*, 10, 132 (1942).
- Ward, I.M. and Hadley, D.W., *An Introduction to the Mechanical Properties of Solid Polymers*, John Wiley and Sons, England (1998).
- Weibull W., *Journal of Applied Mechanics*, 18, 293 (1951).



- William M.L. and Schapery R.A., *Int. Journal of Fracture Mechanics*, 1, 64-72 (1965).
- Wnek, G. and Bowlin, G. L., *Encyclopedia of Biomaterials and Biomedical Engineering*. Informa Healthcare, 1331-1333 (2004).
- Woods, G., *The ICI Polyurethanes Book*. New York: John Wiley & Sons, Inc. (1990).
- Yerzley, F.L. Adhesion of Neoprene to metal, *Ind. and Eng. Chem.*, 31, 950-956 (1939).
- Yong, Z. and Wu, M., *Gaofenzi Xuebao*, 6, 401 (1988)
- Yoo, S. Y., Cohen, C and Hui, C.-H., *Polymer*, 47, 6226 (2006)
- Young, R.J. and Lovell, P.A. *Introduction to Polymers*, Chapman & Hall, (2nd Edition), London (1991).
- Zhuang, H., Sankarapandian, M.S., Ji, Q. and McGrath, J.E., *Journal of Adhesion*, 71, 231 (1999).